

On the physics of multimode polaritons

THÈSE N° 7603 (2017)

PRÉSENTÉE LE 17 MARS 2017

À LA FACULTÉ DES SCIENCES DE BASE
LABORATOIRE D'OPTOÉLECTRONIQUE QUANTIQUE
PROGRAMME DOCTORAL EN PHYSIQUE

ÉCOLE POLYTECHNIQUE FÉDÉRALE DE LAUSANNE

POUR L'OBTENTION DU GRADE DE DOCTEUR ÈS SCIENCES

PAR

Claudéric OUELLET-PLAMONDON

acceptée sur proposition du jury:

Prof. F. Mila, président du jury
Prof. B. M. J. Deveaud, directeur de thèse
Prof. J. Bloch, rapporteuse
Prof. D. Sanvitto, rapporteur
Prof. V. Savona, rapporteur



ÉCOLE POLYTECHNIQUE
FÉDÉRALE DE LAUSANNE

Suisse
2017

To my parents. . .

Acknowledgements

This PhD would not have been the same without the help and collaboration from many people, close or far. First I would like to thank Professors Jacqueline Bloch, Daniele Sanvitto, Vincenzo Savona, and Frédéric Mila for accepting to be part of my thesis jury. My deepest gratitude goes to my supervisor Benoit Deveaud for his guidance, motivation, and support throughout my PhD, but also for giving me the freedom to pursue my own ideas, for better or worse. More importantly, he helped me develop a critical thinking of my own work, and that of others, a teaching that goes beyond the world of polariton physics.

At the front line of our group, I wish to thank Grégory Sallen, who passed on his experimental and technical skills, and helped me develop my own. I kindly thank Fauzia Jabeen for showing me the joy of MBE growth, and bringing to our group much more than microcavity samples. This PhD would not have been the same without her outstanding work with our capricious machine. I wish to thank Daniel Oberli for his continuous help throughout the PhD. His critical eye helped to bring this work to a higher level. I am grateful to Marcia Portella-Oberli for her motivation, and for always bringing new ideas to our discussions.

A special thanks goes to Gwénolé Jacopin, Mehran Shahmohammadi, and Naotomo Takemura for the lively discussions, and for helping me understand the beautiful world of exciton physics. I also thank them for their kind availability whenever I would pass by their office. I would like to thank the members of the LOEQ family who kindly took me in: Francesco Manni, Stéphane Trébaol, Gabriele Grosso, Hadis Abbaspour, François Morier-Genoud, and the ones who followed: Albert Adiyatullin, Mitchell Anderson, Wei Liu, Mahmoud Hezam, Morteza Toupchi; everyone made this journey a pleasant one. Such a family would not hold without its most important member, Claire-Lyse Rouiller. Thank you for all your help, your availability, your support, and your understanding throughout the years. I wish to thank the technical staff Nicolas Leiser, Damien, and Yoan Trolliet, who were always available and helpful.

I cannot thank enough my friends, especially Michael Francis for the good times. I express my gratitude to my family, especially my parents Lise and Réjean for their endless support and encouragement. To my dearest, Clothilde and Marie-Claire who inspired me till the end. Finally, to *meine herzli* Marie-Ève, who followed me in this journey, for always being there for me, and helping me through and through.

Lausanne, December 18, 2016

Claudéric Ouellet-Plamondon

Abstract

This thesis is devoted to the study of microcavity polariton systems, in which the strong coupling occurs between more than one exciton or photon modes i.e. multimode polaritons. The first part of this work states the theoretical background of light-matter interaction starting from quantum well excitons to the non-linear regime of interactions between polaritons. We apply this knowledge to the case of GaAs based microcavities with InGaAs/GaAs quantum wells which are experimentally tested. Sample characterization and optimization are also discussed.

The main results presented on this thesis are separated in two main sections. The first corresponds to non-resonant excitation of 2D microcavity samples, and the second to resonant excitation of laterally confined polariton systems.

We first report on the observation of multiple polariton modes, originating from an electronic coupling between quantum wells inside a planar microcavity. When shallow quantum well stacks are placed at the antinodes of a microcavity, we measure a series of anticrossings when the cavity mode energy crosses that of the different excitonic levels. This is the main characteristic of a multimode polariton system. Comparing our experimental results with a coupled oscillator model that includes the electron and hole wave functions allows us to show that the exciton binding energy is affected by the interwell coupling.

We then study the non-linear properties of these InGaAs based microcavities, in the search for polariton condensation. We study the effect of Indium content, number of quantum wells, types of quantum well stacks, number of pairs of Bragg mirrors and magnetic field on the non-linearity of the system. In all cases, we measure a single threshold, and a clear signature of the transition from strong to weak coupling regime. We discuss the limiting factors for condensation in our system, namely the cavity losses induced by optical disorder, the light-matter coupling strength, and the saturation of the quantum wells.

In the second part of the thesis, we demonstrate the occurrence of spatial multistability using laterally confined polariton modes. We measure a multihysteresis curve of the transmitted intensity when we cycle the excitation power of a blue detuned laser with respect to the polariton modes. At each threshold of the hysteresis loop, we measure a switching of the spatial profile of the transmitted beam, and an energy jump of all the polariton modes. We reproduce all main characteristics of our experiment using

Acknowledgements

a multimode generalization of the Gross-Pitaevskii equations in the exciton photon basis. The mechanism behind the spatial multistability is identified as a repulsive cross-interaction between polaritons in different modes.

Following this experiment, we investigate the effect of decoherence on polariton bistability. We demonstrate how the polariton hysteresis loop collapses when increasing either the temperature or the power of a weak non-resonant laser. We explain this effect by the population of an incoherent reservoir that induces dephasing and repulsive interactions on the driven polaritons. All experimental findings are accurately simulated with the excitonic Bloch equations, and indicate that reservoir induced dephasing can be dominant over the reservoir induced energy blue shift.

In the final chapter, we present ongoing work on polariton lattices, namely measurements of the band structure for a square, and an hexagonal lattice. We also present preliminary results on the effect of a magnetic field on the band structure of a polariton square lattice. We conclude by discussing a series of future experiments to continue the investigation of multimode polaritons.

Key words: III-V semiconductors, InGaAs, photons, Exciton-polaritons, quantum wells, microcavity, light-matter interaction, strong coupling, multimode coupling, oscillator strength, Bose-Einstein condensation, strong to weak coupling transition, multistability, nonlinear optics, cross interactions, dephasing, decoherence.

Résumé

Les travaux présentés dans cette thèse portent sur l'étude de polaritons en microcavité, lorsque le régime de couplage fort a lieu soit entre plusieurs état excitoniques et un état photonique, soit l'inverse : bref le régime de polaritons multimodes.

La première partie de ce travail pose les bases théoriques de l'interaction lumière-matière, en commençant par l'exciton dans un puits quantique et en poursuivant jusqu'au régime d'interactions non linéaires entre polaritons. Ce formalisme est transposé au système étudié expérimentalement, c'est à dire des microcavités à base de GaAs dont les puits quantiques sont formés d'InGaAs/GaAs. Le travail de caractérisation et d'optimisation d'échantillons est mentionné par la suite.

Les principaux résultats de la thèse sont divisés en deux sections principales. La première portant sur l'excitation non résonante de microcavités 2D tandis que la seconde partie étudie l'excitation résonante d'états de polaritons confinés.

La première partie porte sur l'observation de polaritons multimodes, créés par le couplage électronique entre puits quantiques peu profonds placés à l'intérieur d'une microcavité. On mesure une série d'anti-croisements lorsque l'énergie du mode de cavité entre en résonance avec les différents états excitoniques des puits quantiques. Ce comportement est caractéristique d'un système de polaritons multimodes. Les résultats expérimentaux sont analysés à l'aide d'un modèle d'oscillateurs couplés qui prend en considération les fonctions d'ondes d'électrons et de trous et nous permet de montrer l'impact du couplage inter puits sur l'énergie de liaison des excitons.

Par la suite, nous faisons l'étude des propriétés non linéaires de microcavités contenant des puits quantiques d'InGaAs/GaAs dans le but d'obtenir la condensation de polaritons. L'étude porte sur l'effet de la concentration d'Indium, du nombre de puits quantiques, du nombre de puits regroupés, du nombre de paires de miroirs de Bragg, ainsi que de l'effet d'un champ magnétique sur les propriétés non linéaires du système. Pour tous les cas étudiés, on mesure un seuil d'intensité unique, caractérisé par une démonstration claire de la transition depuis le régime de couplage fort vers le couplage faible. Finalement, nous discutons des facteurs pouvant empêcher la condensation de polaritons dans notre système, soit les modes de fuite induits par le désordre optique, la force de couplage lumière-matière, ainsi que la saturation des puits quantiques.

Dans la deuxième partie de cette thèse, nous démontrons l'effet de multistabilité spatiale à partir d'états de polaritons confinés. Le système est excité à l'aide d'un laser décalé

Acknowledgements

à plus haute énergie que les différents modes de polaritons confinés. Lorsque l'on varie de façon cyclique la puissance d'excitation, on mesure une courbe de multi-hystérèse de l'intensité laser transmise par l'échantillon. De plus, pour chaque seuil de la courbe d'hystérèse, on observe un changement du mode spatial du laser transmis ainsi qu'un saut en énergie de chacun des modes de polaritons. Les principales caractéristiques de notre expérience sont toutes reproduites à l'aide d'une généralisation multimode des équations de Gross-Pitaevskii en base exciton-photon. Il est démontré que le mécanisme principal pour obtenir la multistabilité spatiale est l'interaction croisée répulsive entre les différents modes de polaritons confinés.

Suite à cette expérience, nous portons notre attention sur l'étude de la décohérence sur la bistabilité de polaritons. Nous démontrons l'affaissement de la courbe d'hystérésis lorsque la température augmente ou lorsque le système est excité de façon non résonante par un deuxième faisceau laser. Le phénomène est expliqué par l'apparition d'une population dans un réservoir incohérent. Celui-ci induit à la fois un déphasage et des interactions répulsives sur les polaritons cohérents. Les résultats expérimentaux sont simulés avec succès par un modèle basé sur les équations de Bloch excitoniques dans lequel les effets de déphasage et d'interaction du réservoir sont pris en compte. Les simulations permettent de démontrer que le déphasage induit par le réservoir peut être dominant par rapport aux interactions répulsives.

Le dernier chapitre présente des travaux en cours sur l'étude de réseaux de polaritons. Nous présentons les structures de bande associées à un réseau carré et hexagonal, ainsi que des résultats préliminaires sur l'effet d'un champ magnétique sur la structure de bande d'un réseau carré. Le chapitre conclut sur une discussion portant sur de futures expériences pour l'étude de polaritons multimodes.

Mots clés : Semiconducteurs III-V, InGaAs, photons, Exciton-polaritons, puits quantique, microcavité, interaction lumière-matière, couplage fort, couplage multimode, force d'oscillateur, condensation de Bose-Einstein, transition régime de couplage fort à faible, multistabilité, optique non-linéaire, interactions croisées, déphasage, décohérence.

Contents

Acknowledgements	i
Abstract (English/Français)	iii
Introduction	1
I Fundamentals of semiconductor microcavity optics	5
1 Optical properties of 2D semiconductor	7
1.1 From Dipole Interaction to Exciton	7
1.2 Exciton in Quantum Wells	11
1.3 Photon Confinement	15
1.3.1 Distributed Bragg Reflectors Microcavity	16
1.3.2 Lateral Confinement	21
1.4 Strong Coupling in the Linear Regime: Exciton-Polariton	22
1.4.1 Single Mode Coupling	22
1.4.2 Multimode Polariton	26
1.5 Non-linear Regime: Polariton Mean Field Equations	28
1.5.1 Excitonic Bloch and Gross-Pitaevskii Equations	28
1.5.2 Polaritons and Bose-Einstein Condensation	31
2 InGaAs/GaAs quantum well based microcavity	35
2.1 Properties of InGaAs based quantum wells	35
2.2 Sample characterisation and optimization	37
2.2.1 Experimental setup	38
2.2.2 Quantum wells	38
2.2.3 Designing a microcavity in the strong coupling regime	41
II Non-resonant excitation of planar microcavity	45
3 Multimode polaritons originating from coupled quantum wells	47
3.1 Samples and experimental setup	47
3.2 Photoluminescence of quantum well stacks	49

Contents

3.2.1	Simulation of QW stacks	50
3.3	Multimode polaritons in the linear regime	52
3.3.1	Photoluminescence	52
3.3.2	Fit using the multimode coupled oscillator model	53
3.3.3	Discussion	55
3.4	Conclusions	58
4	The quest for polariton condensation using InGaAs-based microcavity	59
4.1	Claims of polariton condensation using InGaAs QWs	59
4.2	Experimental setup	61
4.3	Low Indium content microcavities	62
4.3.1	Power measurements	64
4.3.2	Effect of magnetic field	65
4.3.3	Effect of experimental configuration and other attempts	67
4.3.4	Excitonic Mott transition in coupled quantum wells	69
4.4	High Indium content microcavities	72
4.4.1	Photoluminescence of quantum well stacks	72
4.4.2	Nonlinear property of high Indium microcavities	73
4.5	Discussion	77
4.6	Conclusions	79
III	Optical response of resonantly excited confined polaritons	81
5	Spatial multistability and cross interactions	83
5.1	Polariton bistability and spin multistability	84
5.1.1	Procedure for Numerical Simulations	86
5.1.2	Influence of Key Parameters on the Bistability	87
5.1.3	From spin to spatial multistability	88
5.2	Experimental setup and sample characteristics	89
5.2.1	Setup	89
5.2.2	Mesa sample	91
5.3	Spatial multistability experiment	93
5.4	Evidence for polariton-polariton cross-interactions	95
5.5	Numerical study of cross interactions and discussion	98
5.6	Conclusions	104
6	Probing reservoir induced dephasing with bistable polaritons	107
6.1	Experimental study of polariton bistability under dephasing	108
6.2	Numerical study of Polariton bistability away from the coherent limit	112
6.2.1	Influence of dephasing parameters on the bistability	113
6.3	Numerical study of reservoir-induced dephasing	117
6.3.1	EBE with reservoir	117

6.3.2	Data fitting of the non-resonant excitation experiment	118
6.3.3	Data fitting of the temperature experiment	122
6.3.4	GPE with reservoir	125
6.4	Spatial multistability and dephasing	127
6.5	Conclusions	128
IV	Perspectives	129
7	Polariton lattices and beyond	131
7.1	Polariton lattices	131
7.1.1	Clean room process	132
7.1.2	Measured band structures and real space distributions	134
7.1.3	Square lattice under magnetic field	138
7.2	Proposals for future experiments	142
7.2.1	Multimode interactions with coupled quantum well polaritons . . .	142
7.2.2	Crossover between spatial multistability and polariton lasing . . .	144
7.2.3	Biexciton, exciton reservoir, and RID	144
7.2.4	"Synthetic" gauge fields in polariton lattice	145
	Conclusions	147
V	Appendix	151
A	Derivation of multimode EBE and GPE	153
B	Description of the samples	159
	Bibliography	161
	Curriculum Vitae	181

Introduction

At its heart, the interaction between light and matter comes from the interaction between an electromagnetic field, and an electric dipole. For an atomic system, light will be emitted or absorbed if an electron from one orbital is allowed to jump into another one where an electron is missing. This may happen if there is an electric dipole moment between the two orbitals. In the solid state, particularly for direct band gap semiconductors, a similar situation occurs since there is an electric dipole between the valence and conduction bands, while the band gap energy is in the range of optical frequencies. Hence, we can excite an electron from the valence band to the conduction band while absorbing a photon, or to emit a photon in the reverse process. Such materials have proven to be excellent for harvesting or emitting light, and are commonly used for LEDs, and solid state lasers.

The way semiconductors are engineered for optoelectronic applications is therefore directly linked to our understanding of light-matter interaction in these systems. When a semiconductor is excited, the conduction band is populated by electrons while the valence band is populated by positively charged holes until both recombine, and emit photons. Since both particles are oppositely charged, they will inevitably interact with one another via Coulomb interaction. As a consequence, the interaction between the charged particles will modify the optical response of the material. Hence, studying light-matter interaction in a semiconductor structure implies studying interactions between electrons and holes. In the low density regime, an electron and a hole can bind to form a quasiparticle called an exciton, which is at the basis of low temperature semiconductor optics. It was discovered in 1958 by J. J. Hopfield [1], that if the interaction between an exciton with a photon was strong enough, then both particles would hybridise to form another quasiparticle called an exciton-polariton, a superposition of both light and matter. In order to observe such light-matter quasiparticles, we must find ways to obtain a large coupling strength between the exciton and the photon. First, can we increase light-matter interaction by using quantum wells instead of a bulk material, and second, we can encapsulate them in between two mirrors. That way, photons stay in the system for a longer time, which increases their chance to interact with the quantum well excitons. This is the principle behind microcavity polaritons that were first observed by C. Weisbuch *et. al.* in 1992 [2], and have been commonly used since then to study light-matter interaction.

Although the polariton physics in the linear regime is interesting in itself, the polariton system really shines when we enter the non linear regime. At large densities, electrons, and holes interactions are transposed to the excitons, which, in the strong coupling regime, cause polaritons to interact with one another. These interactions induce a $\chi^{(3)}$ non linearity, and are the basic ingredient for effects like polariton parametric amplification [3–5] or polariton bistability [6]. At the same time, polaritons are bosonic quasiparticles, and they have shown to undergo out of equilibrium Bose-Einstein condensation when excited non resonantly [7–10]. Hence, microcavity polaritons is a system where we can study the physics of quantum fluids, either through the condensed phase or by coherently injecting the polariton fluid using a resonant excitation scheme. These experimental schemes have been used to study vortices [11–13], superfluidity [14], and solitons [15–17] to name a few.

In most cases, the polariton system is studied at the single mode level, for instance the polariton ground state in the condensed phase, or by injecting the polariton fluid at a specific momentum. Fundamentally, a polariton results from the coupling between an exciton, and a photon, and therefore a two mode system. Theoretically, there is no limit to the number of modes that can be strongly coupled, provided that such situations are possible through sample fabrication. Hence, we differentiate the case of single mode coupling, as we described above to the general case where a multiplicity of excitonic or photonic modes can be involved. This situation is called multimode coupling or multimode polaritons.

In the linear regime, multimode polaritons have been observed in a variety of sample designs where the coupling occurs between either a single exciton state in a multimode cavity or the opposite. In the first case, the coupling was demonstrated with coupled planar microcavities [18–21] or by confining the optical mode in more than one dimension [9, 22]. The coupling of a single cavity mode to many exciton states has been achieved through monolayer thickness variation of GaAs/AlAs QWs, [23] with QWs of different thicknesses [24] or when coupling to the charged exciton transition [25, 26]. However, few studies have investigated the nonlinear regime in these systems, where multimode interactions between polaritons is expected.

This thesis is devoted to the study of the physics of polariton when more than two modes are involved. Instead of focussing in a particular aspect of the system, we study it in a wide range of situations. Experimentally, we use both non resonant, and resonant excitation schemes, and are interested in the linear and nonlinear regime. We investigate multimode coupling in two dimensional polariton system, and multimode interactions in the confined polariton system. Such interactions can occur either between polariton modes themselves or involving an exciton reservoir as an effective mode in the system. From the theoretical side, we apply the polariton mean field theory to the multimode case to simulate our findings. More importantly, numerical simulations are used as a tool to interpret our experimental findings, and to understand how multimode polaritons behaves in these situations. This thesis is divided into four parts:

Part I deals with fundamental aspects of light-matter interaction in semiconductor microcavity systems. In chapter 1, we present the theoretical background of light-matter interaction. This chapter focusses on demonstrating key equations used in the field, and also to present the mathematical tools that will be used throughout the thesis. In chapter 2, we discuss the material properties, characterization, and optimization to the samples studied in subsequent chapter.

Part II is dedicated to experiments where two-dimensional multimode polariton microcavities are excited non-resonantly. In chapter 3, we investigate in the linear regime the optical properties of shallow quantum wells when placed in a stack. Specifically, we present how interwell coupling can lead to a multiplicity of polariton modes when such quantum well stacks are placed inside a planar microcavity. The main body of work presented in this chapter has been published in [27]. In chapter 4, we move to the non linear regime to investigate on the possibility to reach Bose-Einstein condensation of polaritons using InGaAs quantum well based microcavity. We present a study on a number of sample designs that was tested to see if it is possible to reach the condensed phase, and not the VCSEL regime.

Part III is devoted to the study of resonantly excited confined polariton modes. We are interested in this part on the study of multimode interactions between polaritons. In chapter 5, we study the polariton multistability that occurs when a series of polariton modes are resonantly excited. Specifically, by studying the optical response of the system, we investigate interactions between different polariton modes. This chapter details a body of work that has been published [28]. In chapter 6, we move to the study of resonant excitation of a single confined polariton mode to investigate the effect of dephasing from its own environment. By analysing how the optical response is affected by temperature or non resonant excitation, we study how an incoherent reservoir affect the coherence of the driven polariton system. This chapter present an extended study on the work that has been published [29].

Part IV discuss perspectives for future work on multimode polaritons. In chapter 7, we present preliminary work on polariton lattices in the linear regime, and under a magnetic field. We also list ideas for future experiments, following the results obtained in the other chapters.

Fundamentals of semiconductor microcavity optics

Part I

1 Optical properties of 2D semiconductor

In this chapter, we give a broad overview of the theory of light-matter interaction in semiconductors, emphasizing on two dimensional systems. We define the basics of light-matter interaction on which the results obtained in this thesis will be analyzed. We focus on showing derivation of some fundamental equations used in microcavity physics in the linear and non-linear regime and on more subtle aspects that are sometimes overlooked in the polariton community. The properties specific to the material used in the thesis will be introduced in the next chapter.

1.1 From Dipole Interaction to Exciton

Generally speaking, the optical properties of matter is based on the interaction of an electric dipole with an electric field. For semiconductor materials, there can be an electric dipole between an electron in the conduction band and a hole in the valence band. Classically, a system of electric dipoles will modify the material's electric permittivity such that a resonance will appear at the dipole's resonant frequency. This can be written as a Lorentzian function for the real part of the permittivity [30]:

$$\epsilon_r(\omega) = 1 + \frac{e^2}{\epsilon_0 m} \frac{f}{\omega_D^2 - \omega^2 - i\gamma}, \quad (1.1)$$

where ω_D is the dipole frequency, γ is a damping factor, and f is the oscillator strength. This equation demonstrates that the material's response to light is given by the oscillator strength, a quantity that can be evaluated based on microscopic considerations of the electron-hole system. It is proportional to the transition probability between the electron and the hole when the electric dipole interacts with the electric field.

We seek to evaluate the transition probability between an electron and a hole, starting

Chapter 1. Optical properties of 2D semiconductor

with the light-matter dipole Hamiltonian:

$$H_{em} = \frac{e}{m} \mathbf{A} \cdot \mathbf{p}. \quad (1.2)$$

Using the Coulomb gauge, we have $\mathbf{E} = -\dot{\mathbf{A}}$, and the light-matter matrix element is:

$$\langle f | H_{em} | i \rangle = \frac{1}{m} A \mu_{cv} = \frac{1}{m\omega} E \mu_{cv}, \quad (1.3)$$

where E is the electric field amplitude, m the mass of the electron, and we define the dipole matrix element between the electron and the hole as $\mu_{cv} = e \langle f | \mathbf{e} \cdot \mathbf{p} | i \rangle = e p_{cv}$, where e is the electric charge [31]. This relation shows that the interaction is stronger when the dipole is parallel to the electric field, perpendicular to the photon propagation. The transition probability is given by Fermi's golden rule [30, 32]:

$$R = \frac{2\pi}{\hbar} \left(\frac{e}{m\omega} \right)^2 |E|^2 |p_{cv}|^2 \delta(\epsilon_f - \epsilon_i - \hbar\omega). \quad (1.4)$$

In the case of absorption, the initial and final states is the hole and the electron respectively, while the opposite is true for light emission. Since the dipole operator is antisymmetric, the initial and final states must be of opposite parity. As the conduction band possesses an s -orbital symmetry and the hole a p -orbital symmetry [30], it assures a non-zero dipole matrix element between the two [33]. The last term of the equation states the conservation of energy; the transition is allowed as long as the energy difference between the electron and the hole equals that of the photon, $\hbar\omega$. Moreover, within the dipole approximation, no momentum is transferred to the photon, and the transition occurs at any momentum, as long as $k_e = k_h$ for direct band gap materials. The transition is said to be direct as represented in figure 1.1.

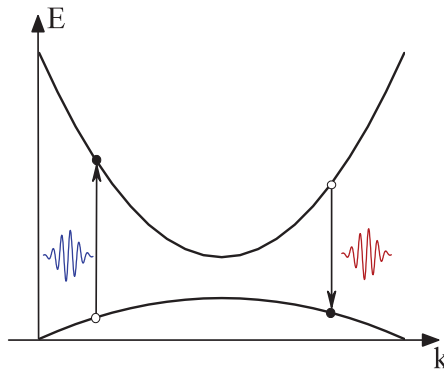


Figure 1.1 – Scheme of electron-hole optical absorption (blue) and emission (red) for parabolic band dispersion (effective mass approximation).

Equations 1.1 and 1.4 are linked through Kramers-Kronig relations, allowing to define

the dimensionless oscillator strength [30]:

$$f = \frac{2|p_{cv}|^2}{m\hbar\omega} = \frac{2|\mu_{cv}|^2}{e^2 m\hbar\omega}. \quad (1.5)$$

Because the electron and hole are oppositely charged particles, the optical response will be affected by the Coulomb interaction between the two quasiparticles, especially at low temperatures. It is possible to evaluate this variation within the effective mass approximation, that is assuming parabolic dispersions for both electron and hole. In the case where the Coulomb interaction is weak due to screening of the lattice, the wave function of the system can be written as a linear combination of electrons and holes wave functions [30]. Because the attractive Coulomb interaction will tend to localize the electron around the hole, we use the Wannier basis to represent the total wave function [30]:

$$\Psi(r) = N^{-1/2} \sum_{R_e, R_h} \Phi(R_e, R_h) a_{R_e}(r) a_{R_h}(r), \quad (1.6)$$

where N is the number of unit cells in the crystal, R_e and R_h are lattice vectors that represent the coordinates for the electron and the hole. Hence we must sum over all lattice sites in order to evaluate the exciton wave function at a given position r . $\Phi(R_e, R_h)$ is the Wannier exciton envelope wave function and $a_{R_e}(r)$ and $a_{R_h}(r)$ are Wannier functions that are related to the Bloch functions by a Fourier expansion:

$$a_R(r) = a(r - R) = N^{-1/2} \sum_k e^{-ik \cdot R} \psi_k(r), \quad (1.7)$$

where $\psi_k(r)$ are Bloch functions. These functions are localized at a given lattice vector R . Writing the electron-hole wave function as such allows to obtain the Schrödinger equation for the exciton envelope wave function. It is similar to the hydrogen problem but with the effective masses of electrons and holes and a screened Coulomb interaction:

$$\left[\frac{\hbar^2}{2m_e} \nabla_{R_e}^2 + \frac{\hbar^2}{2m_h} \nabla_{R_h}^2 - \frac{e^2}{4\pi\epsilon_r\epsilon_0 |R_e - R_h|} \right] \Phi(R_e, R_h) = E\Phi(R_e, R_h). \quad (1.8)$$

This equation can be solved by writing the envelope wave function as the product of wave functions for the center of mass and the relative motion of the electron and the hole. These coordinates are given by:

$$R_{COM} = (m_e R_e + m_h R_h) / (m_e + m_h), \quad (1.9)$$

$$R_{rel} = R_e - R_h. \quad (1.10)$$

The center of mass equation is that of a free particle with a mass $M_x = m_e + m_h$, telling us that the exciton has a parabolic dispersion. The equation for the relative motion is identical to the hydrogen atom problem giving a series of quantized states following the

Chapter 1. Optical properties of 2D semiconductor

same nomenclature as the Hydrogen atom, each with a given binding energy E_B . The solutions are well known both in 3D and 2D. The energy for both cases is, including the center of the mass motion [34]:

$$E_{3D} = E_g + \frac{\hbar^2 k^2}{2M_x} - \frac{E_0}{n^2}, \quad (1.11)$$

$$E_{2D} = E_g + \frac{\hbar^2 k^2}{2M_x} - \frac{E_0}{(n + 1/2)^2}. \quad (1.12)$$

where $E_g = E_c - E_v$ is the band gap energy. Similarly to the hydrogen atom, we define the binding energy and the Bohr radius for the 3D case:

$$E_0 = \frac{e^4 \mu}{2\epsilon_r^2 \epsilon_0^2 \hbar^2} = \frac{\hbar^2}{2\mu a_0^2}, \quad (1.13)$$

$$a_0 = \frac{\hbar^2 \epsilon_r^2 \epsilon_0^2}{e^2 \mu}, \quad (1.14)$$

where $\mu = m_e m_h / (m_e + m_h)$ is the reduced mass. As for the Hydrogen atom, the larger the binding energy, the smaller the Bohr radius. Coming back to light interaction, within the exciton picture, a photon having the same energy as the exciton will be emitted when the exciton is annihilated. Equations 1.11 and 1.12 show that the binding energy of the exciton decreases the energy of the emitted photon compared to the electron-hole transition.

The exciton envelope wave function also modifies the electron-hole transition probability which states that the envelope wave function must be non-zero at its center (the electron and hole relative distance is zero), in order to maximize the electron-hole overlap within the exciton. We can define the exciton oscillator strength as proportional to the modulus squared of the electron-hole dipole matrix element times the hydrogen wave function at its center $f \propto |\mu_{cv}|^2 |\psi(0)|^2$. A direct consequence of this modification is that s -states are optically active while p -states are not. In general, the oscillator strength drops rapidly for excited states so we can safely consider only the ground state that we write as a product of its relative ($r = R_{rel}$) and center of mass motion ($\rho = R_{COM}$):

$$\Phi_x(r) = f(\rho) \chi(r) = \frac{1}{\sqrt{V}} e^{i\mathbf{k} \cdot \rho} \psi_{1S}(r). \quad (1.15)$$

The exciton can be viewed as a freely moving hydrogen-like quasiparticle in the low density limit (the general case will be addressed in section 1.5), although we must sum over all lattice vector for the electron and the hole to get complete wave function for a given position of the center of mass. This means that the exciton is in fact a many-body excitation of the system that involve the contribution of electrons and holes over many lattice sites. At the mean field level and at larger densities, we will talk about the exciton

polarization field.

In table 1.1, we summarize the main differences between 3D and 2D excitons [34]. When passing from three to two-dimensional systems, the binding energy has a fourfold increase, while the Bohr radius decreases by half. More importantly, the oscillator strength per area is increased by a factor 4, meaning that in general, 2D materials have stronger optical response. We will address 2D excitons in more detail in the next section.

Table 1.1 – Comparison between the ground state solution of a 3D and 2D hydrogen problem [34].

	3D	2D
$\psi_{1S}(r)$	$\frac{2}{a_0^{3/2}} e^{-r/a_0}$	$\frac{4}{a_0} e^{-2r/a_0}$
$ \psi_{1S}(0) ^2$	$\frac{4}{a_0^3}$	$\frac{16}{a_0^2}$
E	E_0	$4E_0$
a_B	a_0	$a_0/2$

There is one last point of importance for the optical properties of excitons is their pseudospin (spin for simplicity). Because the electron is the conduction band which has an s -orbital symmetry, its total angular momentum is $|1/2, \pm 1/2\rangle$ while it is $|3/2, \pm 3/2\rangle$, $|3/2, \pm 1/2\rangle$ for the heavy and light holes since it arises from a valence band of p -orbital symmetry. As a result, the exciton spin states are $|1, \pm 1\rangle$, $|2, \pm 2\rangle$. Since the photon has a spin of one, the states $|1, \pm 1\rangle$ are optically active and interact with σ_+ , σ_- photons while the other two states are dark. The optically active exciton behaves as a two-level spin state similarly to a spin-half system, hence the term pseudospin.

1.2 Exciton in Quantum Wells

In the previous section, we saw the advantage of 2D systems over 3D. In the following, we discuss in greater detail the effect of 1D confinement on excitons, or quantum well excitons. The problem of a 1D quantum well is one of the most standard problems in quantum mechanics. A particle is trapped in a one-dimensional well but is free to move in the other spatial directions. The confinement gives rise to a series of quantized energy levels, which depend on the thickness and potential barrier height of the well and the mass of the particle.

Quantum well (QW) structures are fabricated by placing a semiconductor material of band gap energy E_1 and thickness L in between thicker layers of a second material of band gap energy $E_2 > E_1$. Such a structure can trap electrons and holes and form excitons. QW excitons behave as a free particle in the plane, while confined perpendicularly. In

typical III-V semiconductor QW structures, the potential depth is in the range of 0.1-1 eV while the exciton binding energy is of order of 10 meV. Therefore, in order to calculate the exciton energy levels, we can consider the Coulomb interaction as a perturbation of the confined electron and hole instead of considering a single confined exciton as a whole. We will confirm this approximation experimentally in the forthcoming chapters, and discuss its limitation in chapter 3. It is worth noting that in thick QWs (50 to few 100 nm), the propagation of the 3D exciton along the growth axis is affected, giving rise to a series of confined energy levels for the center of mass of the exciton. Similarly to the infinite potential well, these energy levels are inversely proportional to the effective well thickness ($L^* = L - 2a_0$). This effect is called the exciton center of mass quantization [35].

The band structure of a typical type-I QW is represented in figure 1.2. The confinement potential pushes the ground state energy away from the bottom of the well for both particles. Depending on the dept and the width of the well, there can be more than one confined state for both particles, meaning more than one electron-hole transition. We will see in the next chapter that the QWs under study are shallow, such that there is a single electron and heavy-hole state which is confined, hence we will limit our discussion to this case. The situation will be different when more than one QWs are stacked on top of each other. This particular case will be addressed in detail in chapter 3.

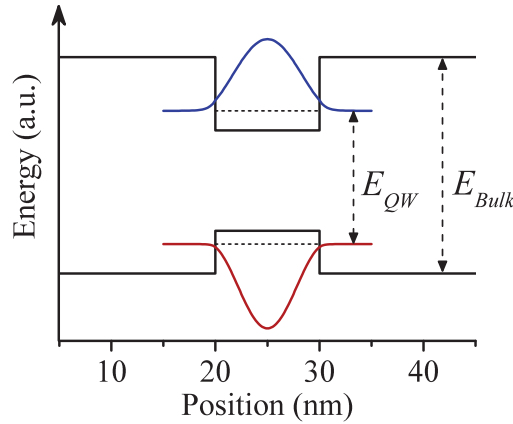


Figure 1.2 – Scheme of the QW band structure with the confined envelope wave functions for the electron (blue) and the hole (red). The dashed line in the well represent the position of the energy level for both particles. The dashed arrows represent the energy of an electron-hole transition inside the QW, E_{QW} , and outside E_{Bulk} .

The optical properties of excitons is also affected by the confinement. Already for the 3D case, there is a difference between an electron-hole transition and photon absorption/emission by an exciton. In the former, the transition is direct and no momentum is transferred to the photon. For the exciton, energy and momentum conservation implies that these processes are allowed only when the linear photon dispersion ($\omega = ck$) crosses the parabolic

exciton dispersion. In this two particle picture, the exciton and photon are degenerate at this crossing point [30]. Moreover, there must be some coupling between them in order for the exciton to absorb or emit a photon (creating or annihilating an exciton). This leads to a hybridization of the exciton and the photon [1] called exciton-polariton, or polariton (since there is no need to distinguish from phonon-polariton). As the noninteracting energy levels crossed, the hybridization causes an avoided crossing between the two, resulting in two polariton branches as represented in figure 1.3, where the parabolic dispersion of the exciton and the linear dispersion of the photon are schematically plotted.

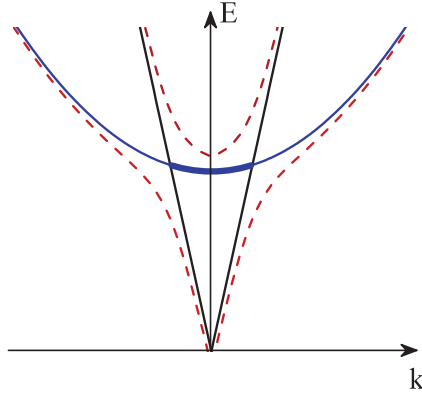


Figure 1.3 – Scheme of the exciton parabolic dispersion (blue), the linear photon dispersion (black), and the 3D polariton branches (dashed red line). The coupling is amplified to better visualize the branches. The thick blue area inside the photon dispersion represents the 2D exciton states which couples to light.

The exciton-photon coupling in 2D is different compared to the 3D case. In 2D, the translational symmetry is broken along the growth axis, meaning that momentum conservation only apply to the in plane wave vector. Writing the photon momentum as $k^2 = k_z^2 + k_{||}^2$, we see that momentum conservation can be respected for any value of k_z , as long as the total momentum k respects the photon dispersion. Hence, the exciton can couple to a continuum of photon states; any exciton state lying inside the cone defined by the photon dispersion (light cone) will fulfill this condition (the thick blue line in figure 1.3). Even for a non-zero electron-hole overlap, any exciton outside the light cone will not couple to light, resulting in dark exciton with a long lifetime.

In the following, we derive the exciton-photon coupling, as well as the oscillator strength and radiative lifetime for QW excitons. The approach presented summarizes the work of V. Savona *et al.* [31, 36, 37] and L. Andreani *et al.* [38]. We start by writing the exciton wave function for a given k as a summation over all electrons and holes wave functions that give rise to an exciton of the right momentum. In second quantization notation, this gives [31, 37]:

$$|\Phi_x(k, k_T)\rangle = \sum_{k_T} A(k, k_T) \hat{c}_{k_T + k \frac{m_e}{M}}^\dagger \hat{d}_{-k_T + k \frac{m_e}{M}}^\dagger |0\rangle. \quad (1.16)$$

Chapter 1. Optical properties of 2D semiconductor

Knowing that the in-plane exciton wave function in real space is the 1S hydrogen function, we notice that the coefficients $A(k, k_T)$ must be related to the real space wave function by a Fourier expansion. In fact we have that:

$$\begin{aligned}\psi_{1S}(\rho) &= \frac{1}{\sqrt{S}} \sum_{k_T} A(k, k_T) e^{ik\rho}, \\ \psi_{1S}(0) &= \frac{1}{\sqrt{S}} \sum_{k_T} A(k, k_T).\end{aligned}\tag{1.17}$$

The exciton-photon coupling is still evaluated through the dipole matrix element, and involves the overlap integral between the exciton and the photon. Since this expression is fundamental in for the field of microcavity polaritons, we give a detailed derivation of this matrix element:

$$\begin{aligned}H_{em} &= \frac{e}{m} \langle 0 | \mathbf{A} \cdot \mathbf{p} | \Psi_x(k, k_T) \rangle, \\ &= \frac{e}{m} \sqrt{\frac{\hbar}{2\epsilon_0 n^2 \omega V}} \sum_{k_T} A(k, k_T) \langle 0 | \mathbf{e} \cdot \mathbf{p} \hat{c}_{k_T + k \frac{m_e}{M}}^\dagger \hat{d}_{-k_T + k \frac{m_e}{M}}^\dagger | 0 \rangle, \\ &= \frac{e}{m} \sqrt{\frac{\hbar}{2\epsilon_0 n^2 \omega L}} \psi_{1S}(0) p_{cv} \int \chi_e(z) E_z \chi_h(z) dz,\end{aligned}\tag{1.18}$$

where E_z is the normalized electric field profile along the growth direction and have used the vector potential amplitude of a single photon $A = E/\omega = \sqrt{\hbar/2\omega n^2 \epsilon_0 V}$, V being the mode volume. We have also taken advantage of equation 1.17 and the fact that the summation over k of the dipole matrix element between the exciton and its vacuum is equivalent as the dipole matrix element between the electron and the hole. From the 2D nature of the problem, the overlap between the carrier and the field is separated in an in-plane (the dipole) and out of plane component, giving rise to the overlap integral between the electron and hole wave function along the growth direction. For a bare QW, E_z can be assumed constant and removed from the integral.

Similarly, the oscillator strength *per area* for a QW exciton is given by [31, 39]:

$$f = \frac{1}{S} \frac{2}{m\hbar\omega} |\langle 0 | \mathbf{e} \cdot \mathbf{p} | \Psi_x(k, k_T) \rangle|^2,\tag{1.19}$$

$$f = \frac{2}{m\hbar\omega} |p_{cv}|^2 |\psi_{1S}(0)|^2 \left| \int \chi_e(z) \chi_h(z) dz \right|^2,\tag{1.20}$$

where we assume that the electric field along the growth axis z is large compared to the QW thickness. This equation tells us that, assuming the identical dipole matrix element and spin selection rules between the different electron and hole states (for instance in coupled QWs), we can evaluate the relative transition probability by calculating the overlap of the electron and hole wave function along the growth axis. These envelope

wave functions can be evaluated within the effective mass approximation in order to simulate real sample designs. This will be addressed in the next chapter specifically for the case of InGaAs/GaAs QWs.

We can combine equations 1.18 and 1.19 to obtain the equation for the exciton-photon coupling strength:

$$H_{em} = \hbar \sqrt{\frac{e^2}{2\epsilon_0 n^2 m L}} f. \quad (1.21)$$

This equation tells us that for 2D excitons, the coupling is independent on the sample size or on the number of excitons in the system since the oscillator strength is already normalized by the area. This means that changing the excitation spot size will increase the light being emitted without changing the coupling strength (in contrast to 2-level systems where the number of particles directly affect the coupling strength). Furthermore, the coupling strength is inversely proportional to the mode length; the smaller the mode volume, the larger the coupling. Equation 1.21 will be the basis to define the strong coupling regime in a microcavity.

Finally, the exciton radiative width can be evaluated perturbatively by replacing the delta function in Fermi's Golden rule (equation 1.4) by the 1D photon density of state and the single photon amplitude [38]:

$$\rho_{h\nu} = \frac{V}{\pi S} \left(\frac{n}{\hbar c} \right)^2 \frac{\hbar \omega}{\sqrt{k_0^2 - k_{||}^2}} \theta(k - k_0) \approx \frac{V}{\pi S} \frac{n}{\hbar c} \quad (1.22)$$

where S is the sample area, and we have used the photon linear dispersion $k_0 = n\omega/c$. $\theta(k - k_0)$ is a Heaviside function to assure that the photon density of states outside the light cone is zero. This equation corresponds to the well-known equation for the density of states: $\rho(E) \propto E^{(N/2-1)}$, where N is the dimensionality of the system. The exciton radiative width can be obtained as a function of the oscillator strength per area by combining equations 1.4, 1.19, and 1.22 [36, 38]:

$$\Gamma_0 = \frac{1}{4\pi\epsilon_0} \frac{\pi}{n} \frac{e^2}{mc} f. \quad (1.23)$$

This last equation shows that the radiative width is directly proportional to the oscillator strength. Since the radiative lifetime is inversely proportional to the radiative width, then the stronger excitons interact with light, the shorter its lifetime will be.

1.3 Photon Confinement

We saw in the previous section that the light-matter coupling strength was inversely proportional to the photon mode volume. Therefore, in order to maximize the coupling,

it is favorable to have a small mode volume and to increase the photon-exciton overlap. We show in the following how we can confine photons so they behave as 2D quasiparticles, and also how we can impose lateral confinement in order to achieve 0D photons.

1.3.1 Distributed Bragg Reflectors Microcavity

The principle behind light confinement is to force light in a small area by reflecting it. Facing a mirror with perfect reflectivity, the photon must bounce back. If the photon is trapped between two mirrors then it will bounce back and forth in a volume defined by the distance between the two mirrors. When both mirrors are separated in free space by a certain distance L , the system has an optical resonance at a given wavelength λ when $L = n\lambda/2$. This is the principle of a Fabry-Perot resonator. In reality, since the mirrors are not perfectly reflecting, the photon will stay inside the resonator for a certain amount of time before it leaks out of the cavity. The cavity mode linewidth will be given by this photon lifetime. The smaller the linewidth, the fewer the losses, hence the higher the photon lifetime.

It is possible to design mirrors that are close to perfection using a structure called a distributed Bragg reflector or DBR. As a comparison, typical gold or silver mirrors have a reflectivity of $R \approx 0.95$, whereas DBR mirrors can reach $R \approx 0.9999$, decreasing the losses by several orders of magnitude. The principle of the DBR is to stack alternating layers of thickness $\lambda/4n_{1,2}$, where n_1 and n_2 are refractive indices of two materials (see figure 1.4(a)). This causes destructive interference for a propagating beam at wavelength λ (constructive interference in reflection). If a large number of pairs is used, then the DBR can reach a reflection coefficient close to unity. The number of pairs needed depends on the refractive index difference (Δn) between the two materials; fewer pairs will be needed if Δn is increased. Although the DBR mirror is designed for a given wavelength, it is reflective over a range of wavelengths called the stop band, which is centered on the λ of the DBR. The larger Δn is, the larger is the stop band.

We create a DBR microcavity by placing two mirrors in between a spacer layer of thickness L (figure 1.4(b)). The resonance wavelength of the microcavity will depend on the materials and the thickness of the spacer. For a spacer made of material n_1 , if $n_1 < n_2$, there is a π phase shift in reflection which impose the field to be zero at the interface. The cavity will resonate for thicknesses of multiples of half λ , $L_{cav} = m\lambda/2n_1$, with $m = 1, 2, 3, \dots$. For the opposite case, the boundary conditions dictate that the field will be maximum at the interfaces of the spacer layer, hence the cavity spacer will be $L_{cav} = (m + 1)\lambda/2n_1$.

We simulate the reflectivity of the DBR mirror and DBR microcavity using the transfer matrix formalism. This tool is quite powerful to design or optimize microcavities to obtain the strong coupling regime. In order to calculate the reflection coefficient of the structure,

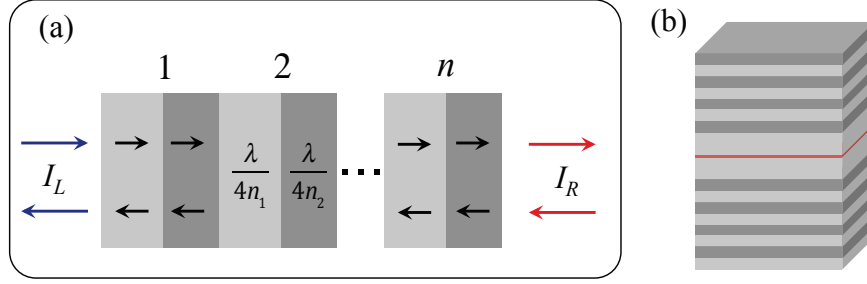


Figure 1.4 – (a) Scheme of a DBR consisting of n pairs of $\lambda/4$ layers. The black arrows represent the transmitted and reflected field at each interface, the red and blue ones indicate the initial and final field linked by the product of transfer matrices. (b) Scheme of a DBR microcavity. The spacer is made of the same material as one of the components of the mirrors. The red layer indicates the position of a QW in order to get strong coupling between the exciton and the photon, see section 1.4.

we need to solve Maxwell's equations for a propagating beam in a system consisting of different layers of materials. The problem can be simplified by noting that we can express the field transferred from one side of an interface in an optical system to the next by a transfer matrix M : $I_R = MI_L$, where $I_{L,R}$ is a two-component vector composed of the transmitted and reflected field amplitude, as shown in figure 1.4(a). The transfer matrix is given by the reflection and transmission coefficient of the optical system [40]:

$$M = \begin{pmatrix} 1/t^* & r/t \\ r^*/t^* & 1/t \end{pmatrix} \quad (1.24)$$

For a given dielectric interface, the transmitted and reflected fields are related by a matrix M_I whose input is simply the refractive indices. Another matrix M_P is used to propagate the field for a distance d from one interface to the other. These matrices are [40]:

$$M_I = \frac{1}{2n_2} \begin{pmatrix} n_2 + n_1 & n_2 - n_1 \\ n_2 - n_1 & n_2 + n_1 \end{pmatrix} ; \quad M_P = \begin{pmatrix} e^{\frac{2\pi i d n}{\lambda}} & 0 \\ 0 & e^{\frac{2\pi i d n}{\lambda}} \end{pmatrix} \quad (1.25)$$

The propagation matrix simply adds a phase factor to the field when the refractive index is real, and will describe absorption when the refractive index has an imaginary part. Simulating a DBR mirror or a microcavity then simply becomes a problem of multiplying matrices to obtain the relationship between the input and output field of the structure and is summarized by the following equation:

$$\begin{aligned} I_R &= \tilde{M} I_L \\ I_R &= M_I^{n+1} M_P^n M_I^n \dots M_P^2 M_I^2 M_P^1 M_I^1 I_L \end{aligned} \quad (1.26)$$

Once the complete transfer matrix \tilde{M} is known, we extract the reflection coefficient by

comparing it with the matrix 1.24 and noting that $R = |r|^2 = |\tilde{M}_{1,2}/\tilde{M}_{2,2}|^2$. This will give the reflectivity for a given wavelength. The complete stop band of the optical system can be accurately simulated when the proper refractive index curve ($n(\lambda) = \tilde{n}(\lambda) + i\kappa(\lambda)$) of the chosen materials are known.

Examples of this procedure is shown in figure 1.5, for structure resonant at $\lambda = 840$ nm, made of GaAs/AlAs at 10 K. First in figure 1.5(a) we simulate the stop band of a single DBR mirror with increasing number of pairs. We notice the appearance of a flat reflectivity band, the stop band, when the number of pairs is increased, as well as an increase in the reflectivity. This demonstrates the principle of the DBR mirror. A dip in reflectivity at 818 nm is noticeable for all structures and corresponds to the absorption gap of GaAs. The absorption causes a decrease in reflectivity for wavelength below the gap, clearly visible when comparing the low and high wavelength side of the band.

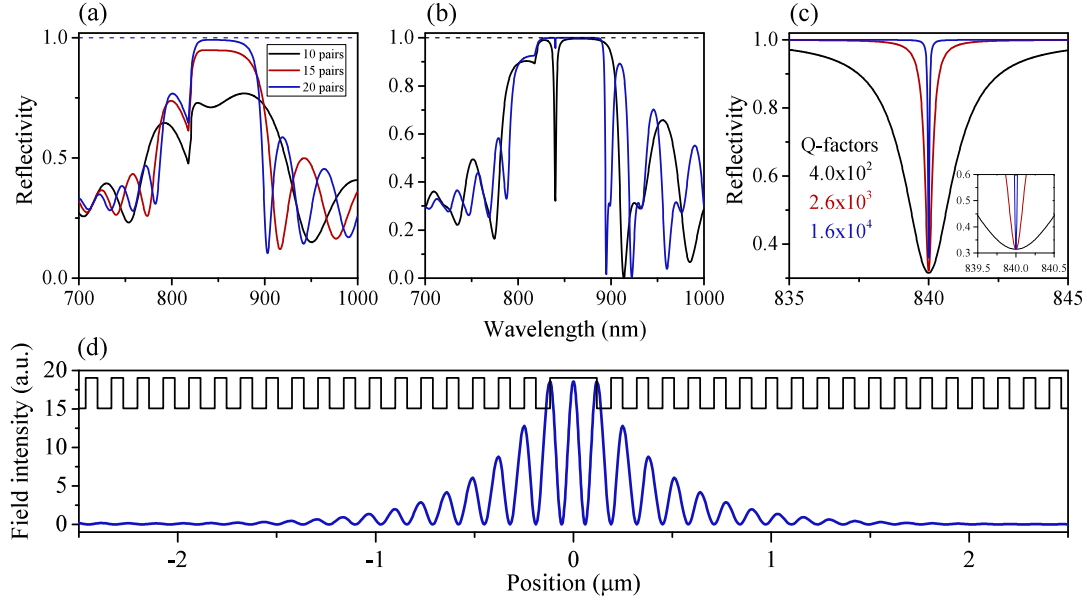


Figure 1.5 – Reflectivity calculated using the transfer matrix formalism. All structures are resonant at $\lambda = 840$ nm and made of AlAs/GaAs. On all figures, the black, red and blue indicates structures of 10, 15 and 20 DBR pairs. (a) Reflectivity of a single DBR mirror for increasing number of pairs. (b) Reflectivity of a λ -cavity made of a GaAs spacer and either 10 (black) or 20 (blue) DBR pairs on both sides of the spacer. (c) Reflectivity at the position of the cavity mode when increasing the number of DBR pairs of a λ -cavity. (d) Field intensity profile calculated for a λ -cavity with 20 DBR pairs at the cavity resonance of $\lambda = 840$ nm.

In figure 1.5(b), we simulate a full microcavity at the same resonant wavelength with either 10 or 20 DBR pairs on both sides of the spacer. For this design and all samples presented in this thesis, the cavity spacer is made of GaAs. Following the conditions mentioned above, since $n_{GaAs} > n_{AlAs}$, the smallest spacer possible is $L = \lambda/n_{GaAs}(\lambda)$, hence a λ -cavity. Two points are noticeable in this figure. First, in both cases, the

reflectivity of the stop band is almost one and has improved compared to the reflectivity of a single mirror. Second, we see a dip in reflectivity at the center of the stop band, exactly at $\lambda = 840$ nm. This is the optical resonance, the cavity mode. If we zoom in this region, as it is shown in figure 1.5(c), we clearly see that increasing the number of DBR pairs decreases the cavity linewidth $\Delta\lambda$, hence the cavity losses. We define the quality factor of the cavity as $Q = \lambda/\Delta\lambda$. As shown, we roughly gain an order of magnitude in the Q -factor of the cavity each time we add 5 DBR pairs on both sides of the spacer. In reality, this effect will saturate as the optical disorder will increase for a large number of pairs, which will increase the cavity's inhomogeneous linewidth. Finally, we can see that the minimum of the reflectivity of the cavity mode, is slightly different between each cavity design. This is a consequence of the low energy tail of the GaAs absorption. If we remove the GaAs absorption in the simulation, all designs have exactly the same reflectivity, as the inset shows.

The effect of confinement of the electromagnetic field by the microcavity can be seen by plotting the field intensity at the resonant wavelength along the cavity, as it is done in figure 1.5(d). We do observe that the field is most intense inside the cavity spacer, and that it is maximum at the interfaces as the design dictates. The three intensity maximum of the field inside the cavity spacer correspond to the three amplitude extrema of the λ spacer. Clearly visible from this figure is that the field, although confined, extends appreciably inside the DBR mirrors. Hence to evaluate the mode volume of the cavity, this extension must be considered. We define the effective length of the cavity as:

$$L_{eff} = L_{cav} + L_{DBR}, \quad (1.27)$$

where L_{cav} is the cavity spacer thickness and L_{DBR} is the field penetration depth inside both DBRs and is given by [36, 41]:

$$L_{DBR} \approx \frac{\lambda_c}{2n_c} \frac{n_1 n_2}{|n_1 - n_2|}, \quad (1.28)$$

where λ_c is the cavity resonance in vacuum, n_c is the refractive index of the cavity spacer. Typically $L_{DBR} \approx 2 \mu\text{m}$, much larger than $L_{cav} \approx 0.237 \mu\text{m}$ for our example. This is of crucial importance because it means that, contrary to a Fabry-Perot resonator where the resonance is directly linked to the spacer, for a DBR microcavity, the cavity resonance is more affected by the DBR mirrors than the cavity spacer.

To illustrate this effect, we compute the cavity mode for a λ -cavity at $\lambda = 840$ nm while changing the spacer thickness by ± 6 nm. In figure 1.6(a) we compare the cavity modes obtained with the ones computed if we assume a proportional variation of all layers of the cavity by $\pm 2\%$. When the cavity layers are varied proportionally, the cavity resonance is at its expected value (2% of 840 is ≈ 17 nm). The deviation from a slope one comes from the wavelength dependence of the refractive indices. When we modify only the spacer, the cavity resonance is much less sensitive, a 2% increase of the cavity spacer only

changes the cavity resonance by 0.6%. When the spacer thickness deviates from the DBR resonance, the cavity resonance is pulled closer to the DBR resonance. In figure 1.6(b), we show the stop band of the microcavities when the spacer has been varied by ± 6 nm. Changing the spacer thickness has barely any effect on the stop band. This effect is particularly useful when optimizing microcavities. It means that we can position a cavity resonance simply by adding or removing material from the spacer from one growth to the other and overcome growth fluctuations.

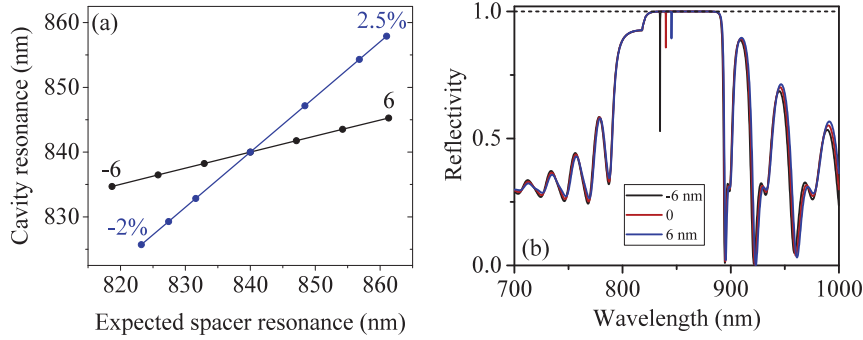


Figure 1.6 – (a) Transfer matrix simulation the cavity resonance of a λ -cavity at $\lambda = 840$ nm when the cavity spacer thickness is varied by ± 6 nm (black) or when the whole structure is changed by a scaling factor (blue). The expected cavity resonance is defined by $(\lambda_0 \pm \Delta\lambda)/n_c$. (c) Corresponding reflectivity for spacer thickness variation of -6 , 0 and 6 nm.

One last important point for our discussion of exciton-polaritons below is to understand how do photons propagate in the cavity. We start by decomposing the photon wave vector k as in-plane and perpendicular component with respect to the DBR such that $k^2 = k_{\parallel}^2 + k_{\perp}^2$. Since the photon is confined in the perpendicular direction, k_{\perp} represents the mode quantization of the cavity. Limiting ourselves to the ground state (cavity mode), we have $k_{\perp} = 2\pi n_c/\lambda_c$. Because the DBR has no effect on the lateral propagation of the photon, it is therefore free to move in the plane. Starting from the linear photon dispersion, we obtain the energy of a photon in the cavity:

$$E_{cav} = \frac{\hbar c}{n_c} \sqrt{k_{\perp}^2 + k_{\parallel}^2}. \quad (1.29)$$

In the limit where $k_{\perp} \gg k_{\parallel}$, we get the following approximation for the energy of the cavity photon [41]:

$$E_{cav} \approx E_{cav}(0) + \frac{\hbar^2 k_{\parallel}^2}{2m_{cav}}, \quad (1.30)$$

with $E_{cav}(0) = \hbar c/\lambda_c$ and $m_{cav} = n_c^2 E_{cav}(0)/c^2 = \hbar n_c/(c\lambda_c)$. Equation 1.30 tells us that a photon in a DBR microcavity behaves as if it was a 2D free particle with an effective mass m_{cav} . The cavity photon mass is of order 10^{-5} the mass of the electron. Typically, the parabolic dispersion within the experimental reach is in the range of tens of meV

while $E_{cav}(0)$ is of orders 1-2 eV. This justifies our approximation.

1.3.2 Lateral Confinement

Starting from a 2D DBR microcavity, it is possible to increase the photon confinement by imposing lateral boundary conditions in a small volume. The dimensionality of the system will depend on the potential geometry. There are two main ways of achieving this, either by removing some parts of the 2D cavity in order to obtain small pillars with an interface with air [9, 42], or by creating small steps in the cavity spacer [22, 43, 44] or by the use of oval defects [45]. We focus here on the second technique since it will be studied in this thesis. The technicality on how to create such structure will be described in section 7.1.1.

The principle for 3D confinement is shown in figure 1.7(a). First, we locally increase the cavity thickness by some amount $\Delta\lambda$. Doing so, we decrease the cavity resonance energy as we illustrated in figure 1.6, which therefore creates a potential well for the photon. If the lateral size of the potential well is small enough, the light will be confined and the cavity mode energy will blue shift, similarly to the case of electrons in the QW (the resonance wavelength will decrease by some amount: $\lambda + \Delta\lambda - \Delta$). In figure 1.7(b), we show the position of the cavity mode for our λ -cavity and compare it when the spacer is increased by 6 nm. This creates an energy shift of about 9 meV that will define the height of the trap.

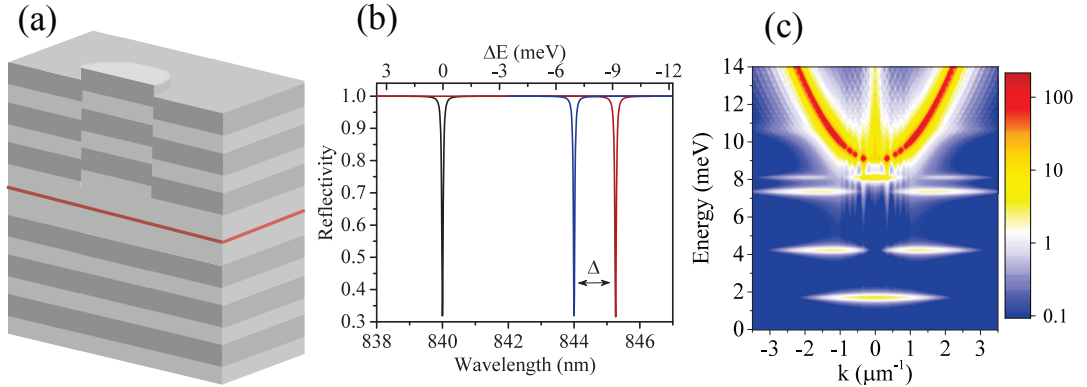


Figure 1.7 – (a) Microcavity design for 3D confinement of light. (b) Reflectivity of a 2D DBR cavity for $\lambda = 840$ nm (black) and the same cavity when an extra 6 nm is included in the spacer (red). The blue curve shows the effect of lateral confinement on the cavity ground state. It is blue shifted by a value Δ . (c) Simulated dispersion of a mesa of $3 \mu\text{m}$ in diameter and potential height of 9 meV, following ref. [46].

The case of interest here is for circular traps or mesas, structures that will be studied in later chapters. In this case, we can calculate the energy levels of the trap by solving Maxwell's equations in radial coordinates [46]. By imposing that the electric field is zero

at the boundary of the trap, we get that the in-plane solutions are Bessels functions times an angular phase factor. The photon modes calculated using the approach of ref. [46] are shown in figure 1.7(c) for the case of a trap of $3 \mu\text{m}$ in diameter and a potential of 9 meV . The confined states are clearly visible below a 2D continuum of state with the expected parabolic dispersion.

1.4 Strong Coupling in the Linear Regime: Exciton-Polariton

Having discussed both 2D excitons and photons, we now move to the case of strong coupling between the two, in the linear regime, that is for low exciton density. The general case for high density will be addressed in the next section.

1.4.1 Single Mode Coupling

So far, the 2D exciton-photon coupling has been discussed only perturbatively, as a transition probability between an electron and a hole and characterized by an oscillator strength. When the coupling becomes strong enough, the perturbative treatment is no longer correct and one must diagonalize the complete Hamiltonian. This regime is achieved when the QW is placed at the antinode of a DBR microcavity with a large Q -factor. The coupling is maximized since the exciton-photon overlap along the growth axis is almost perfect and the mode volume is decreased, and given by the effective cavity length (equation 1.27). In general, the exciton-photon coupling can be described within the dipole and rotating wave approximation by the following Hamiltonian:

$$H_{lm} = \sum_k \left\{ \epsilon_x \hat{x}_k^\dagger \hat{x}_k + \epsilon_c(k) \hat{c}_k^\dagger \hat{c}_k + \frac{\Omega_0}{2} \left(\hat{x}_k^\dagger \hat{c}_k + \hat{c}_k^\dagger \hat{x}_k \right) \right\}, \quad (1.31)$$

where ϵ_x is the exciton energy and $\epsilon_c(k)$ is the cavity dispersion, $\hat{x}_k^\dagger(\hat{c}_k^\dagger)$ and $\hat{x}_k(\hat{c}_k)$ are exciton (photon) creation and annihilation operators for a given k . Since the effective mass of the exciton is quite large compared to that of the photon, we can safely assume the exciton dispersion to be flat over the range of k vectors of interest. Assuming DBR mirrors of reflectivity $R \approx 1$, the coupling constant Ω_0 is called the Rabi splitting and is given following equation 1.21, by [31, 36, 47]:

$$\Omega_0 = 2 \sqrt{\frac{e^2}{2\epsilon_0 n^2 m L_{eff}}} f. \quad (1.32)$$

Although written in second quantization form, this Hamiltonian is identical to the classical problem of two coupled oscillators, hence the term coupled oscillator model. Diagonalizing

1.4. Strong Coupling in the Linear Regime: Exciton-Polariton

this Hamiltonian lead to two new eigenstates or normal modes, whose energy is given by:

$$E_{LP,UP}(k) = \frac{1}{2} \left(\epsilon_x + \epsilon_c(k) \pm \sqrt{\delta^2 + \Omega_0^2} \right), \quad (1.33)$$

where we have defined the cavity detuning $\delta = \epsilon_c(k) - \epsilon_x$. The corresponding set of annihilation operators are defined as linear combinations of the exciton and photon operators [1, 41]:

$$\hat{L}_k = X\hat{x}_k + C\hat{c}_k, \quad (1.34)$$

$$\hat{U}_k = C\hat{x}_k - X\hat{c}_k, \quad (1.35)$$

with $|X|^2 + |C|^2 = 1$. The coefficient X and C are called the Hopfield coefficients and are given by:

$$|X|^2 = \frac{1}{2} \left(1 + \frac{\delta}{\sqrt{\delta^2 + \Omega_0^2}} \right) \quad ; \quad |C|^2 = \frac{1}{2} \left(1 - \frac{\delta}{\sqrt{\delta^2 + \Omega_0^2}} \right). \quad (1.36)$$

In this normal mode coupling scheme, the eigenmodes are called lower and upper polariton branches. We see that $|X|^2$ and $|C|^2$ represent the excitonic and photonic fraction of the lower polariton branch. These coefficients solely depend of the cavity detuning δ and the Rabi splitting Ω_0 . Therefore, the polariton system is entirely defined by those two parameters in the linear regime. The polariton branches given by equations 1.33 are plotted in figure 1.8(a) for $k = 0$ as a function of the normalized cavity detuning δ/Ω_0 . This shows the typical anticrossing of the exciton and photon energy, as the photon becomes resonant with the exciton. When both energies are equal, at $\delta = 0$, the energy splitting equals Ω_0 . The corresponding Hopfield coefficients are given in figure 1.8(b). As expected, the excitonic and photonic fraction varies as a function of the cavity detuning. The more negative detuning, the closer the lower branch is to the cavity mode, hence the larger is the photonic fraction, and the lower is the excitonic fraction. In particular, for $\delta = -\Omega_0$, $|X|^2 \approx 0.15$ and $|C|^2 \approx 0.85$. These values are interchanged for $\delta = \Omega_0$.

It is worth mentioning that giving only the Rabi splitting without the cavity detuning has no meaning in itself, because the properties of a polariton mode are defined by its exciton and photon fractions. A cavity detuning normalized by Ω_0 is more meaningful. For example, a cavity detuning of $\delta = -3$ meV might seem small, but if $\delta/\Omega_0 = -1$ this corresponds to a polariton which is 85% photon, while it would be 60 % if the $\delta/\Omega_0 = 1/5$. Hence, indicating the Hopfield coefficient is essential in order to know under which configuration the system is studied. Although this seems obvious, this simple fact is often missed in the literature or omitted, and, as a consequence it makes it difficult to verify the validity of some results, especially at large densities.

In figure 1.8(c) we show the polariton dispersion and the corresponding Hopfield coefficients in figure 1.8(d). In this case, the characteristic anticrossing occurs at the k -vector for

which the cavity detuning is zero. The deviation from the parabolic dispersion has great implications for the polariton system since it affects the relaxation dynamics. When the cavity detuning is large and negative, phonon scattering into small k -vector is almost suppressed leading to an accumulation of polaritons at higher energies above the inflection point, the so-called bottleneck region [48].

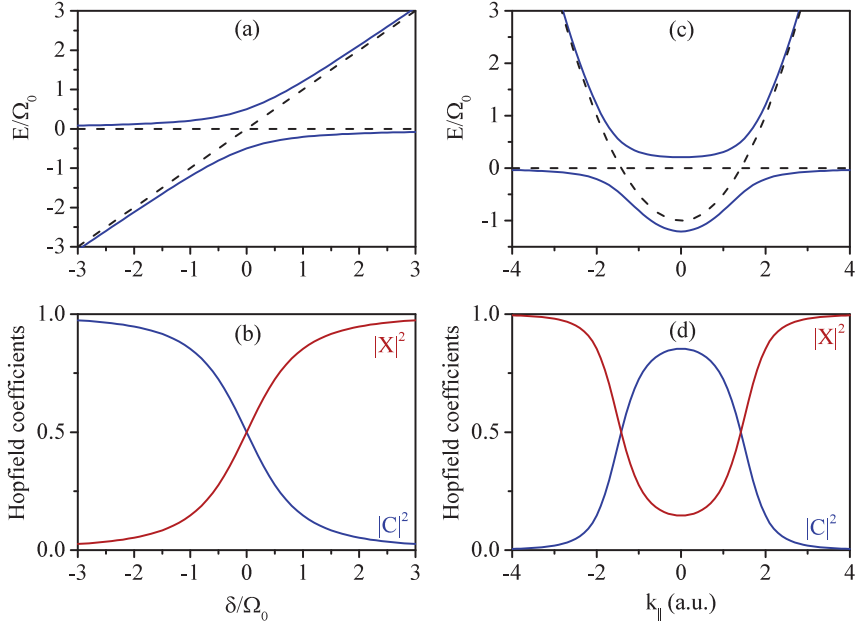


Figure 1.8 – (a) Polariton mode energies as a function of the cavity detuning. The energy and detuning is scaled with respect to the Rabi splitting Ω_0 . The black dashed lines represent the energy of the uncoupled exciton and photon modes. (b) Hopfield coefficients of the lower polariton branch shown in (a). (c) Polariton dispersion and (d) corresponding Hopfield coefficients of the lower polariton branch.

One last point important to discuss for this section is the validity of the strong coupling picture. Strictly speaking, the system will be in strong coupling as long as at least one exciton-photon oscillation can be done before either one of them disappear. For the photon, it means leaking out of the cavity whereas for the exciton it can be non-radiative recombination, emission through a leaky cavity mode or other dephasing mechanism. The exciton radiative lifetime does not represent a loss for the polariton system if the photon is emitted in the cavity mode (the photon still contributes to the strong coupling).

The loss of strong coupling can be evaluated by including losses to the Hamiltonian of equation 1.31, making it non-hermitian:

$$H_{LM} = \begin{pmatrix} \epsilon_c - i\gamma_c & \Omega_0/2 \\ \Omega_0/2 & \epsilon_x - i\gamma_x \end{pmatrix}, \quad (1.37)$$

where γ_x and γ_c are the exciton and photon *homogeneous* linewidths. Combining these

1.4. Strong Coupling in the Linear Regime: Exciton-Polariton

linewidths with the Hopfield coefficients allow to define the polariton homogeneous linewidths:

$$\gamma_{LP} = |X|^2\gamma_x + |C|^2\gamma_c, \quad (1.38)$$

$$\gamma_{UP} = |C|^2\gamma_x + |X|^2\gamma_c. \quad (1.39)$$

These equations will tend to overestimate the polariton linewidth since it assumes exciton-phonon scattering γ_x instead of polariton-phonon scatterings (evaluated through Fermi's Golden Rule by taking into account the polariton dispersion and not the exciton one). As for the inhomogeneous linewidths, it causes to average over a number of states and cannot be properly included within this framework [49–51]. It is still needed to explain why the upper branch tend to have a larger linewidth compared to the lower branch, even for positive detuning [52].

The loss of strong coupling can be simulated while increasing the losses of the system, either through the photon or the exciton, as shown in figure 1.9, where we plot the real and imaginary part of the eigenvalues of the non-hermitian Hamiltonian for a polariton system at $\delta = 0$. We can see that, once the linewidth equals the Rabi splitting, the anticrossing between the real parts of the eigenvalues disappear while one is created in the imaginary parts. In reality, for a given microcavity sample with defined linewidths, this point corresponds to a phase transition of the polariton system, namely the excitonic Mott transition. The inset of figure 1.9(a) shows the loss of coupling when the cavity detuning is different from zero. The loss of coupling occurs around $\gamma \approx \Omega_0$ where the polariton branches return to the uncoupled modes energy. We can define the condition for a system to be in the strong coupling regime by the fact that the losses from the system must be smaller than the Rabi splitting $\gamma_x, \gamma_c > \Omega_0$.

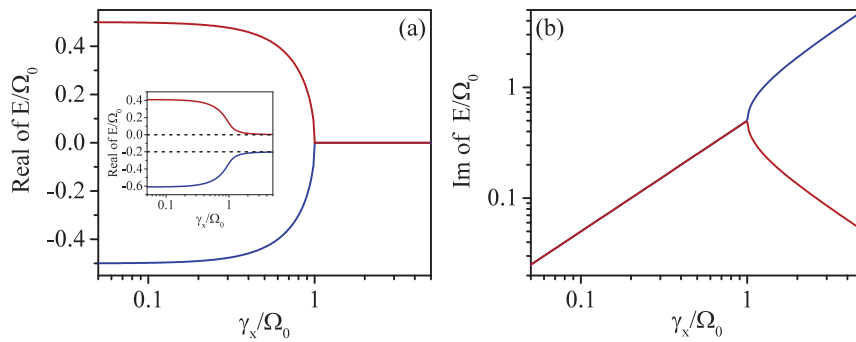


Figure 1.9 – (a) Polariton mode splitting as a function of the exciton linewidth for zero cavity detuning δ . The strong coupling is lost when $\gamma_x = \Omega_0$. The inset shows the same but for a cavity detuning of $\delta = -0.2\Omega_0$. (b) Imaginary part of the eigenvalues as a function of the exciton linewidth.

1.4.2 Multimode Polariton

Up to now, we have considered the strong coupling between a single exciton and a single photon state at each given k . We can easily generalize the system for the case of more than one exciton or photon states. We define the set of polariton branches for the general case as multimode polariton. Of course, by definition, the polariton system is multimode since it is the coupling of two modes. The use of the term here is to differentiate between single mode coupling and multimode coupling. The multimode polariton Hamiltonian can be derived from the one of equation 1.31 by adding a summation over exciton and photon states:

$$H_{mlm} = \sum_k \left\{ \sum_i \epsilon_{ci}(k) c_{ki}^\dagger c_{ki} + \sum_i \epsilon_{xi} x_{ki}^\dagger x_{ki} + \frac{1}{2} \sum_{ij} \Omega_{ij} (x_{ki}^\dagger c_{kj} + x_{ki} c_{kj}^\dagger) \right\}. \quad (1.40)$$

In general, not all exciton and photon states will couple to each other, meaning that Ω_{ij} can be zero or vary from one coupled mode to another. As a general rule, the exciton will couple to a photon mode that has the same properties as the one it would emit without the cavity. For instance, σ_+ excitons will not couple to a σ_- photon (assuming no disorder or asymmetry). This rule was implicitly used in the summation over k , since there is no coupling between exciton or photon of different k vectors.

To illustrate the multimode coupling, we consider first the case where two exciton modes are coupled to a single photon mode. The three coupled modes will give three polariton branches as shown in figure 1.10(a). Two points are worth noting from this figure. First, even if the two exciton states are not coupled by themselves, they get coupled through their own interaction with the same photon state. This yields polariton branches that are linear combination of both exciton states and photon. The Hopfield coefficients can be generalized to determine the excitonic fraction of both exciton states and photon. Second, we notice a strong similarity between the lower and upper branch of the three mode coupling and that of the 2 mode coupling. In fact, it is easy to show that, if the splitting between the exciton modes tends to zero, the Rabi splitting between the upper and lower branch becomes $\Omega = \sqrt{n}\Omega_0$, where n is the number of identical exciton levels. The Hamiltonian of n excitons strongly coupled to a single photon mode is mathematically equivalent to a Hamiltonian coupling a single exciton and photon mode but with a coupling strength increased by \sqrt{n} . This scenario is achieved when more than one QW of the same thicknesses is placed at the antinode of a microcavity. Coming back to figure 1.10(a), we can see that, as the energy splitting between the two exciton modes tends to zero, the middle polariton branch gets stuck between the exciton modes; it will become completely flat once the splitting is zero. As a result, this polariton mode is 100% exciton like and no longer coupled to the cavity. In general, when n exciton modes of identical energy are coupled to a single photon mode, we obtain $n - 1$ dark modes.

Using the same three coupled modes as in figure 1.10(a), we can describe a second

1.4. Strong Coupling in the Linear Regime: Exciton-Polariton

scenario of multimode coupling: the case of spin polarized coupling. We consider the case where two exciton spin states coupled to an unpolarized cavity mode, called independent coupling. Each exciton will couple to the orthogonal polarization of the degenerate photon mode, which occurs for microcavity polariton under a magnetic field [53]. The Zeeman effect of the exciton lifts the degeneracy of both spin up and spin down state. As for the cavity mode, it is unaffected by the field, hence for the case of low material disorder, the cavity mode is unpolarized or equally σ_+ and σ_- . The resulting system will be the sum of two independent orthogonally spins polarized polariton branches as depicted in figure 1.10(b). Comparing figures 1.10(a) and (b), we notice that the main difference between a multimode polariton and an independent polariton system is that a system of $n + 1$ coupled mode where n is the number of exciton modes will give $n + 1$ polariton branches for the former whereas $2n$ polariton branches will occur for the latter.

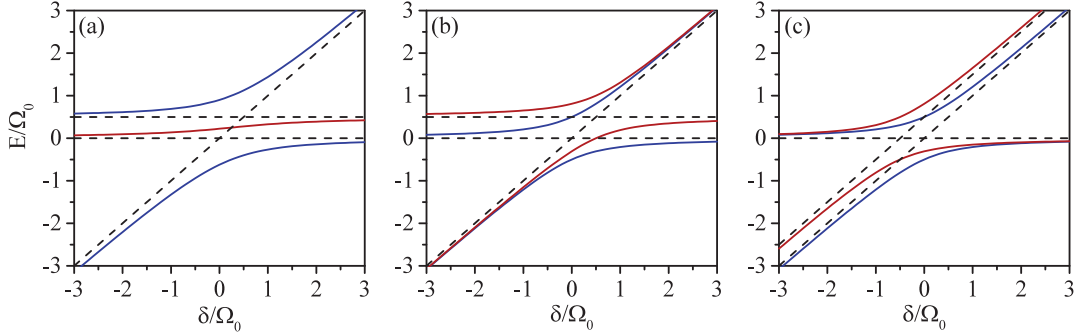


Figure 1.10 – (a) Polariton branches of three strongly coupled modes, two excitons and one cavity mode as a function of the cavity detuning. (b) Polariton branches of independent coupling between two excitons and one cavity mode. The red and blue curves represent the two independent polariton system, where the zero detuning is shifted. (c) Independent coupling between a single exciton mode and two cavity modes. In all cases, the energy and detuning is scaled with respect to the Rabi splitting Ω_0 and the black dashed lines represent the energy of the uncoupled exciton and photon modes.

There is one last case of multimode polariton which is of interest for the thesis is the complementary one to the independently coupled state where more than one photon couples to a single exciton mode. It occurs for a multimode microcavity that supports more than one orthogonal cavity mode, specifically for the case of 1D or 0D microcavities. Because of the orthogonality of the cavity modes, the system will be independently coupled meaning that, as the degenerate cavity mode could accommodate for the spin of the exciton, the degenerate plane wave motion of the exciton will accommodate for the orthogonality of the cavity modes. The case of a double mode microcavity is depicted in figure 1.10(c).

1.5 Non-linear Regime: Polariton Mean Field Equations

In the following section, we are interested to see how we can describe the polariton system in the case of large densities, when interaction between quasiparticles is expected. We proceed in a brief derivation of the mean field equations commonly used to describe this non-linear regime, and discuss the validity of the polariton picture at high densities.

1.5.1 Excitonic Bloch and Gross-Pitaevskii Equations

The interaction between polaritons comes from exciton-exciton interaction, since photons do not interact. So far, we have assumed that the exciton wave function could be described as a linear combination of electrons and holes wave functions as shown with equation 1.16. The interaction between two excitons comes from the Coulomb interaction, the well-known direct and indirect exchange interaction. In the simplest case, the Hamiltonian for interacting excitons is obtained by replacing electron and hole operators in the general electron-hole Hamiltonian by exciton operators. In fact, it can be shown that this transformation is not unitary, mainly because we are passing from a fermionic Hamiltonian to a bosonic Hamiltonian. To make the proper change of basis, one must apply the Usui transform, which turns the electron-hole Hamiltonian into an infinite sum of exciton-exciton interaction terms [54]. If we limit ourselves to quadratic terms, the exciton Hamiltonian, including the light-matter interaction can be written as [54–56]:

$$\begin{aligned}
 H = & \int d\mathbf{r} \left[\hat{\psi}_x^\dagger \left(\epsilon_x - \frac{\hbar^2 \nabla^2}{2m_x} \right) \hat{\psi}_x + \hat{\psi}_c^\dagger \left(\epsilon_c - \frac{\hbar^2 \nabla^2}{2m_c} \right) \hat{\psi}_c \right. \\
 & \left. + \frac{\Omega_0}{2} \left(\hat{\psi}_x^\dagger \hat{\psi}_c + \hat{\psi}_x \hat{\psi}_c^\dagger \right) \right] \\
 & + \frac{1}{2} \int d\mathbf{r} \int d\mathbf{r}' \left[\hat{\psi}_x^\dagger \hat{\psi}_x'^\dagger V_{exch}(\mathbf{r} - \mathbf{r}') \hat{\psi}_x \hat{\psi}_x' \right. \\
 & \left. - V_{pae}(\mathbf{r} - \mathbf{r}') \left(\hat{\psi}_c^\dagger \hat{\psi}_x'^\dagger \hat{\psi}_x \hat{\psi}_c' + \hat{\psi}_x^\dagger \hat{\psi}_x'^\dagger \hat{\psi}_x \hat{\psi}_c \right) \right], \quad (1.41)
 \end{aligned}$$

where $\hat{\psi}_x^\dagger$ and $\hat{\psi}_c^\dagger$ are excitons and photons field creation operators. The first line of the Hamiltonian represents the kinetic part, the second is the light-matter coupling that we have used previously. The third term is the exciton-exciton exchange interaction, while the last terms originate from the expansion of the light-matter coupling terms when passing from the electron-hole picture to the exciton. It represents the effect of phase space filling, which is fermionic in nature. Simply put, at large exciton density, the exciton-photon coupling strength is decreased. This can be understood as a decrease of the oscillator strength with density. At large density, the exciton dipole is further screened by the surrounding charges which lowers its ability to couple to light.

1.5. Non-linear Regime: Polariton Mean Field Equations

The representation in real space is advantageous because it allows to easily simplify the Hamiltonian 1.41. Instead of summing over all possible momentum exchange between excitons, we simply integrate over the sample volume and consider all the excitons in the system. The Hamiltonian can be simplified by evaluating the exciton-exciton exchange interaction [57]. It was shown that, in the limit of small momentum exchange between excitons, namely in the region of strong coupling, the direct interaction is zero while the indirect term is constant in momentum space. Therefore, we can assume that the exciton interaction is a contact interaction: $V_{exch}(\mathbf{r} - \mathbf{r}') = g\delta(r - r')$ [58]. Using the same assumption for the phase space filling terms: $V_{pae}(\mathbf{r} - \mathbf{r}') = 2g_{pae}\delta(r - r')$ and performing the integration over space allows to write the Hamiltonian as:

$$\begin{aligned} H = & E_x \hat{x}^\dagger \hat{x} + E_c \hat{c}^\dagger \hat{c} + \frac{\Omega_0}{2} (\hat{c} \hat{x}^\dagger + \hat{c}^\dagger \hat{x}) \\ & + \frac{g}{2} \hat{x}^\dagger \hat{x}^\dagger \hat{x} \hat{x} - g_{pae} (\hat{c} \hat{x}^\dagger \hat{x}^\dagger \hat{x} + \hat{c}^\dagger \hat{x}^\dagger \hat{x} \hat{x}). \end{aligned} \quad (1.42)$$

This Hamiltonian describes single mode interaction, namely a single exciton and photon operator. The generalization to the multimode case will be given in chapter 5, where we will investigate cross interactions between confined polaritons, and in appendix A. Starting from this Hamiltonian, we can derive the equations of motion for the exciton and photon operators as well as the exciton number operator $\hat{x}^\dagger \hat{x}$ using Heisenberg's equation of motion: $-i\hbar \dot{\hat{a}} = [\hat{H}, \hat{a}]$. This gives:

$$i\hbar \dot{\hat{x}} = \frac{\Omega_0}{2} (\hat{c} \hat{x}^\dagger - \hat{c}^\dagger \hat{x}) - g_{pae} (\hat{c} \hat{x}^\dagger \hat{x}^\dagger \hat{x} - \hat{c}^\dagger \hat{x}^\dagger \hat{x} \hat{x}), \quad (1.43a)$$

$$i\hbar \dot{\hat{x}} = E_x \hat{x} + g \hat{x}^\dagger \hat{x} \hat{x} + \frac{\Omega_0}{2} \hat{c} - 2g_{pae} \hat{c} \hat{x}^\dagger \hat{x} - g_{pae} \hat{c}^\dagger \hat{x} \hat{x}, \quad (1.43b)$$

$$i\hbar \dot{\hat{c}} = E_c \hat{c} + \frac{\Omega_0}{2} \hat{x} - g_{pae} \hat{x}^\dagger \hat{x} \hat{x}, \quad (1.43c)$$

where we have dropped the hat symbol for simplicity. These equations show that in order to obtain the equation of motion of either the exciton or the photon, we need to evaluate terms that include an increasing number of products of the operator. This is the well-known hierarchy problem [33]. A way to obtain solvable equations is to use the mean value of these operators instead of the correlator between them. We define:

$$N = \langle \hat{x}^\dagger \hat{x} \rangle, \quad (1.44a)$$

$$P = \langle \hat{x} \rangle, \quad (1.44b)$$

$$E = \langle \hat{c} \rangle, \quad (1.44c)$$

as the exciton population, the exciton polarization and the photon mean field or simply the electric field. We then need another set of approximations in order to write higher order terms of the type $\langle \hat{x}^\dagger \hat{x}^\dagger \hat{x} \rangle$ as a product of our mean fields. One way of doing so is to ensure particles number conservation. This can be achieved with the following

assumptions [58, 59]:

$$\langle x^\dagger x x \rangle = \langle x^\dagger x \rangle \langle x \rangle, \quad (1.45a)$$

$$\langle x^\dagger x^\dagger x \rangle = \langle x^\dagger \rangle \langle x^\dagger x \rangle, \quad (1.45b)$$

$$\langle x x \rangle = 0. \quad (1.45c)$$

Although such approximations is not so obvious, they are well justified by the experimental results. Indeed, early experiments on microcavity polaritons showed that the polariton non-linearity is Kerr-like [3, 4, 6], which is represented by a $\chi^{(3)}$ term. In other words, it is proportional to the product of three field amplitudes. We then get:

$$i\hbar\dot{N} = -i\Gamma_x N - 2i(\Omega - g_{pae}N) \text{Im}(PE^*), \quad (1.46a)$$

$$i\hbar\dot{P} = (\epsilon_x - i\gamma_x + g_0 N)P + (\Omega - 2g_{pae}N)E, \quad (1.46b)$$

$$i\hbar\dot{E} = (\epsilon_c - i\gamma_c)E + (\Omega - g_{pae}N)P, \quad (1.46c)$$

where we have used the relation $E^*P - P^*E = 2i\text{Im}(PE^*)$ and added the lifetime loss terms by hand. These equations are called the Excitonic Bloch equations (EBE) due to their similarity to the optical Bloch equations. These equations are useful to simulate resonantly excited polaritons, which can be done by adding a term $f_{ext} = \sqrt{I_0}e^{\frac{-E_I t}{\hbar}}$ in the photon equation. Moreover, we can include the effect of dephasing directly by considering different loss rates for the exciton polarization and population. If the system is not fully coherent then the exciton population will be larger than the coherent exciton population: $N > |P|^2$. For example, the effect of excitation-induced dephasing can be implemented by assuming that the interaction strength has a real and imaginary part $g = g_0 - ig'$. This will lead to a density dependent exciton linewidth $\gamma_x = \Gamma_x/2 + g'N + \gamma^*$, where γ^* is a pure dephasing term.

The analogy with the optical Bloch equations should not be pushed too far. First because we are dealing with QW excitons and not two-level systems. In the latter, there is an intrinsic saturation that comes from the fact that, once excited, a two-level system can no longer be populated. In the case of QW excitons, the saturation comes from the phase space filling and the reduction of the oscillator strength. Both are called saturation but have different physical meaning.¹

If we limit ourselves to the coherent limit of the EBE, that is setting $g' = \gamma^* = g_{pae} = 0$,

¹There is a factor 2 missing in front of g_{pae} in the N equation compared to the original one from Rochat *et al.* [54]. This is indeed correct. The original derivation of the N equations was done using the chain derivative of $\partial_t x^\dagger x$ instead of the commutation relation of the number operator $x^\dagger x$. This necessarily leads to the coherent limit [60]. A more recent derivation done in ref [58] added this factor 2 in order to have a saturation in the coherent limit, in analogy to the optical Bloch equations which, as stated, is not justified. In any case, when relating to experiments, this parameter is a fitting parameter, meaning that a factor 2 is meaningless. This difference is only stated for mathematical rigor.

1.5. Non-linear Regime: Polariton Mean Field Equations

we get another set of coupled equations:

$$i\hbar\dot{\chi} = (\epsilon_x - i\gamma_x + g_0|\chi|^2)\chi + \frac{\Omega_0}{2}\phi, \quad (1.47a)$$

$$i\hbar\dot{\phi} = (\epsilon_c - i\gamma_c)\phi + \frac{\Omega_0}{2}\chi, \quad (1.47b)$$

where the exciton polarization and photon mean field are now given by χ and ϕ , in accordance to the literature. This set of equations are the Gross-Pitaevskii equations in the excitation-photon basis, in analogy to the equation describing the order parameter of atomic condensates. In fact, we retrieve the same equations as for atomic condensates if we limit ourselves to the lower polariton mean field, that is, we use the Hopfield coefficients to transform the system in the polariton basis and only keep the lower branch:

$$i\hbar\dot{\psi}_{LP} = (\epsilon_{LP} - i\gamma_{LP} + \alpha_1|\psi_{LP}|^2)\psi_{LP}, \quad (1.48)$$

where $\alpha_1 = |X|^4 g_0$. Since the polariton lifetime is of the order of 4-50 ps, the system needs to be continuously pumped in order to maintain the condensate. This is usually considered by coupling the GPE with a reservoir [61, 62]:

$$i\hbar\dot{\psi}_{LP} = (\epsilon_{LP} + i(RN_R - \gamma_{LP}) + \alpha_1|\psi_{LP}|^2 + gN_R)\psi_{LP}, \quad (1.49)$$

$$\dot{N}_R = -(\gamma_R + R|\psi_{LP}|^2)N_R + P, \quad (1.50)$$

where polariton-reservoir interaction is assumed and P represents the pumping into the reservoir which itself is depleted at a rate that depends on the coherent polariton density.

1.5.2 Polaritons and Bose-Einstein Condensation

The similarity between the polariton mean field equations and the GPE for atomic condensates already suggests that polaritons should form condensates. Of course this comparison alone is not enough to imply polariton BEC. Therefore we must evaluate under which conditions polaritons can be considered as bosons and whether they undergo bosonic stimulation. In the low-density regime, the polariton operators defined in equations 1.34 follow the bosonic commutation relation $[\hat{L}_k, \hat{L}_{k'}^\dagger] = \delta_{k,k'}$. However, this relation is no longer valid at large densities, due to the higher order exciton terms in the Hamiltonian. As a simple rule, for the polariton picture to be valid, the exciton-exciton interaction and phase space filling terms should be smaller than the light-matter coupling. Comparing

with the EBE equations 1.46 this condition is written as:

$$g_0 N \ll \frac{\Omega_0}{2}, \quad (1.51a)$$

$$g_{pae} N \ll \frac{\Omega_0}{2}, \quad (1.51b)$$

where, as stated in equations 1.46, N is the exciton density *per quantum well*. If these conditions are well satisfied, then polariton Bose-Einstein condensate of polariton might be possible. For a 3D gas of weakly interacting bosons, the bosonic stimulation occurs when the gas is cold enough [63]:

$$T_c = \frac{2\pi\hbar^2}{m} \left(\frac{n}{2.612L^3} \right)^{2/3}. \quad (1.52)$$

Although the microcavity polariton system is two-dimensional, we can use this equation to get an insight of what to expect for a polariton BEC. In fact, for 2D systems, the phase transition should be a BKT one and not a BEC. However, a 2D BEC is allowed if there is an extra trapping potential, which is usually the case for polaritons.

Equation 1.52 tells us that the critical temperature is inversely proportional to the boson mass. This is ideal for polaritons since its photonic fraction gives it a mass about five orders of magnitude smaller than the electron mass. As atomic condensates occurs for temperatures in the range of nK to μK , polariton condensates can be obtained at regular cryogenic temperatures [7]. Moreover, the temperature can be extended to room temperature for certain materials, namely for wide band gaps [10] and organic semiconductors [64]. Experimentally, the sample temperature will be fixed, meaning that the polariton bosonic stimulation will be reached for a critical density. Therefore, the whole goal for polariton condensates is to reach this critical density before the exciton density in the quantum well becomes too large and polaritons no longer behaves as bosons.

In principle, this limitation can be overcome by increasing the number of QWs in the microcavity. For a given polariton density, the exciton density per QW will decrease when the number of wells increases. This point is crucial because it is the density per QW that defines the validity of the polariton picture, as shown in equations 1.51a and 1.51b. These conditions should be easier to fulfill when increasing the number of QWs since we decrease the exciton density while we increase the Rabi splitting. In fact, we can show that it is true only for the condition on the exciton-exciton interaction (the polariton blue shift). To understand this, we use the EBE for n QWs (these equations are different than what we will obtain for multimode interactions in the chapter 5). For a given exciton

1.5. Non-linear Regime: Polariton Mean Field Equations

density per QW, the right-hand side of the equations can be written as:

$$\begin{pmatrix} \epsilon_c & \Omega_0^1/2 - g_{pae}N & \Omega_0^2/2 - g_{pae}N & \dots & \Omega_0^n/2 - g_{pae}N \\ \Omega_0^1/2 - g_{pae}N & \epsilon_x + g_0N & 0 & \dots & 0 \\ \Omega_0^2/2 - g_{pae}N & 0 & \epsilon_x + g_0N & \dots & 0 \\ \vdots & \vdots & \vdots & \ddots & \vdots \\ \Omega_0^n/2 - g_{pae}N & 0 & \dots & \dots & \epsilon_x + g_0N \end{pmatrix}, \quad (1.53)$$

where the subscript indicates the QW number. We should be careful with this description since we are including the exciton density into the Hamiltonian, hence it should not be used to study polariton dynamics. In this description, representing the system with the Hamiltonian 1.53, we assume that, for a fixed exciton density, the system is the same as the polariton Hamiltonian but with a shifted exciton resonance. We can use the mathematical equivalence for a system of n coupled oscillator to write it as:

$$\begin{pmatrix} \epsilon_c & \sqrt{n}(\Omega_0/2 - g_{pae}N) \\ \sqrt{n}(\Omega_0/2 - g_{pae}N) & \epsilon_x + g_0N \end{pmatrix}. \quad (1.54)$$

From the diagonal, we see that the exciton blue shift stays the same when increasing the number of QWs. For a given polariton density $N_{pol} \approx nN$, the *polariton* blue shift (or the polariton-polariton interaction) decreases as the number of well increases. As we mentioned previously, the coupling constant is increased by a factor \sqrt{n} . However, the saturation per QW is increased by the same amount. This is also logical, since the breakdown of the exciton depends on the density in each well. Consequently, as we increase the Rabi splitting with the number of wells, the blue shift due to saturation is also amplified. Although the Rabi splitting increase pushes the lower polariton branch farther away from the uncoupled modes, it does not mean that the system can sustain a larger blue shift (or exciton density) coming from the saturation term before reaching the weak coupling regime.

It is commonly stated that increasing the Rabi splitting with the number of QWs allow to maintain the strong coupling at large density. With the simple formulation mentioned above, we see that this statement is incorrect, since the saturation only depends on the relative strength of $g_{pae}N$ to Ω_0 of a single QW. The stability of polaritons is given by the light-matter coupling of a single well. However, increasing the number of QWs decreases the exciton density for a given polariton density, meaning that the system can sustain a larger *polariton* density before the QWs saturate. If saturation starts to occur before reaching the condensation threshold, the blue shift due to saturation will grow \sqrt{n} faster compared to a single QW cavity. We see that the loss of strong coupling is a question of QW exciton density and not of total Rabi splitting. We can rephrase the previous statement as: increasing the number of QW allows to maintain the strong coupling regime at large *polariton density* by lowering the *exciton density* of each QW.

We can state the condition to reach polariton condensation in terms of the exciton density per QW as:

$$N_{pol}^{crit} \approx n N_x^{crit}, \quad (1.55)$$

$$N_x^{crit} \approx \frac{N_{pol}^{crit}}{n} < N_{sat} = \frac{\Omega_0}{2g_{gpae}}. \quad (1.56)$$

These equations state that for the critical polariton density needed to form a condensate, N_{pol}^{crit} , there is a corresponding exciton density per QW, N_x^{crit} . This exciton density should be much lower than the saturation density which is given by the ratio between the Rabi splitting of a single QW Ω_0 to the phase space filling term g_{gpae} . As an example, if there is an order of magnitude between the two, then there will be an order of magnitude of excitation power between the condensation threshold and the lasing threshold. Similarly, if both densities are too close, then the weak coupling crossover will occur as we go through the condensation threshold. Hence, no true polariton condensate will form.

The increase of Rabi splitting might not have a direct impact on the validity of the polariton picture, but it will greatly affect how polaritons relax to the ground state. By increasing the Rabi splitting, we modify the shape of the dispersion and change the polariton-phonon scattering coefficients [49, 65]. If the scattering is not efficient, it will not be possible to reach the critical density anywhere on the polariton dispersion before the system transits into weak coupling.

To summarize, there are three key aspects that need to be considered for polariton condensation. The first is phonon scattering in order to reach bosonic stimulation, the second is the long range coherence that the macroscopic state gets in the condensed phase and the third is the dissipative nature of the polariton condensate. The first one can be simulated by a set of Boltzmann equations to study polariton relaxation [65, 66], but this approach will not be able to account for the coherence properties of the condensate. Conversely, the GPE is built to study the coherence of the condensate properly but cannot take into account bosonic stimulation. In this formalism, the order parameter is zero below stimulation and non-zero above. Bosonic stimulation only enters as a gain to maintain the condensate as depicted in equations 1.49. Two approaches have been recently proposed to simulate both the stimulation and the coherence. The first one is to couple a Boltzmann system of equations with GPE [67] while the second relies on jump operators built from the density matrix for the polariton [68]. In the latter, the appearance of long range coherence at the onset of condensation was accurately simulated. It is worth mentioning that none of these approaches work in the exciton-photon basis hence they do not consider phase space filling or other types of dephasing that the EBE includes.

2 InGaAs/GaAs quantum well based microcavity

In the previous chapter, we presented the theoretical background of light-matter interaction of quantum well excitons and DBR microcavities. In this chapter, we focus on properties that are specific to the samples that will be studied, namely InGaAs/GaAs quantum wells and GaAs/AlAs microcavities. Although GaAs-based microcavities are the most common for studying polariton physics, there are distinctions to be made between GaAs/AlAs and InGaAs/GaAs quantum wells. After discussing these particularities, we give an overview of sample optimization and characterization.

2.1 Properties of InGaAs based quantum wells

All the samples studied have been grown by molecular beam epitaxy (MBE). The principle behind this technique is to send fluxes of heated materials on a thick ($350\text{ }\mu\text{m}$) GaAs substrate to grow the desired material one atomic layer at a time. For instance, sending a flux of Ga and As on the substrate at a temperature of $\sim 600\text{ }^\circ\text{C}$, will form atomic layers of GaAs. For a given flux, the thickness grown will be proportional to the amount of time the materials are sent to the substrate. We can make a quantum well (QW) structure by growing a thin layer of material in between two layers having a higher band gap. For instance, GaAs QWs are grown using AlAs or AlGaAs as the barrier material. To grow InGaAs QWs, we use GaAs as the barrier material. If we send an In flux together with the Ga and As ones we obtain a ternary material, $\text{In}_x\text{Ga}_{1-x}\text{As}$, where x is the fraction of In included. Since In is from the group V on the periodic table, it will replace as Ga in the crystal composition to make a stable compound. Furthermore, since the band gap of InAs is lower than GaAs, incorporating In in GaAs will push the band gap of the ternary compound closer to that of InAs. We can control the height of the potential well by controlling the amount of In which is incorporated. Hence, growing a thin layer of $\text{In}_x\text{Ga}_{1-x}\text{As}$ in between two GaAs layers will form a quantum well.

The main drawback of growing $\text{In}_x\text{Ga}_{1-x}\text{As}$ is the appearance of strain and disorder.

This is because GaAs and InAs are not lattice matched ($a_{\text{GaAs}} = 5.64 \text{ \AA}$, and $a_{\text{InAs}} = 6.06 \text{ \AA}$ [30]). The resulting QW layer will be strained, even for In content as low as 3 %. This has a major consequence: the light hole is not confined in these QWs [69–71]. Disorder can occur because of In segregation at the top interface of the QW [72, 73]. These effects will cause an increase of the inhomogeneous linewidth of the exciton as the In content increases.

We can simulate InGaAs/GaAs QW using the software Nextnano [74], which is commonly used for semiconductor simulation. For a given QW structure, it allows to calculate the band structure, the confined electron and hole states (energy and wave function), and the oscillator strength of the electron-hole transitions (through the overlap of the wave functions). The calculation is based on the effective mass approximation ($k \cdot p$ calculation gave similar results) where the material parameters are taken from known values in the literature [75, 76]. Furthermore, the effect of strain can be added, which is mandatory for InGaAs/GaAs QW.

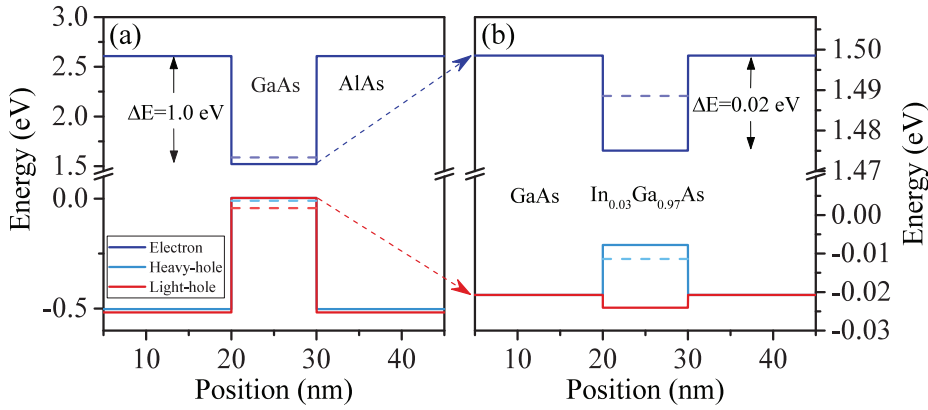


Figure 2.1 – (a) Calculated band structure for a GaAs/AlAs QW. (b) Calculated band structure for a $\text{In}_{0.03}\text{Ga}_{0.97}\text{As}$ QW. The dashed lines inside each well represent the energy levels for the electron and the holes. The dashed arrows show how the energy scale changes between the two panels with respect to the GaAs bands.

In figure 2.1 we compare the band structure of a typical GaAs/AlAs QW in (a) to that of an $\text{In}_{0.03}\text{Ga}_{0.97}\text{As}$ /GaAs QW in (b). Since the QW material in (a) becomes the barrier material in (b), we must zoom in the energy scale to look at the band structure of the InGaAs/GaAs QW (as represented by the dashed arrows). The carriers are well localized in the GaAs/AlAs QW because of the large barrier of 1 eV. In contrast, InGaAs QWs have quite shallow barriers, hence there is a considerable extension of the carriers wave function inside the barrier material. This difference is also clear by looking at the position of the electron ground state in each well. The simulation also demonstrates that the light-hole band is inverted compared to the heavy-hole for the InGaAs/GaAs QW. Hence, the light-hole is not confined as a consequence of the strain. Both bands are identical if we remove strain from the calculation. This effect does not occur for GaAs/AlAs QWs

2.2. Sample characterisation and optimization

since they are almost lattice matched. The difference in energy between the two hole states comes from the difference in effective mass between GaAs and AlAs.

We can compute the influence of Indium, and well thickness on the electron-hole transition which is shown in figure 2.2. In (a), we plot the energy difference between the electron or hole ground state and their respective band edge (the band edge difference of the two materials is shown by the black dashed lines). Clearly, increasing the Indium content increases the potential depth for both particles. However, because the barrier material is the same in all cases, the transition energy decrease rather abruptly with Indium content as panel (b) shows (and sketched in (a)). As expected, for a given material composition, the thinner the well, the higher the transition energy.

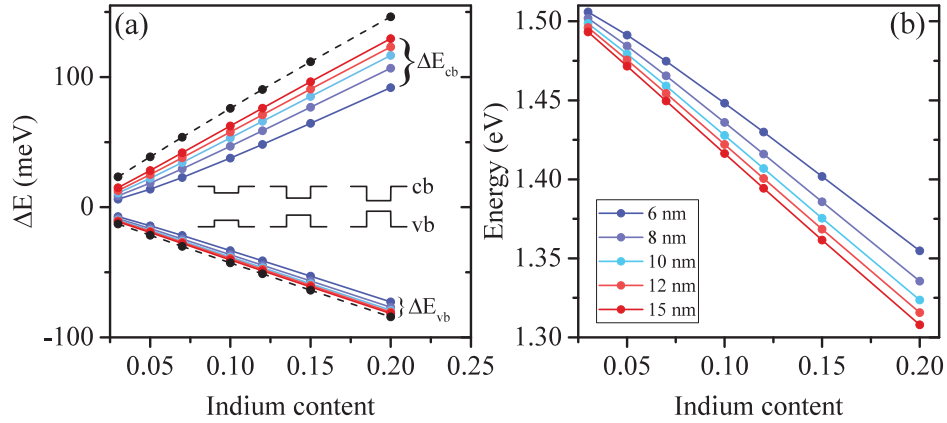


Figure 2.2 – (a) Calculated electron and heavy hole energy levels with respect to their band edges as a function of In content, and well thickness. The black dashed lines represent the potential height in both cases. $\Delta E_{cb} = E_{cbGaAs} - E_{cbQW}$, $\Delta E_{vb} = E_{vbGaAs} - E_{vbQW}$. Since the band gap energy is subtracted, the difference between the electron and hole energy for a given point does not equal the optical transition energy. The inset show schematically the evolution of the band structure as a function of In content. (b) Energy of the e_1-hh_1 transition as a function of In content and well thickness.

The growth of ternary material is in general more complicated than for binary. However, from an optical point of view, $\text{In}_x\text{Ga}_{1-x}\text{As}/\text{GaAs}$ QWs have one main advantage: the light emitted will not be absorbed by the substrate. Indeed, since the QW is at a lower energy than the substrate band gap, the light can go through the substrate with minimal absorption. This is not the case for GaAs/AlAs QW. Therefore, using InGaAs QWs allows for resonant excitation of the sample while working in transmission.

2.2 Sample characterisation and optimization

In this section, we give an overview of typical results for the characterization of QWs and microcavity samples. Apart from sample 1485 used for part III, all samples were grown

by F. Jabeen in our group (details of the structure of all samples presented in the thesis is given in appendix B). The premise for these characterizations was to design a microcavity sample to study non-resonant polariton condensation, hence a cavity with a large number of QWs and DBR pairs. The choice of InGaAs/GaAs QWs over the GaAs/AlAs QWs was primarily due to the fact that most experiments done in the group involve resonant excitation. Therefore it would be easy to prepare samples for other experiments once the know-how of InGaAs growth was mastered. In the next chapter we will discuss in greater detail the linear regime of such microcavity samples, while the non-linear regime will be the topic of chapter 4.

2.2.1 Experimental setup

The characterization setup that was designed is presented in figure 2.3. It consists in a typical photoluminescence (PL) setup in reflection geometry, with three optical sources that join on a single optical excitation axis. The HeNe laser is used for standard PL, while a high power laser diode (Cobolt Flamenco laser, 660 nm, 0.5 W) can be used to characterize nonlinear thresholds for microcavity samples. The white lamp allows to perform reflectivity measurements necessary for measuring the stop band of microcavities (with a gold mirror placed inside the cryostat for reference). The samples are cooled to 10 K by a closed circuit He cryostat which is mounted on a mechanical stage with a displacement of ~ 1.5 cm at a step size of $2\text{ }\mu\text{m}$. The microscope (camera) objective has an aperture of 2 inch and a pinhole inside that allow selecting only emission from $k = 0$. The lens L_1 of focal length $f_1 = 20$ cm is used to send the outgoing signal into a 50 cm spectrometer and CCD camera (resolution of $\sim 120\text{ }\mu\text{eV}$).

The lenses L_2 to L_4 can be added to perform k -space imaging. By matching the focal planes of each lens, the k -space is propagated adequately from the MO to the slits of the spectrometer. The $l = 2$ inch aperture of the beam out of the MO must be decreased to $l = 1$ inch in order to pass into the 1 inch beam splitter without cutting the sides of the k -space signal. This is achieved by using a 2 inch lens L_4 with focal length $f_4 = 15$ cm and a one-inch lens L_3 of focal length $f_3 = 3$ cm. With this, we can recover the full k -space available by our objective. However, adding lenses L_3 and L_4 increases the size of the excitation spot which decreases the excitation density. The inset of the figure represents the real space propagation of the signal when the k -space optics are placed. Although this system works well, the limited NA of the objective does not allow to image the polariton dispersion up to the bottleneck region (for negative detuning), hence such images are generally taken in another setup with a high NA objective.

2.2.2 Quantum wells

Bare QW samples are grown to optimize the material quality before the growth of microcavities. In general, the single QW is placed between GaAs layers of 100 nm and

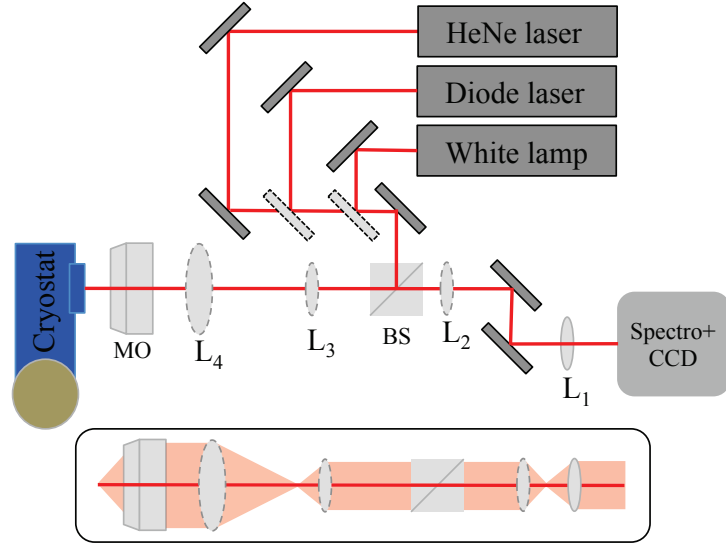


Figure 2.3 – Scheme of the experimental setup for sample characterization. L_i are lenses, and MO is a microscope objective. The lenses and mirrors with dashed lines are placed on flip mounts. The box represent a scheme of the real space propagation when the lenses for *k*-space imaging a placed. The collimated beam in real space at the spectrometer slits means that the *k*-space image is focused.

AlGaAs layers on both sides. These AlGaAs layers allow to keep the carriers in a given GaAs thickness which is ideal to compare the PL intensity of different samples. The top AlGaAs layer is also mandatory to avoid non radiative recombination at top GaAs surface. We focus here on the best single QW sample that was obtained for low In content. The case of QW stacks will be the topic of the next chapter whereas higher In content ($< 15\%$) will be addressed in chapter 4.

Figure 2.4 (a) presents the PL of a single 9 nm QW with $\sim 4.5\%$ In. We notice a bright emission peak that corresponds to the 1S exciton of the QW with a narrow linewidth of 0.6 meV. Apart from the exciton peak, there is additional structure that does not occur in the QW simulation. Starting from the low energy side, we see the typical double peak of donor-acceptor transition which is likely caused by carbon impurities inside the QW (the energy position of these peaks depends on the In content). There is a small shoulder at low energy of the exciton peak which has been identified to the trion line [77–79]. The shoulder on the high energy side shows the first exciton excited state (2S) and the continuum band edge, which allows to measure a binding energy of 7 meV. This identification is based on previous work on high-quality InGaAs QW [77, 80]. They identified the 2S and band edge by combining PL and reflectivity. They showed the appearance of a plateau in absorption on the high energy side of the band edge peak observed in PL which corresponds to the 2D density of states of the free carriers. In the same work, the second brightest peak (~ 16 meV above the exciton) was attributed to the light-hole transition although no comment was made regarding the confinement.

This transition in principle corresponds to a delocalized hole bound to the electron by Coulomb interaction. In fact, the measured energy difference between the 1S and the light-hole transition is close to the one we obtain by calculating it from the $e-hh$ and the $e-lh$ transition as shown in the inset. In analogy to the 1S transition, we can assume that the high energy shoulder is the light-hole band edge. This means that the light-hole exciton binding energy is smaller than the heavy-hole exciton counterpart. The small peak at lower energy has not been assigned, although the simulation indicates it could arise from a delocalized electron bound by the heavy-hole. Finally, the highest energy peak on the figure is the GaAs free exciton emission.

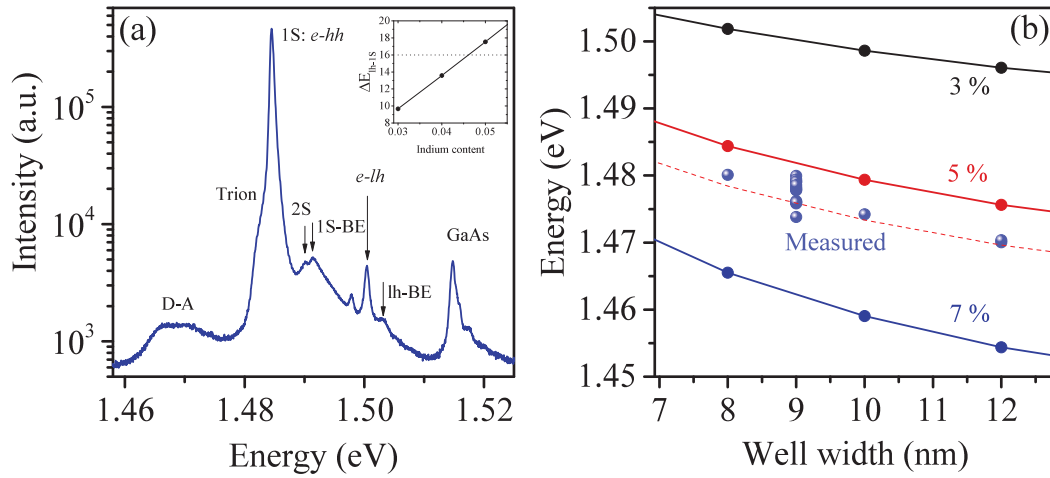


Figure 2.4 – (a) PL of a single 9 nm QW with 4.5% In (sample D-03). The inset shows the calculated energy difference between the $e-hh$ and $e-lh$ transition as a function of In content. (b) Calculated $e-hh$ transition energy as a function of well width and In content. The blue dots are measured exciton transitions on a series of samples, and the dashed line corresponds to the 5 % curve shifted by 6 meV.

In most cases, the linewidths are larger, which smears the 2S transition and the structure around the light-hole transition. The exciton band edge is always present in PL, and the light-hole emission varies from sample to sample. All of these features are almost invisible if the emission is analyzed in linear scale, over a single order of magnitude. In general, it is advisable to use long integration times and accumulations to extract all of the features of PL spectrum.

In figure 2.4 b we compare the measured energy for various QW samples of $\sim 5\%$ In content to calculations of $e-hh$ transition for different well thicknesses and In content. Some QW have the same trend as for the calculation, only shifted by about 6 meV in energy. This indicates that the Nextnano calculation gives reasonable agreement with our measurements although Coulomb interaction is not included. It also shows that there can be some fluctuation of the In content from sample to sample that affect the actual thickness of the well.

2.2.3 Designing a microcavity in the strong coupling regime

Once the growth of QW is optimized and reproducible, we can move to the growth of full microcavity samples. This growth is performed on a full 2 inch GaAs wafer that rotates to assure a radial homogeneity of the material. Because of the large surface of the wafer, the incoming flux of material is not uniform, causing the layers thicknesses to decrease from the center to the edge of the wafer. This is actually a great advantage to design a microcavity in the strong coupling regime as it allows to tune the cavity resonance with respect to the exciton energy by moving along the radius of the wafer. Since the cavity thickness decreases, the resonance energy will increase from the center to the edge of the wafer. Hence, in order to measure the anticrossing of the modes, we must design a microcavity that will be in resonance with the exciton at a certain radius, ideally at the middle of the wafer. That way we get access to both negative and positive detuning on a single sample.

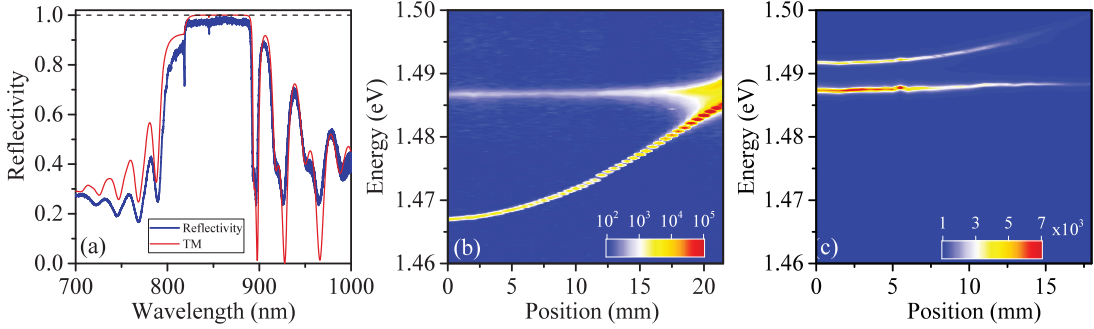


Figure 2.5 – (a) Measured reflectivity of sample D-49 (λ -cavity with 20/24 top/bottom DBR pairs, and a single QW with 5 % In) at the center of the wafer (blue) and corresponding fit using the transfer matrix formalism (red). (b) PL intensity map in log scale as a function of position on the sample. (c) PL intensity map in linear scale as a function of position for sample D-55.

The design procedure is to use the transfer matrix formalism to determine the material thicknesses needed at the center of the wafer since this is where the growth rates are evaluated. The desired cavity thicknesses should be slightly larger than the ones corresponding to the QW energy to be able to tune the cavity in and out of resonance. The growth is usually performed in a single run once the growth rates have been calibrated (growth lasting up to 24h for a 20/24 DBR microcavity). This design procedure works well if the refractive indices of the materials are known, and the MBE growth is reproducible. The refractive index curves used in the simulation were adapted from known values in the literature for GaAs, and $\text{Al}_x\text{Ga}_{1-x}\text{As}$ [81]. In reality, there is always some deviation between the expected thicknesses, and the ones grown. We can evaluate these deviations by comparing measured reflectivity and the simulated using the transfer matrix formalism, as shown for example in figure 2.5(c). In this case, the simulation allowed to determine a deviation of 2 % above the desired thicknesses. This is also noticeable when we measure

the PL as a function of position on the sample, as shown in figure 2.5 (b). In this case, we do not reach the zero detuning since the cavity is too thick. We also see from this figure that the wedge of the sample is parabolic instead of linear, meaning that the range for tuning the cavity is in fact half of the wafer's radius. Using the results from the simulation, we can in principle optimize the growth parameters in order to converge rapidly to the desired sample.

In reality, the task is much more complicated because the MBE machine has a poor reproducibility from one growth to another. We evaluated that, in general, the growth thicknesses are about 2% less than the expected ones. This can be compensated by overshooting the input thicknesses. The main problem that we encountered is that this 2% fluctuates between growths. Moreover, a 2% fluctuation might seem small, but it corresponds to the range available with our sample wedge. Hence, even if we try to optimize the growth, the uncertainty is comparable to the range of energy which we can tune our sample. As an example, figure 2.5 (c) shows the sample grown after the one shown in (b). Since the stop band was close to being centered at the right energy, only a correction of 6 nm was made on the spacer. However, the actual sample was about 2% thinner than expected meaning that the sample was only in positive detuning.

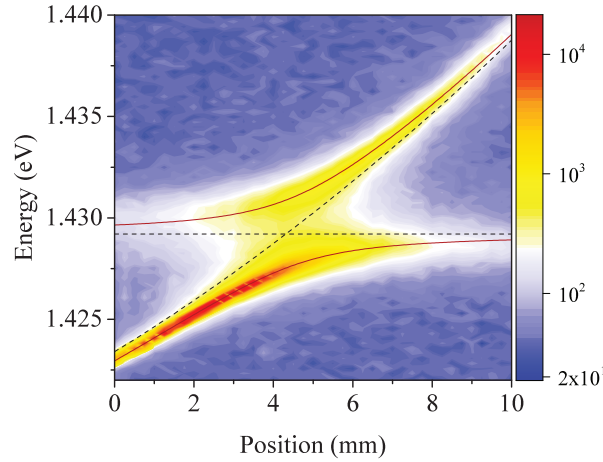


Figure 2.6 – (a) PL intensity map in log scale as a function of position for sample E-65 (measured at 10 K). The red curve represents a fit using the coupled oscillator model, while the dashed line represents the energy of the uncoupled exciton and photon.

The stability of the MBE machine has varied a lot during the course of this PhD. In some cases the convergence was quick while almost impossible in others. Moreover, different problems on the machine (broken Al cell due to power cuts, faulty power supply, blocked Ga shutter to name a few), forced five shutdowns of the machine for repairs or openings of the growth chamber. In each case, when the MBE was back online after months of standby, the material quality had to be re-optimized from the start, which brought additional delays to the optimization of the samples. Nonetheless, a number of high

2.2. Sample characterisation and optimization

quality samples (both QW and microcavity) were obtained during the course of the PhD. As an example, figure 2.6 shows the measured PL signal as a function of position for a λ -cavity with 20/24 top/bottom DBR pairs and a single 9 nm QW with 10 % In. The anticrossing of the modes is clearly seen, indicating that we are indeed in the strong coupling regime. A fit of the data using the coupled oscillator model is shown in red, from which we can extract the Rabi splitting of $\Omega_0 = 3.35$ meV.

Non-resonant excitation of planar microcavity

Part II

3 Multimode polaritons originating from coupled quantum wells

In the last chapter, we discussed the material properties and optimization of our samples. The main goal has been to reach non-resonant condensation using InGaAs QWs. As we discussed in section 1.5.2 there are two main sample characteristics that are needed for polariton condensation. First, the number of DBR pairs should be large enough in order to limit the cavity losses. Second, the polariton density to trigger bosonic stimulation should be reachable before the onset of the excitonic Mott transition within the QWs. The main idea to achieve this second criterion is to increase the number of QWs inside the microcavity. In order to maximize the light-matter coupling, QWs must be placed where the electric field is maximal inside the cavity. However, by placing shallow InGaAs QWs close to one another, there is a possibility for the electron and hole energy levels of individual wells to hybridize [71, 82, 83], creating a series of excitonic transitions. The topic of this chapter is to investigate the effect of coupled QWs in the strong coupling regime where multimode coupling is expected as discussed in section 1.4.2. Most of the work presented in this chapter has been published in [27].

It is worth mentioning that InGaAs QWs have been frequently used to study exciton-polariton, either for single QW microcavity [21, 22, 84–86] or QW stacks with varying Indium content [87–93]. In the latter, the multimode polaritons were not observed but, in almost every case, an additional emission peak between the lower and upper polariton branch was present in the spectra. This transition was assigned to an uncoupled exciton transition [88, 92] as a consequence of the quality of the samples with an inhomogeneously broadened transition.

3.1 Samples and experimental setup

Two samples were grown by MBE to study the effect of interwell coupling in microcavities. The first one consists of a single stack of three 12 nm $\text{In}_{0.03}\text{Ga}_{0.97}\text{As}$ QWs with a barrier of 10 nm (sample D1-12-10-13C). The low Indium content is purposely chosen to create

a low tunnelling barrier between the QWs in order to obtain electron and hole wave functions that extend over the whole QW stack. The second sample is a microcavity consisting of 20(23) top(bottom) AlAs/GaAs distributed Bragg reflector (DBR) pairs with a 2λ spacer (sample D1-12-12-14C). Three stacks of three QWs (identical to the first sample) are placed at the antinodes of the electromagnetic field inside the cavity. As mentioned in the previous chapter, the microcavity is grown with a wedge along the radius of the wafer allowing to vary the exciton-cavity detuning when probing different sample positions. The quality factor of the cavity is around $Q \cong 27000$, measured by scanning a narrow tunable laser (see section 5.2.1) across the cavity resonance (FWHM = $56 \mu\text{eV}$) at negative cavity detuning (see figure 3.1). For this sample, we cannot properly define the vacuum Rabi splitting as for the case of a single exciton resonance since the coupling occurs with up to seven excitonic transitions (see equation 3.1 and figure 3.6).

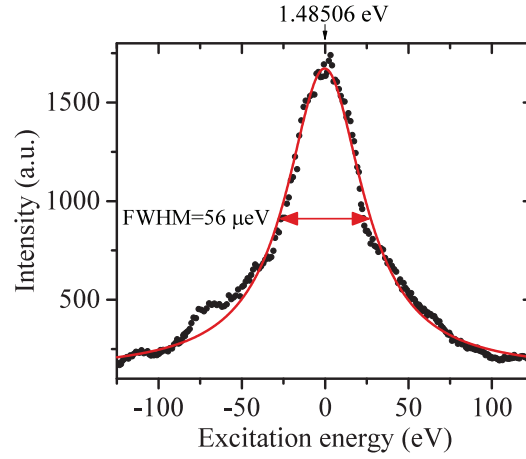


Figure 3.1 – Transmitted intensity measured as a function of resonant laser energy for sample D1-12-12-14C. The red line is a lorentzian fit. The energy axis is scaled relative to the lower polariton energy shown on top of the figure.

Photoluminescence (PL) studies were carried out using a standard confocal configuration exciting with a HeNe laser at low excitation power ($P = 100 \mu\text{W}$) and a spot size of $\sim 25 \mu\text{m}$, as detailed in section 2.2.1. A diaphragm inside the confocal microscope objective allows selecting only the emission from $k = 0$. The samples were cooled to 10 K using a closed circuit He cryostat. Photoluminescence excitation (PLE) was performed in transmission geometry, exciting with a cw Ti:sapphire laser ($P = 10 \mu\text{W}$) and a spot size of $\sim 25 \mu\text{m}$ (see figure 3.2). The main usage for this setup is to perform k -space filtering in resonant excitation. On the excitation path, the use of a retro reflector and a microscope objective (MO₁) with an aperture of 2 inch allow to excite the sample with a large angle. On the detection path, the light is collected by a microscope objective MO₂ with an NA=0.5, combined with two lenses of focal length $f = 25 \text{ cm}$ to image the Fourier plane of the objective MO₂ onto the slits of the spectrometer. Since the excitation laser has a large k -vector, it can be filtered out since its focusing point is not

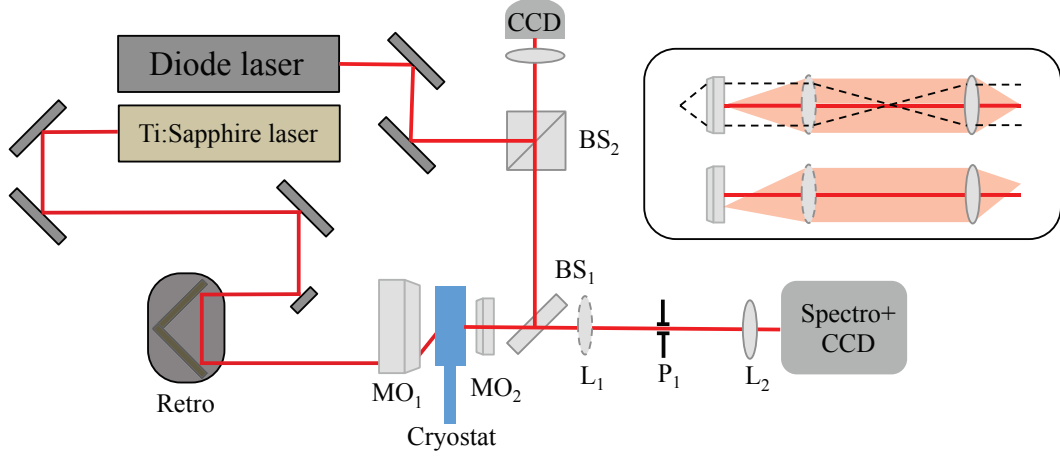


Figure 3.2 – Setup used for PLE in transmission, and high density experiments. MO_i are microscope objectives, BS_i are beam splitters, L_i are lenses and P_1 is a pinhole. The box shows the principle of k -space filtering for resonant excitation in transmission. The dashed line represents the real space whereas the red area is the k -space. For the Mott transition experiment (see section 4.3.4), the lens L_2 is replaced by a set of two lenses in order to image the real space onto the slits of the spectrometer. The top CCD is used to image the surface of the sample.

on the slits. The box in figure 3.2 presents a scheme of the optical path for the real and k -space that shows the principle of this filtering. For these measurements, the sample was cooled to liquid helium temperature (~ 4 K) using a cold finger cryostat. The use of a 75 cm spectrometer equipped with a 1800 grooves per mm grating and a CCD with $13.5 \mu\text{m}$ pixels gave a resolution of $\sim 50 \mu\text{eV}$.

3.2 Photoluminescence of quantum well stacks

Figure 3.3 (a) shows the PL spectrum of the bare stack of QWs as well as its PLE when detecting on the energy of the lowest exciton line (1.4894 eV). One clearly sees a sharp emission peak and additional structures at higher energy. The free exciton line from the GaAs is largely suppressed in PL, suggesting an efficient carrier capture to the QWs. The inset shows the PL when exciting below the GaAs band gap, at an energy of 1.5 eV, indicating that the dominant peak measured in PL is composed of two transitions separated by 0.39 ± 0.05 meV. This structure was further confirmed by fitting the spectrum using a lorentzian profile (see figure 3.3 (b) and (c)). A total of six excitonic transitions can be identified from the PL, with linewidths ranging from 0.4-0.6 meV for the low energy doublet and 1-2.6 meV for the others, demonstrating the high quality of the sample. When comparing the PL and PLE, we confirm that for each PL transition, there is a resonance in the PLE signal, indicating these are sharp excitonic transitions. Although the resonance in PLE at a relative energy of 5.7 meV is not clearly seen in PL,

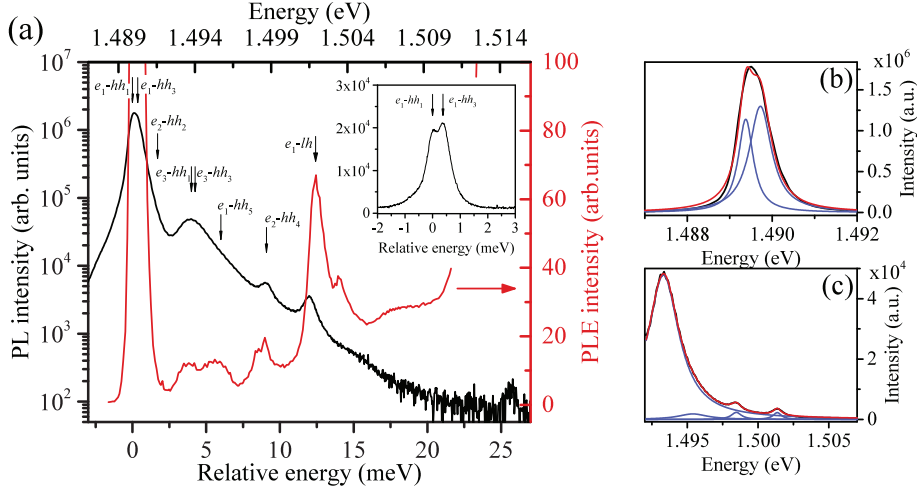


Figure 3.3 – (a) PL spectrum of a stack of three 12 nm $\text{In}_{0.03}\text{Ga}_{0.97}\text{As}$ QWs with 10 nm spacer (sample D1-12-10-13C) and the corresponding PLE when detecting at the energy of the lowest exciton transition. The inset shows the PL when the excitation laser is at an energy of 1.5 eV. (b) Close up of the PL around the $e_1\text{-}hh_1$ and $e_1\text{-}hh_3$. The blue curves show lorentzian fits the red curve their sum. (c) Same as in (b) but for the peaks around 1.5 eV.

it is still needed to obtain a proper lorentzian fit of the entire spectrum.

3.2.1 Simulation of QW stacks

In order to determine the origin of the measured excitonic transitions, we calculate the electron-hole confined states of the QW structure using Nextnano [74], as in the previous chapter. The system of three QWs is solved using the effective mass approximation to obtain the wave functions and energy of electron and hole states confined to the QW stack. As demonstrated in the previous chapter, strain due to the small lattice mismatch between GaAs and InGaAs has to be included to properly simulate the structure. As a result, heavy-holes are confined while the light-holes are not, as it is known from earlier studies with InGaAs QWs [69, 71].

In figure 3.4, we present the resulting envelope wave functions (not to scale) of confined electron and hole states for a stack of three $\text{In}_{0.03}\text{Ga}_{0.97}\text{As}$. Three electron states are confined in the QW stack whereas the calculation is limited to five states for the heavy-holes (additional hole states can be calculated, but giving either an exciton transition too high in energy or with a negligible oscillator strength). We evaluate the transition probability amplitude between the electron and hole states using these wave functions through the dipole matrix element [32] (see section 1.2): $\langle i|\varepsilon p|f\rangle \propto \langle F_c|\varepsilon p|F_v\rangle \int dz \chi_e^*(z) \chi_{hh}(z)$, where $\chi_e(z)$, $\chi_{hh}(z)$ are the electron and hole envelope wave functions along the confinement direction and $|F_{c,v}\rangle = f_{c,v}(r)|u_{c,v}\rangle$, is the product of the in-plane wave function and of

3.2. Photoluminescence of quantum well stacks

the Bloch wave function for the conduction and valence bands. If one assumes identical dipole moments and in-plane wave functions for all transitions, the relative transition probability is simply evaluated through the overlap integral squared between χ_e and χ_{hh} . When comparing the wave functions from figure 3.4, we notice that the integral is non-zero only for electron and hole states of the same parity, which sets a strict selection rule for the allowed transitions. The allowed transitions are shown by the arrows in figure 3.4. The energy of the excitonic transitions are obtained by taking the energy difference between the electron and hole state, without considering possible corrections due to Coulomb interaction (changes in the exciton binding energy).

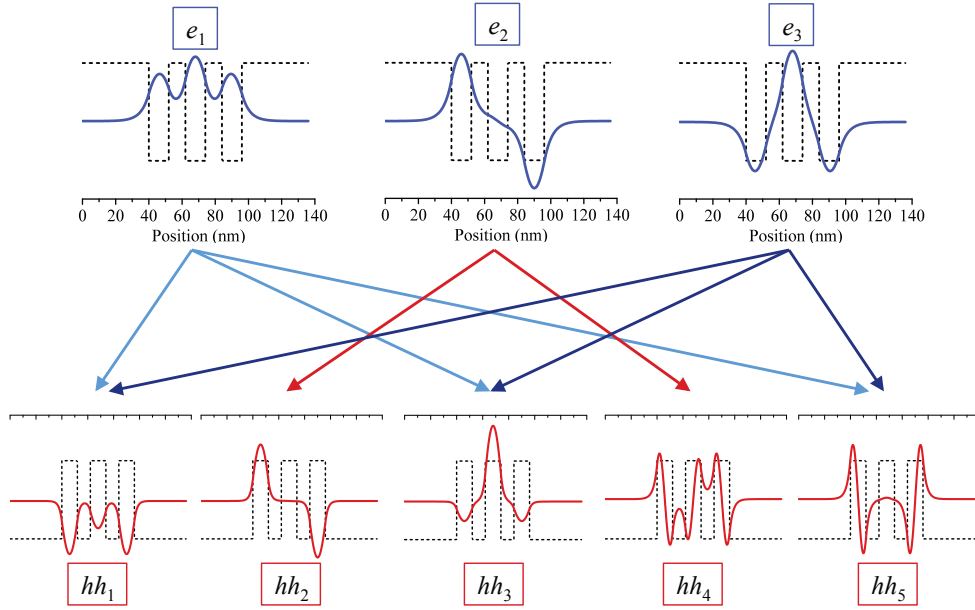


Figure 3.4 – Calculated wave functions for bound electron (e_i) and heavy-hole (hh_i) states. The black dashed lines show schematically the position of the potential barriers. The integer (i) indicates an increase (decrease) in energy for electrons (holes) and corresponds to $(i - 1)$ nodes of the eigenfunction. The colored arrows represent the allowed $e_i - hh_j$ transitions.

Results from the calculation are shown in figure 3.5, where we plot the calculated and measured transition energies relative to their respective lowest transition, labeled E_{e1-hh1} . The calculation accurately reproduces the energy separation of the measured excitonic transitions with a quadratic error of $\Delta E_{cQW} = 1.62$ meV. This confirms that all measured transitions are associated to excitons arising from interwell coupling. Therefore, we can use the calculation to label each of the measured transitions using the electron and hole index as in table 3.1. Two transitions, namely e_2-hh_2 and e_3-hh_1 , are not resolved in the PL spectrum but cause a broadening of the transitions at $\Delta E_{e1-hh3} = 0.35$ meV and $\Delta E_{e3-hh3} = 3.9$ meV respectively. From the calculation, the transition situated at 11 meV from the ground state can be assigned to the e_3-hh_5 transition, to a transition between the first electron and the unconfined light-hole bound by Coulomb interaction or to a

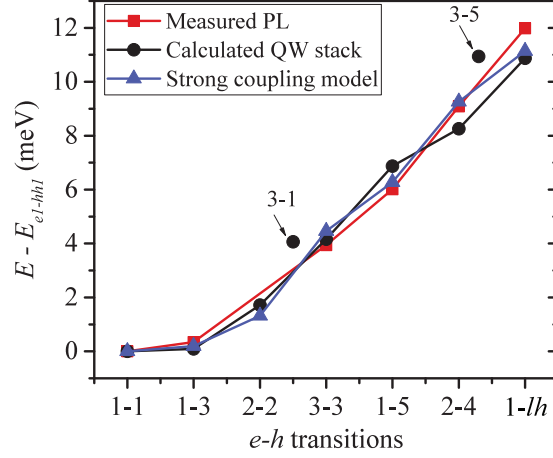


Figure 3.5 – Energy of electron-hole transitions relative the first transition E_{e1-hh1} for the bare QW sample (red), calculated for a single QW stack (black) and the relative values used for the strong coupling model. The relative value for the e_3-hh_1 and e_3-hh_5 are shown for comparison.

light-hole confined inside the barrier in between wells. The comparison with the PLE clearly shows a stronger resonance compared to the other transitions, indicating that this transition corresponds to the light-hole one. The PL from single QW that we presented in the previous chapter also supports this identification [78].

3.3 Multimode polaritons in the linear regime

3.3.1 Photoluminescence

In the following, we study the microcavity sample to evidence the effect of the additional exciton states on the coupling to the cavity field. The PL intensity is shown as a function of the position on the sample in figure 3.6(a) and the spectrum for specific positions in figure 3.6(b) as indicated by dashed lines in (a). As the cavity mode gets closer to the exciton resonances from the low energy side, the exciton states are blue shifted in energy, the maximum shift being fixed by the energy difference between the two neighbouring states. Such a behavior is the main characteristic of strongly coupled states (as explained in section 1.4). Moreover, when comparing the spectra in figure 3.6(b), we clearly see that the two transitions initially at around 1.489 eV are displaced to higher energy as they get in resonance with the cavity. Although this energy shift is small (450-550 μeV), it can only be explained by an interaction with the cavity for the following reasons. As evidenced in figure 3.6(b), the blue shift of the low energy transition of this doublet stops once its energy reaches the initial value of the second doublet transition. Alternatively, the small energy shift could be assigned to a monolayer variation of the QWs thickness [94]; the measured shift would, however, be more than twice the calculated value if each QW in

3.3. Multimode polaritons in the linear regime

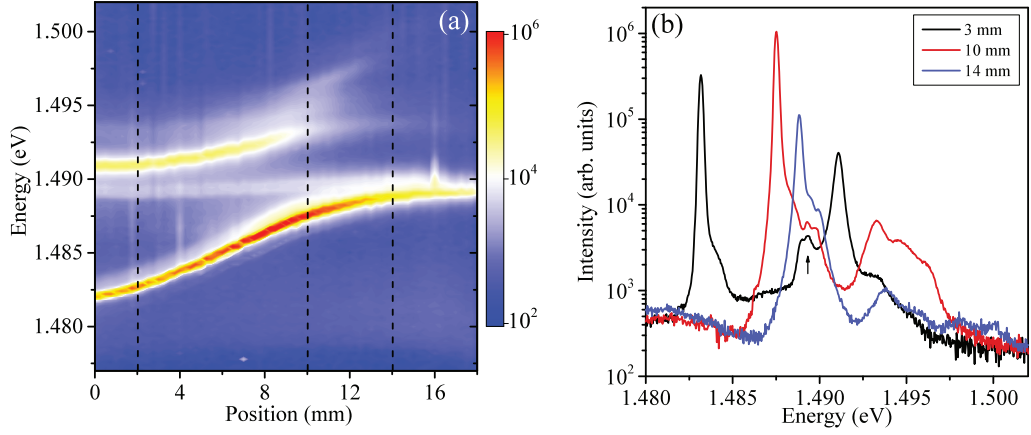


Figure 3.6 – (a) PL intensity map in log scale as a function of the position on the microcavity sample. (b) PL spectra for three positions on the sample as indicated by the dashed lines in (a). The arrow indicates the doublet of peaks at 1.489 eV.

the stack would be thinned by one monolayer ($\sim 250 \mu\text{eV}$, simulated by adding a single monolayer to either well in the stack), which rules out this possibility. Furthermore, a monolayer variation of one or more QW within the stack would also imply a breaking of the symmetry of the stack, hence additional excitonic transitions would be allowed while none are observed within our resolution ($\sim 150 \mu\text{eV}$). From these observations, we conclude that all measured exciton states are strongly coupled with a single cavity mode. Finally, the high energy shoulder present on the lower polariton branch in the spectra is due to our finite resolution in k , hence, emission at low k from the polariton dispersion. The linewidth of the lower polariton mode at negative cavity detuning is $\sim 150 \mu\text{eV}$ when measured on a higher resolution setup (the magnetic field setup described in section 4.2).

3.3.2 Fit using the multimode coupled oscillator model

We use the following multimode light-matter interaction Hamiltonian to model our data, with $\hbar = 1$ (see section 1.4):

$$H = \omega_c c^\dagger c + \sum_{i,j} E_{ij} x_{ij}^\dagger x_{ij} + \sum_{i,j} \frac{\Omega_{ij}}{2} (x_{ij}^\dagger c + c^\dagger x_{ij}), \quad (3.1)$$

where the i, j indices correspond to the electron and hole state numbers, $\hbar\omega_c$ is the cavity mode energy, E_{ij} is the exciton energy and $x^\dagger(x)$, $c^\dagger(c)$ are creation (annihilation) operators for the exciton and cavity photon. The allowed excitonic transitions used for the sum are shown in table 3.1. This Hamiltonian has been successfully used to simulate coupling from inhomogeneously broadened excitonic transitions [23, 88] where the coupling strength is assumed to be constant for all excitonic sub-transitions. For the

case of coupled QWs, the light-matter coupling strength is evaluated for each transition through the overlap between the electron and hole wave function and the electromagnetic field inside the cavity [33,46]:

$$\Omega_{ij} = \frac{\Omega_0}{I_M} \int \chi_{h_j}^*(z) E(z) \chi_{e_i}(z) dz, \quad (3.2)$$

where χ_{e_i} , χ_{h_j} are the i^{th} electron and j^{th} hole wave function as calculated above and I_M is the integral between the states i - j having the highest overlap. Assuming the same dipole strength for all transitions and normalizing the integrals to I_M , the coupling strengths between the cavity and all transitions can be fitted using a single parameter, Ω_0 , which would be the vacuum Rabi splitting for the coupling of a cavity with a single exciton state. The Hamiltonian is diagonalized in order to obtain the polariton energy as a function of position on the sample (cavity detuning). For the calculation, we use a single QW stack at the antinode of a λ -cavity (see figure 3.9), the number of stacks is considered simply by increasing the coupling strength by a factor $\sqrt{3}$ [88].

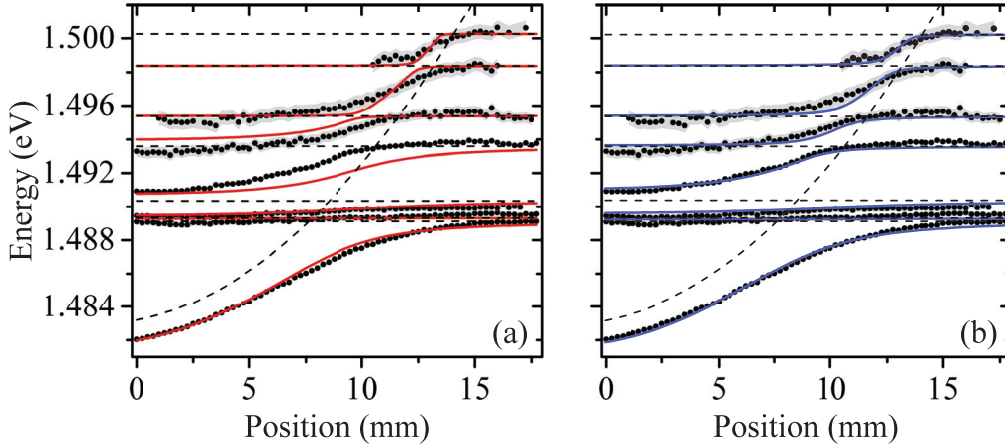


Figure 3.7 – Polariton energy as a function of sample position. The dots shows the extracted peak energy and the gray region shows the uncertainty for each of the states. The full lines shows the best fit using equation (3.1) and (3.2) in (a) (red) or by manually adjusting the overlap parameter in (b) (blue). The dashed lines represent the energy of the cavity mode (parabola) and exciton transitions (straight). In both cases, the coupling parameter is $\Omega_0=4$ meV and the values of the overlap integrals are given in table 3.1.

Results from such calculations are shown in figure 3.7(a) where the dots represent the energy position of each polariton line measured as seen in figure 3.6 and the gray region surrounding them corresponds to the error bar. The full red lines show the best fit obtained after diagonalizing Hamiltonian (3.1) for a coupling parameter of $\Omega_0 = 4.0 \pm 0.1$ meV and the value of the overlap integral are given in table 3.1. Because the light-hole wave function in the continuum is not known, we use the value of overlap of the state e_3 - h_5

3.3. Multimode polaritons in the linear regime

due to its similar relative energy. The quadratic error from fitting all polariton transitions in this case is $\Delta E_1 = 8.17 \pm 0.05$ meV, which is quite low considering the number of data points. The straight dashed lines are the uncoupled excitonic transitions. As the binding energy is not precisely known and as some transitions are measured in the microcavity sample but not in the bare QW, we allow a slight energy variation for each transitions in order to improve the fit. The relative values used are shown in figure 3.5 confirming their validity with respect to the measured bare QW excitonic transitions. The e_3-hh_1 transition is not included in the fitting procedure because of its relatively small overlap compared to the other transitions. The cavity mode shown by the curved dashed line was determined by PL using a pump laser diode ($\lambda = 660$ nm, see section 2.2.1) at high power to reach the VCSEL lasing threshold in order to precisely extract the cavity mode, as shown in figure 3.8. The emission energy was measured at different positions on the sample just after the threshold occurred to limit any possible multimode behavior from the cavity (see section 4.3). Since the cavity shows a perfect parabolic variation, only the fit is shown in figure 3.7.

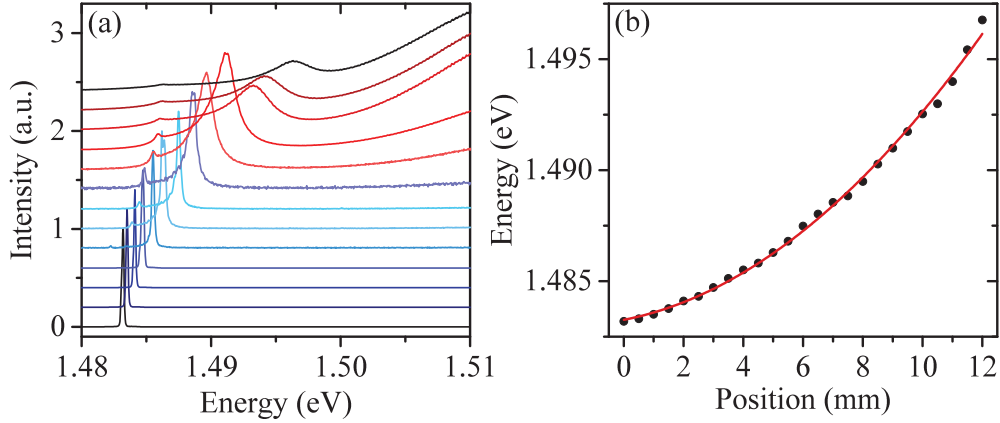


Figure 3.8 – (a) PL at the onset of the VCSEL threshold for different positions on the sample. The curves are normalized since the intensity and excitation power varies for each curve, and shifted for visualization purposes. (b) Extracted cavity mode energy from (a) as a function of sample position. The red line is a quadratic fit that was used in the simulation shown in figure 3.7.

3.3.3 Discussion

The difference of the relative coupling strength of each transition (table 3.1) can be explained qualitatively by comparing the wave functions displayed in figure 3.4. From the figure, it is clear that the e_i-hh_j transitions have a smaller coupling compared to the e_i-hh_i ones because the wave functions of the initial and final states do not share the same number of nodes. We also notice that the e_3-hh_3 has a slightly higher coupling strength compared with the other two symmetrical transitions. This difference corresponds to the fact that, compared to the other two hole wave functions, the hh_3 has its highest value at

Chapter 3. Multimode polaritons originating from coupled quantum wells

the center of the stack where the electromagnetic field is the strongest. The e_2-hh_2 has a lesser coupling strength because there is a node of the wave function at the antinode of the electromagnetic field.

Since our microcavity includes three stacks of QWs, the highest coupling strength for a single exciton state is [88]: $\Omega_0/\sqrt{3} = 2.31$ meV. This value is smaller than the typical 3.5 meV measured for single InGaAs QW in a λ -cavity [22, 84, 86]. This decrease of coupling strength is caused by three main factors: a decrease of the exciton binding energy which reduces the oscillator strength, a decrease of the overlap between the carrier wave function and the electromagnetic field and an increase of the effective cavity length.

It is expected that the exciton binding energy in the QW stack should be less than its value in a single QW (~ 6 -7 meV for low Indium QW [80, 95], see also figure 2.4) because its delocalization over the QW stack should decrease the strength of the Coulomb interaction. As shown in figure 3.4, the wave function extends over the full QW stack width corresponding to a thickness of 56 nm. Comparing with the usually assumed Bohr radius of about 10-12 nm for such III-V single QWs [96], one concludes that the 2D approximation for Coulomb interaction is no longer justified as the wave function extension along the confinement direction is much larger than the typical in-plane extension. As a result, the exciton Bohr radius should increase, leading to a reduction of the oscillator strength and therefore a decrease of the coupling strength. Same conclusions were also found for excitons in superlattices [97].

The relative impact of the three factors affecting the coupling strength of the coupled QWs can be estimated by noting that $\Omega_0 \propto L_{eff}^{-\frac{1}{2}} F(0) \mu_{cv} I_z$, where $L_{eff} = L_{cav} + L_{DBR}$ is the sum of the cavity spacer length and the penetration depth of the electromagnetic field inside the DBR, $F(0)$ is the exciton relative motion envelope wave function evaluated at its center, μ_{cv} the dipole matrix element and I_z the overlap integral as stated in equation (3.2) [31, 36] (see section 1.4). We define the ratio of the coupling strengths $\frac{\Omega_{cQW}}{\Omega_{1QW}} = L^{-1/2} \cdot I \cdot F_{os}^{1/2} \cdot I_{fz}^{-1/2}$, where $L^{-1/2}$ represents the ratio of the square root of the cavity effective lengths, I is the ratio of the overlap integrals, $F_{os}^{1/2}$ is the ratio of the square root of the oscillator strengths of the bare QW exciton and $I_{fz}^{-1/2}$ is the square root of the inverse ratio of integrals of wave function overlap in the confinement direction without the cavity. This last term compensates the contribution of the overlap integral in $F_{os}^{1/2}$, since it is taken into account in I . Calculation of the overlap integrals in both cases yields a ratio of $I \cong 0.90$ (see figure 3.9). To estimate the influence of the effective cavity length, we note that, the penetration depth being of the order of $2 \mu\text{m}$, an increase of the cavity spacer from λ to 2λ will decrease the coupling by a ratio of $L^{-1/2} \cong 0.95$. Combining these ratios and assuming $I_{fz}^{-1/2} = 1$ gives $F_{os}^{1/2} \cong 0.77$, meaning that the oscillator strength decreases by about 40% when passing from a single QW to a stack of 3 QW and, consequently, decreases the coupling strength by 23%.

Finally, we can achieve an even better fit of the measured polariton modes by adjusting

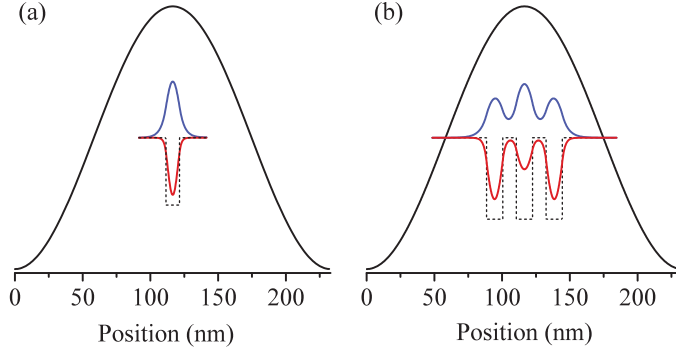


Figure 3.9 – Scheme of the overlap between the electric field of a λ -cavity and the electron (blue) and hole (red) wave functions of the e_1 - hh_1 transition for (a) single QW and (b) QW stack.

the overlap integral manually. Doing so, all coupling strengths are slightly modified to get the best fit while keeping the parameter Ω_0 unchanged. The result of this calculation is shown in figure 3.7(b) and the values of the integrals are given in table 3.1. The quadratic error is reasonably decreased to $\Delta E_2 = 4.66 \pm 0.02$ meV, an improvement of 43 %. One sees a much better agreement of the fourth polariton line (the second brightest polariton mode in figure 3.6), and an excellent agreement within the experimental error bar. The highest coupling strength is now arising from the transition e_2 - hh_2 instead of e_3 - hh_3 as was found in the case of the first fitting procedure. The manual adjustment for the light-hole transition is justified since its wave function is not known. For the other transitions, the deviation between the calculated and adjusted coupling strengths indicates that the correction from the Coulomb interaction is not the same for each of the transitions. Neglecting this interaction in our modeling is equivalent to assuming that all exciton transitions have the same binding energy and thus the same in-plane matrix element. Comparison between the measurements in bare QW and our calculations (see figure 3.5) indicates indeed that this assumption is not justified. A calculation of the binding energy for each transition as well as possible state mixing (since some states share the same electron or hole) would be needed to properly explain the adjusted coupling strengths. Such calculation is beyond the scope of this PhD. Furthermore, it is likely that high index transitions are resonant with the continuum of the first transition. This interaction is expected to decrease further the coupling to the electromagnetic field and also broadens the transition, which might explain the linewidth and large coupling strength deviation obtained for the e_3 - hh_3 exciton. Moreover, we expect the e_2 - hh_2 transition to be less affected by coupling effect than the e_1 - hh_1 , the node at the center of the wave function making it more likely to find the exciton confined in the outer wells instead of being delocalized over the whole stack. This might also explain why the e_2 - hh_2 transition becomes more strongly coupled to the cavity mode in the manual fit.

Chapter 3. Multimode polaritons originating from coupled quantum wells

Table 3.1 – Calculated relative energy and light-matter coupling strength for electron-hole transition. The last column shows the values of the normalized integral used for the manual fit. The values in parentheses indicate the values before normalization.

e - h transitions	ΔE (meV)	Ω_{ij}/Ω_0	manual fit
e_1 - hh_1	0	0.96 (0.83)	0.95 (0.81)
e_1 - hh_3	0.09	0.23 (0.20)	0.62 (0.53)
e_2 - hh_2	1.72	0.88 (0.76)	1.00 (0.85)
e_3 - hh_1	4.07	0.02 (0.01)	0.02 (0.01)
e_3 - hh_3	4.16	1.00 (0.87)	0.39 (0.33)
e_1 - hh_5	6.87	0.13 (0.11)	0.39 (0.33)
e_2 - hh_4	8.26	0.16 (0.14)	0.31 (0.27)
e_1 - lh	10.87	0.07 (0.06)	0.18 (0.15)

3.4 Conclusions

In this chapter, we studied the effect of the electronic coupling between the stacked QWs on the strong coupling in a planar microcavity. The QW electronic coupling was evidenced when comparing PL and PLE spectra of a bare QW stack with effective mass calculation. When the QW stack was placed inside the microcavity, the existence of a coupling between QWs causes two main effects, first an increase of the number of polariton modes and a decrease of the coupling strength compared to that of a single QW. The latter is interpreted as a decrease of the exciton binding energy and of the oscillator strength due to the delocalization of the exciton wave function over the QW stack. Using a coupled oscillator model accounting for the calculated electron-hole transitions, we simulated all measured polariton modes using a single coupling parameter. The deviation from this simple model was understood as an interplay between the Coulomb interaction and the extension of e - hh wave function over the QW stack.

4 The quest for polariton condensation using InGaAs-based microcavity

In the last two chapters, we gave an overview of the sample characterization and optimization and discussed the linear properties of microcavities with low In content. All this work was done with one goal in mind: to achieve polariton condensation using microcavity with InGaAs/GaAs QWs. More precisely, we seek to understand what are the dominant parameters that induce or prevent this phase transition. In this chapter, we present our main results obtained in our search for polariton condensation. Namely, we studied the effect of Indium content, cavity design, type and number of QW stacks, and magnetic field. Unfortunately, our investigation did not allow us to achieve non-resonant condensation with these samples. Therefore, we conclude this chapter with a discussion on the major factors that limit condensation in our system.

4.1 Claims of polariton condensation using InGaAs QWs

In recent years, there has been a number of claims for achieving non-resonant condensation using InGaAs QWs. However, none of them is actually showing a true condensed phase. Most of these studies try to observe two nonlinear thresholds of the emitted intensity as a function of the excitation power. The main reason for this idea comes from a seminal paper by D. Bajoni *et al.* [9] which clearly demonstrated that, when measuring two intensity thresholds, the first one corresponded to the condensed phase, and the second to the VSCEL (weak coupling) regime. The main result of this work showed that strong coupling was maintained after the first threshold, and that the strong to weak coupling crossover occurred at higher excitation power. The emission energy at the second threshold was on the bare cavity mode, clearly demonstrating that the system was in the weak coupling regime. This point is crucial: whatever the nonlinear processes, a strongly coupled system does not exist at the energy of the uncoupled modes, hence polariton condensation cannot occur at these energy positions. This is the fundamental principle behind the anticrossing of strongly coupled modes, and can be understood by comparing the strength of the different interaction terms of the system. If exciton-exciton

Chapter 4. The quest for polariton condensation using InGaAs-based microcavity

interaction is strong enough to shift the lower polariton mode up to the cavity mode, it means the energy associated to this process is comparable to the light-matter coupling constant. Hence, the polariton basis no longer accurately represents the exciton-photon system.

The first claims for polariton condensation using InGaAs QWs came from electrically pumped devices with either a single stack of four 10 nm $\text{In}_{0.15}\text{Ga}_{0.85}\text{As}$ with a spacer of 6 nm [98], or four pairs of $\text{In}_{0.1}\text{Ga}_{0.9}\text{As}$ QWs (10 nm, unknown spacer) [99, 100]. In both cases, the claim of a condensed phase came from the observation of two thresholds in intensity as a function of excitation power. Both had to apply a magnetic field in order to see the second threshold (magnetic field is supposed to enhanced phonon-polariton relaxation for a fixed detuning [99]). However, there are a few points which indicate that the system never reaches the condensed phase. In the first study, the use of only four QWs makes it highly unlikely that the critical density was reached before the saturation density (see our results below). Furthermore, the saturation is clearly seen at zero field, and the high field experiments show exactly the same curve. The only difference is a sudden jump in intensity and energy before following exactly the same trend as the zero field experiments. As for the second work [99, 100], the data clearly show that, just after the first threshold, the emission energy is at the cavity mode and strong coupling is lost. Hence, whatever the nature of the second threshold, the first one corresponds to the loss of strong coupling, which cannot be assigned to a polariton condensate.

A second set of experiments worked on reducing the disorder in DBR due to strain propagation induced by the InGaAs QW. A first work [101] used three pairs of 6 nm $\text{In}_{0.08}\text{Ga}_{0.92}\text{As}$ (unknown spacer thickness) as well as two QWs at the first node of the field closest to each DBR mirrors (hence six QW in strong coupling). Strain relaxation was achieved by placing layers of AlP in the AlAs layers of the DBR. A single threshold was measured using a 35 μm excitation spot using a fs-laser while doing time integrated measurements. The threshold was assigned to the condensed phased, however, careful analysis of the energy after the threshold indicates that the polariton mode has reached the cavity, hence that the system is in weak coupling. In order to use the two threshold arguments, they performed the experiment using a small excitation spot. In this case, a first threshold was measured with emission at high k while a second was seen mainly as a drop of linewidth at higher excitation power (less visible in intensity, compared to the uncertainty in the experiment). The first threshold was assigned to a condensate at high k due to repulsion from the dense reservoir coming from the small excitation spot as it was observed [102, 103]. However, a careful look at the energy of the observed transitions allows us to see that the emission at large k is in fact on the cavity mode dispersion, and not on the polariton dispersion.

Strain relaxation was also achieved by replacing AlAs with $\text{Al}_{0.85}\text{Ga}_{0.15}\text{As}$ in microcavity with up to six $\text{In}_{0.04}\text{Ga}_{0.96}\text{As}$ QWs [104]. In this study, non-linearity was only seen in the OPO configuration. In contrast, ghost branches were supposedly observed after

measuring a single threshold using a $\lambda/2$ -cavity and highly strained $\text{In}_{0.3}\text{Ga}_{0.7}\text{As}$ QW (unknown number, most likely one) [105]. Clearly, the observed behavior is a consequence of inhomogeneous emission due to a high disorder and not of Bogoliubov excitations of a condensate. The cavity design is also incorrect for $\text{InGaAs}/\text{GaAs}$ QWs since there is a node of the electric field at the center of a $\lambda/2$ -cavity.

Finally, a single threshold was observed using a optical fiber cavity with a half cavity grown with three stacks of 11 nm $\text{In}_{0.08}\text{Ga}_{0.92}\text{As}$ QWs (spacer thickness unknown) [106]. In this case, it is difficult to assess whether the system is still in strong coupling since no detuning map is given (and interwell coupling might be present). The cavity mode energy can be estimated from the given coupling strength and detuning only. In any case, the system is essentially 0D since the waist of the field out of the fiber is $2.6\text{ }\mu\text{m}$.

To conclude this overview of the literature, as of now, there is no convincing evidence that 2D polariton condensation is indeed possible using InGaAs -based microcavities.

4.2 Experimental setup

The experimental setup that was mostly used for this study is presented in figure 4.1, and is based on a standard confocal setup for PL. The He-flow cryostat used has a built-in supraconducting coil magnet to perform magneto-PL measurements, and has to be placed at $\sim 40\text{ cm}$ from the optics table to avoid any effect from the metal surface. All the excitation and detection optics are placed on a small breadboard at the same height as the cryostat to avoid any mirror reflection of the signal before the polarization is analyzed. A liquid crystal retarder and a Glan polarizer are used to analyze the polarization. Two periscopes are used to bring the excitation up to the cryostat, and down to the spectrometer. Since the cryostat cannot be moved due to its weight, exciting different position on the sample is done by moving the microscope objective (MO). The MO has to be inserted in a small area which limits the travel range to $\sim 5\text{ mm}$. It also implies that the excitation and detection path must be realigned each time we move on the sample. The cryostat design imposes a large working distance (13 mm), meaning that, in order to have a MO with an $\text{NA} = 0.5$ to image the k -space, the resulting spot size is $\sim 1\text{ }\mu\text{m}$. For a larger spot size, the MO can be replaced by a lens of $f = 5\text{ cm}$ which greatly limits the range available in k -space (the effect of the spot size on our experiment will be discussed in section 4.3.3).

The k -space imaging is performed using a series of 4 lenses with matching adjacent focal plane. That way, it is possible to propagate the k -space over a large distance (2.1 m). Lenses $L_{1,2}$ have a focal length of $f_{1,2} = 40\text{ cm}$, while the other two have focal lengths of $f_3 = 5\text{ cm}$, and $f_4 = 20\text{ cm}$. The smaller focal length of L_3 is chosen to expand the incoming beam and gain in resolution for k -space imaging. The real space imaging is achieved simply by removing L_3 . The focusing lens L_4 is placed on a motorized translation

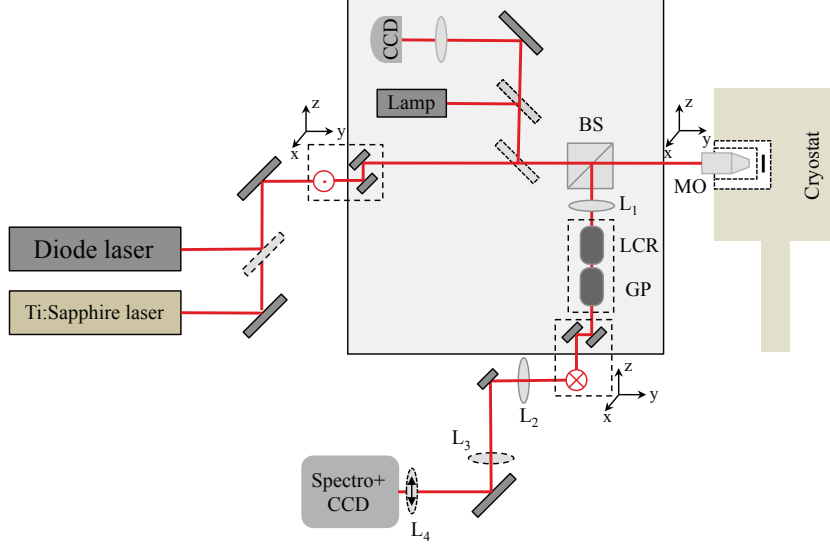


Figure 4.1 – Scheme of the experimental setup for high power, and magnetic field experiments. L_i are lenses, and MO is a microscope objective. The lenses and mirrors with dashed lines are placed on flip mounts, while L_4 is placed on a translation stage. LCR is a liquid crystal retarder, and GP is a Glan polarizer. All the optics inside the rectangle are placed on a small breadboard at 40 cm above the optics table, this correspond to the optical axis of the cryostat. The two dashed boxes on the side of the breadboard are periscopes to bring the excitation to the cryostat and to bring the signal to the spectrometer. The x - y - z axis indicates three axis positioning.

stage to perform energy resolved tomography in both real and k -space. The resolution of the setup is $\sim 40 \mu\text{eV}$ when working with a 1800 grooves per mm grating in the 75 cm spectrometer. Finally, the excitation is performed either by a tunable cw Ti:sapphire laser (spectra physics 3900, pumped by a 5 W millennia laser), or a high-power diode laser (the same as described in section 2.2.1). The use of cw excitation was preferred over pulsed since it is better suited to study the steady state of the condensate. Although the excitation density can be much higher in pulsed excitation experiment, it is not the best tool to study the phase transition itself because the full dynamic of the system is integrated at each excitation pulse. Therefore, the use of a streak camera is necessary to avoid doing a time integration. Finally, the small CCD on the breadboard combined with a white light allow to image the surface of the sample.

4.3 Low Indium content microcavities

We begin our investigation of the nonlinear behavior of InGaAs-based microcavities with a sample similar to the one presented in the previous chapter, consisting of QW stacks with low Indium content and where multimode polariton is expected. Here, we are interested in the nonlinear behavior of the polariton ground state from a k -space point of view,

meaning that we look at the image on the CCD instead of binning the pixels. Hence, we lose a factor 100 in intensity due to the number of CCD pixels, and in most cases, the multimode structure is absent from the dispersion. As shown in the previous chapter, we must integrate the PL signal over more than two orders of magnitude to be able to see the multiple polariton modes. To observe these modes in k -space, we would need to acquire for longer times which is not the purpose here. For example, figure 4.2 (a) shows the PL intensity map in log scale as a function of position for a sample (D1-13-02-15C) of the same structure as sample D1-12-12-14C presented in the previous chapter (20/23 top/bottom DBR pairs, three stacks of three 12 nm $\text{In}_{0.03}\text{Ga}_{0.97}\text{As}$ with 10 nm spacer, see appendix B for a complete description of the samples used). The multimode coupling is clearly present in the detuning map of the PL (as for figure 3.6). However, this structure is barely seen in the PL map for the dispersion at low excitation power shown in figure 4.2 (b).

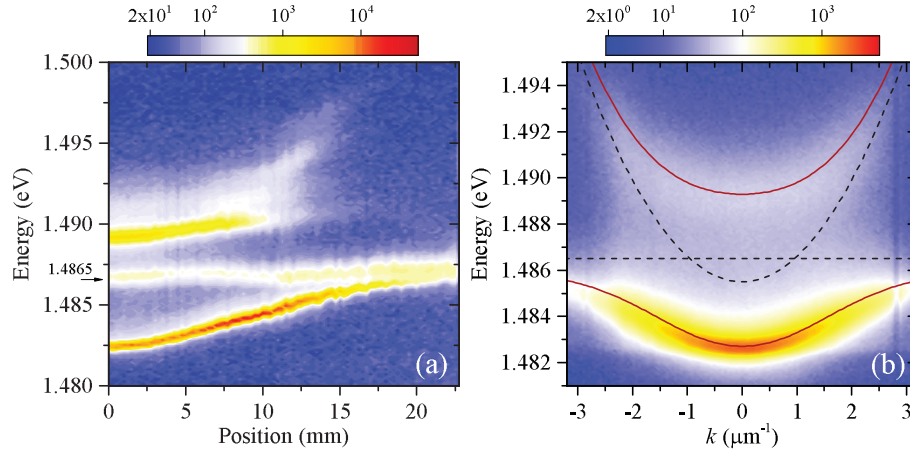


Figure 4.2 – (a) PL intensity map in log scale as a function of the position on the microcavity sample for sample D1-13-02-15C, measured at $k = 0$ using the characterization setup described in section 2.2.1. (b) PL map in log scale of the dispersion at the center of the wafer (position ~ 0 mm in (a)) at an excitation power of $P=400 \mu\text{W}$ (measured with the setup shown in figure 4.1). The red curve is a fit of an effective single mode strong coupling model whereas the dashed lines are the uncoupled exciton and cavity modes.

Since we are interested in knowing the position of the uncoupled modes to determine the nature of the non-linearity (BEC or VCSEL), we use an effective single mode coupling to fit the lower branch and second brightest one (labeled upper from now on). This procedure is justified since the lower branch is barely affected by the exciton excited states. As for the upper branch, the effect of the other polariton modes will occur at larger k where the signal is weak. Therefore, the result from the effective single mode coupling is reasonably accurate and allows to determine the position of the bare cavity dispersion. Result of the fit is presented in figure 4.2 (b) where the red and dashed black curves show the polariton and uncoupled modes respectively. The position of the exciton mode was fixed to the value of the second polariton branch indicated by the arrow in figure 4.2 (a) which is mainly exciton-like. The fit gave a value for the effective Rabi

Chapter 4. The quest for polariton condensation using InGaAs-based microcavity

splitting of $\Omega_0^* = 6.5$ meV, effective cavity detuning of $\delta^* = 0.15\Omega_0^* = -1$ meV, and an excitonic fraction of $|X|^2 = 0.42$.

4.3.1 Power measurements

For the threshold measurements, we tune the cw laser to a minimum of the reflectivity of the cavity ~ 750 nm. Figure 4.3 (a)-(d) shows the evolution of the dispersion for increasing power. First we notice an increasing signal at an energy between the strongly coupled branches in (a), compared to the dispersion shown in figure 4.3 (b). At a power of $P=6$ mW, three features are clearly seen. First, the dominant intensity is no longer on the lower polariton branch but close to the bare cavity mode at $k = 0$. Second, the emission at higher k -vector follows a parabolic dispersion instead of the polariton one. Third, we see a low energy tail that goes from the cavity mode down to the polariton dispersion. This is due to the Gaussian profile of our excitation laser meaning the excitation density decreases away from the center of the spot. Since we do not filter in real space, we collect the PL from a relatively large area around the center of the spot. Hence, the emission at lower energy originates from polaritons away from the excitation spot. This was later confirmed by repeating the experiment while filtering in real space (which has to be done by placing a pinhole horizontally inside the second periscope since it is the position where the real space is focused, see also section 4.4.2).

As we further increase the excitation power, the emission becomes dominant on the cavity mode. Finally, at maximum power, we see the appearance of a multimode emission limited by the cavity dispersion. This clearly demonstrates that the system is in the weak coupling regime. Conversely to what was measured in [107], we do not measure a red shift of the bare cavity mode above the weak coupling threshold (as for all measurements presented in this chapter). In figure 4.3 (e) we plot the integrated intensity at $k = 0$ as a function of excitation power while the energy and linewidth are shown in (f). Prior to reaching the threshold, we notice a strong energy blue shift of the polariton mode until it reaches the bare cavity mode energy. Above threshold, we can no longer track the energy shift properly because of the multimode lasing. The onset of laser coherence is also seen in the sudden decrease of linewidth of the dominant mode at the threshold. These results indicate that two of the main characteristics of the condensate phase transition are also characteristic of VCSEL lasing, namely the nonlinear intensity increase linked to a drop of linewidth. It is only by analyzing both intensity dispersion and the energy at the threshold that we can clearly differentiate between the two regimes.

The multimode behavior above lasing threshold is a consequence of optical disorder in the top DBR mirror. Indeed, moving the excitation spot on the sample above threshold changes the relative intensity of the modes. It is known that optical disorder does not prevent polariton condensation [7, 10]. Instead, disorder can lead to multimode condensation where localized condensates share the same wave function and phase as it

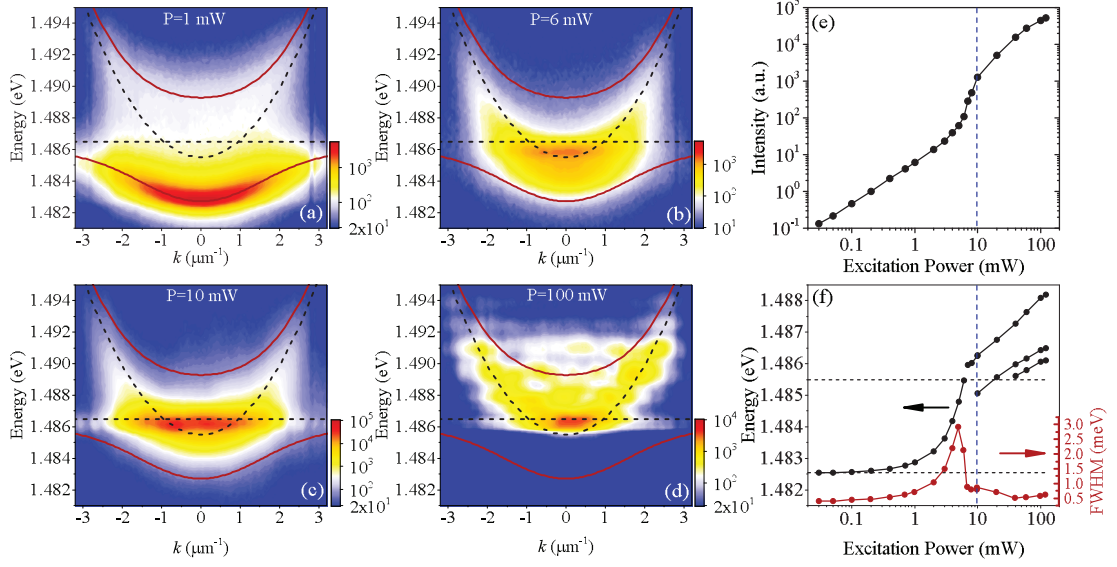


Figure 4.3 – (a)-(d) PL intensity map in log scale of the dispersion for increasing excitation power for sample D1-13-02-15C. The red curves are the effective strong coupling model fit presented in figure 4.2 (a) and the dashed lines are the uncoupled modes. The fit was performed on the low power data and is the same for each panel. (e) Integrated intensity at $k = 0$ as a function of excitation power. (f) Energy (black) and linewidth (red) at $k = 0$ as a function of excitation power. The horizontal dashed lines indicate the position of the lower polariton and the cavity mode extracted from the fit at low power. The blue dashed line is a guide to the eye to indicate the threshold.

was demonstrated in the CdTe samples [108]. It is also the basis for creating potential landscape for the condensate, which was used to study topological defects [11, 13]. Hence, the absence of bosonic stimulation is not a consequence of optical disorder. However, as we will discuss later, optical disorder can lead to an increase of leaky modes which might be detrimental.

4.3.2 Effect of magnetic field

Similarly to the works mentioned in section 4.1, we investigated whether applying a magnetic field would enhance polariton-phonon scattering and help to reach the condensation threshold. The effect of a magnetic field on the polariton modes is accurately described within a four mode coupling model (two spin states for the exciton, and the cavity) where the exciton energy depends on the magnetic field [53, 109, 110]. Its effect on the exciton is two fold, first the diamagnetic shift causes an energy blue shift (about 2 meV at $B = 5$ T) [111], and a Zeeman splitting between the degenerate spin up and down excitons. For InGaAs QW, the Zeeman splitting saturates with the field [112]. At $B = 5$ T we measured a value $\sim 400 \mu\text{eV}$ for 3% Indium QWs. Hence, the dominant effect is the diamagnetic shift. This effect not only induces a blue shift of the energy but

Chapter 4. The quest for polariton condensation using InGaAs-based microcavity

also tends to increase the localization of the electron and hole within the exciton. This causes a decrease of the Bohr radius, which increases the oscillator strength ($\sim 15\text{-}20\%$ increase), hence the Rabi splitting is also enhanced. To summarize, for a fixed position on the sample, as the magnetic field is increased, the detuning becomes more negative, and the Rabi splitting increases.

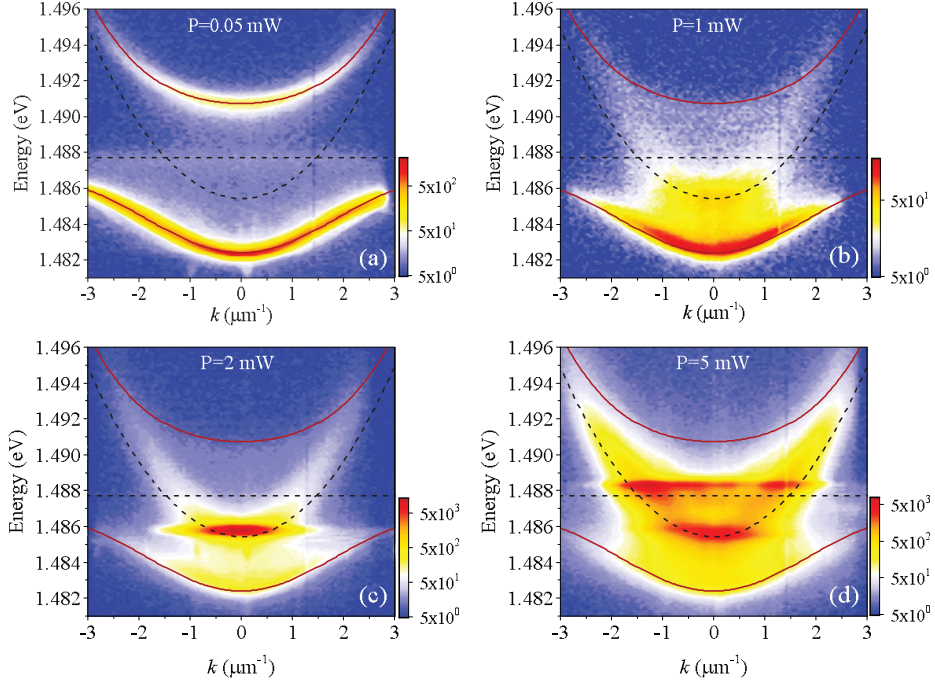


Figure 4.4 – (a)-(d) PL intensity map in log scale of the dispersion for increasing excitation power for sample D1-13-02-15C, under a magnetic field of $B = 5$ T, detected for σ_+ polarization. The red curves is the effective strong coupling model fit and the dashed lines are the uncoupled modes. The fit was performed on the low power data and is the same for each panel.

Figure 4.4 (a)-(d) shows the measured dispersions for the same position on sample D1-13-02-15C at a magnetic field of $B = 5$ T. From the low power dispersion (a), we can extract the effective single mode coupling parameters: $\Omega_0^* = 8$ meV, $\delta^* = -0.28\Omega_0^* = -2.3$ meV, and $|X|^2 = 0.36$, in accordance with our description of the magnetopolariton above. As the power is increased, we notice a behavior which is almost identical to the results at zero magnetic field presented in figure 4.3. The dominant intensity transfers from the lower polariton branch to the bare cavity mode, demonstrating once again that the transition corresponds to VCSEL lasing. The low energy tail is again due to the integration of the signal away from the center of the excitation spot.

In figure 4.5 we plot the integrated intensity at $k = 0$ as a function of excitation power for increasing magnetic fields from zero to 5 T. For each case, a single threshold is measured, and each time the emission energy is located on the bare cavity mode. The only noticeable

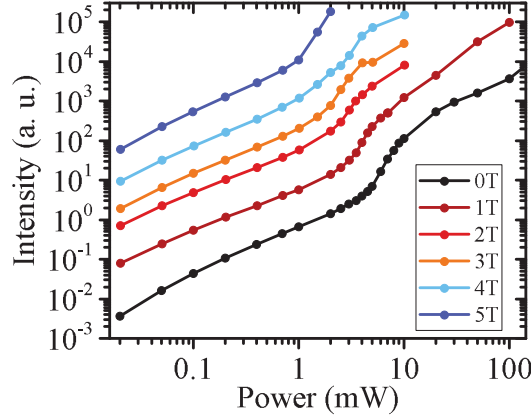


Figure 4.5 – Integrated intensity at $k = 0$ as a function of excitation power and increasing magnetic field (sample D1-13-02-15C). The curves are shifted in intensity for better visualization.

effect of the magnetic field is to lower the lasing threshold power up to $B = 2$ T. This can be explained by the increased PL intensity from zero to 2 T for a given power which is due to a change in the emission profile from circular to Gaussian as the field increases.

4.3.3 Effect of experimental configuration and other attempts

From these first results, we can list some effects that are detrimental for condensation. First, the number of QWs might not be large enough to reach the critical density before reaching the Mott density. Second, the fact that we use a small spot size and a cw laser might cause heating of the sample. It is known that a large spot size is preferred to show unambiguously the appearance of long range coherence [7]. However, a small spot size does not prevent condensation, only that the condensed phase will occur at $k \neq 0$ since the large reservoir induced energy blue shift is transferred to kinetic energy for the condensate [103, 113].

Nonetheless, we checked that these effects were minor by replacing our microscope objective with a $f = 5$ cm lens to increase the spot size ($\sim 20 \mu\text{m}$), and placed a chopper on the excitation path in order to reduce sample heating. In this configuration, we only have access to a small portion of the dispersion because of the small NA of the lens. Still, we compare power measurements to the ones obtained with the microscope objective. Furthermore, we proceed with another cavity sample with 12 QWs that is, 4 stacks of 3 in a 2λ -cavity, of the same composition as for the previous sample (sample B-31, see appendix B).

In figure 4.6 (a)-(b) we present the dispersion for two specific excitation powers to highlight the transition to weak coupling. In this case, the total blue shift is of the order of 2 meV.

Chapter 4. The quest for polariton condensation using InGaAs-based microcavity

In figure 4.6 (c) we show the normalized intensity at $k = 0$ measured using the lens for low and high excitation power. The measured dispersion is not shown since it is mainly flat. We can see from this figure that the total blue shift is comparable to the MO measurements. Finally, in figure 4.6 (e)-(f) we compare the intensity, energy and linewidth measured with both configuration. We always measure a single threshold, the difference of threshold position is due to the spot size. The initial polariton energy is different in both cases due to a difference between the alignment of the lens and the MO. This lowering of detuning between both cases is transposed in a lower blue shift needed to reach the cavity mode. Although, it is difficult to evaluate the position of the cavity mode in this case, the blue shift of almost 2 meV is comparable to the MO experiment. Therefore, we conclude that the observed behavior is independent of the excitation spot size.

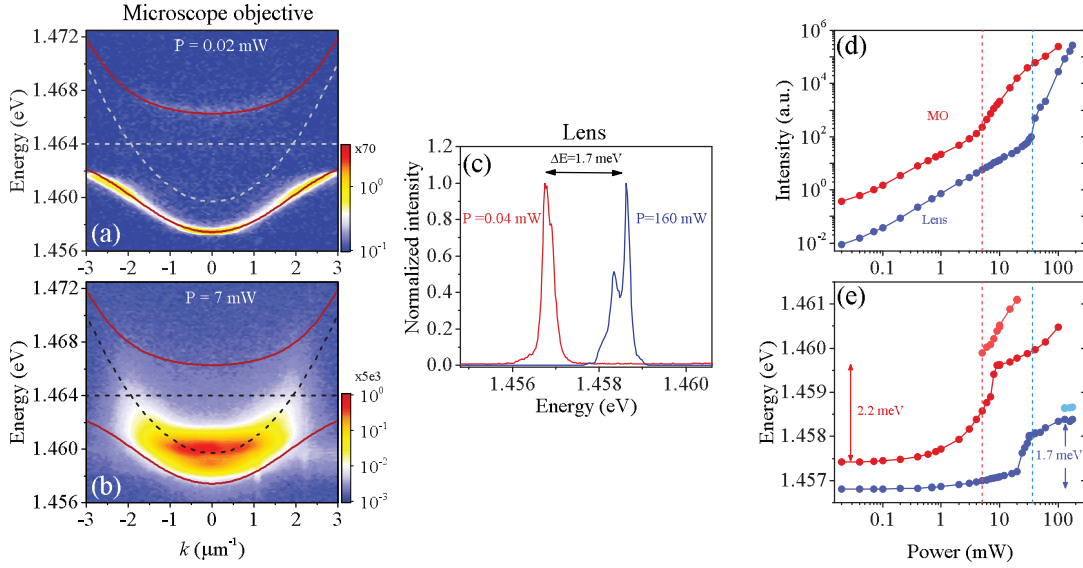


Figure 4.6 – PL intensity map in log scale of the dispersion for sample B-31 acquired using the microscope objective for excitation power (a) below and (a) at the threshold. The red curves are the effective strong coupling model fit and the dashed lines are the uncoupled modes. The fit was performed on the low power data and is the same for each panel. (c) Integrated intensity at $k = 0$ for two excitation powers acquired using the lens instead of the MO. (d) Integrated intensity at $k = 0$ as a function of excitation power for both cases. (e) Energy at $k = 0$ as a function of excitation power. The vertical dashed lines indicate the position of the threshold for the MO (red) and the lens (blue). Additional modes appear above threshold

Finally, to make sure that our experimental setup was not the problem, we also performed these measurements using the original setup used for the demonstration of polariton condensation [7] (with the help of F. Manni who was in charge of the setup at the time). For this setup, the spot size is $40 \mu\text{m}$, and the excitation is quasi-cw (μs pulses prepared

with an acousto-optic modulator [114]). We tested samples with 9 QWs (D1-12-12-14C, D1-13-02-15C), and 12 QWs (B-31), and got the same results as the one presented above, confirming yet again that the observed behavior is a consequence of the sample alone.

4.3.4 Excitonic Mott transition in coupled quantum wells

With a first set of negative results for samples of low In content, we investigated whether the interwell coupling could be detrimental for condensation. We showed in the previous chapter that the oscillator strength of the exciton states in coupled QWs was lower compared to the single QW case. The question is to determine whether the exciton saturation is similarly affected. Therefore, we seek to extract the Mott transition density for a single QW and a stack of three by comparing PL measurements. Ideally, if three uncoupled QWs are used, the measured PL at saturation should correspond to three times that of a single well.

Generally speaking, the Mott transition describes the conducting (or sometimes superfluid) to insulator transition [115]. This transition is usually described within the (Bose-) Hubbard model in terms of the ratio between hopping and on-site interaction [116]; for large hopping constant, the particles are delocalized (superfluid phase) while strong interaction means that the particles are localized (insulating phase or Mott insulator). The excitonic Mott transition represents the transition from an exciton gas to an electron-hole plasma [117]. Here the exciton gas is insulating while the electron-hole plasma is not (although not a superfluid). Two effects mainly come into play: the exciton blue shift due to exciton-exciton interaction and the renormalization of the band gap with density which is proportional to $n^{1/3}$, n being the carrier density [118, 119]. The Mott transition should occur when the exciton, and band gap energies are equal. Usually, we assume that this transition occurs for the same density needed to lose the strong coupling (it is not possible to have excitons in weak coupling at large density). A more detailed description can be found in [120].

The experiment was performed using the setup described in section 3.1 in reflection geometry, and using the laser diode for excitation (spot size of 10 μm). In order to measure the QW saturation, we must use a pinhole to filter the real space and collect only the PL signal coming from the highest excitation density. For each sample, the alignment of the MO and pinhole is adjusted at high excitation power to properly measure the saturation plateau, and to make sure that we are measuring the right position. This means that the excitation density might vary for both sets of experiments.

Figure 4.7 presents the PL measurements for a single QW sample (a)-(c) and a QW stack (b)-(d). The main characteristics of the transition are clearly observed for both samples. First we see a broadening of the exciton peak. At around $P = 2$ mW, the lineshape is no longer lorentzian, the exponential tail at high energy reaches the peak maximum, and the

Chapter 4. The quest for polariton condensation using InGaAs-based microcavity

coupled QW states are no longer visible. This is where the Mott transition should occur. As the excitation is increased further, the QW saturates which is seen by the appearance of a plateau (corresponding to the 2D density of states). We also see indications of the exciton Mott transition from the thicker GaAs layers (100 nm on both sides of the QW).

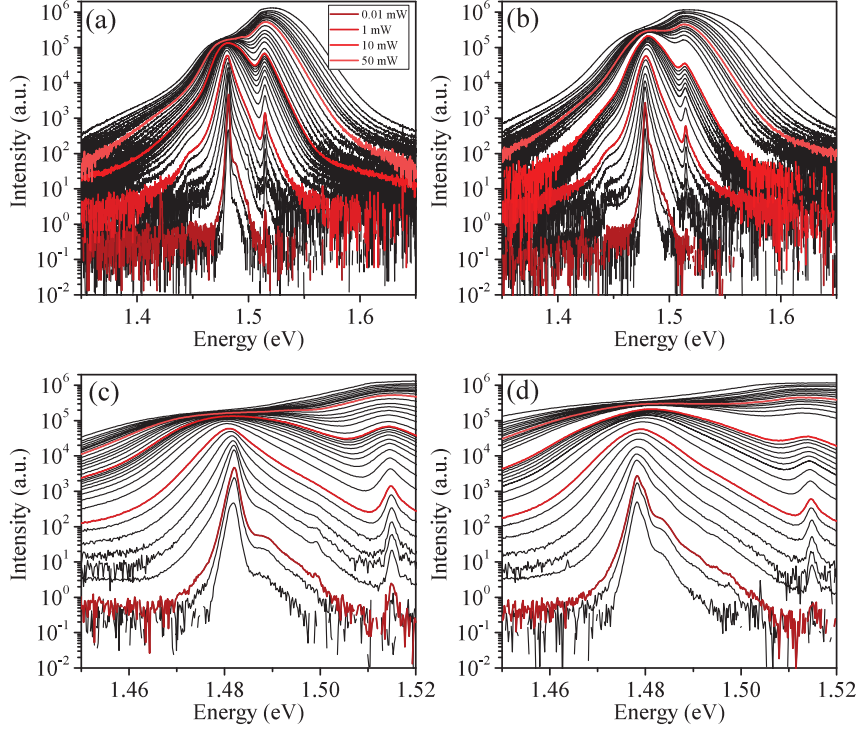


Figure 4.7 – PL spectra for increasing excitation density for (a) single QW (sample D-13, 10 nm, 5% In) and (b) a single stack of three QWs. (sample D-15, 10 nm well with 6 nm spacer, 5% In). (c)-(d) same as for (a) and (b) but for a smaller energy window.

From these measurements, we can extract the density in the electron-hole plasma phase by fitting the measured PL lineshape by the convolution of a lorentzian and the radiative recombination of the electron-hole system. The latter is given by:

$$R_{sp}(\hbar\omega) = \frac{\pi e^2}{2\hbar m_0^2 \omega^2} |E|^2 D_{cv}^{2D}(\hbar\omega) f_e(\hbar\omega) (1 - f_h(\hbar\omega)) \quad (4.1)$$

where f_e , and f_h are electron and hole quasi-Fermi distribution. For a 2D system, they are directly linked to the carrier density, since the quasi-Fermi energy depends on density. These functions are [120, 121]:

$$f_e(\hbar\omega) = \left[\exp\left(\frac{\mu^*(\hbar\omega - E_G)/m_e^* - E_{F,e}}{k_B T}\right) + 1 \right]^{-1}, \quad (4.2)$$

$$1 - f_h(\hbar\omega) = \left[\exp\left(\frac{\mu^*(\hbar\omega - E_G)/m_h^* - E_{F,h}}{k_B T}\right) + 1 \right]^{-1}, \quad (4.3)$$

$$E_{F,e} = k_B T \ln \left(\exp\left(\frac{\pi \hbar^2 n}{em_e^* k_B T}\right) - 1 \right), \quad (4.4)$$

$$E_{F,h} = k_B T \ln \left(\exp\left(\frac{\pi \hbar^2 n}{em_h^* k_B T}\right) - 1 \right). \quad (4.5)$$

D_{cv}^{2D} is the electron and hole joint density of state (JDOS) given by [121]:

$$D_{cv}^{2D}(\hbar\omega) = \frac{\mu^*}{\pi \hbar^2} \theta(\hbar\omega - E_G), \quad (4.6)$$

where μ^* is the carrier reduced mass, and θ is the Heaviside function, and E_G the band gap energy. We fit the PL signal and extract the dependence of the carrier density n with excitation power. These equations do not apply for the exciton (the fit gets worse as we go to lower excitation power), hence we extrapolate the density down to the excitation power where the Mott transition seems to occur. These fits do have a large number of free parameters (linewidth, E_G , n , T). In our case, we are able to extract the temperature from the high energy tail of the GaAs signal. Furthermore, the width of the signal is primarily given by the carrier density n , hence the uncertainty is reasonable even if the complete lineshape is not perfectly reproduced. The height of the signal is given by a scaling factor which is determined at high power and constant for all fits of the same series.

Figure 4.8 (a) compares the measured signal from both samples for specific excitation power. Both samples seem to pass the Mott transition around $P = 2$ mW. Close to the transition, we notice that the PL intensity from both samples is almost the same while the QW signal from the coupled QWs is higher passed the Mott transition. This is a consequence of the number of wells in the stack which changes the JDOS for the coupled QWs compared to the single QW case. In principle, we should fit using a step function for the three main electron-hole states. However, these steps come almost invisible due to the large linewidth used in the convolution. Instead we simply multiply by three the amplitude factor obtained from the single QW fit which allows to compare the carrier densities.

Figure 4.8 (b) shows an example of the fit for the single QW sample at an excitation power of $P=30$ mW, where the dark blue curve is the convolution of equation 4.1 with a lorentizan. The light blue curve corresponds to the donor-acceptor in GaAs. The light

Chapter 4. The quest for polariton condensation using InGaAs-based microcavity

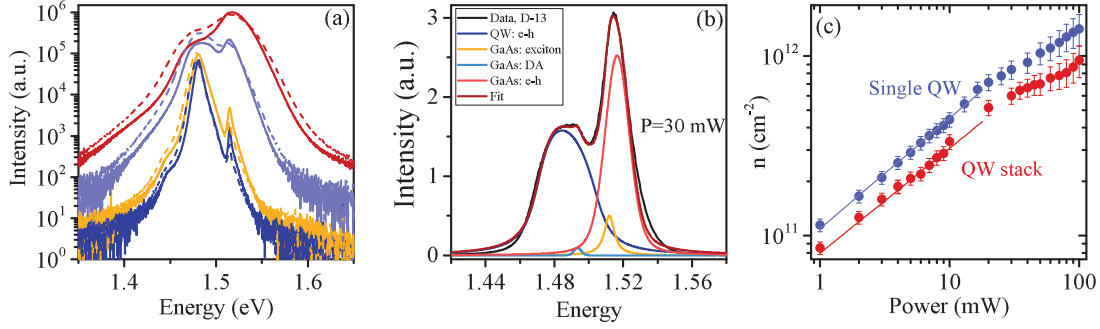


Figure 4.8 – (a) PL spectra for increasing power of the single QW sample (D-13, solid lines) and the QW stack (D-15, dashed lines). (b) PL spectrum of the single QW sample for an excitation power of $P=30$ mW, and details of the fit used to evaluate the density. (c) Carrier density as a function of excitation power. The solid line is a guide to the eye.

red curve is the dominant signal from GaAs fitted with a Voigt function. Its energy position depends on the excitation power to consider the effect of saturation (instead of electron-hole recombination pass the Mott transition). The orange curve is the GaAs exciton signal which comes from the bottom layer of GaAs where the excitation density is lower (its energy does not change with density). Finally, figure 4.8 (c) shows the carrier densities obtained from the fitting procedure for both samples as a function of excitation power. For a given excitation power, the carrier density is always lower for the QW stack compared to the single QW. Since the Mott transition occurred around $P=2$ mW where the Mott density for the QW stack is $\sim 70 \pm 5\%$. This value is reasonable compared to the decrease of oscillator strength measured in the previous chapter. Hence, interwell coupling might accelerate the strong to weak coupling transition. However, the difference is not significant enough that such a change of the Mott density could be the dominating factor preventing polariton condensation in our samples.

4.4 High Indium content microcavities

For a second series of samples, we turned to QWs with high In content (8-14%). First, this should limit the effect of interwell coupling provided that the barrier is large enough. Second, it should allow for the capture and the relaxation via LO-phonon scattering (for electron and hole) by the use of LO-phonon (~ 36 meV). The main drawback as we will see is the increase of disorder in the top DBR mirror.

4.4.1 Photoluminescence of quantum well stacks

As for the low In QWs, we begin by characterizing the QW quality to the design giving the highest sample quality. Figure 4.9 shows the PL for three samples, each with a single 7 nm QW, but for different In contents (when increasing In, the quality will be better for

thinner QWs). As expected, increasing the In content lowers the exciton energy. The band edge is visible as a shoulder on the high energy side for all samples (binding energy of ~ 8 meV), while the linewidth varies between 2-2.2 meV (mainly inhomogeneous, due to disorder). Although it is almost four times that of 3% In QWs, these values are comparable to the best found in the literature [122–124], demonstrating the high quality of our samples.

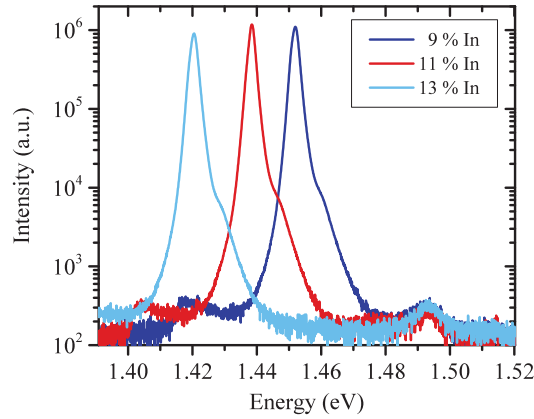


Figure 4.9 – PL for three single QW samples with increasing In content (D-37, D-39, and D-40 see appendix B for a description of the samples).

Second, we checked whether the QWs would be coupled when stacked. Figure 4.10 compares the PL from a single 7 nm $\text{In}_{0.09}\text{Ga}_{0.91}\text{As}/\text{GaAs}$ to the PL of stacks of three identical QWs with decreasing spacer thickness. For a spacer of 12 nm, the linewidth and energy between the single QW and the stack are almost the same. However, the PL of the QW stack starts to red shift for a spacer of 10 nm, indicating a slight appearance of coupling. At a spacer thickness of 6 nm, the single exciton peak becomes structured, meaning that the coupling between the wells is considerable. These results show that a spacer of 12 nm or more should be used in order to minimize the effect of multimode coupling in the microcavity.

4.4.2 Nonlinear property of high Indium microcavities

We used a slightly different approach to optimize the microcavity samples for this set of experiments. The samples are grown in two steps to overcome as much as possible the fluctuation of the MBE (see section 2.2.3). First, the bottom DBR is grown followed by the cavity spacer and QWs. The growth is stopped before the end of the desired spacer thickness to have a half cavity with a thin cavity spacer. Then, we perform a room temperature reflectivity of the half-cavity sample (without cleaving the sample) and compare the result with the transfer matrix simulation to evaluate the growth fluctuation. Having a thinner spacer turns out to be ideal since, for the case of half cavity, we are able

Chapter 4. The quest for polariton condensation using InGaAs-based microcavity

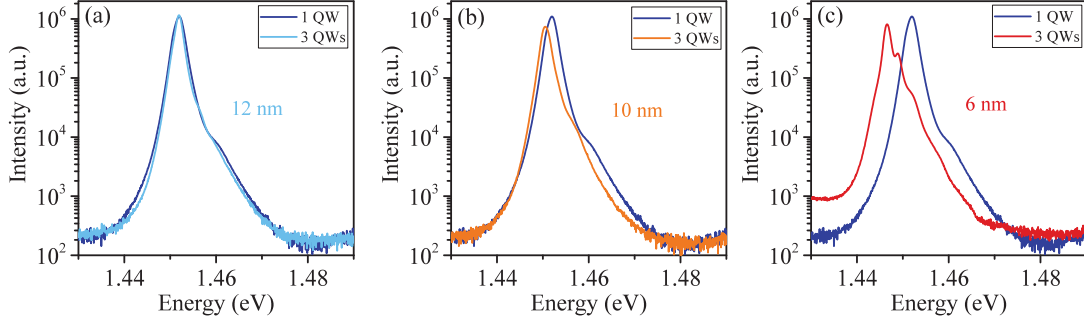


Figure 4.10 – Comparison of PL from a single 7 nm QW with 9% In (sample D-34, dark blue) with stacks of three QWs of same composition. (a) QW stack with 12 nm spacer (sample D-35), (b) 10 nm spacer (sample D-37), and (c) 6 nm spacer (sample D-36). See appendix B for a description of the samples.

to see the bottom of the broad cavity mode in reflectivity when its energy is higher than the GaAs band gap (~ 868 nm at room temperature). Hence, we can evaluate the actual thicknesses grown with a better precision. Afterward, we can adjust the design of the top part of the sample to position the cavity mode at the right energy. Before the regrowth, we must clean the surface of the sample with a hydrogen plasma otherwise the native oxide of GaAs will not allow to get a high-quality material. Finally, in some cases, the half cavity is cleaved in half, and regrowth is performed on the half wafer. That way, we get two chances to get the sample right. The half sample is mounted in the MBE with a dummy half substrate on a full wafer holder to keep the wedge of the sample identical for the bottom and top part.

In the following, we present the results obtained for sample F-40. It consists in a 27/30 bottom/top DBR $7\lambda/2$ -cavity with 6 pairs of 8 nm, $\text{In}_{0.09}\text{Ga}_{0.91}\text{As}$ QWs with a 12 nm spacer. Each QW stack is centered at the antinode of the electric field inside the microcavity. Although the cavity spacer is relatively large (~ 850 nm), it is still smaller than the effective length inside the DBRs ($\sim 2 \mu\text{m}$). However, the Rabi splitting will decrease if we continue to increase the spacer thickness to include additional QW stacks. The power measurements were done using the high power laser diode at $\lambda = 660$ nm with the same setup as for the Mott transition experiment (see section 3.1). The excitation spot in the case is $\sim 10 \mu\text{m}$. We also placed a pinhole in between the two lenses as shown in figure 3.2 in order to extract the PL only from the center of the excitation spot.

Figure 4.11 (a) shows the dispersion of sample F-40 for low excitation power. Both polariton branches are clearly seen, allowing to extract a Rabi splitting of only $\Omega_0 = 6$ meV, a cavity detuning of $\delta = -\Omega_0/3 = -2$ meV, hence an excitonic fraction at $k = 0$ of $|X|^2 = 0.34$. The linewidth for the ground state is $\text{FWHM} = 230 \mu\text{eV}$ (Q-factor of $Q \approx 6100$), indicating a relatively large inhomogeneous broadening. Figure 4.11 (b)-(d) shows the dispersion for different excitation power. A linear scale is used here to emphasize the

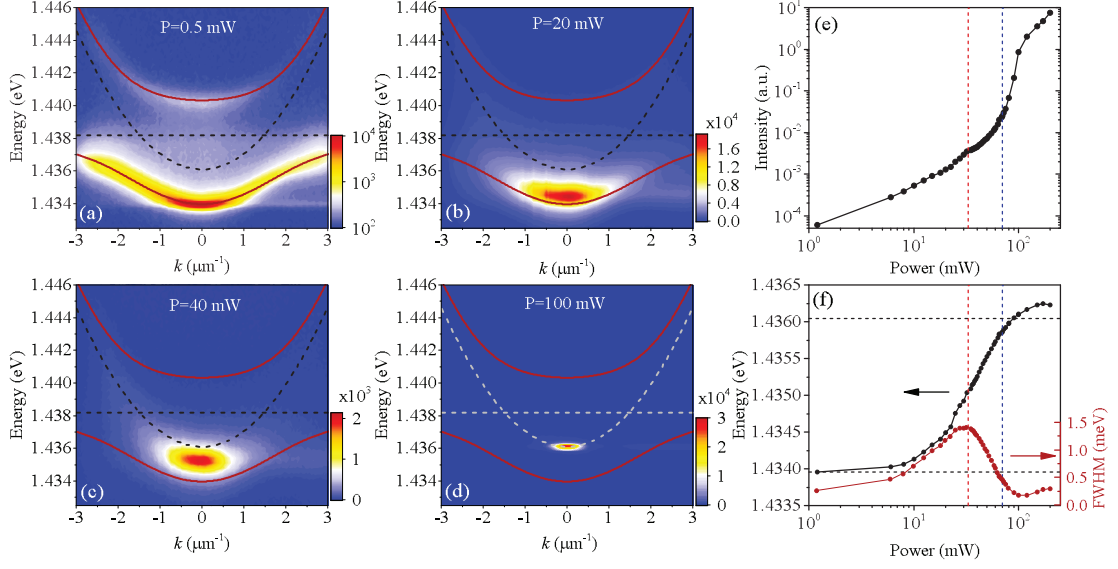


Figure 4.11 – (a)-(d) PL intensity map in log scale of the dispersion for increasing excitation power for sample F-40. The red curves are the strong coupling model fit and the dashed lines are the uncoupled modes. The fit was performed on the low power data and is the same for each panel. (e) Integrated intensity at $k = 0$ as a function of excitation power. (f) Energy (black) and linewidth (red) at $k = 0$ as a function of excitation power. The horizontal dashed lines indicates the position of the lower polariton and the cavity mode extracted from the fit at low power. The red and blue dashed lines are a guide to the eye to indicate the linewidth extremum and the intensity threshold.

energy variation of the peak intensity. We clearly see that the lower polariton mode blue shifts until it reaches the bare cavity mode.

One might be tempted to claim a polariton condensate by only looking at figure 4.11 (c). However, the integrated intensity as a function of power as well as the evolution of the emission energy and linewidth says otherwise (see figure 4.11(e), and (f)). There is a single intensity threshold, and it occurs when the emission energy coincides with the bare cavity mode. Hence, what we observe is again a nice transition from strong to weak coupling. An interesting feature for this case is that the decrease of linewidth is less abrupt, and occurs before the threshold (the small feature in intensity at this position is not a non-linearity, but an artefact caused by the normalization of the intensity). This represents a more accurate evolution of the linewidth compared to previous cases. Here the lorentzian fit of the emission at $k = 0$ includes only the signal from the center of the beam.

To emphasize that any claim for condensation cannot rely simply on intensity map, we compare in figure 4.12 the same image taken for a power of $P=40$ mW either in linear color scale as in figure 4.12 (c) or in log scale. With a proper choice of boundary and color scale, it is easy to mimic a polariton condensate (large intensity at $k = 0$, below the

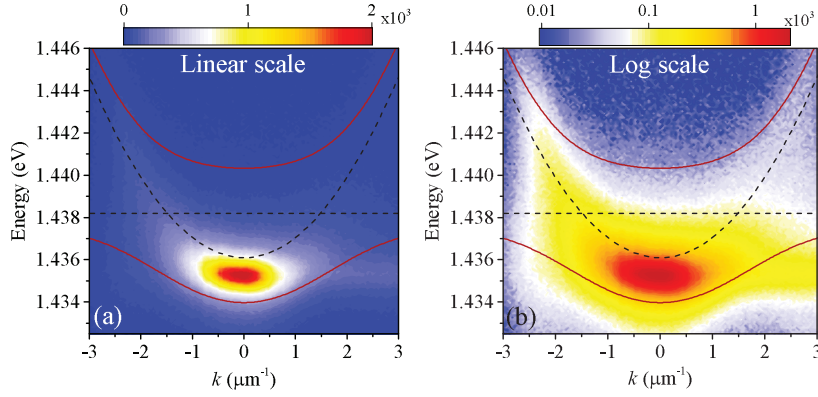


Figure 4.12 – PL intensity map of the dispersion for sample F-40 for an excitation power of $P=40$ mW in (a) linear color scale, and (b) in log scale.

bare cavity mode). However, the same image in log scale clearly shows the appearance of the cavity dispersion. In general, it is advisable to work with a large intensity dynamic and a logarithmic color scale to properly show the state of the system. This is why we used a color scale where the highest color contrast is placed on the weak signal for all our color maps.

Finally, we studied one last microcavity design with 15 QWs, placed in 5 stacks of three QW (15 nm spacer, to avoid interwell coupling) in a 3λ -cavity (sample F-46b, see appendix B). That way the coupling should be increased ($\Omega_0 \sim 7.5$ meV), while the carrier density per well is decreased. In this scenario, the disorder became so large that photon confinement occurred at different positions on the sample (see figure 4.13). The power measurements showed first weak coupling lasing on the confined mode before lasing on the 2D cavity mode.

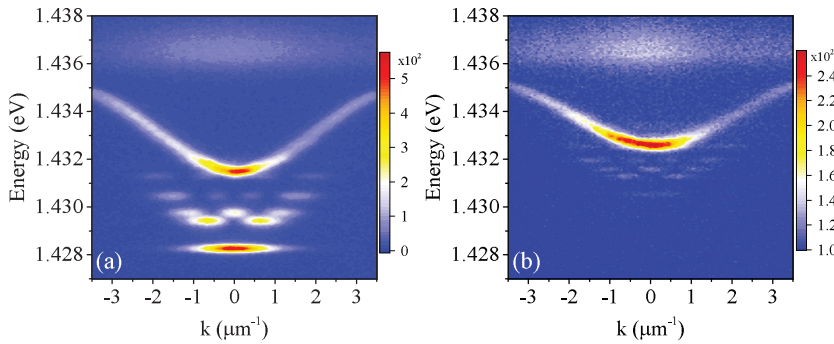


Figure 4.13 – (a)-(b) PL intensity map of the dispersion for sample F-46 for two positions on the sample.

4.5 Discussion

By the time these last results were obtained, the MBE growth was focused mainly on single QW microcavities for the realization of new confined structures like the one realized back in 2004 [22] (see chapters 5, and 7), hence we were not able to pursue our investigation. Although condensation was not achieved, there are a few points to discuss in order to understand what could be the limiting factors for condensation with InGaAs QWs compared to GaAs/AlAs QWs.

The first criterion is the cavity losses. Similarly to laser cavity, stimulation will take place only if the gain compensate the losses. This was the main criteria to achieve condensation for GaAs-QW based microcavity, where increasing the number of DBR pairs from 16/20 to 26/30 (while keeping a Rabi splitting of $\Omega_0 = 15$ meV) allowed to reach condensation [8,107]. In the present study, we used higher number of DBR pairs, with a higher refractive index contrast (AlAs/GaAs compared to $\text{Al}_{0.8}\text{Ga}_{0.2}\text{As}/\text{Al}_{0.05}\text{Ga}_{0.95}\text{As}$). Hence, the theoretical photon lifetime in our cavity should be higher. The increased amount of disorder might be the problem here. As we stated earlier, disorder by itself does not prevent condensation, but it might lead to the appearance of leaky modes that increase cavity losses. Indeed, the low quality factor obtained for a sample with 27/30 DBR pairs might be an indication of this. In that regard, incorporating strain compensating layers in the DBR [101] or using AlGaAs [104] might prove useful to increase the Q-factor. High Q-factors (>10000) were obtained for low In QW microcavity, but interwell coupling limited the coupling strength.

This leads to the second criterion which is the value of the Rabi splitting. From our measurements, it seems that the Rabi splitting obtained for the case of 12 or 15 QWs, is not that high. We discussed in section 1.5.2 that the important factor for condensation (to maintain the bosonic character of the system) was the ratio between the Rabi splitting of a single well to the saturation density ($g_{pae}N$), not the Rabi splitting of the full cavity. Nonetheless, if the Rabi splitting of the full cavity is not maximized, this might indicate that the coupling strength of some of the QWs is less than the optimal case (single QW microcavity). Three things must be considered here. First, increasing the Indium content tends to decrease the oscillator strength which will lower the coupling strength of each well. Second, for the large number of QW needed, the cavity spacer thickness starts to influence the coupling strength. Third, the placement of the QWs inside the cavity spacer can greatly affect the overlap with the field. For example, for the stacks of three QWs with 15 nm spacer, the overlap changes by ~ 20 % between the center well and the other two. If the stack is misplaced in the cavity due to growth fluctuations, then one of the outer QW of the stack will saturate quicker simply because its coupling strength is less. Due to the problems encountered with the MBE machine, it was not possible to evaluate whether we obtained the highest coupling strength for a given cavity design. We can evaluate the relative oscillator strength for a low In content QW to the one expected for the 15 QWs microcavity by comparing the Rabi splittings ($\Omega_0 \propto \sqrt{N^*f/L_{eff}}$, where N^*

Chapter 4. The quest for polariton condensation using InGaAs-based microcavity

is the effective number of QW, due to the overlap with the field). Using a Rabi splitting of $\Omega_0 = 3.5$ meV for a λ -cavity as a reference, and a coupling strength of 0.8 that of the center QW for the 15 QW microcavity, we get a ratio of oscillator strength of ~ 0.44 . This would correspond to the ratio between the oscillator strength of a 9% In QW to a 4% In QW. This value seems a bit low, indicating that it should be possible to improve the coupling inside the microcavity.

The third criterion is the saturation density leading to the Mott transition and the transition to the weak coupling regime. From the last comment, we see that the saturation density should be compared to the coupling strength of the least coupled QWs. Of course, this would induce a weak coupling transition quicker than expected. However, what we have not considered up to now is the effect of the reservoir density on the weak coupling transition. It is well known that the effect of the reservoir must be considered to understand the polariton blue shift and the pumping of the condensate. We will see in chapter 6 that in general, reservoir terms must be added as dephasing, and as a saturation of the light-matter interaction (also see appendix A). Hence, the condition for condensation stated in equation 1.51b should also include the density inside the reservoir. We can restate this condition as:

$$g_0 N^- + \sum_i g_i N_R^i \ll \frac{\Omega_0^-}{2}, \quad (4.7a)$$

$$g_{pae} N^- + \sum_i g_{pae}^i N_R^i \ll \frac{\Omega_0^-}{2}, \quad (4.7b)$$

where N^- is the exciton density in the least coupled QW, Ω_0^- is its corresponding coupling strength, N_R^i is the reservoir density for a given state i , g_i is a reservoir-exciton repulsion interaction term, and g_{pae}^i is the phase space filling from the same reservoir state. Provided the reservoir density is large, then it is possible that the saturation starts to take place before bosonic stimulation. In other words, the density at $k = 0$ must compete with the total exciton density of the system in order to reach polariton condensation and not VCSEL lasing. Furthermore, including reservoir-induced dephasing effect will tend to decrease the density of the polariton ground state which is also detrimental.

The remaining question is to understand why polariton condensation does not seem to work for InGaAs QWs while it does for GaAs QWs. For this, we can look at the material parameters themselves. We can compare our results to other GaAs QW based microcavity that showed condensation. Four notable cavity designs have demonstrated condensation, their cavity designs are given in table 4.1.

As expected, the highest coupling strength occurs for a small cavity spacer, a design which is not possible for InGaAs QW because of the shallowness of the QWs and the boundary conditions imposed by the GaAs spacer. AlGaAs could be used as the spacer material; however the growth of high-quality QWs using two ternary materials is far from trivial.

Table 4.1 – Description of the microcavity samples that showed condensation. $\Omega_{QW} = \Omega_0/\sqrt{N_{QW}}$ is the estimated Rabi splitting of a single QW in a cavity having N_{QW} QWs. All samples use different ratio of $\text{Al}_x\text{Ga}_{1-x}\text{As}$ for the spacer and DBR mirrors.

Cavity spacer	DBR (top/bottom)	N_{QW}	Ω_0 (meV)	Ω_{QW} (meV)	ref.
$\lambda/2$	26/30	12 (3x4)	15	4.33	[8]
$5\lambda/2$	32/35	12 (4x3)	9	2.6	[125, 126]
$3\lambda/2$	34/40	12 (3x4)	16	4.6	[127, 128]
$\lambda/2$	32/37	8 (2x4)	11.5	4.06	[44]

Apart from the second sample, all samples show a larger coupling strength than the typical value for a single InGaAs QW ($\Omega_0 = 3.2 - 3.6$ meV). This gives some indication that the oscillator strength is indeed larger for GaAs QW, and that the Mott transition should occur at higher densities. Moreover, the fact that the single QW coupling strength is less for the $5\lambda/2$ -cavity than for InGaAs QW suggest that the saturation (or phase space filling) term g_{pae} is lower for GaAs QW compared to InGaAs/GaAs QW. If the saturation density is twice that of InGaAs QW, we would need to double the number of QW in the cavity which will decrease the overall coupling strength. Hence, it may be that from a design point of view, InGaAs QW microcavity do not allow to satisfy the criteria for condensation. This should be tested for instance by comparing Mott transition density of a single InGaAs QW to a GaAs one to see if this is the dominant factor.

Finally, there is another difference between InGaAs and GaAs microcavity which is the use of GaAs in the spacer, and DBR mirrors. For GaAs QW microcavity samples, all the carriers are created directly in the QW layers since the band gap of AlGaAs is at a higher energy than the laser. For our samples, we create carriers in all GaAs layers which then relax in the QWs. Although excitons in the DBRs will not tunnel down to the QWs, the carrier density inside the spacer may act as a considerable reservoir for the system. It might be possible that this reservoir in fact accelerates the saturation of the QW, which is what we stated in equation 4.7b. The best way to test this would be to design a microcavity with high In content such that the first minimum of the reflectivity is below the GaAs band gap energy. That way, we could excite directly inside the QW, and avoid having carriers in the GaAs layers. Of course, the best way to verify this would be to use a sample where the optical disorder is small, and the coupling strength has been optimized.

4.6 Conclusions

In this chapter, we have studied the non-linear properties of microcavities designed with InGaAs QWs. We have tested samples with low and high In content, with QW stacks of

Chapter 4. The quest for polariton condensation using InGaAs-based microcavity

two or three QWs, and for 9 to 15 QWs inside the cavity spacer. For every design studied, a single threshold only was measured and the resulting emission energy was always on the bare cavity mode. Hence, all of the samples showed photon lasing and not polariton condensation. We have also confirmed that applying a magnetic field had almost no effect on the strong to weak coupling transition, and did not allow to reach polariton condensation. In order to obtain condensation with InGaAs QWs, optical disorder should be decreased by the use of strain compensation layers in the DBR mirrors, the Rabi splitting for a given microcavity sample optimized, and the stop band designed to have a first minimum in reflectivity below the GaAs band gap energy. Mott density should also be compared between GaAs and InGaAs QWs in order to evaluate whether InGaAs QWs have much lower saturation density, and if we are instead limited by the material parameters themselves.

Optical response of resonantly excited confined polaritons

Part III

5 Spatial multistability and cross interactions

This chapter is the first of two devoted to the study of resonantly excited confined polaritons. In the previous chapters, the polariton population originated from charge relaxation in the microcavity. Here we are interested in the case where the laser energy is resonant or quasi-resonant to the polariton energy. In this experimental scheme, the laser imprints its phase and in-plane momentum onto the polariton fluid. This allows for example to launch a fluid at a given speed and study effects like superfluidity [14], dark [16, 17] and bright solitons [15] as well as vortex nucleation [12] and vortex streets [129]. Early studies of resonantly excited polaritons also demonstrated the effect of polariton parametric scattering when the polariton is excited at the inflection point of its dispersion [3–5, 130].

In this chapter, we are interested in a different type of experiment, where instead of launching a polariton fluid, we excite one or more confined polariton modes inside a mesa. The principle of the zero dimensional microcavity was discussed in section 1.3.2. The confinement allows to obtain large density of polaritons which is ideal to investigate polariton-polariton interactions (see section 1.5), specifically through the polariton multistability.

The polariton bi-multistability is a special case of optical bistability, where an optically driven system has two possible output intensities over a range of input powers [131]. When more than two output intensities are allowed either when cycling the input power or for a given input value, the result is an optical multistability, as was observed for example for atomic systems in an optical resonator [132–135].

There exists a different kind of optical multistability called spatial multistability which consists of having specific transverse spatial profiles for each of the stable states of the optical multistability. This effect was first demonstrated using a HeNe laser cavity [136], as well as other gas lasers [137, 138] and was theoretically discussed in Refs. [139, 140]. It relies on being able to select and switch between laser cavity modes out of a superposition of modes either by injecting the right phase pattern or by displacing a saturable absorber inside the cavity. In this chapter, we demonstrate this effect using confined polaritons,

and through it, discuss polariton-polariton cross interactions. Part of the work presented has been published in [28].

5.1 Polariton bistability and spin multistability

The bistability and spin multistability of microcavity polaritons have been extensively studied both theoretically [141–147] and experimentally [6, 148–156]. It relies on exciting the microcavity using a laser blue detuned with respect to the lower polariton branch (LP) and to measure the transmitted laser intensity. When cycling the excitation power, a hysteresis curve is observed that is a consequence of the Kerr-like nonlinearity induced by exciton-exciton interactions [6].

In order to understand the origin of this effect, we start with the Gross-Pitaevskii equation in the polariton basis. We recall equation 1.48:

$$i\hbar\dot{\psi}_{LP} = (\epsilon_{LP} - i\gamma_{LP} + \alpha_1|\psi_{LP}|^2)\psi_{LP} + f_{ext}. \quad (5.1)$$

The driving field is defined as:

$$f_{ext} = \sqrt{I_0}e^{-iE_l t/\hbar}, \quad (5.2)$$

where I_0 and E_l are the laser intensity and energy. If we take this equation and multiply it by its complex conjugate, we obtain a simple analytical equation which is a third order polynomial in polariton density [157]:

$$I_0 = [(\alpha_1 n_p - \Delta)^2 + \gamma_{LP}^2] n_p, \quad (5.3)$$

where $\Delta = E_l - \epsilon_{LP}$ is the laser detuning. It is easy to demonstrate that when $\Delta \geq \sqrt{3}\gamma_{LP}$, this intensity has the characteristic *s*-shape of a third order polynomial, meaning that for a range of excitation power, this equation has three solutions, one of which is unstable. This is the principle of the optical bistability and it is sketched in figure 5.1. As the excitation power is increased, the polariton intensity follows the given polynomial. When it reaches the local maximum, it jumps to the upper branch as shown by the black lines. When the power is decreased, the intensity follows again the polynomial solution until it drops down once the local minimum is reached.

We can obtain a better understanding of the process by evaluating the polariton blue shift at different points on the bistability curve. From equation 5.3 we obtain expressions for the polariton density at the two extrema of the *s*-shaped curve [157]:

$$n_{\pm} = \frac{2\Delta \pm \sqrt{\Delta^2 - 3\gamma_{LP}^2}}{3\alpha_1}. \quad (5.4)$$

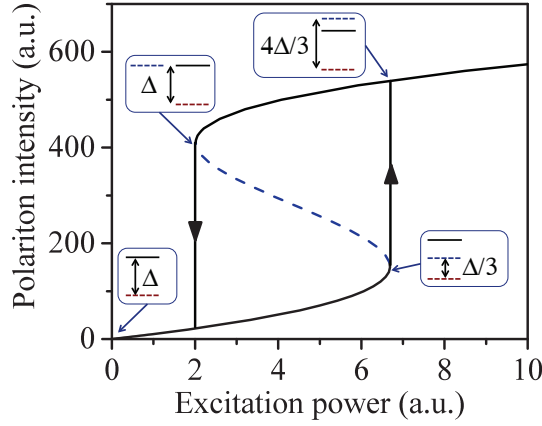


Figure 5.1 – Scheme of the polariton bistability, showing the polariton intensity as a function of resonant excitation power. The blue dashed lines shows the analytical solution of GPE. The value of the polariton blue shift obtained with the analytical model for specific positions on the bistability is also depicted. The black line is the laser energy, the dashed red line is the initial energy of the polariton mode, and the dashed blue line is the blue shifted polariton mode. Δ is the initial laser detuning with respect to the polariton mode.

Moreover, we can estimate the polariton density just above the upward threshold by solving for the excitation density of the upward threshold:

$$I_0^{up} = \frac{2\Delta - \kappa}{27\alpha_1} (6\gamma_{LP}^2 + 2\Delta^2 + 2\Delta\kappa), \quad (5.5)$$

with $\kappa = \sqrt{\Delta^2 - 3\gamma_{LP}^2}$. Combining equations 5.3 and 5.5 allows to determine the polariton density above the upward threshold, n'_+ , and therefore the polariton blue shift $\delta_p = \alpha_1 n_p$. If we set $\gamma_{LP} = 0$, the blue shift for these particular points are:

$$\delta_+ = \alpha_1 n_+ = \frac{\Delta}{3}, \quad (5.6a)$$

$$\delta'_+ = \alpha_1 n'_+ = \frac{4\Delta}{3}, \quad (5.6b)$$

$$\delta_- = \alpha_1 n_- = \Delta. \quad (5.6c)$$

We can summarize the bistability process as follows, When the power is increased, the polariton mode blue shifts due to repulsive polariton-polariton interactions. A strong nonlinear jump of the transmitted intensity occurs when the energy shift equals the critical blue shift δ_+ (one third the laser detuning if there is no loss, higher when losses are considered). At this point, the polariton mode energy is shifted above that of the resonant laser. As the power is decreased, the polariton mode stays locked to the laser until the gain from the input laser can no longer compensate the polariton losses. This

occurs for the following reason. As the density decreases, so does the blue shift. Because the polariton mode is above the laser energy, a decrease of blue shift increases its overlap with the laser, hence increasing the density. Once the polariton mode energy equals the laser energy, the slight decrease of density will push the mode below the laser, causing it to unlock. The upward threshold power P_{up} is therefore sensitive to the polariton density while the downward threshold power P_{down} is sensitive to the polariton linewidth and dephasing.

5.1.1 Procedure for Numerical Simulations

The analytical model is useful to understand the polariton bistability but its usage is limited when we want to study the phenomenon in greater detail. For this, we turn to numerical simulations of the system and use the GPE in the exciton-photon basis, as given by equation 1.47:

$$i\hbar\dot{\chi} = (\epsilon_x - i\gamma_x + g_0|\chi|^2)\chi + \frac{\Omega_0}{2}\phi, \quad (5.7a)$$

$$i\hbar\dot{\phi} = (\epsilon_c - i\gamma_c)\phi + \frac{\Omega_0}{2}\chi + f_{ext}, \quad (5.7b)$$

where χ and ϕ is the exciton polarization and the photon mean field, and f_{ext} is given by equation 5.2. Working in the exciton-photon basis has one main advantage: namely that the exciton and photon fractions are automatically renormalized with density when the system is solved as a function of excitation density. Therefore, both the exciton-exciton interaction and the pumping efficiency of the excitation laser into the cavity (or quasimode coupling [5]) are adjusted directly from solving the system of equations. Indeed, we know that the higher the excitonic fraction, the more the polariton should interact, and the more photon-like polariton is, the more efficient it will couple to a photon mode out of the cavity. Since the Hopfield coefficients vary with the density, these coupling constants will also vary within a bistability cycle, something that cannot be done using the GPE in the polariton basis as in equation 5.1.

To simulate a bistability curve, we solve equations 5.7 temporally for a given input intensity I_0 until a steady state is reached, as depicted in figure 5.2 (a). Once this is obtained, we inject the steady state value of the complex exciton and photon amplitudes as initial conditions for the second step of power. We obtain the bistable curve numerically by cycling the input intensity and plotting the steady state photon intensity $|\phi|^2$ as a function of the excitation power as shown in figure 5.7 (b). The advantage of this method is that the bistability thresholds occur directly within the simulation.

Three things must be considered carefully when performing these simulations. First, when the system evolves in time, there is a given phase relation between the input laser and the polariton mode. This phase relation must be maintained when the resonant power

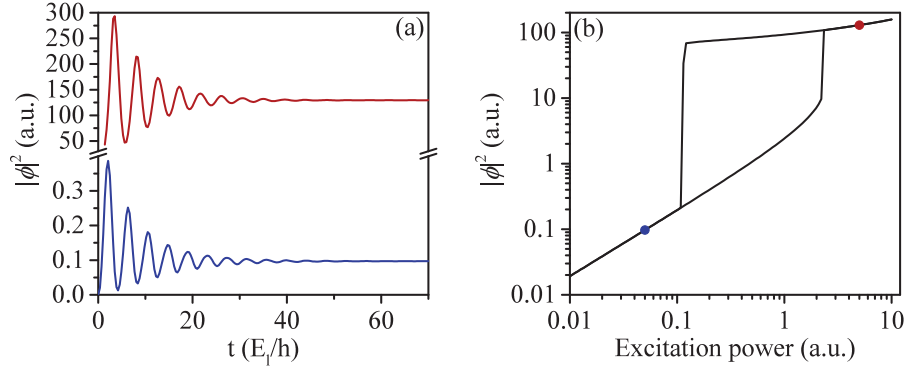


Figure 5.2 – Numerical simulation of polariton bistability using the GPE in the exciton-photon basis (equations 5.7). (a) Temporal evolution of the photon mean field $|\phi|^2$ and (b) complete hysteresis loop simulated. The temporal scale is normalized by the resonant laser energy E_l . The blue (red) curve corresponds to low (high) excitation power at the position indicated by the colored dots in (b).

is increased (when the steady-state solution is used as initial conditions), otherwise we generate a phase jump which falsely affects the bistability width. This can be avoided by normalizing the time scale by the laser energy. Second, the discretization in time should be sufficient and the time window large enough in order to reach the steady state. Finally, the accuracy on the threshold powers will depend on the power discretization. An appropriate compromise must be reached between the number of points, in time and power, and the actual time needed to perform the simulation.

5.1.2 Influence of Key Parameters on the Bistability

The polariton hysteresis loop depends mainly on three parameters: the laser detuning Δ , the cavity detuning δ , and the polariton linewidth (see equations 5.7). We can study the effect of these key parameters through simulation by scanning one parameter while keeping the other two fixed. The exciton-exciton interaction strength g_0 only act as a scaling parameter; changing its value only affects the range of excitation power of the hysteresis loop. The Rabi splitting Ω_0 is also a scaling parameter since it changes the Hopfield coefficients for a given absolute value of the cavity detuning.

Figure 5.3 presents simulated hysteresis loops as a function of (a) the laser detuning Δ , (b) exciton linewidth, and (c) cavity detuning. In each panel, the red curve corresponds to the same set of default parameters. First, in figure 5.3 (a) we see that the increase of laser detuning Δ pushes both thresholds to higher power while increasing the bistability width. This is in agreement with the criteria for the polariton blue shift at the onset of the upward and downward thresholds (equations 5.6a and 5.6c). Since the critical polariton blue shift depends on Δ , the larger the laser detuning, the more power will be needed to reach this critical value. The locking of the polariton mode to the laser will

also last longer, hence increasing the bistability width.

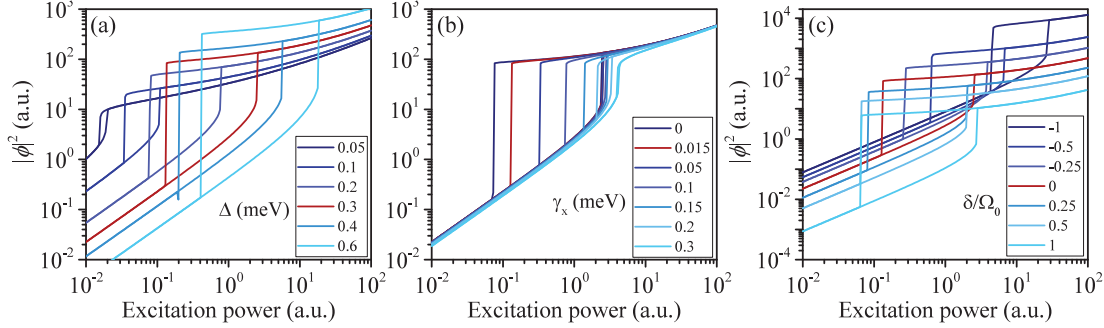


Figure 5.3 – Numerical simulations of polariton hysteresis loops using the GPE in the exciton-photon basis (equations 5.7) while varying (a) the laser detuning Δ , (b) the exciton linewidth γ_x and (c) the cavity detuning δ . In each panel, the red curve represents the same set of parameters namely $\Delta = 0.3$ meV, $\gamma_x = 15$ μ eV, and $\delta = 0$.

Next, we see from figure 5.3 (b) that increasing the exciton linewidth (which increases the polariton linewidth) has almost no effect on the upward threshold power P_{up} while the downward threshold power P_{down} is pushed to higher excitation power. This also reflects our basic interpretation of the polariton bistability; P_{up} is dominated by the repulsive interactions while P_{down} is sensitive to the losses.

Finally, figure 5.3 (c) shows that if the photonic fraction of the polariton mode changes from 85 % to 50 % ($-\Omega_0 < \delta < 0$ see section 1.4.1), both thresholds are pushed to lower values. This is caused by the increase of the interaction strength with the excitonic fraction. However, by changing the excitonic fraction from 50 % to 85 % ($0 < \delta < \Omega_0$ see section 1.4.1), the upward threshold goes back to slightly larger values. This is caused by the quasimode coupling of the laser field to the polariton mode. The more the polariton mode is excitonic, the less it couples to the excitation laser, which compensates for the increase of interaction strength. The optimal condition is found around $\delta = 0$ where the interaction strength is considerable and the thresholds are reached for lower excitation power.

5.1.3 From spin to spatial multistability

The idea behind the spatial multistability induced by cross interactions is closely linked to the polariton spin multistability. Specifically, the spinor multistability is achieved by rotating the polarization of the input laser on the Poincaré sphere to trigger the polariton-polariton spinor interactions in order to obtain a multistable pseudo-spin system [148]. Part of the effect is due to the asymmetry of the polariton trap. Because the mesas are slightly elliptical, the unpolarized ground state of a circular mesa is split into two linearly polarized states, oriented along its symmetry axes. We can represent the system using the

5.2. Experimental setup and sample characteristics

spinor GPE in the exciton-photon basis [158] which is a generalization of equations 5.7:

$$i\hbar\dot{\chi}_{\pm} = (\epsilon_x - i(\gamma_x + \beta|\chi_{\mp}|^2) + \alpha_1|\chi_+|^2 + \alpha_2|\chi_-|^2)\chi_{\pm} + \frac{\Omega_0}{2}\phi_{\pm}, \quad (5.8a)$$

$$i\hbar\dot{\phi}_{\pm} = (\epsilon_c - i\gamma_c)\phi_{\pm} + \frac{\Omega_0}{2}\chi_{\pm} + \frac{\epsilon_{lin}}{2}\phi_{\mp} + f_{ext}, \quad (5.8b)$$

$$\dot{n}_R = 2\beta|\chi_+|^2|\chi_-|^2 - \gamma_R n_R \quad (5.8c)$$

where the subscript \pm denote either σ_+ or σ_- polarized mean fields. The spinor exciton-exciton interaction strengths are denoted α_1 and α_2 for same and opposite spins (with $\alpha_2 \approx -0.1\alpha_1$). The term ϵ_{lin} simulates the linear splitting of the trap and the driving field can excite both branches depending on its degree of polarization. Equation 5.8c represents the loss due to biexciton formation and is added for completeness, although it is not needed for the present discussion. We see from this system of equations that at low density, the polariton eigenmodes are orthogonal and linearly polarized due to ϵ_{lin} . The basis turns to circularly polarized at large density because of the spinor interactions and the two independent modes interact with one another. Moreover, the population of both states will depend on the degree of polarization of the excitation laser. Then, the overall competition between the excitation laser polarization, spinor interactions and cavity anisotropy dictates the possible outcome of the multistability [152, 155, 158].

Having these considerations in mind, we can ask whether it is possible to generate a multistable system using many excited states of a mesa instead of its polarization-split ground state. If it is the case, do these polariton modes interact with one another, similarly to the spinor case. We will see in the rest of the chapter that indeed, cross interactions are not limited to spinor interactions, and that the resulting multistable system exhibits distinct spatial properties.

The mechanism can be seen as a generalization of the spinor multistability that is, a cross interaction of more than two independent polariton modes. At low density, the polarized polariton states are orthogonal as a consequence of in-plane momentum conservation of the exciton-photon interaction [46, 53]. At high enough density, these polaritons start to interact due to the spin dependence of the exciton-exciton interactions. For our circular traps, the confined polariton modes are initially orthogonal due to the orthogonality of the photon modes [46, 159]; however, they evolve with increasing density since they originate from the same exciton state.

5.2 Experimental setup and sample characteristics

5.2.1 Setup

A scheme of the experimental setup used for this study is presented in figure 5.4. The setup allows for both resonant and non-resonant excitation, independently or simultaenously

(see chapter 6). A standard HeNe laser is used for non-resonant excitation in reflection geometry. The microscope objective MO of NA=0.5 is used for both the non-resonant excitation and collection and the sample is kept at ~ 4 K in a helium flow cryostat. The emitted or transmitted signal can either be sent to a simple CCD (with its own focusing lens, not depicted here) to image the surface of the sample or to a spectrometer and CCD. The set of lenses L_2 to L_5 is used to either image the real space or k-space simply by removing or keeping L_4 ($f_4 = 30$ cm). When L_4 is placed, all focal points of adjacent lenses coincide in order to propagate the k-space image. The first two lenses have the same focal length of $f_{2,3} = 10$ cm, and propagate the collimated beam while L_5 of focal length $f_5 = 25$ cm focuses the image on the slits of the spectrometer. The focal length of L_5 is chosen in order to create a large spot onto the entrance slits. This allows to perform an energy resolved tomography by translating the focusing lens L_5 with a motorized stage in front of the spectrometer. With this procedure, we can recover the full spatial or dispersion profile of the polariton. Finally, the 1 m spectrometer is equipped with a 600 grooves per mm grating and a CCD with $26 \mu\text{m}$ pixels, which, combined with the spot size at the entrance gives a measured resolution of $70 \mu\text{eV}$.

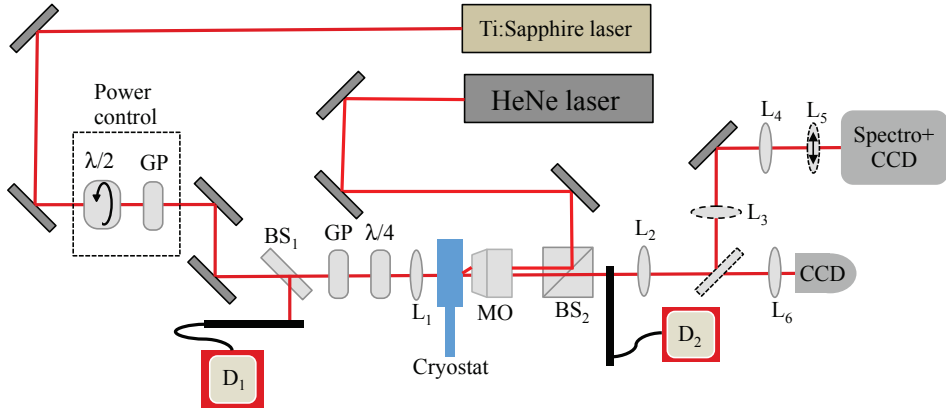


Figure 5.4 – Scheme of the experimental setup for bistability experiments. GP are Glan polarizers, BS are beam splitters, L_i are lenses, MO is a microscope objective and D_i are power meters.

For the resonant excitation we use a tunable single mode cw-Ti:Sapphire laser (Spectra-physics Matisse pumped with a 5 W Millennia laser). The laser is stabilized in frequency and has a narrow linewidth of 10 MHz (~ 40 neV) and amplitude noise of 1.5 % rms. The amplitude stability is particularly important for bistability measurements since it directly affects the measured threshold powers and bistability width [156]. The input power is controlled by a $\lambda/2$ wave plate mounted on a motorized rotational stage placed in front of a Glan polarizer (GP). This allows to vary the power over four orders of magnitude. The range over which the sweep is performed can be adjusted with a variable neutral density filter placed on the optical path. The laser beam then passes through a 90:10 pellicle beam splitter (BS_1) to measure the power with a Thorlabs Si photodiode power meter D_1 . A combination of Glan polarizer and $\lambda/4$ wave plate on a rotational stage

5.2. Experimental setup and sample characteristics

allows to prepare the beam in any polarization state. It is placed just before the sample to avoid any dephasing due to reflection. Of course, both polarizers are aligned with the same axis to maximize the signal. The beam is focused on the sample with the lens L_1 of focal length $f_1 = 5$ cm creating an excitation spot size of $\phi \approx 30 \mu\text{m}$. The transmitted beam is collected by the same microscope objective MO.

To obtain the hysteresis curve, a Thorlabs power meter D_2 is placed directly at the output. The rotation of the $\lambda/2$ wave plate as well as the two power meters are controlled through a labview program that records the input and output powers as it is cycled with the wave plate. This method is somewhat slow (few minutes per hysteresis loop) but it allows to measure the signal over many orders of magnitude which is important in our studies. A previous version of the setup used electro-optic modulators (EOM) to control the input power and photodiodes to measure the signal [160]. It allowed to perform the measurement by sending a 1kHz sine wave into the EOM and do statistics over many hysteresis curves. However, the photodiode used had a limited dynamical range; in many cases the lower branch of the loop corresponded to the detection noise whereas the photodiode was saturated above the threshold. The slower method was preferred in order to measure the real intensity dynamics of the hysteresis loop.

5.2.2 Mesa sample

The sample used in this study is the famous *1485* sample that was grown by F. Morier-Genoud and processed by O. El Daïf back in 2004 [22]. It was grown by molecular beam epitaxy (MBE) and consists of a 21 (22) top (bottom) GaAs/AlAs distributed Bragg reflectors (DBR) λ microcavity with a single $\text{In}_{0.04}\text{Ga}_{0.96}\text{As}$ QW placed at the antinode of the electromagnetic field inside the cavity spacer with a vacuum Rabi splitting of $\Omega_0 = 3.5$ meV. The spacer has been chemically etched before the overgrowth of the top DBR to create circular mesas of 6 nm in height and 3 to 20 μm in diameter that acts as a confinement potential (9 meV) for light [161]. The resulting number of cavity modes for a specific mesa depends on its diameter and defines the number of confined polariton modes (one lower and one upper branch for each cavity mode, see section 5.5). In the present study, we use a mesa of 9 μm in diameter where the fundamental cavity mode has a detuning of $\delta = -0.73$ meV with respect to the exciton state (1.4845 eV) and a corresponding polariton ground state excitonic fraction of $|X|^2 = 0.40$. The measured linewidth of this mode is $\text{FWHM} = 115 \mu\text{eV}$ corresponding to a Q -factor of about 13000. The energy, excitonic fraction and respective cavity detuning for the excited polariton states are given in table 5.1.

The spatial distribution of these confined states can be visualized via non-resonant PL either by energy resolving a slice of the spatial profile as shown in figure 5.5 (a), or by performing a full tomography of the states, as explained above. With this procedure, we image the polariton ground state (labeled E_1) in figure 5.5 (b) and the first five excited

Chapter 5. Spatial multistability and cross interactions

Table 5.1 – Energy, cavity detuning δ and excitonic fraction $|X|^2$ of the first five polariton states of the studied $9\ \mu\text{m}$ mesa. $\Delta E_{LP} = E_i - E_1$ is the polariton energy relative to the energy E_1 of the ground state. The cavity detuning for the i th polariton state is defined as $\delta = E_{ci} - E_x$ where E_{ci} is the energy of the i th cavity mode and E_x the exciton energy.

E_i	Energy (eV)	ΔE_{LP} (meV)	δ (meV)	$ X ^2$
1	1.48235	0.00	-0.73	0.40
2	1.48248	0.13	-0.50	0.43
3	1.48260	0.25	-0.29	0.46
4	1.48284	0.50	0.18	0.53
5	1.48297	0.60	0.47	0.57

states in figures 5.5 (c)-(g) (labeled E_2 to E_6). Since the trap is elliptical, the full circular symmetry is broken, which lifts the degeneracy of the states of angular quantum number m for a given radial quantum number n [46, 162]. Hence, the first two excited states E_2 and E_3 correspond to the $(n = 1, m = 1)$ doublet (figures 5.5(c),(d)) and the excited state E_4 in figure 5.5 (e) corresponds to a superposition of the even and odd solutions of the $(n = 2, m = 2)$ state, the energy splitting of which is less than our spectral resolution [162].

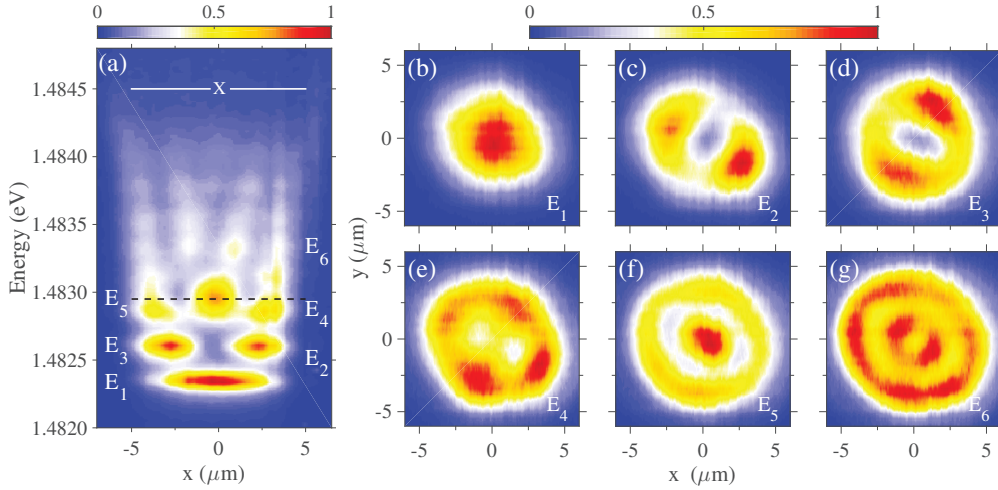


Figure 5.5 – (a) PL intensity as function of energy and position for a $9\ \mu\text{m}$ mesa under non-resonant excitation. The black dashed line indicates the energy position of the excitation laser for the multistability experiment and the x marked white line is the position of the bare exciton. (b)-(g) Spatial profile of the first six confined states starting from the ground state labeled E_1 to E_6 . All intensities are normalized and shown in linear color scale. The first excited state E_2 in (c) is hidden in (a) due to the position of the slit cutting the spatial profile.

5.3 Spatial multistability experiment

As discussed above, the goal is to excite resonantly a series of confined polariton modes, and perform the standard experimental procedure to observe the polariton bistability. In order to observe the spatial multistability, the energy spacing between the polariton modes should not be too large, otherwise polariton lasing might switch on when increasing the input power before the multistability occurs. This was observed in 3 μm mesa [163] and is a consequence of efficient phonon scattering in the mesa [164] and the onset of bosonic stimulation when the occupation of the ground state reaches the critical density. For this reason the experiments are performed on a 9 μm mesa instead of a 3 μm one. The large excitation spot size assure that the mesa is pumped uniformly.

To demonstrate the effect, we excite resonantly the fifth polariton state (E_5 situated at around 1.48297 eV, see figure 5.5 (a)), well below the fundamental cavity mode (situated at 1.48378 eV) to maintain the strong coupling regime at high densities. This state is chosen because its large component at $k = 0$ allows for an efficient pumping of the system and its detuning allows to observe the non-linearity of the polariton ground state before reaching our maximum excitation power.

Figure 5.6 presents the multi-hysteresis cycle resulting from the excitation scheme explained above while detecting with the power meter (spatially integrating the signal). As the excitation power is increasing (following the red arrows), we measure three distinct upward jumps of the transmitted intensity, whereas four downward jumps are observed when the power is decreasing (blue arrows). A small non-linearity is also visible on the way up at around 4 mW. To highlight the spatial multistability, we present the spatial transverse profiles of the transmitted signal at the energy of the laser for selected power positions as indicated by the black arrows in figure 5.6. By comparing these profiles with the ones measured non resonantly, we clearly recognize that each stable state on the multi-hysteresis corresponds to one of the excited states of the mesa, starting with the fifth excited state (see figure 5.5 (f)) at low excitation power, and shifting down to the ground state at maximum power. The states are scanned back in opposite order from the ground state to the fifth excited state when the power is decreased. The spatial profile of the beam is therefore determined by the lateral confinement of the optical modes; this mechanism differs from the one based on spontaneous pattern formation due to transverse instability in resonantly pumped planar microcavity, which was recently proposed [165, 166]. Although the ordering in energy is respected, not all of the states appear when we increase or decrease the excitation power. On the way up, we are able to differentiate the odd from the even ($n = 2, m = 2$) four-lobe states originating from E_4 ; however, a single ($n = 1, m = 1$) two-lobe state appears. The opposite is observed on the way down: both ($n = 1, m = 1$) states are scanned (states E_2 and E_3) but a single state appears for ($n = 2, m = 2$). Finally, we observe that, whenever two steady states are allowed for a given excitation power, they have distinct spatial profiles: this demonstrates the spatial character of the multistability. Simply put, we can switch the

transverse profile of the laser beam when transmitted through the mesa by only varying the power, while keeping the wavelength fixed.

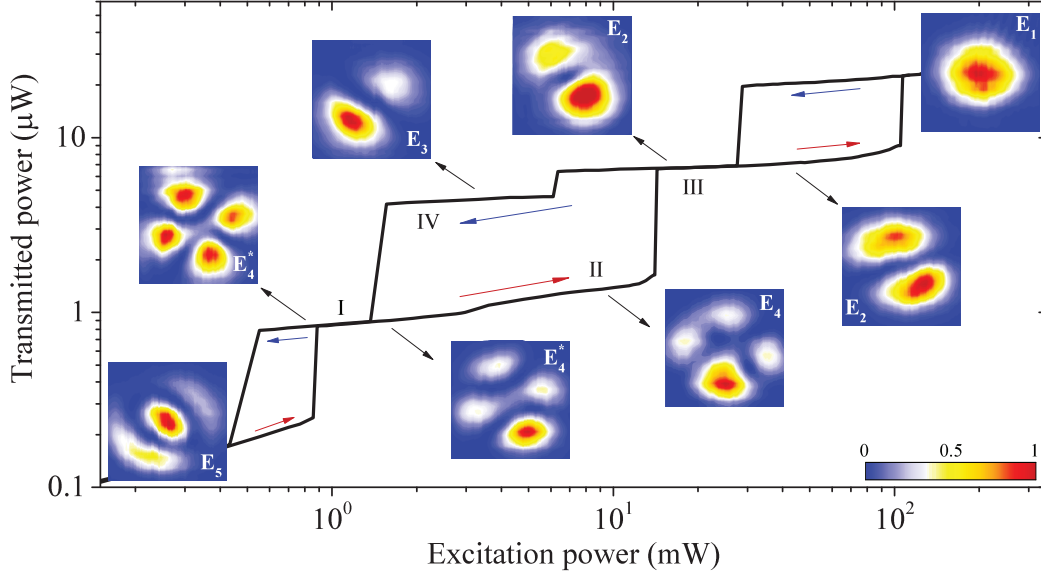


Figure 5.6 – Spatial multistability measured on a $9\ \mu\text{m}$ mesa. The black curve shows the multi-hysteresis cycle when we integrate spatially the transmitted signal. The red (blue) arrows indicate the path taken when increasing (decreasing) the excitation power. Each color map represents the spatial profile measured at the energy of the laser for the specific power indicated by the black arrows. Each image corresponds to a $10 \times 10\ \mu\text{m}$ square and the intensity is normalized from zero to one and shown in linear color scale. The roman numerals indicate regions on the curve, where the transmitted light was spectrally resolved and displayed in figure 5.8.

Additional features are also present on this multistability curve. First, apart from the three upward thresholds, we observe a smoother non-linearity on the E_4 four-lobes state at around 4 mW, right after the first upward threshold. As opposed to the other thresholds, no bistability is observed when ramping the power up and down this non-linearity (not shown), but we do measure a change of the spatial profile between the odd and even solution of the $(n = 2, m = 2)$. Second, when comparing the transverse profile of the E_2 state before the last upward threshold and after the first downward threshold, we notice a slight rotation of the symmetry axis as we approach the upward threshold. A rotation of the spatial pattern was shown to occur through coherent control by imprinting the phase of the input beam [167]. In our case, the observed phenomena originates from the cross interactions between polaritons in different modes, as explained in section 5.5. Near the upward threshold, a state that has almost blue shifted up to the laser may induce a slight rotation of the spatial profile, hence it affects the phase relation it has with the excitation laser.

We can perform a complementary multi-hysteresis cycle when starting from the point IV

5.4. Evidence for polariton-polariton cross-interactions

in figure 5.6 instead of the lowest excitation power. Figure 5.7 present the multi-hysteresis cycle obtained in this case, starting on the state E_3 up to E_1 , and going back to E_4^* . This procedure highlights that the transition between state E_2 and E_3 is bistable, with a bistability width of only 1 mW. The energy spacing between the two states explains why we observe a bistable behavior here and not between E_4^* and E_4 .

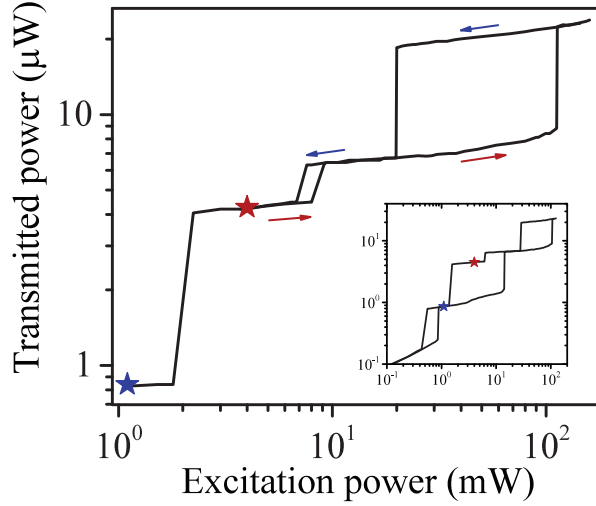


Figure 5.7 – Multi-hysteresis cycle obtained when initializing the system on the second multistable branch (state E_3) and going down to the state E_4^* . The red (blue) arrows indicate the path taken when increasing (decreasing) the excitation power. The red (blue) stars show the starting (finishing) points of the cycle. The inset shows the complete loop as in figure 5.6.

5.4 Evidence for polariton-polariton cross-interactions

Based on our derivation of polariton-polariton interaction done in section 1.5, we understand that the spatial multistability must depend on the evolution of the polariton density within each mode. The question now is to understand how the polariton-polariton interactions occur in a multimode system and whether polaritons in different modes interact. When we excite a single polariton mode, it blue shifts until it is locked to the resonant laser, then it unlocks to create the bistable loop. With the same reasoning, we can expect that, if the system is driven by a laser blue detuned with respect to N polariton modes without cross interactions, then we should observe the superposition of N independent bistable loops, with each polariton mode getting locked to the laser once their energy equals that of the laser. Since each polariton mode has a particular spatial profile, the spatial profile of the transmitted laser at each stable branch on the multistability will be the sum of the profiles of each of the states locked to the laser at that excitation power. However, if repulsive cross interaction exists between the confined

polariton modes, then, when a polariton mode blue shifts up to the laser energy, it should unlock the former state from the laser. Having a single polariton mode locked to the laser on each stable branch of the multistability will result in the spatial multistability.

Therefore, the existence of the polariton spatial multistability is a consequence of cross interactions. To further confirm this point, we performed direct measurement of the polariton energy shifts along different parts of the full multi-hysteresis cycle (see roman numerals in figure 5.6) for a given slice in the x direction of the spatial profile (defined by the slit of the spectrometer). For example, figure 5.8(a) presents the spectral evolution when the excitation power is increased starting after the first threshold upward (I), passing the small non-linearity (II), and crossing the second upward threshold to reach region (III). Figure 5.8(b) shows the same measurement while decreasing the excitation power, passing by region (IV) back to (I). The dominant intensity is always at the energy of the excitation laser, and the white dashed lines indicates the thresholds that are found in figure 5.6. In all these PL spectra, one clearly identifies at least one mode much weaker in intensity (two orders of magnitude) and below the laser energy; moreover, at each threshold on the multistability curve, we observe an energy jump of each of these lower energy states. If we perform a tomography of the lowest energy state on either side of the thresholds up or down (not shown), we find that its transverse profile always corresponds to that of the ground state, while the spatial profile of the transmitted laser changes according to figure 5.6.

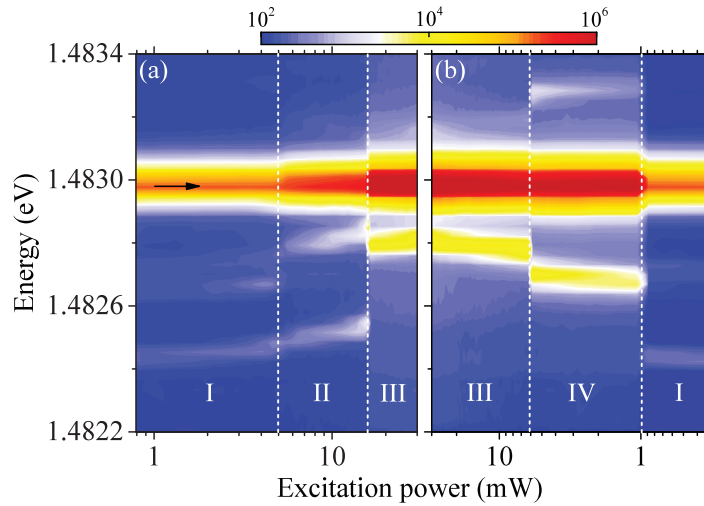


Figure 5.8 – PL intensity maps measured in transmission as function of the excitation power. (a) Spectra acquired while increasing power for regions I, II and III in figure 5.6 and (b) following regions III, IV and back to I for decreasing power. The black arrow indicates the energy position of the excitation laser. The lower intensity lines at a lower energy correspond to states that have not reached the laser whereas the ones at higher energy are states expelled from the resonance. The dashed white lines indicate the position of the upper (a) and lower (b) thresholds in figure 5.6.

5.4. Evidence for polariton-polariton cross-interactions

Two mechanisms involved in the multistability are evidenced with these measurements. First, when analyzing the upward thresholds, we see that due to polariton-polariton self interaction, the polariton state closest in energy to the laser blue shifts up to the laser energy, where a sharp increase in population occurs (as for polariton bistability). A drastic switching of the mode profile occurs at this point. Second, when this threshold occurs, all the lower energy states experience a sudden blue shift, indicating a cross interaction with the population of the state resonant with the laser. The reverse mechanism is responsible for the sudden red shifts when the excitation power is decreased and one of the state suddenly unlocks from the laser. Even though the non-linearity measured on the multistability at 4 mW in figure 5.6 is weak, we clearly observe an energy jump, which confirms the measured switching of the modes. Finally, the slight variation of the threshold positions measured in PL compared to figure 5.6 is caused by the sensitivity of the experiment to intrinsic noise, especially close to the thresholds. Since we need a longer integration time to acquire the spectra compared to the spatially integrated measurements with the power meter (instantaneous value), we increase the probability of the system to undergo a noise-induced jump [156].

We are able to identify not only polariton states below the laser, but as seen between the two thresholds in figure 5.8 (b), we are able to observe polariton modes above the energy of the laser. In order to follow what happens to an upper state once a lower state's spatial profile becomes dominant, we excite the sample in linear polarization and detect in cross polarization. In that situation, the overall behavior of the spatial multistability is unchanged, and allows to filter out the dominant intensity from the state at the excitation laser energy (by about four orders of magnitude) and to look for weak signals from the other states. Figures 5.9 (a) and (c) present PL intensity maps for low and maximum excitation power, respectively, and for a given slice in the x direction of the spatial profile. In both cases, we clearly identify a series of polariton states either below the excitation laser energy (the highest intensity on the maps) for low power or above it for high excitation power. In order to confirm the nature of these states, we show the transverse spatial profiles for each of them, as indicated by the roman numerals in figures 5.9 (b) and 5.9 (d) for low and high excitation power. Notice that in both cases, the energy ordering of these states is conserved independently from their relative position with respect to the excitation laser and corresponds to the energy levels measured non resonantly as shown in figure 5.5.

With these results, we can easily understand how the modes evolve during the spatial multistability. Whenever a polariton mode is blue shifted at the energy of the laser, we measure a sharp increase of the transmitted intensity accompanied by a switching of the transverse profile and correlated blue shifts for the other energy states. When a state is pulled by the laser and gets locked, it expels the previous mode above the laser energy. As explained below, the repulsive cross interactions between the polariton modes prevent them from crossing each other; therefore, we observe the same ordering of the modes in energy at any excitation power.

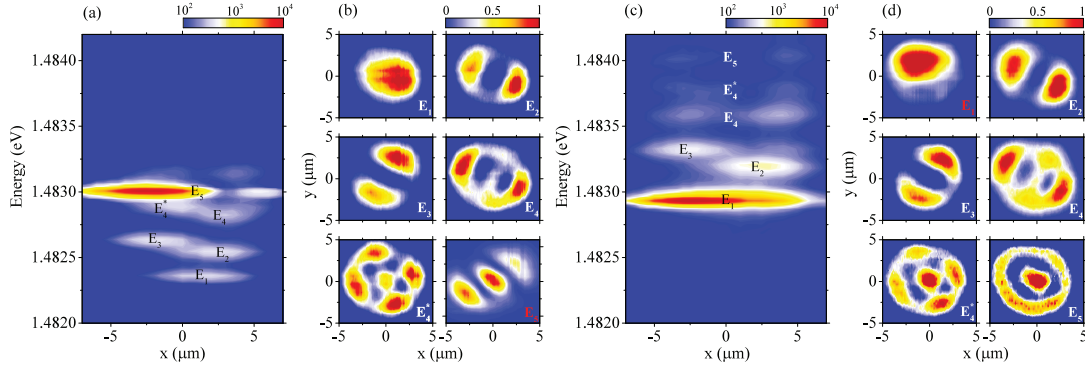


Figure 5.9 – (a) PL intensity as a function of position and energy for low excitation power (bottom of the multistability curve) for a given slice in the x direction of the spatial profile. (b) Tomography for each state as indicated by the labels E_i (a). (c) and (d) are the same as (a) and (b) but for maximum excitation power (top of the multistability curve). For (a) and (c) the color map is in log scale whereas for (b) and (d) the intensities are normalised and shown in linear color scale. The labels E_i in red indicate the tomography at the energy of the laser. For each panel, the excitation laser is linearly polarized and the detection is done in cross polarization.

5.5 Numerical study of cross interactions and discussion

The rich physics of microcavity polaritons builds upon exciton-exciton interactions. Numerous examples of these interactions have been studied, ranging from polariton condensates interacting with an exciton reservoir in non-resonant excitation experiments [113, 125, 168–171] to spinor interactions in resonant [17, 172–176] or non-resonant excitation [13, 177]. They are, however, different in nature from the spinor effects induced by the effective magnetic field caused by TE-TM splitting of the microcavity mode [178–180] or by the birefringence field induced by disorder [11, 181]. In all these studies, the interaction is essentially between two *modes* or components that can be either the condensate with a reservoir or interaction with opposite spins for the spinor case. Such interactions have been analyzed through the Gross-Pitaevskii formalism at the mean field level. In view of the success of these approaches to study polariton-polariton interactions, we derive a similar approach based on a set of coupled differential equations, which takes into account interactions between N modes. Since each polariton mode has its own cavity detuning, it has a specific excitonic fraction (see Table 5.1) and an energy blue shift of its own. As a consequence, a set of coupled equations in the polariton basis will not fully take into account the polariton-polariton interactions as a function the excitation power and also the pumping efficiency (which varies according to the photonic fraction); it would need to be solved iteratively. All of this can be avoided by describing the system in the exciton-photon basis, which directly renormalizes the components of the polariton modes as a function of the excitation power.

5.5. Numerical study of cross interactions and discussion

To derive the multimode mean field coupled equation system, we start with the exciton-photon Hamiltonian presented in section 1.5, equation 1.41 [54–56]:

$$\begin{aligned}
 H = & \int d\mathbf{r} \left[\hat{\psi}_x^\dagger \left(E_x - \frac{\hbar^2 \nabla^2}{2m_x} \right) \hat{\psi}_x \right. \\
 & + \hat{\psi}_c^\dagger \left(E_c - \frac{\hbar^2 \nabla^2}{2m_c} \right) \hat{\psi}_c + \frac{\Omega}{2} \left(\hat{\psi}_x^\dagger \hat{\psi}_c + \hat{\psi}_x \hat{\psi}_c^\dagger \right) \\
 & \left. + \frac{g_0}{2} \hat{\psi}_x^\dagger \hat{\psi}_x^\dagger \hat{\psi}_x \hat{\psi}_x \right], \tag{5.9}
 \end{aligned}$$

where $\hat{\psi}_x^\dagger$ and $\hat{\psi}_c^\dagger$ are exciton and cavity photon creation field operators. The Hamiltonian can be decomposed into four parts: the first two are the kinetic terms for the exciton and photon, the third is the light-matter interaction, and the last is the exciton-exciton interaction. For simplicity, we do not consider the effect of quasimode coupling nor the saturation of the exciton oscillator strength [5] as it is done in the EBE (see section 1.5). This will be the topic of the next chapter. We also assume circular symmetry of the system, which allows us to expand the photon operator in modes corresponding to solutions of Maxwell equations for a circular trap, namely Bessel functions of first kind and order m :

$$\hat{\psi}_c = \sum_{n,m} c_{n,m} J_m(\kappa_{n,m} r) e^{im\phi} \hat{b}_{n,m}, \tag{5.10}$$

where $\kappa_{n,m}$ is fixed by the boundary conditions of the mesa and gives the energy of the confined photon states. The symmetry of the system implies the conservation of the angular quantum number in the light-matter coupling [46] indicating that we should describe the exciton field operator using the same expansion in Bessel functions for the center of mass part of the exciton wave function as [46, 55, 159]:

$$\hat{\psi}_x = \sum_{\{\nu,m\}} c_{\nu,m} e^{im\phi} J_m(k_{\nu,m} r) \hat{x}_{\nu,m}, \tag{5.11}$$

where the $J_m(k_{\nu,m} r)$'s are again Bessel functions of first kind and order m , $k_{\nu,m}$ is an exciton eigen-momentum, $\hat{x}_{\nu,m}$ is the annihilation operator for an exciton with angular quantum number m , and the sum is over sets of $\{\nu, m\}$ indices, which are determined by the boundary conditions. The index ν has a similar meaning as the radial quantum number for the photon as it sets the condition on the exciton momenta $k_{\nu,m}$ through the boundary condition of the system [159]. Nevertheless, the exciton motion is not affected by the mesa, and the boundary conditions are then defined by the quantization area chosen for the computation [46]. As a result, the exciton energy is barely affected and assumed to be single-valued, which is consistent with the usual flat exciton dispersion

measured in microcavities. Using Eq. (5.11), we can rewrite the light-matter Hamiltonian to properly consider the strong coupling between an exciton and a photon of the same angular quantum number. In principle, the breaking of k symmetry in the mesa allows for light-matter coupling between an exciton in any state n and a photon in any state n' with the same m [46, 159]. Such a coupling would create numerous polariton modes for which a single exciton state couples with photons of various spatial profiles, resulting in an in-plane polariton distribution composed of all of them (weighted by their respective photon fraction). Since this type of coupling is not realized experimentally, we therefore use a single index i to identify each allowed pair of quantum numbers (n, m) to an exciton or a photon state. Furthermore, to simplify the calculation, we do not compute the full spatial evolution of the system and assume that for each mode i , there is a corresponding spatial profile. Finally, we can rewrite the system Hamiltonian accounting for the existence of multiple confined cavity modes:

$$H = \sum_i E_{xi} \hat{x}_i^\dagger \hat{x}_i + \sum_i E_{ci} \hat{b}_i^\dagger \hat{b}_i + \frac{1}{2} \sum_i \Omega_i \left(\hat{x}_i^\dagger \hat{b}_i + \hat{x}_i \hat{b}_i^\dagger \right) + \frac{1}{2} \sum_{i,j,k,l} g_{ijkl} \hat{x}_i^\dagger \hat{x}_j^\dagger \hat{x}_k \hat{x}_l, \quad (5.12)$$

where \hat{b}_i^\dagger is the creation operator for a cavity photon in mode i , E_{ci} is its associated energy, and E_{xi} is the energy of the exciton of state i . The coupling constant between the i th exciton and photon modes Ω_i depends on the oscillator strength of the exciton as well as on the spatial overlap between the exciton and the photon. For the case of perfectly circular 9 μm mesas, the change of Ω_i and E_{xi} between the different modes is negligibly small, and therefore we may safely assume that they are constant. Following the same approach as in Ref. [56], it can be shown that only the terms conserving the number of particles in the initial and final states are important if we limit ourselves to first order perturbation theory. Therefore, the summation over four indices in Eq. (5.12) is replaced by a summation over two, such that $g_{ijkl} \rightarrow g_{ij}$ and $\hat{x}_i^\dagger \hat{x}_j^\dagger \hat{x}_k \hat{x}_l \rightarrow \hat{x}_i^\dagger \hat{x}_j^\dagger \hat{x}_i \hat{x}_j$. Then, using Heisenberg's equation we derive the equation of motion for each exciton and photon operator. We Follow the usual mean field approximation and extend our set of approximations done in section 1.5 to the multimode case [58, 59]:

$$\langle \hat{x}_i^\dagger \hat{x}_i \hat{x}_j \rangle \cong \langle \hat{x}_i^\dagger \hat{x}_i \rangle \langle \hat{x}_j \rangle, \forall (i, j), \quad (5.13)$$

$$\langle \hat{x}_i^\dagger \hat{x}_i^\dagger \rangle = \langle \hat{x}_j \hat{x}_j \rangle = 0, \forall (i, j). \quad (5.14)$$

These approximations give rise to a set of coupled differential equations (see appendix A

for a more detailed derivation):

$$\begin{aligned} i\hbar\dot{\chi}_i &= (E_x - i\gamma_x + \sum_j g_{ij}|\chi_j|^2)\chi_i + \frac{\Omega_i}{2}\phi_i \\ i\hbar\dot{\phi}_i &= (E_{ci} - i\gamma_{ci})\phi_i + \frac{\Omega_i}{2}\chi_i + f_{ext}, \end{aligned} \quad (5.15)$$

were $\chi_i = \langle \hat{x}_i \rangle$ and $\phi_i = \langle \hat{b}_i \rangle$ are the i th exciton polarization and photon mean field respectively and $\gamma_x(\gamma_{ci})$ is their respective homogeneous linewidth. For a perfectly circular mesa, the exciton-exciton interaction terms are:

$$g_{ij} = 2^\alpha g_0 \int d\mathbf{r} |c_i|^2 |c_j|^2 |J_i(kr)|^2 |J_j(kr)|^2, \quad (5.16)$$

and $\alpha = 0$ if $i = j$ and $\alpha = 1$ if $i \neq j$. Since the mesa studied here is slightly elliptical, we instead consider the g_{ij} as fitting parameters. Finally, the external driving field of energy E_l which pumps each photon mode is defined by equation 5.2. Equations 5.15 can be understood as a multimode generalization of the Gross-Pitaevskii equation in the exciton-photon basis [158].¹ These equations include the usual population exciton-exciton self interaction terms g_{ii} but also cross interaction terms g_{ij} that couple the exciton polarization of state i with the population of state j . These terms are the ones responsible for the correlated blue shifts at each threshold as shown in figure 5.8. Note that a similar set of equations can also be obtained in the case of an exciton state coupled to a single photon mode when two pumping beams are used at different energies [143] or in the case of a polariton double well system [182], even if the cross interaction terms were neglected in the latter case due to the specific geometry of the system.

The result of the simulation is shown in figure 5.10 (a), where the sum of all photon field intensities $|\phi_i|^2$ is plotted as a function of the excitation power. For the simulation, we consider the five cavity modes associated with the polariton modes measured non resonantly (see Table 5.1), meaning that one of the $(n = 2, m = 2)$ four-lobe states is not included. The laser energy is at the energy of the fifth state E_5 . We see a very nice agreement when comparing the simulation with the measured multistability in figure 5.6 (a), which is reproduced in the inset of figure 5.10 (a). For the same range of excitation power, the simulation shows a higher photon intensity compared to the experimental data. We will see in the next chapter that the lower amplitude of the transmitted signal can be explained by including excitation induced dephasing.

In order to limit the number of free parameters in the simulation, we assumed that the g_{ii} 's were different from one another and that the first off diagonal terms $g_{ij=i+1}$'s were identical such that $g_{12} = g_{23} = g_{34} = g_{45}$ and $g_{ij} = g_{ji}$. All other g_{ij} 's are fixed to a

¹We do not include the spin in these equations as it is done in Ref. [158]. Although straight forward to include, this would double the number of interaction constants. We would also need to double the number of photon modes as the breaking of circular symmetry in real mesas lead to linearly polarized cavity modes.

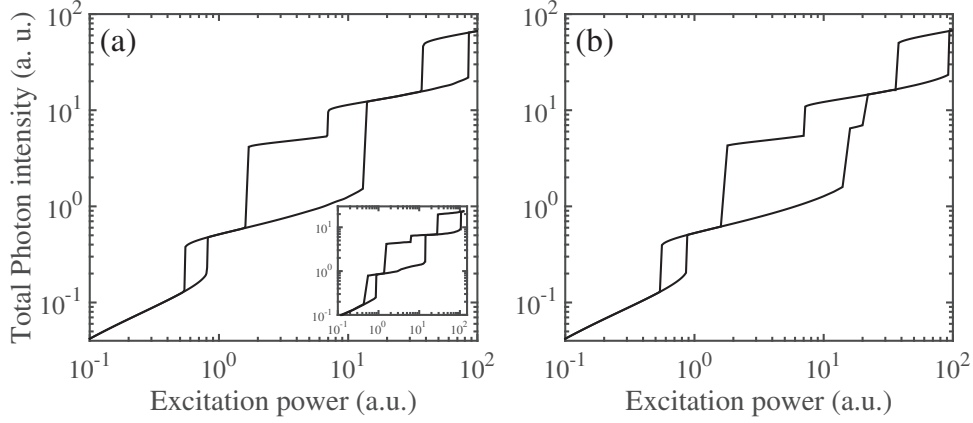


Figure 5.10 – (a) Simulation of the multi-hysteresis cycle. The inset shows the experimental data as presented in figure 5.6 for comparison. (b) Simulated multi-hysteresis cycle when the parameter g_{12} is decreased from $0.14g_0$ to $0.1g_0$.

single value because the accuracy of the simulation in that case did not allow to justify otherwise. Finally, we allowed for a slight variation of the cavity mode linewidths to adjust the positions of the lower thresholds, as they are most sensitive to this value (see section 5.1.2). The values of the parameters used for the simulation are given in Table 5.2. The unequal number of thresholds for increasing and decreasing power can only be reproduced with $g_{12} \neq 0$. In fact, if we decrease its value by about 30 % (from $0.14 g_0$ to $0.10 g_0$), the second threshold is split back into two, as shown in figure 5.10 (b). This is a clear indication that, although the polariton modes are initially independent (only a single exciton mode for a single photon mode), the polaritons in different modes interact together through the exciton-exciton interaction. The small size of the first hysteresis loop compared to the other two is the result of the small laser detuning which barely satisfies the criteria for bistability ($\Delta_{laser} > \sqrt{3}\gamma_{c3}$).

Table 5.2 – Values of the interaction constants g_{ij} and of the homogeneous linewidths for the five cavity and exciton modes used for the simulation. The g_{ij} are given in units of the scaling parameter $g_0 = 3.8 \cdot 10^{-4}$ meV/density, where the density is fixed to one.

Interaction constants g_{ij} (g_0)		linewidths (μeV)	
g_{11}	0.355	γ_{c1}	55
g_{22}	0.629	γ_{c2}	55
g_{33}	0.629	γ_{c3}	32
g_{44}	1.000	γ_{c4}	65
g_{55}	1.000	γ_{c5}	65
g_{12}	0.140	γ_x	20
g_{13}	0.100	—	—

Figure 5.11 shows the individual mode intensities as a function of the excitation power in order to understand which of the photon modes dominates in the multistability. Each curve is offset by a multiplication constant (given in the figure) to better visualize the simulation, even though it hides their relative intensities. To circumvent this visual inaccuracy, we highlight in red (blue) on each curve the state of highest intensity at each increasing (decreasing) power value. Then, adding all the red and blue fragments separately reproduces the multistability curve in figure 5.10 (a). In this way, we highlight that at each threshold, the dominant mode alternates, keeping an order that is given by the energy ordering at low power, which reproduces well our findings.

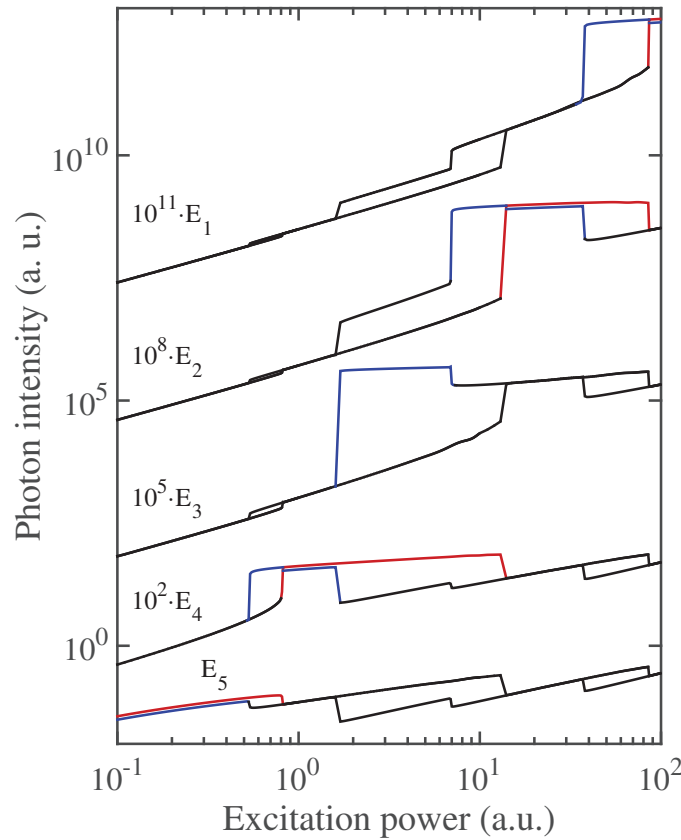


Figure 5.11 – Calculated multi-hysteresis curve for each of the five cavity photon modes included in the simulation. E_1 is the cavity mode associated to the polariton ground state. Each curve has been shifted by a fixed multiplication factor given in the figure. The red (blue) parts highlighted on each curve indicates the state of highest intensity for increasing (decreasing) excitation power. Adding each red and blue fragment gives the final curve plotted in (a).

From this figure, the influence of the cross interactions can easily be seen as, each time one of the modes becomes dominant, all the other modes jump as well. If the mode energy is below the dominant one, then its intensity increases and remains below the

dominant intensity. If the mode was previously locked to the laser, then its intensity drops. This explains why we measure a single transverse profile at the energy of the laser and why the other polariton modes are orders of magnitude weaker in intensity as shown in figure 5.8. By considering equations 5.15, we conclude that any abrupt jump in photon mode intensity will cause a jump in exciton population resulting in a jump in energy as observed in figure 5.8. Finally, the simulation clearly shows that both E_2 and E_3 jump at the second upper threshold and that E_2 becomes the dominant one, as observed in the experiment. In the simulation, the exciton-exciton self interaction terms are equal ($g_{22} = g_{33}$), which implies that the only way for the two states to have their upward threshold at the same power is through the cross interaction g_{23} ; for this specific simulation, it is equal to $0.22g_{22}$. Leaving g_{23} to zero would create distinct thresholds for E_2 and E_3 . The identical values of g_{22} and g_{33} are a direct consequence of the similar spatial profile of modes E_2 and E_3 since these modes originate from the same state ($n = 1, m = 1$).

Since the exact conversion of the input laser power to the photon density per mode is difficult to evaluate, the interaction constants are scaled with a parameter g_0 for an arbitrary density. It is worthwhile noting that at low power, the laser is resonant with the fifth polariton mode, and thus we do not get a separate bistable behavior due to its self interaction. Therefore, we used g_{44} as the scaling parameter and simply gave to g_{55} the same value. The numerical values for the g_{ij} should be interpreted as effective parameters since our model does not consider saturation effects that will decrease the coupling strength Ω_i and alter the excitonic fractions at high densities. We also neglect polariton-phonon scattering which leads to scattering between the different polariton modes and becomes efficient at high densities [163]. Nonetheless, the accuracy of the simulated predictions of the model does confirm that the main processes involved in the spatial multistability are the polariton-polariton self- and cross-interactions.

5.6 Conclusions

In this chapter, we have demonstrated the polariton spatial multistability by resonantly exciting a sample that exhibits a set of five polariton modes. We measured a series of thresholds of the transmitted intensity when we increased or decreased the excitation power, resulting in polariton multistability. Furthermore, each stable position along the multistability curve corresponded to a specific transverse spatial profile of the transmitted laser beam, which arose from the profile of the corresponding confined polariton mode. This behavior has an important implication: the transverse spatial profile of the transmitted laser beam can simply be varied by changing its input power.

In general, the polariton bistability is driven by the polariton-polariton self interactions mediated by the exciton; in these measurements, however, we have shown that cross interactions occur between the polariton modes and trigger the observed spatial multistability.

We confirmed this mechanism by tracking the spectral shift of the polariton modes below and above the excitation laser energy and by observing that the energy jumps of the modes is concomitant with the intensity jumps of the transmitted laser beam at each threshold.

Finally, all the main features of the observed multistability have been successfully simulated using a multimode version of the Gross-Pitaevskii equations in the exciton-photon basis. Our equations contain the non-linear effects of cross interactions among different modes in order to explain the energy blue shifts, the asymmetry in the upward and downward thresholds and the transmission of a laser beam, the profile of which switched between the polariton mode profiles. This formalism could be applied, in principle, to the study of multimode polariton-polariton interactions in a variety of confined exciton-polariton systems.

6 Probing reservoir induced dephasing with bistable polaritons

In this chapter, we continue our study of resonantly excited confined polaritons while focusing on what happens when the system deviates from the fully coherent picture. We have already seen some indication that the system is not fully coherent at large polariton densities. We will investigate these effects in greater detail both theoretically and experimentally.

In recent years, there has been an increasing number of proposals to use microcavity polaritons as a source of single photons [183, 184], entangled photons [185–189] as well as quantum computing devices [190–193]. On the one hand, the interest for using polaritons lies on their peculiar dispersion that weakens phonon scattering [48, 49, 194, 195] or their ability to overcome dephasing by increasing the number of particles in the condensate [190, 192]. On the other hand, early attempts to generate entangled photons through parametric scattering [196–198] indicate that dephasing does limit the correlations. Furthermore, a recent theory [144] predicts that, for resonantly pumped polariton condensates, phonon absorption can generate a significant exciton reservoir even at low temperatures. Efficient polariton relaxation between confined modes was also observed [163, 164]. Inevitably, the viability of these proposals depends on how robust polaritons are against any source of dephasing through the interaction with the environment.

Although the effect of reservoir repulsive interactions on polariton has been clearly demonstrated [113, 125, 168, 199], the reservoir-induced dephasing (RID) has usually been neglected. Earlier studies have demonstrated that reservoir density fluctuations affect the energy and linewidth of non-resonantly pumped polariton condensates [108, 200]. Recently, it was shown that dephasing may be increased under pulsed resonant excitation through the relaxation of upper polaritons that populates a reservoir [58, 201]. The effect of an incoherent reservoir and the biexciton formation was also suggested to explain the apparent repulsive interaction between polaritons of opposite spins [144, 158, 202] evidenced in polariton multistability [148].

We have seen in the previous chapter and through the work of previous PhD students of the

group [148, 151, 156] that the confined polariton system is ideal to investigate the polariton bistability. Particularly, its sensitivity to intensity noise was put forward [154–156]. The former study showed that a symmetrical collapse of the polariton hysteresis loop occurs for increasing noise strength on the polariton population. The intensity noise changes the laser power profile from a singled value to a Gaussian distribution. Hence, as the mean laser power gets closer to the bistability thresholds, the probability to jump increases due to this power distribution, which results in a narrower bistability width.

If we view polariton dephasing as high frequency noise, we may expect that it should be reflected in the variations of the bistability thresholds. Therefore, the aim of this chapter is to use the sensitivity of the polariton bistability as a tool to study polariton dephasing. We expect that the results presented on reservoir induced dephasing should manifest in different ways for a broader class of polariton systems. This chapter present an extended study on the work that has been published [29].

6.1 Experimental study of polariton bistability under dephasing

In this section we investigate the effect of dephasing experimentally by performing two sets of experiments. First, we study how the bistability evolves as a function of temperature. Second, we investigate how the bistability evolves when we excite resonantly and non-resonantly at the same time.

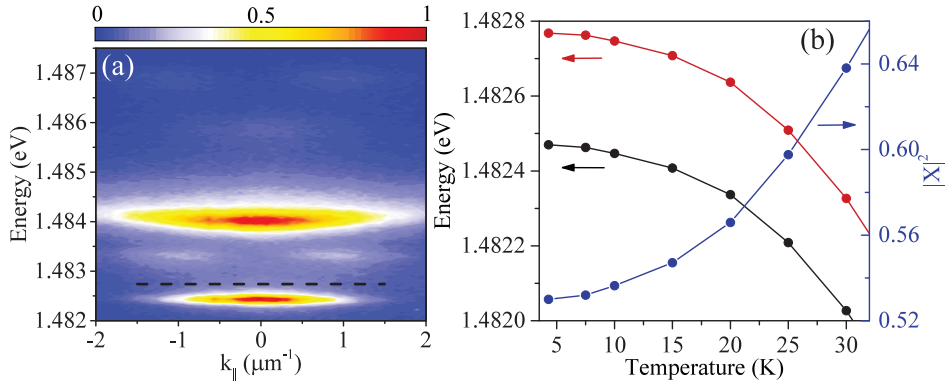


Figure 6.1 – (a) Photoluminescence of the 3 μm mesa as a function of in-plane wave vector and energy, measured at 4.3 K. The black dashed line indicates the resonant laser energy. (b) Polariton ground state energy (black) and corresponding excitonic fraction (blue) as a function of temperature. The resonant laser energy, shown in red, is kept at $\Delta = 300 \mu\text{eV}$ above the polariton energy.

We use the sample 1485 that was presented in section 5.2.2. We focus our attention on a 3 μm mesa to avoid the effect of cross-interactions. The mesa has a slightly positive cavity detuning of $\delta = 0.2 \text{ meV}$, and a Rabi splitting of $\Omega_0 = 2\Omega = 3.3 \text{ meV}$ (measured at

6.1. Experimental study of polariton bistability under dephasing

4.3 K, see figure 6.1 (a) and (b)). The polariton ground state is excited resonantly with a circularly polarized single mode cw Ti:sapphire laser, and the sample is maintained at low temperature in a helium flow cryostat. The setup used is the same one presented in section 5.2.1.

First, we perform bistability measurements as a function of temperature. Since the polariton mode energy red shifts with increasing temperature, the laser energy is adjusted at each temperature to maintain a constant laser detuning Δ . This fixes the blue shift needed to reach the nonlinear threshold while increasing the cavity detuning and excitonic fraction (see figure 6.1 (b)), hence it increases the polariton-polariton interactions. figure 6.2 (a) presents the recorded hysteresis curves obtained for a laser detuning of $\Delta = 300 \mu\text{eV}$. We observe a drastic collapse of the bistability, the hysteresis loop being completely quenched at only 22.5 K. This behavior is different from the effect of intensity noise for which a symmetrical collapse of the thresholds was found [156]. The threshold power for the upward and downward intensity jumps are plotted as a function of temperature in figure 6.2 (b) as well as the transmitted intensity just above the upward threshold, I_{up} . The upward threshold power P_{up} decreases significantly when increasing temperature while the P_{down} is barely affected. The transmitted intensity also decreases steadily with increasing temperature.

These results are unexpected because, at least for a 2D microcavity, polariton-phonon scattering strength from polaritons at $k = 0$ is supposedly small and almost independent of temperature for temperatures below the LO-phonon energy (~ 40 K) [48, 49, 194, 195]. Therefore, we might expect that the effect of temperature on the bistability is minor. However, these results suggest that polariton-phonon scattering will transfer polariton from $k = 0$ to exciton states at large k . Then, we can assume that the observed phenomenon is linked to the creation of an incoherent population of excitons in a reservoir that interacts with the resonantly excited polariton population, as suggested in Ref. [144]. Although this work studied the full 2D case, we can expect similar phonon absorption process to occur between a confined polariton mode and a delocalized one (the exciton reservoir). It was shown theoretically in Ref. [164] that phonon absorption process involving two 0D confined polariton modes is more efficient than its 2D counterpart since a larger number of phonon modes contribute to the scattering. The phonon scattering strength from a delocalized exciton in the reservoir to a confined polariton mode was estimated for a $3 \mu\text{m}$ mesa to be 10% of the full 0D case. This suggests that the efficiency of the polariton-phonon scattering mechanism transferring a confined polariton mode to the exciton reservoir is intermediate between that of the full 2D and 0D cases.

To demonstrate the effect of such a reservoir population, we repeat the experiment at a fixed temperature of 4.3 K while injecting an incoherent population in the reservoir in a controlled way. This is achieved experimentally by focusing a HeNe laser onto the top surface of the mesa while the resonant laser excites the same mesa from the back of the sample. A single microscope objective is used to inject non-resonantly and to

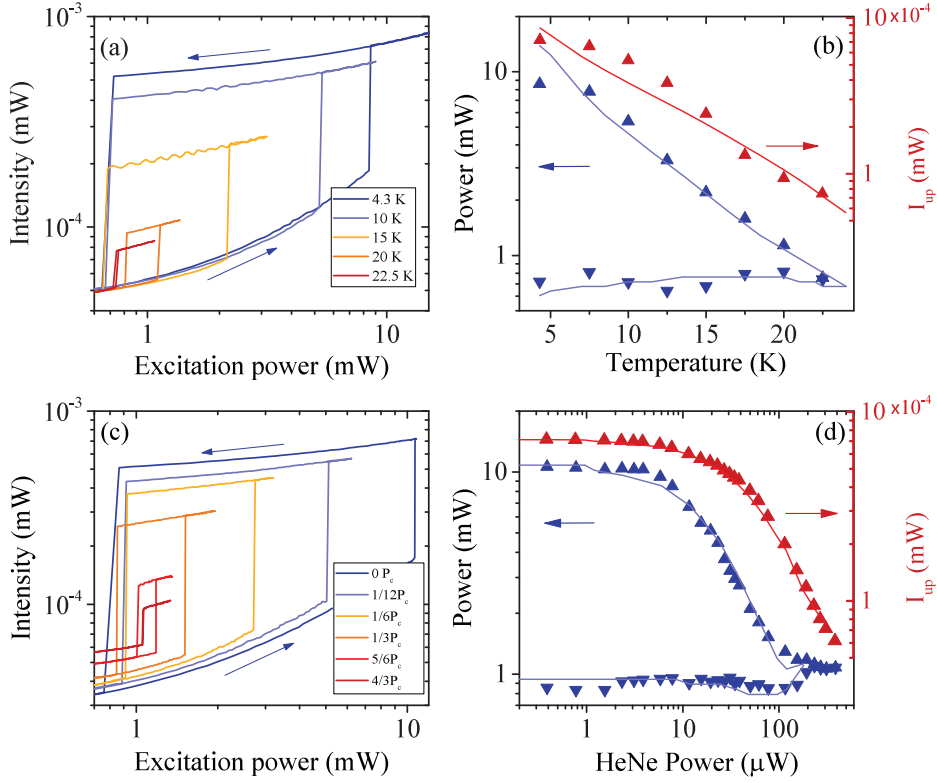


Figure 6.2 – Polariton bistability for $\Delta = 300 \mu\text{eV}$. (a) Hysteresis curves for increasing temperature. The blue arrows indicate the path when cycling the input power. (b) Excitation power at the upward and downward thresholds (blue) and transmitted intensity above the upward threshold I_{up} (red) for a given temperature. The up (down) triangles correspond to the upward (downward) thresholds. The solid lines are fits using equations 1.46. (c) (d) is the same as in (a) and (b) but for increasing non-resonant laser power. $P_c = 233 \mu\text{W}$ represents the non-resonant power needed for the hysteresis loop to collapse.

collect the transmitted resonant laser beam (see setup description in section 5.2.2). The bistability curves measured in this experimental configuration for specific HeNe powers are shown in figure 6.2(c) and the corresponding threshold power and transmitted intensity in figure 6.2 (d). We observe again a rapid decrease of P_{up} while P_{down} is almost unaffected. Interestingly, at higher HeNe power, the decrease of P_{up} levels off asymptotically. For a HeNe power of $P_{HeNe} \geq 100 \mu\text{W}$ and above, there is an increase of P_{down} until the collapse of the hysteresis loop. Similarly to the temperature experiment, the transmitted intensity in the upper branch of the hysteresis loop decreases steadily until the bistability collapses. The qualitative agreement between both series of experiments strongly suggests that an increase in temperature leads indeed to a larger incoherent population in the reservoir which interacts with the driven polariton population. Finally, the slight increase of the intensity of the lower branch with increasing HeNe power for resonant excitation

6.1. Experimental study of polariton bistability under dephasing

below 1 mW seen in figure 6.2 (c) corresponds to unfiltered luminescence from the sample and most likely originates from the thick GaAs layers of the DBR mirrors excited by the HeNe laser.

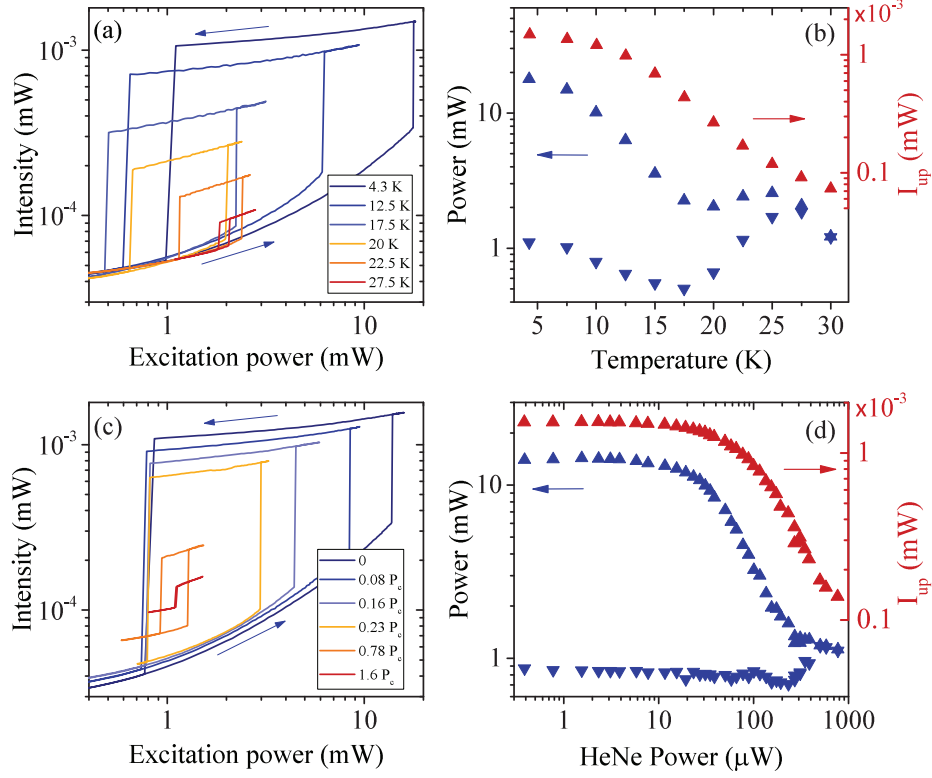


Figure 6.3 – Polariton bistability for $\Delta = 500 \mu\text{eV}$. (a) Hysteresis curves of the transmitted intensity for increasing temperature. The blue arrows indicate the path when cycling the input power. (b) Excitation power at the upward and downward thresholds (blue) and transmitted intensity above the upward threshold (red) for a given temperature. The up (down) triangles correspond to the upward (downward) thresholds. (c) (d) is the same as in (a) and (b) but for increasing non-resonant laser power. $P_c = 500 \mu\text{W}$ represents the non-resonant power needed for the hysteresis to collapse.

Although the leveling off of P_{up} is not pronounced in the temperature experiment, increasing the laser detuning changes this behavior considerably. Results when repeating the same experiments with a laser detuning of $\Delta = 500 \mu\text{eV}$ are presented in figure 6.3. For the temperature measurements (figure 6.3 (a)-(b)), both the leveling off of P_{up} and the increase of P_{down} are accentuated and occur for temperatures above 20 K. For the case of non-resonant pumping (figure 6.3 (c)-(d)), the increase of laser detuning only causes the upward threshold evolution to be shifted to higher power, compared to $\Delta = 300 \mu\text{eV}$. Because of the larger laser detuning, a higher energy blue shift is needed, and thus a larger reservoir density in order to drive the collapse of the hysteresis loop. For the non-resonant pumping, this only shifts the whole behavior to higher pump power. However, for the

case of temperature, in order to reach higher reservoir density, the temperature must be increased further, leading to possible changes in the reservoir dynamics and scattering coefficients. This is why figure 6.2 (a)-(b) and figure 6.3 (a)-(b) differ for $T > 20$ K.

6.2 Numerical study of Polariton bistability away from the coherent limit

Before we dive into the study of RID, it is worthwhile to understand numerically how dephasing affects the bistability. For this, we turn to the excitonic Bloch equations (EBE), that were derived for single mode interactions in section 1.5 (equations 1.46):

$$i\hbar\dot{N} = -i\Gamma_x N - 2i(\Omega - g_{pae}N) \text{Im}(PE^*), \quad (6.1a)$$

$$i\hbar\dot{P} = (\epsilon_x - i\gamma_x + g_0N)P + (\Omega - 2g_{pae}N)E, \quad (6.1b)$$

$$i\hbar\dot{E} = (\epsilon_c - i\gamma_c)E + (\Omega - g_{pae}N)P + f_{ext}, \quad (6.1c)$$

where N is the exciton population, P is the exciton polarization (or mean field) and E is the electric field amplitude. The resonant laser field f_{ext} is defined as in equation 5.2. The notation is slightly different from the Gross-Pitaevskii equations (GPE) of the last chapter to follow the EBE literature; we use the Rabi coupling instead of the Rabi splitting $\Omega = \Omega_0/2$. The lifetime of the exciton polarization is defined as:

$$\gamma_x = \Gamma_x/2 + g'N + \gamma^*, \quad (6.2)$$

where γ^* is a pure dephasing term, and g' is the term accounting for the excitation-induced dephasing (EID), namely a density dependent linewidth. In the coherent limit (for $\gamma^* = g' = g_{pae} = 0$), the exciton linewidth is $\Gamma_x/2$. Contrary to the GPE where a dephasing is only included as a loss of polaritons, in the EBE, a polariton or exciton dephased from the driving laser can still contribute to the blue shift. As we already discussed, working in the exciton-photon basis is advantageous since the interaction strengths and couplings are automatically renormalized as a function of pump, reservoir density and temperature. The 2D polariton linewidths can be overestimated because we include exciton and photon linewidths instead of the polariton linewidths directly. This is equivalent to assuming exciton-phonon scattering instead of polariton-phonon scattering.

Fortunately, this approximation works well for the case of confined polaritons close to zero detuning. As we mentioned in section 1.3.2 there is a 9 meV energy difference between the confined and the 2D cavity mode. Hence, for a mesa at zero cavity detuning, the 2D lower polariton is $\approx 97\%$ excitonic ($\delta/\Omega_0 = 2.7$), meaning that exciton-phonon scattering is well justified the once polaritons are scattered out of the mesa (the reservoir). Since we do not evaluate all these scatterings directly, it is understood that the linewidths in the model are effective and also include other effects like experimental noise or other fluctuations.

6.2.1 Influence of dephasing parameters on the bistability

There are three effects included in the model that cause the system to lose its coherence: pure dephasing, EID, and phase space filling (or photon assisted exchange). Although these parameters are fixed in the experiment (or for a given mesa), we can change their values in the simulation to understand their effect on the bistability. We perform these simulations (using the same procedure as discussed in section 5.1.1) for a single polariton mode at a detuning of $\delta = 0$ meV, a laser detuning of $\Delta = 300$ μ eV, $\gamma_c = \Gamma_x = 30$ μ eV, and a Rabi coupling of $\Omega = \Omega_0/2 = 1.665$ meV. The effect of the reservoir, and of the temperature on the exciton energy, will be added and discussed in the next section.

First, we study the effect of pure dephasing γ^* . This term increases the coherent exciton linewidth, and is constant throughout the hysteresis loop. To start, it is interesting to compare these simulations to the ones performed in the coherent limit in section 5.1.2. In figure 6.4 we plot the simulation of the photon intensity while increasing the pure dephasing in EBE, and the increase of exciton linewidth obtained with GPE (simulation in the coherent limit of EBE, already presented in figure 5.3(b)). All other parameters are identical in both simulations. Clearly, the bistability evolves in opposite ways depending on whether the system is coherent or not. In the coherent limit, the linewidth increase has a dominant effect on P_{down} , and almost no effect on P_{up} . In the EBE framework, P_{up} steadily decreases until the collapse of the bistability while P_{down} initially decreases before increasing until both threshold meet. The increase of exciton pure dephasing also causes a decrease of the intensity above threshold whereas it stays almost constant in the coherent limit.

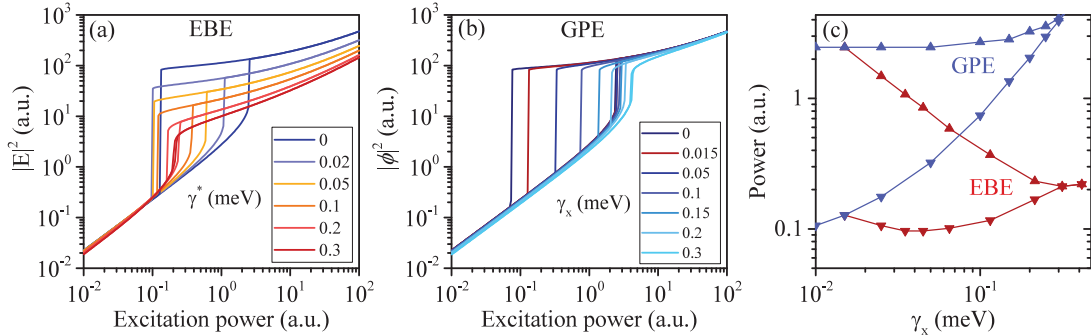


Figure 6.4 – Comparison of hysteresis loops simulated using either the EBE or the GPE (coherent limit of EBE) while varying the exciton linewidth. (a) EBE while changing the pure dephasing γ^* , as in figure 6.5 (a). (b) GPE while changing the exciton linewidth $\gamma_x = \Gamma_x/2$, identical as in figure 5.3 (b). (c) Comparison of the upward and downward thresholds as a function of exciton linewidth for both cases. The red (blue) is the values obtained from the EBE (GPE). The up (down) triangles represent the upward (downward) threshold powers. The EBE curves start as 0.015 meV because of the initial value of $\gamma_x = \Gamma_x/2 = 0.015$ meV.

This highlights the different interpretation of the linewidths in both models. In the GPE,

the linewidth corresponds to losses of the polariton system. This barely impacts the upward threshold but affect how quickly polaritons will unlock from the laser. In the EBE picture, dephasing switches excitons from coherent to incoherent with respect to the excitation laser. Contrary to the coherent case, incoherent excitons still participate to the non-linear response of the system. Figure 6.4 (c) summarizes these trends by plotting the evolution of both threshold powers for the two scenarios.

The EBE simulation allows to visualize all the components of the system. In figure 6.5 (a)-(c) we plot the hysteresis curves for the photon intensity (same as in figure 6.4 (a)), the coherent exciton and the exciton population respectively. The effect of dephasing is clearly seen when comparing the coherent exciton population $|P|^2$ and the full population $N = |P|^2 + N_{incoh}$. While the exciton population just above threshold is roughly constant, the coherent population decreases by one order of magnitude, meaning that the exciton population is dominated by its incoherent part N_{incoh} . We also notice from these figures that the photon intensity $|E|^2$ differs from the polarization $|P|^2$ even for $\gamma^* = 0$. This is because we pump only the photon part, which induces an asymmetry between the two polariton components.

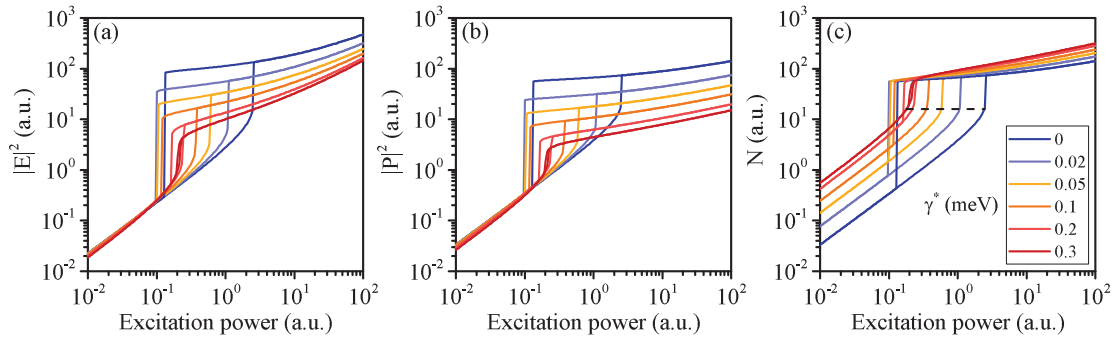


Figure 6.5 – Numerical simulation of polariton hysteresis loops using the EBE (equations 6.1) while varying the pure dephasing γ^* from 0 to 0.3 meV. The other parameters are: $\Delta = 300 \mu\text{eV}$, $\delta = 0$, $\gamma_c = \Gamma_x = 30 \mu\text{eV}$, $g_0 = 0.012 \text{ meV/density}$ where the density is arbitrary and fixed to one. (a) Photon mean field intensity, (b) exciton polarization (coherent) and (c) population. The black dashed line in (c) is a guide to the eye showing the fixed exciton population just before the upward threshold.

Figure 6.5(c) shows an interesting feature: the exciton population N just before the upward threshold is independent of the pure dephasing, and the excitation power (as indicated by the black dashed line). We saw in the previous chapter that, in the coherent limit, the upward threshold occurs when the polariton mode reaches a critical blue shift which is proportional to the density (see section 5.1). With pure dephasing, the system always reach the same critical density even though P_{up} decreases. This is because the blue shift depends on N instead of $|P|^2$. The decrease of P_{up} is due to the increased overlap between the polariton and the laser as the linewidth increases. Therefore, we create excitons more efficiently while increasing the imbalance between coherent and incoherent

6.2. Numerical study of Polariton bistability away from the coherent limit

population. Hence, the upward threshold density is obtained for a lower excitation power.

Interestingly, the behavior of the bistability with pure dephasing is scaled by the exciton linewidth Γ_x and laser detuning Δ . In figure 6.6, we compare the photon intensities for two values of Γ_x and Δ . The variation of both threshold powers is amplified if we decrease Γ_x or increase the laser detuning. As expected, increasing the laser detuning increases the bistability width and the linewidth needed to collapse the bistability. The decrease of Γ_x initially pushes P_{down} to lower values (as for the coherent limit) and amplifies its variation as γ^* is increased.

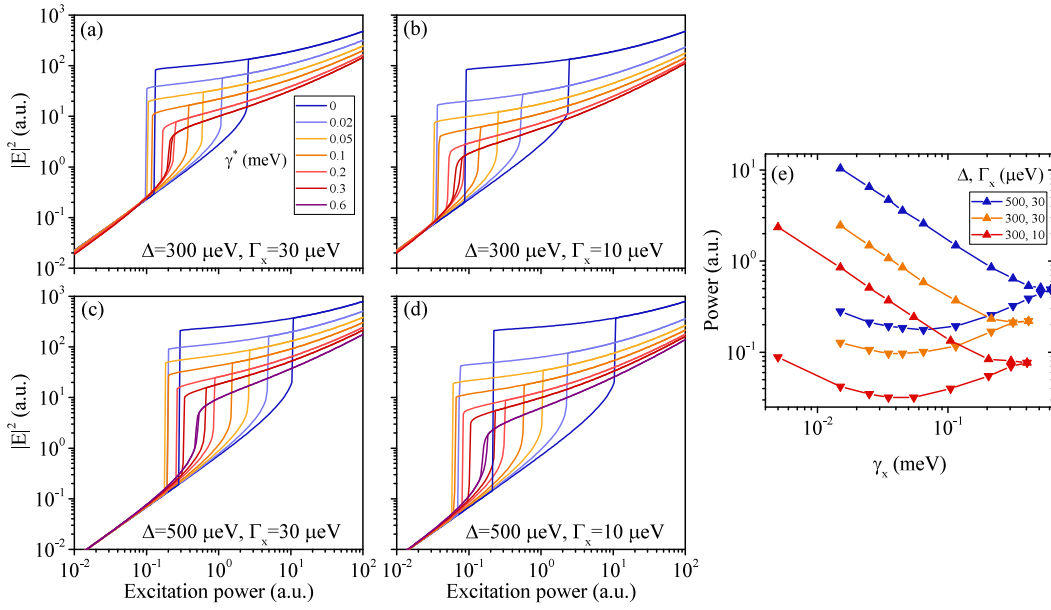


Figure 6.6 – Numerical simulation of polariton hysteresis while varying the pure dephasing γ^* from 0 to 0.6 meV for different values of Γ_x and Δ . The other parameters are as in figure 6.5. (a) $\Gamma_x = 30 \mu\text{eV}$, $\Delta = 300 \mu\text{eV}$ (b) $\Gamma_x = 10 \mu\text{eV}$, $\Delta = 300 \mu\text{eV}$ (c) $\Gamma_x = 30 \mu\text{eV}$, $\Delta = 500 \mu\text{eV}$ (d) $\Gamma_x = 10 \mu\text{eV}$, $\Delta = 500 \mu\text{eV}$ (e) Upward and downward threshold powers for cases (a) (orange), (b) (red), and (c) (blue).

Next, we study the effect of EID. Since it is proportional to N , the coherent exciton linewidth will vary throughout the hysteresis cycle. Figure 6.7 (a)-(c) shows the simulated photon intensity, coherent exciton and exciton population while increasing the value of the parameter g' from zero to g_0 (changing from a coherent system to one where the EID is as important as the exciton-exciton repulsive interactions). At a glance, the effect of increasing the EID parameter is similar to increasing the pure dephasing. P_{up} decreases until the collapse of the bistability. The downward threshold power P_{down} is initially constant and increases for $g' > 0.1 g_0$ until the collapse. The main difference compared to pure dephasing is that, when the bistability collapses, the photon intensity and coherent population above threshold has dropped by two orders of magnitude instead of one.

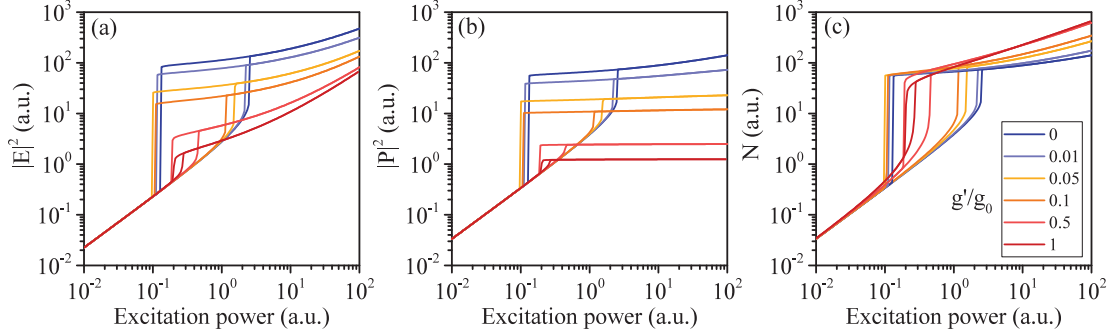


Figure 6.7 – Numerical simulation of polariton hysteresis loops using the EBE (equations 6.1) while varying the EID parameter g' from 0 to g_0 . The other parameters are as in figure 6.5. (a) Photon mean field intensity, (b) exciton polarization (coherent) population, (c) exciton population.

Finally, we look at the effect of phase space filling on the bistability, which is shown in figure 6.8. For a given value of g_{pae} , the exciton-photon coupling ($\Omega - g_{pae}N$) will decrease throughout the bistability, causing an additional blue shift to the lower polariton mode. Accordingly, it will also modify the Hopfield coefficients during the cycle (the only exception is for $\delta = 0$). We see that changing the strength of g_{pae} essentially act as a scaling parameter that shifts almost rigidly the bistability to lower excitation powers. The effect on coherence is also minor as seen in figure 6.8 (b). This indicates that even though g_{pae} contributes to dephasing, the original proposal of keeping this term in the coherent limit does not introduce a sizable error (see discussion in section 1.5).

Surprisingly, the system is still in strong coupling even if we force a very large value of $g_{pae} = 10g_0$. At first this might seem unreasonable if we think simply in terms of the coherent limit. For a laser detuning of $300 \mu\text{eV}$, the critical blue shift is in the range of $g_0 N_c \approx 100 \mu\text{eV}$, hence we would get $g_{pae} N_c \approx 1 \text{ meV}$, almost equal to our Rabi coupling of $\Omega = 1.665 \text{ meV}$ given above. In fact, if we plot the product $g_{pae}N$ normalized to the Rabi coupling (figure 6.8 (c), where N is taken from figure 6.8 (b)), we see that this condition never occurs. Even at the largest value of g_{pae} , the phase space filling term barely reaches 10 % of the Rabi coupling above the upward threshold. The phase space filling term induces a blue shift on the polariton mode that increases throughout the bistability. Evidently, as the density increases so does the blue shift, hence it decreases the critical density needed to reach the upward threshold. This is clearly seen in figure 6.8 (b). Because of that, the system never reaches large enough densities to break the strong coupling. In reality, we expect g_{pae} to be in the range of $\approx 0.1 - 0.25g_0$ or less, meaning the bistability always occurs for densities far from the Mott density.

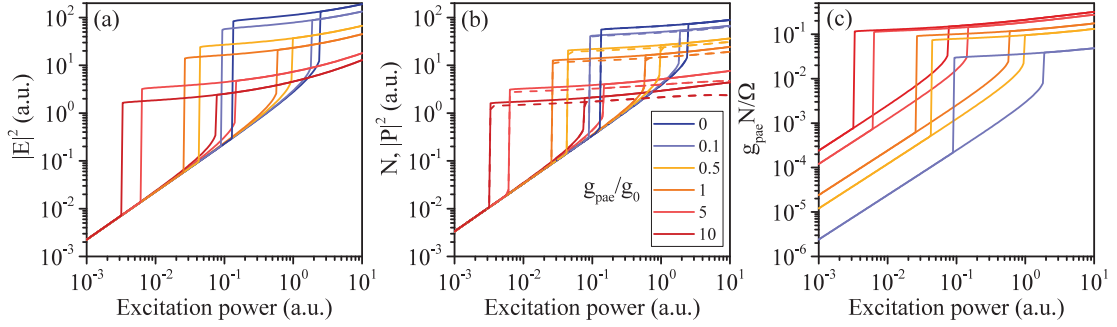


Figure 6.8 – Numerical simulations of polariton hysteresis loops using the EBE (equations 6.1) while varying the phase space filling parameter g_{pae} from 0 to $10 g_0$. The other parameters are given in figure 6.5. (a) Photon mean field intensity, (b) exciton polarization (coherent) and population. The full (dashed) curve represents N ($|P|^2$). (c) Phase space filling term $g_{pae} N$ for each values of g_{pae} normalized to the Rabi coupling. N is obtained from (b).

6.3 Numerical study of reservoir-induced dephasing

Comparing our experimental results to the above simulations above indicates that the polariton system does suffer from dephasing. The question now it to see whether the EBE formalism can help us understand how and why the system is dephased the way it does in the experiment. To answer these questions, we seek to fit our experimental data, for both non-resonant excitation or when increasing the temperature. We are interested in fitting the evolution of both thresholds as a function of temperature or HeNe power as well as the decrease of intensity above threshold. From the simulation discussed above, it is clear that the intensity is a measure of the coherent population whereas the threshold indicates the strength of the interactions. Hence, it is mandatory to fit both powers and intensity variation to extract the right physical behavior of the system. First, we must extend our model so as to include the influence of the reservoir on the polariton state.

6.3.1 EBE with reservoir

The similarity between the pure dephasing simulation and the HeNe experiments suggest that including a linewidth that depends on a reservoir density should reproduce our data. However, since the density dependent linewidth ($\gamma = g' N$) enters as an imaginary part of the exciton-exciton interaction ($g = g_0 - i g'$), it should be logical to include a reservoir-polariton interactions as well. This step can be achieved using a multimode derivation of the EBE, which is performed in appendix A.

We can obtain the reservoir terms in the EBE by considering the reservoir as an effective exciton mode that does not couple to the photon field. This is a simplified model compared to the one presented in Ref. [144] that was used to simulate the evolution of

the bistability as a function of the reservoir density. Other models based on the master equation for the density matrix of the lower polariton have been proposed to study the effect of temperature on the bistability [145, 203]. However, these models neglect the presence of an incoherent reservoir and predict a symmetrical collapse of both thresholds at temperatures up to 100 K, in contrast to what is observed here. Polariton bistability under incoherent pumping was theoretically investigated in Ref. [146], but no RID was included in the model. It is worth noting that the dephasing can be implemented by assuming different linewidths for the lower and upper polariton branches when both are coherently excited [201].

The EBEs with additional reservoir terms read:

$$i\hbar\dot{N} = -i\Gamma_x N - 2i\Omega_P^N \text{Im}(PE^*), \quad (6.3a)$$

$$i\hbar\dot{P} = (\epsilon_x - i\gamma_x^N + g_0 N + g_R N_R)P + \Omega_P^N E, \quad (6.3b)$$

$$i\hbar\dot{E} = (\epsilon_c - i\gamma_c)E + \Omega_E^N P + f_{ext}, \quad (6.3c)$$

where the density dependent parameters are defined as:

$$\Omega_P^N = \Omega - 2g_{pae}N - 2g_{pae}^R N_R, \quad (6.4)$$

$$\Omega_E^N = \Omega - g_{pae}N - g_{pae}^R N_R, \quad (6.5)$$

$$\gamma_x^N = \Gamma_x/2 + g'N + g'_R N_R + \gamma^*. \quad (6.6)$$

The term N_R is the reservoir population, either created by the HeNe laser ($N_R \propto P_{HeNe}$) or through phonon scattering ($N_R \propto T$, see discussion below). E is the photon mean field, $f_{ext} = \sqrt{I_0}e^{-iE_l t/\hbar}$ is the resonant laser of intensity I_0 and energy E_l , ϵ_x and ϵ_c are the exciton and photon energy. The exciton-exciton interaction strength is noted g_0 , and g_R represents the interaction of the coherent exciton with the reservoir. The effect of phase space filling is included through the parameters g_{pae} and g_{pae}^R that describe the reduction of the coupling strength at high densities. We recover GPE in the coherent limit ($N = |P|^2$) when g'_R , g' , g_{pae} , and γ^* are put to zero.

6.3.2 Data fitting of the non-resonant excitation experiment

To fit our data, we simulate a series of bistability curves for increasing N_R and minimize the error for P_{up} , P_{down} and I_{up} simultaneously by adjusting the parameters. Each run of experiments can converge to slightly different sets of parameters, mainly because of intrinsic noise fluctuation between experiments as well as fluctuations of the excitation density. Based on the previous simulations (see figure 6.8), we set $g_{pae} = g_{pae}^R = 0$. The value of N_R and I_0 are scaled proportionally in order to fit the excitation densities. For the HeNe experiment, the fit presented in figure 6.2 was obtained using the values of parameters listed in table 6.1. This set of parameters is not unique; other sets of parameters could as well give reasonable fits.

6.3. Numerical study of reservoir-induced dephasing

Table 6.1 – Value of the parameters of EBE with reservoir (equations 6.3) used for the simulation of the HeNe experiment for a laser detuning of $\Delta = 0.3$ meV (see figures 6.2, 6.9, and 6.10). The density is arbitrary and is fixed to one. The parameter α is defined in equation 6.7.

Parameters	Value	units
Δ	0.3	meV
Ω_0	3.33	meV
δ	0.2	meV
γ_c	0.03	meV
Γ_x	0.03	meV
g_0	0.012	meV/Density
g'	$0.09g_0$	meV/Density
g_R	$0.4g_0$	meV/Density
g'_R	$0.1g_0$	meV/Density
$g_{pae}; g_{pae}^R$	0	meV/Density
α	0.013	1/Density

Using our best fit parameters, we can study the effect of each N_R term on the evolution of the bistability. First, we focus on the simulations of figure 6.2 (d) since the HeNe and temperature experiments lead to the same trend. Temperature based simulations will be discussed in the next paragraph. figure 6.9(a) shows the evolution of the thresholds, when N_R is increased, for three specific sets of parameters, case 3 being the fit presented in figure 6.2(d). For case 1, we set the reservoir induced blue shift to zero ($g_R = 0$), while all other parameters are fixed. That way, the only contribution from the reservoir is the RID. Similarly to the pure dephasing discussed above, the increase of RID causes a slow decrease of the upward threshold but, importantly, an increase of P_{down} . The increase is more pronounced compared to the one obtained for pure dephasing (see figure 6.5) because we are at a slightly positive detuning.

For case 2, we study the opposite scenario as in case 1 ($g_R \neq g'_R = 0$). For low values of N_R , P_{up} is essentially given by g_0N and it decreases when $g_R N_R$ becomes large enough. The same is true for P_{down} ; both threshold powers decrease rapidly with N_R , leading to a quicker collapse of the bistability. Since the term $g_R N_R$ pushes the polariton mode closer to the resonant laser, both thresholds occur at lower excitation power. Comparing cases 1 and 2 shows that the measured steady value of P_{down} is an indicator of the competition between the reservoir induced blue shift and the RID. Close to the bistability collapse, the increase of P_{down} shows that the effect of RID is dominant over the energy blue shift induced by the reservoir population.

Combining cases 1 and 2 does not allow to fit the data over the complete range of power. This is a consequence of the rapid decrease of the thresholds caused by the reservoir

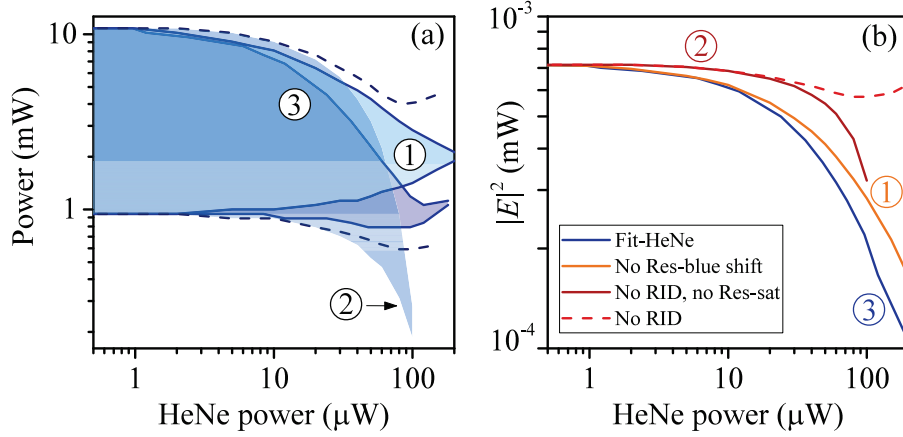


Figure 6.9 – (a) Simulated upward and downward threshold power for different reservoir parameters. Case 1 is a simulation when g_R is set to zero. Case 2 includes g_R without the asymptotic decrease with density and with $g'_R = 0$. The dashed line represents the same case with the asymptotic decrease, and case 3 is the fit shown in figure 6.2(d) where all effects are included. All other parameters are kept constant in all cases. (b) Simulated intensity above the upward threshold for the same cases as in (a).

induced blue shift as seen in figure 6.9(a). Whatever the parameters used, it not possible to fit the last decade of HeNe power since the bistability always collapses too quickly. This indicates that the leveling off of P_{up} must reflect a saturation of the reservoir-exciton interaction strength. This effect is not a consequence of the saturation of the Rabi coupling strength Ω by phase space filling terms g_{pae} . Indeed, the saturation of the oscillator strength would decrease the Rabi coupling, providing an extra blue shift to the lower polariton mode, hence accelerating the whole process (see figure 6.8). Other mechanisms that transfer the populations between N and N_R would reduce the blue shift induced by one population while increasing the contribution of the other one. The same behavior occurs if we include bosonic stimulation (N_R dependent gain for the exciton polarization) to deplete the reservoir. This would also lead to an increase of $|P|^2$ with N_R while the opposite is seen experimentally. Furthermore, increasing the gain would keep the polariton mode locked to the laser for a longer time, resulting in a decrease of P_{down} with an increase of HeNe power.

Therefore, the leveling off of P_{up} is either caused by a saturation of the reservoir density with increasing HeNe power or by a decrease of the interaction strength with density. Photoluminescence measurement while exciting the sample with the HeNe laser showed a linear dependence of the integrated intensity of both 0D and 2D polaritons, over the complete range of power available, suggesting that the reservoir population should have a linear dependence with the excitation power. Therefore, the variation of reservoir-exciton interaction strength with density is more likely. This could occur for example in the case of large momentum transfer between interacting excitons [57] i.e. redistribution of the reservoir population toward large k -vector with increasing excitation density. Since

6.3. Numerical study of reservoir-induced dephasing

our simplified model does not include a detailed calculation of exciton interactions, we parametrize this decrease of reservoir interaction strength by a sigmoid function that converges asymptotically towards zero:

$$g_R \rightarrow g_R(N_R) = 2g_R/(1 + e^{\alpha N_R}). \quad (6.7)$$

The parameter α is used to fit the leveling off of P_{up} , and with this we obtain the fit presented in case 3 (solid line in figure 6.2 (c) and (d)). The effect of equation 6.7 on the bistability is shown by the dashed line in figure 6.9(a) where we put the RID to zero, as in case 2.

The RID also affects the intensity in the upper branch of the hysteresis loop (shown in figure 6.9 (b)). For example, if we compare the intensity obtained in case 2 and 3 (red and blue curve), we see that for a given value of P_{up} , the transmitted intensity is always higher for case 2. The RID must be present in order to obtain the same combination of threshold power and intensity that was measured.

Having access to both the coherent and incoherent populations in the simulation allows us to study the system's coherence. figure 6.10 (a) and (b) show the calculated hysteresis loop of the coherent photon intensity $|E|^2$ and of the exciton population N for different reservoir densities (HeNe power). As N_R increases, the coherent population at the onset of the upward threshold decreases, as well as P_{up} . Conversely, N slightly increases at the onset as shown by the dashed line in figure 6.10 (b) and it remains relatively constant above the upward threshold. Since the RID broadens the polariton mode, it increases the overlap between the resonant laser and the polariton mode and contributes to the transfer of the polariton population from coherent to incoherent (see figure 6.10 (c) and discussion below). Therefore, the transfer to the incoherent population is enhanced by the interaction of the coherent population with that of the exciton reservoir. This also allows the system to reach the upward threshold for a lesser resonant excitation power.

Finally, the effect of RID is summarized in figure 6.10 (c) where we show the evolution of N and $|P|^2$ for a resonant laser power of 0.1 mW (full lines) and at the onset of the upward threshold (dashed lines). The difference between the blue and red curves gives the incoherent exciton population $N_{incoh} = N - |P|^2$, excluding that of the reservoir N_R . We see that for low resonant power and reservoir density, the system is fully coherent, $N = |P|^2$. As the reservoir population increases, the initial incoherent population increases compared to the coherent one, meaning that the resonant laser contribute more efficiently to the incoherent part. This imbalance is maintained at the onset of the upward threshold. For low reservoir density, $N > |P|^2$ since $g' \neq 0$. As the RID is increased, the onset density increases slightly while the density of the coherent population decreases, which is reflected by the decrease of transmitted laser intensity.

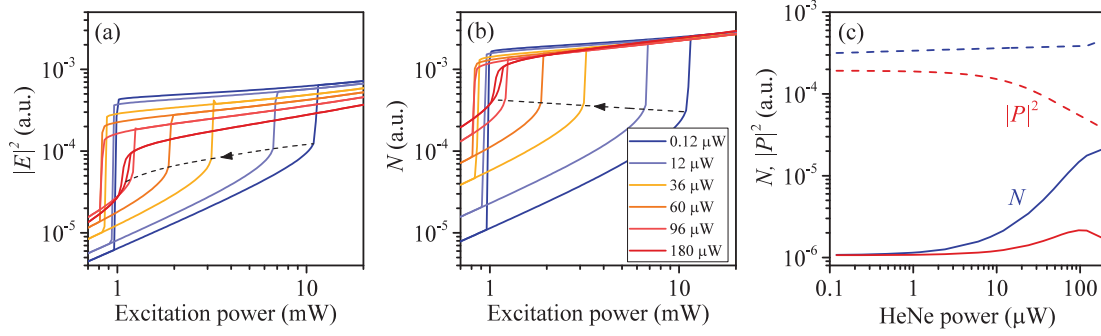


Figure 6.10 – (a) Simulated photon intensity $|E|^2$ as a function of excitation power for different values of incoherent pumping intensity (HeNe power). (b) Simulated exciton population $N = |P|^2 + N_{incoh}$ for the same conditions as in (a). The dashed lines indicate the evolution of the coherent (a) and total (b) population before the upward threshold. (c) N and $|P|^2$ as a function of HeNe power. The full lines correspond to the population for the initial resonant laser power whereas the dashed lines correspond to the values at the onset of the upward threshold.

6.3.3 Data fitting of the temperature experiment

We followed the same procedure to fit the temperature data presented in figure 6.2 (b). For these simulations, we included the exciton red shift, and assumed, as a first approximation that the population of the reservoir is proportional to the temperature: $N_R \propto aT$. We have seen in the previous section that we had to include a dephasing term of the type $\gamma_{EID} = g'N_R$. At the same time, the effect of temperature is usually considered as a pure dephasing term: a linewidth proportional to temperature $\gamma^* = \alpha_T T$ (neglecting LO-phonon term $\gamma_{LO} = b(\exp[\hbar\omega_{LO}/kT] - 1)^{-1}$) [204]. We mentioned in section 6.1 that the effect of temperature was linked to a reservoir population, hence it is logical to equate both equations which gives $N_R \propto T$.

We set $\alpha = 0$ since the leveling off is not clearly observed. Since the first data point is taken at 4.3 K, we must adjust g'_R in order to get the right initial bistability width as well as the right decrease of P_{up} with temperature. However, for a given $T \rightarrow N_R$ conversion factor, increasing g'_R will decrease the bistability width at 4.3 K. To compensate this effect, we remove the $\Gamma_x/2$ term in the definition of γ_x , and decrease γ_c . This might seem unphysical, but is actually linked to our first convergence of the model for the HeNe simulations. In principle, these fits should include the temperature dependent linewidth as well, and inevitably change the values of Γ_x and γ_c . This would be tedious since a single run of temperature or HeNe fit take a minimum of 15 minutes on a parallelized quadcore laptop (with reasonable number of discretizations in time (200 points) and power (120 points over three decades) and reservoir values (20)), and would not change our discussion about the underlining physics.

Under these conditions, the model converged to a similar set of parameters, given in

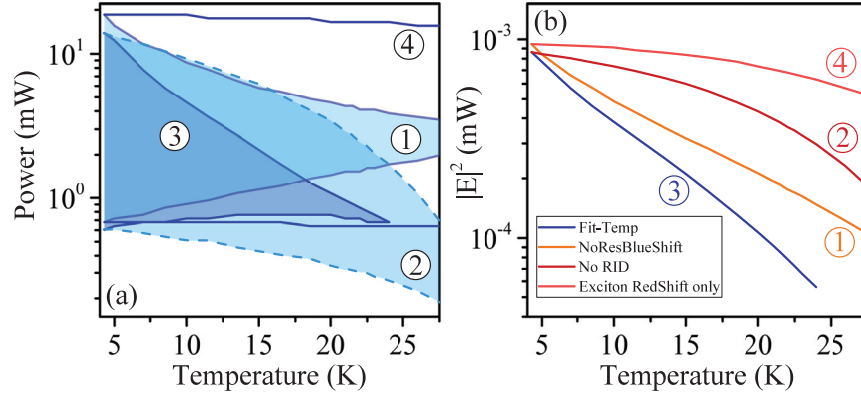


Figure 6.11 – (a) Simulated upward and downward threshold power as a function of temperature for different reservoir parameters. Case 1 is a simulation when g_R is set to zero. Case 2 includes g_R and $g'_R = 0$. Case 3 is the fit shown in figure 6.2 (d) where all effects are included. For case 4, we only include the exciton redshift ($g_R = g'_R = 0$). All other parameters are kept constant in all cases. (b) Simulated intensity above the upward threshold for the same cases as in (a).

table 6.2. However, our model did not converge for the temperature data at $\Delta = 500 \mu\text{eV}$ with $\alpha \neq 0$, indicating that N_R is no longer proportional to T for higher temperatures. The distribution of N_R in k -space might also evolve with temperature, changing the effective value of g_R .

With this fit, we can analyze again the effect of the reservoir/temperature parameters on the bistability, as presented in figure 6.11 where case 3 is the fit presented in figure 6.2 (b). Similarly to the HeNe fits, we clearly see that the effect of RID (case 1) and the reservoir blue shift (case 2) on P_{down} cancels out, while they add up for P_{up} in order to collapse the bistability. This is also seen in the intensity just above threshold, presented in figure 6.11 (b). For case 4, we have removed all contributions from the reservoir, and kept only the exciton red shift. Clearly, the temperature dependence of the Hopfield coefficients produces only a minor effect compared to the reservoir. This is because we vary the detuning from $\delta = 0.06\Omega_0$ (0.2 meV) to $\delta = 0.2\Omega_0$ (0.66 meV), which, as seen in the coherent limit (see figure 5.3 (c)) as only a small effect on the thresholds.

To complete our analysis, we give in figure 6.12 the simulated hysteresis loops for the photon intensity and exciton population as well as a comparison between the coherent population $|P|^2$ and the exciton population N . These figures have similar features as for the HeNe simulations. We see that the exciton population is almost constant just before the threshold, and that the coherence decreases with increasing temperature. Interestingly, the system is never fully coherent even for low temperatures and low excitation power (see figure 6.12 (c)). This is due to the independence of the temperature dependent linewidth on the excitation power. Of course, the true relative value between N and $|P|^2$ might differ from the fit because it depends on the set of parameters. Nonetheless, it does

not affect the main conclusion. Another indication of the lack of full coherence at low temperature will be given in section 6.4 below.

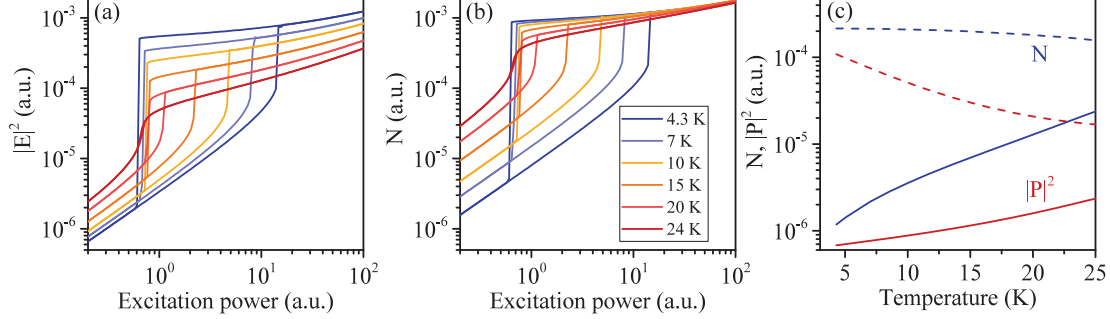


Figure 6.12 – (a) Simulated photon intensity $|E|^2$ as a function of excitation power for increasing temperature. (b) Simulated exciton population $N = |P|^2 + N_{incoh}$ for the same conditions as in (a). (c) N and $|P|^2$ as a function of temperature. The full lines correspond to the populations for the initial resonant laser power whereas the dashed lines correspond to the values at the onset of the upward threshold.

Table 6.2 – Value of the parameters of EBE with reservoir (equations 6.3) used for the simulation of the Temperature experiment for a laser detuning of $\Delta = 0.3$ meV (see figures 6.2, 6.11, and 6.12). The density is arbitrary and is fixed to one.

Parameters	Value	units
Δ	0.3	meV
Ω_0	3.33	meV
δ	0.2	meV
γ_c	0.012	meV
Γ_x	0.03	meV
g_0	0.012	meV/Density
g'	$0.02g_0$	meV/Density
g_R	$0.26g_0$	meV/Density
g'_R	$0.3g_0$	meV/Density
$g_{pae}; g_{pae}^R$	0	meV/Density
α	0.0	1/Density

6.3.4 GPE with reservoir

We have seen at the beginning of the chapter that there was a large difference between the EBE framework and the coherent limit in terms of dephasing. Before concluding this chapter it is worth verifying what happens in the coherent limit if we include the reservoir. Such a model is similar to the one used to simulate non-resonantly excited polariton condensates (as described in section 1.5, equations 1.49). The main difference here is that we replace the gain term from the reservoir (describing bosonic stimulation) with a loss term for the RID. We are taking the coherent limit of equations 6.3 while keeping the reservoir-exciton blue shift and dephasing. Strictly speaking, the RID in GPE acts as a reservoir induced loss since every exciton in the system is coherent.

Figure 6.13 (a), shows the threshold powers that were obtained for the HeNe experiment (blue) and the coherent limit simulation (red) using the same parameters. As expected from the previous comparison, the bistability in the coherent limit evolves oppositely compared to the experiment (represented here by the EBE simulation). The increase of bistability width between both cases is due to the decrease of the coherent exciton linewidth since $g' = 0$ in the coherent limit.

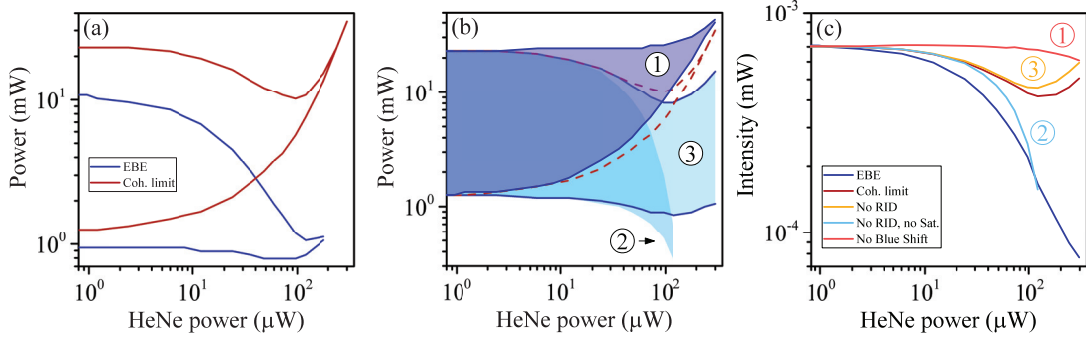


Figure 6.13 – (a) Simulated bistability thresholds as a function of reservoir density using EBE with reservoir (blue), and its coherent limit. The parameters used are given in table 6.1, and represent the fit of the HeNe experiment. (b) Simulated upward and downward threshold power for different reservoir parameters for the coherent limit. Case 1 is a simulation when g_R is set to zero. Case 2 includes g_R , and $\alpha = g'_R = 0$. Case 3 is the same as case 2 but for $\alpha = 0.013$, as for the EBE fit. All other parameters are kept constant in all cases. The dashed red curve is the coherent limit shown in (a). (c) Intensity above threshold for the cases described in (b) as well as the EBE simulation.

The difference between both models mainly comes from their opposite behavior when the coherent exciton linewidth is increased. This is clearly seen in figure 6.13 (b) where we decompose the effect of RID and reservoir induced blue shift. The latter has almost the same effect in both models (see figure 6.9 (a)), but it is the RID that works in opposite ways. Even if we add the leveling off (α parameter), P_{up} is still barely affected by the reservoir, in contrast to our experiment. This divergence is also noticeable in the intensity above threshold as shown in figure 6.13 (c). Even though the reservoir induced blue shift

does decrease the intensity, the combined effect is never as strong as in the experiment.

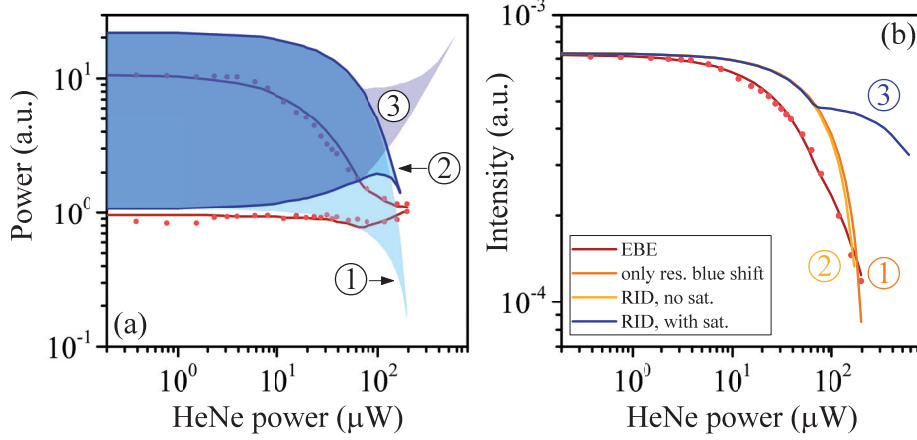


Figure 6.14 – (a) Simulated upward and downward threshold power as a function of reservoir density for a different set of parameters. All the parameters are the same as in table 6.1 except that $g_R = 0.43g_0$, $g'_R = 0.17g_0$, and $g' = 0.12g_0$. The red curve shows the EBE fit of the data. Case 1 is a simulation when g_R is set to zero. Case 2 includes g_R and $g'_R = 0$. Case 3 is the fit shown in figure 6.2 (d) where all effects are included. For case 4, we only include the exciton redshift ($g_R = g'_R = 0$). All other parameters are kept constant in all cases. (b) Simulated intensity above the upward threshold for the same cases as in (a).

Furthermore, the simulated behavior is not parameter dependent. To demonstrate this, we purposely chose another set of parameters and lowered the effect of RID (see figure 6.14). The red curve represents another EBE simulation that gave a good fit to the experiment. In this case, instead of using the asymptotic decrease of g_R as stated in equation 6.7, we impose that $g_R N_R$ becomes constant passed a cutoff value of N_R . When we turn to the coherent limit, we see the rapid collapse of the bistability if we include only the reservoir induced blue shift without the saturation (case 1). For case 2, we add the RID but using g'_R at half the value used for the EBE simulation. Again, the variation of P_{down} is too strong and the collapse occurs too quickly. In order to fit the data using the coherent model, we also need to translate the curve to lower reservoir density to fit the initial variation of P_{up} . This pushes the bistability collapse at roughly half of the reservoir density compared to the experiment.

The effect is even worse if we turn on the saturation based on the EBE simulation. Right after the saturation, P_{down} continues to increase since it is no longer affected by the reservoir induced blue shift whereas P_{up} stays fixed for the same reason. This also causes a strong modification of the intensity as seen in figure 6.14 (b) in strong disagreement with our experiment. Our discussion shows that, using only the simplest parametrisation of the system, it is not possible to fit the experiment in the coherent limit. It might be possible to fit the experiment by varying the reservoir parameters at each step of HeNe power, but it would be difficult to draw any conclusion from it. Even for this case, a

reservoir dependent loss will be mandatory to fit the variation of P_{down} . The need of a reservoir induced loss therefore makes the transition to the EBE framework a necessity.

6.4 Spatial multistability and dephasing

In the previous chapter, we showed that the multimode GPE accurately reproduces the cross interactions between polariton modes. However, we also noticed that the simulations overestimated the full amplitude of the multistability. Fortunately, the EBE simulations presented above showed that any type of dephasing caused a decrease of the photon intensity compared to the coherent limit. Hence, we have another indication that the resonantly excited polariton system is never fully coherent.

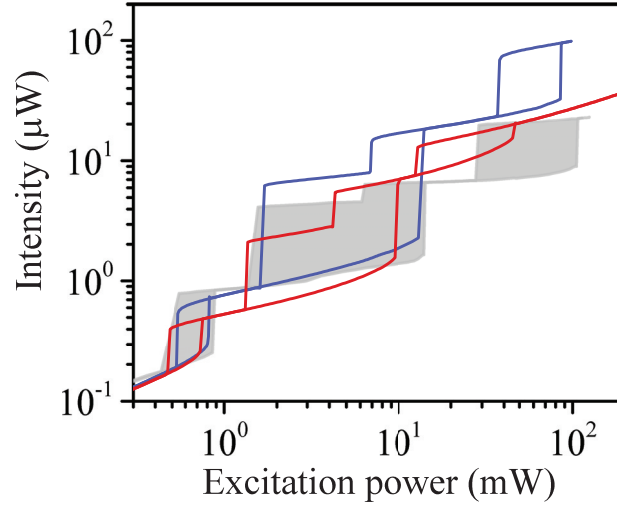


Figure 6.15 – Multihysteresis curve of the spatial multistability experiment. The gray area is the experimental results presented in figure 5.6 while the blue curve is the simulation done with the multimode GPE (equations 5.15) and presented in figure 5.10. The red curve is a simulation using the multimode EBE (equations A.33) where all parameters are identical as the blue curve, and we include an EID coupling matrix $g'_{ij} = 0.05 g_{ij}$ where g_{ij} is the exciton-exciton interaction matrix.

To confirm this, we compare our experimental data and simulations presented in the last chapter with another simulation where we use the multimode EBE (see appendix A). Simply put, the multimode EBE changes the parameters g' and g_{pae} to coupling matrices g'_{ij} and g_{pij} , the same way we change from g_0 in the single mode coupling to g_{ij} in the multimode GPE. Figure 6.15 shows the experimental data in gray, the multimode GPE simulation in blue and the multimode EBE in red. For the later, the same parameters as the GPE simulation were used, and we added a small EID matrix $g'_{ij} = 0.05 g_{ij}$. Under these conditions, we can accurately simulate the multistability amplitude. Of course, the other parameters should be adjusted to fit perfectly the experimental data which

is not the goal here. We can easily expect that by adjusting the 15 exciton-exciton interaction strengths g_{ij} , 15 EID terms g'_{ij} , and 5 exciton/photon linewidths (γ_{xi}/γ_{ci}) that the accuracy of the fit will be good, without affecting the main conclusions of the last chapter.

6.5 Conclusions

We have demonstrated the drastic effect of an incoherent reservoir on a coherent polariton system. Comparing experiments with simulation evidences that a reservoir population can be generated at low temperature, even if the excitation laser is tuned below the reservoir energy. This reservoir either originates from a population transfer of polaritons by means of an acoustic phonon absorption as suggested in [144] or from exciton-polariton scattering.

We have shown that a loss of coherent population $|P|^2$ does not imply a loss of population N of the full system. This explains the decrease of the upward threshold power when the reservoir population is increased since the energy blue shift is mostly defined by the total exciton population N . We also showed that the transmitted intensity is an indicator of the coherent polariton population whereas the blue shift is an indicator of the total exciton population. When the coherent population decreases, the optical response of the system is dominated by the incoherent population. This implies that evaluating the polariton density using the emission intensity will always underestimate the total polariton density present in the system. Since the latter determines the amplitude of the blue shift and the saturation of the oscillator strength, it should be considered carefully especially when trying to differentiate between polariton condensate and photon lasing thresholds.

Finally, we have shown that the downward threshold power is an indicator for the RID. Its value increases when the RID is more important on the system than the reservoir induced blue shift. This effect will need to be considered in schemes using polariton for high fidelity quantum light source and quantum information processing. Of course, due to the small binding energy of excitons in InGaAs and the small Rabi energy of our system, the effects described here occur at amazingly low temperatures. Similar effects will also show up, possibly at higher temperatures, in other polariton systems with a larger Rabi splitting.

Perspectives Part IV

7 Polariton lattices and beyond

In this chapter, we present ideas for future work based on multimode polaritons. We have discussed multimode polariton physics from the point of view of exciton coupling, and light confinement. The next step is to couple polariton modes themselves, which can be achieved by coupling the confined polariton modes of adjacent mesas. In the first part of the chapter, we present the work that we started for the study of polariton lattices. In the second part, we propose experiments that could be done based on the results obtained in this thesis (recommendation for the non-resonant condensation was already discussed in section 4.5).

7.1 Polariton lattices

The idea behind polariton lattices is to use 0D polaritons as building blocks for more complex structures. The advantage of using polariton over other photonic structures is the possibility to have interactions, hence to move toward the simulation of lattice Hamiltonians with interactions. For example, it was shown that spin-orbit coupling can be engineered using micropillar microcavities arranged in a hexagonal molecule [205]. Hexagonal lattices were also realised using the same micropillars, showing the usual Dirac cones of the graphene band structure [206], edge states [207], and polariton condensation in the bulk [206]. 1D arrays of mesas [208] and square lattices [44] have also been studied above the condensation threshold (mesa structure with GaAs/AlAs QWs).

Recently, a number of theoretical works have discussed the possibility to create topological edge states using lattice polaritons under a magnetic field, the so called topolariton [209–211]. Contrary to edge states in a honey comb lattice, topolaritons have chiral edge modes, where clockwise (counter clockwise) propagation only occurs for spin up (down) polaritons. These states are of great interest because they are topologically protected from disorder, hence disorder should not prevent their propagation.

In this section, we present preliminary work aimed at realising topolaritons experimentally.

We begin by a review of the clean room process developed to create polariton lattices before presenting some typical band structures measured as well as first results on square lattice under magnetic field.

7.1.1 Clean room process

We have discussed in section 1.3.2 the principle behind 3D photon confinement in microcavities, and presented two studies based on that principle (chapter 5, and 6). In this section, we give an overview of the clean room process needed to achieve fabricate mesas, that can also be used to realize lattices or more complex structures. The basic principle is the same as the one used for sample 1485, although the whole process was reoptimized, partly because of a new mask aligner (MA6), and also because of the poor reproducibility of the previous process. All this sample processing work, and optimization was done jointly with A. F. Adiyatullin.

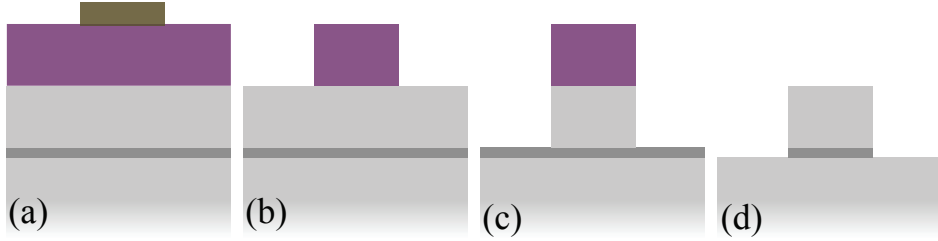


Figure 7.1 – Scheme of the photolithography and wet etching process (not to scale). The light gray represents GaAs, the dark gray is the AlAs etch stop, the purple layer is the photoresist, and the gold layer represents the mask. (a) Initial step after spin coating of the photoresist. (b) After removal of the exposed resist. (c) After the wet etching, and (d) after the removal of the photoresist and etchstop layer.

For the process, we use a half cavity (24 bottom DBR, λ -spacer with a single QW) where the top of the spacer is completed by six mono layers of AlAs followed by 6 nm of GaAs, as depicted in figure 7.1. First, we spin-coat a photoresist on top of the sample (resist S1805, 500 μm thickness). Using a photolithography mask, we expose the photoresist with a UV lamp (1.9s exposure on vacuum contact, to get the best resolution; exposure should be checked from time to time since the lamp intensity can change). The exposed photoresist is removed by dipping the sample in a developer solution (MF-319, 30-35s while stirring the beaker). This allows to transfer the patterns from the mask to the photoresist, as shown in figure 7.1 (b). We perform a wet etching to remove the exposed part of GaAs (see the clean room lab book for more detail on the procedure) using a 1:500 $\text{NH}_4\text{OH}:\text{H}_2\text{O}_2$ solution (15 s etch, while the solution is set in rotation at 700 rpm). This solution was optimized to have a selectivity of about 1:500 between AlAs and GaAs, which allows to stop the etch with only the six monolayers of AlAs. After the sample is rinsed in water, we let it exposed to air for 3 min. This part is crucial because it allows to oxidize the AlAs layer properly before we remove it in a single dip in a 1:1 $\text{HCl}:\text{H}_2\text{O}$

solution. If the oxidation is not long enough, the HCl solution creates holes in the samples up to 100 nm deep, which destroys the quality of the surface. The photoresist is removed in heated 1165 solution (60°C) for 10 min. Acetone can be used to remove the photoresist, but it leaves a thin film on the sample which can be problematic. After one last cleaning, we are left with structures of ~ 8 nm as shown in figure 7.1 (d). Finally, the growth of the top mirror is done after a hydrogen plasma cleaning (same procedure as described in section 4.4.2).

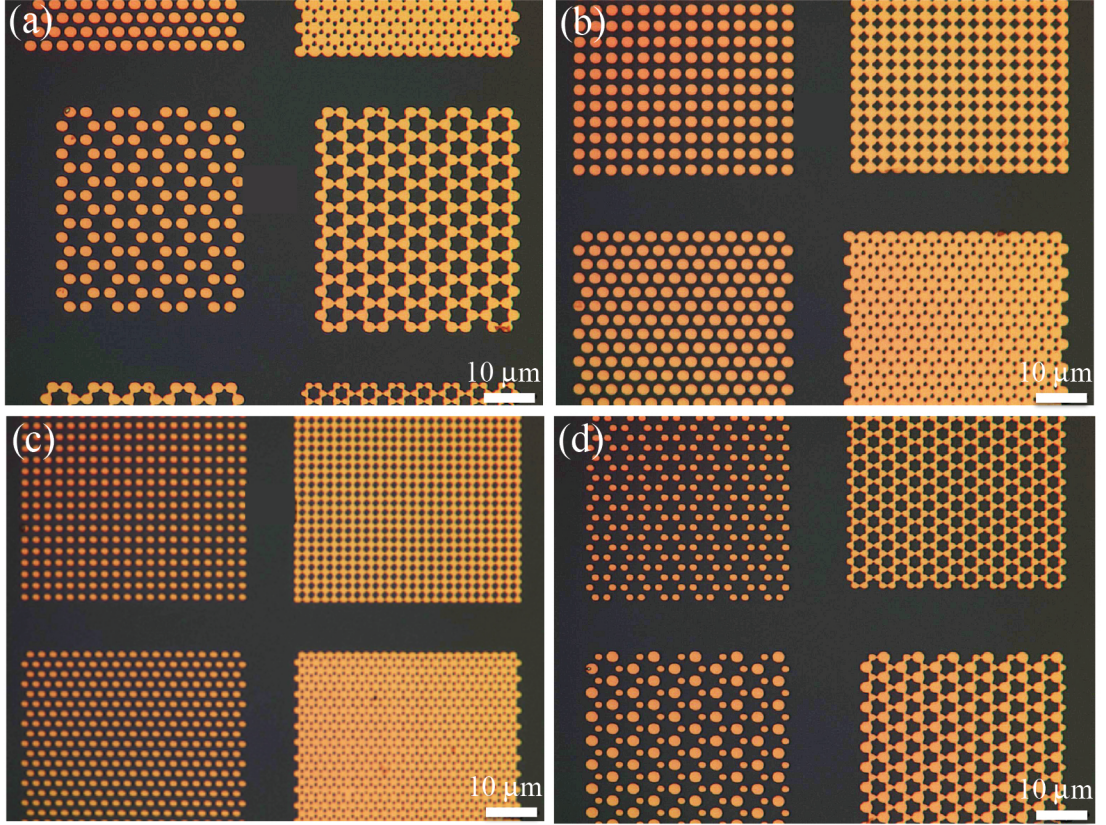


Figure 7.2 – Images of the mask used for the photolithography process for lattices designed with (a)-(b) 3 μm structures (measured to be 2 μm), and (c)-(d) 2 μm structures (measured to be 1 μm).

A new mask was designed to make polariton lattices with sites of either 2 μm or 3 μm in diameter, and different lattice constants. Images of the mask used are presented in figure 7.2. When the mask was made, the resolution was less than expected, and the writing beam was slightly oval, which affected the designs. The lattice sites were ~ 1 μm thinner than expected, and the gap between sites was increased. Hence, some lattices with larger gaps were not coupled while those with small 1 μm no longer confined light (for a sample designed for 3 μm mesa). For the lattices with touching mesas, the resulting design left small links between the sites as seen in the figures. These are the lattices which gave the best results, as we will see below. The effect of the beam shape on the

mask design can be seen mainly for the hexagonal lattices where the lattice seem to be stretched in the y direction.

Although a resolution of $0.5 \mu\text{m}$ can be reached with photolithography and a proper mask, a higher resolution should be achievable with e-beam lithography which implies replacing the first part of the process.

7.1.2 Measured band structures and real space distributions

We measured the band structures of our polariton lattices using the magnetic field setup and Fourier imaging while exciting non-resonantly (see section 4.2). By translating the lens in front of the spectrometer, we are able to scan the momentum space (first (FBZ) and second Brillouin zone), and extract the energy dispersion either along k_x , or k_y or to plot the momentum space for a given energy. The procedure is identical for the real space imaging except that we remove the lens L_3 from the detection path (see figure 4.1). The sample studied consist in a 20/24 top/bottom DBR λ -cavity with a single $\text{In}_{0.06}\text{Ga}_{0.94}\text{As}$ QW (F-043b-II, see appendix B). We present here the results for a square and for an hexagonal lattice of $2\mu\text{m}$ mesa. The lattice constant is $a = 3 \mu\text{m}$ (center to center), and a small link ($\sim 0.5 \times 1 \mu\text{m}$) remains between the mesas, as can be seen in figure 7.2 (a)-(b).

Square lattice

Figure 7.3 (a) presents the band structure along k_y measured for a 16×16 square lattice. The dispersion nicely shows the S band, and part of the P band. At higher energy, we see the polariton upper branch, which is almost identical to the 2D upper branch and corresponds to the 2D continuum (better seen in figure 7.7). This is an indication that the coupling seem to occurs between the confined polariton modes, and not between a photonic band and a QW exciton. If the latter case occurred, we would expect to have a lower and upper branch for both S band and P band, similarly to strong coupling inside a single mesa. For example, a photonic S band would couple to the exciton, the same way a 2D cavity dispersion is strongly coupled. In fact, the band structure measured can be seen as a 2D polariton dispersion with a gap opening at the edge of the FBZ ($k_{x,y} = \pm\pi/a$).

We can estimate the coupling strength by fitting the S band with the well-known analytical solution for the energy dispersion of a square lattice obtained in a tight-binding model with nearest neighbour coupling:

$$E(k) = -2J(\cos(k_x a) + \cos(k_y a)). \quad (7.1)$$

The fit is shown by the black curve in figure 7.3 (a), giving a coupling strength of $J = 110 \mu\text{eV}$. We can have a better look at the band structure of the lattice by plotting

the momentum space for specific energy positions as shown in figure 7.3 (b)-(c) for the S band, and (d) for the bottom of the P band. We notice that the maximum of the S band along k_x or k_y does not correspond to the maximum energy of the band, which is found instead at $E=1.45915$ eV. This is easily explained with equation 7.1; the maximum bandwidth occurs for $\cos(k_x a) = \cos(k_y a) = 1$, hence on the k_x - k_y diagonal.

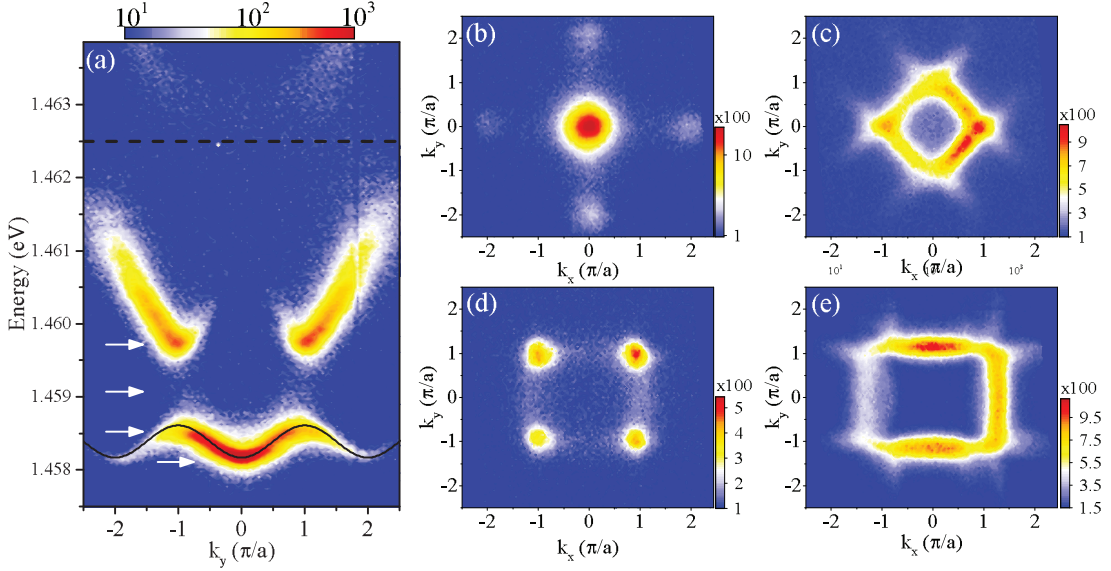


Figure 7.3 – (a) PL intensity of the band structure of a polariton square lattice measured along the y direction. The lattice sites have a diameter of $2 \mu\text{m}$, and a center to center distance of $3 \mu\text{m}$. The full black line is a fit using equation 7.1, and the dashed line shows the position of the QW energy. (b)-(e) Measured PL in momentum space for increasing energy, as indicated by the white arrows in (a). (b)-(d) corresponds to the S band while (e) is at the bottom of the P band. The color scale is logarithmic for (a)-(b), and linear for (c)-(e) because of the small intensity measured.

We can obtain additional information on the system by performing the real space tomography. In figure 7.4 (a), we show the real space profile of the PL intensity for a given slice taken along y at the center of the beam (dashed black line in figure 7.4 (c)). We notice that the PL intensity is located in two bands and that the distribution follows the periodicity of the lattice. Furthermore, the difference between the S band and P band is clearly seen if we follow the intensity at $y = 0$ as the energy increases. Since the S band has an even symmetry, the maximum of intensity is at the center of the lattice sites while it is a node for the P band due to its odd symmetry. This is clearly seen by comparing the real space distribution of polaritons in the S band (figure 7.4 (b)-(c)) to the distribution in the P band (figure 7.4 (d)-(e)). These figures also highlight that the polariton emission occurs in an area much larger than the excitation spot (located only of the central site). The intensity distribution is Gaussian which indicates minimal effect from disorder (from the lattice or optical). This would create inhomogeneous patterns with respect to the expected gaussian distribution.

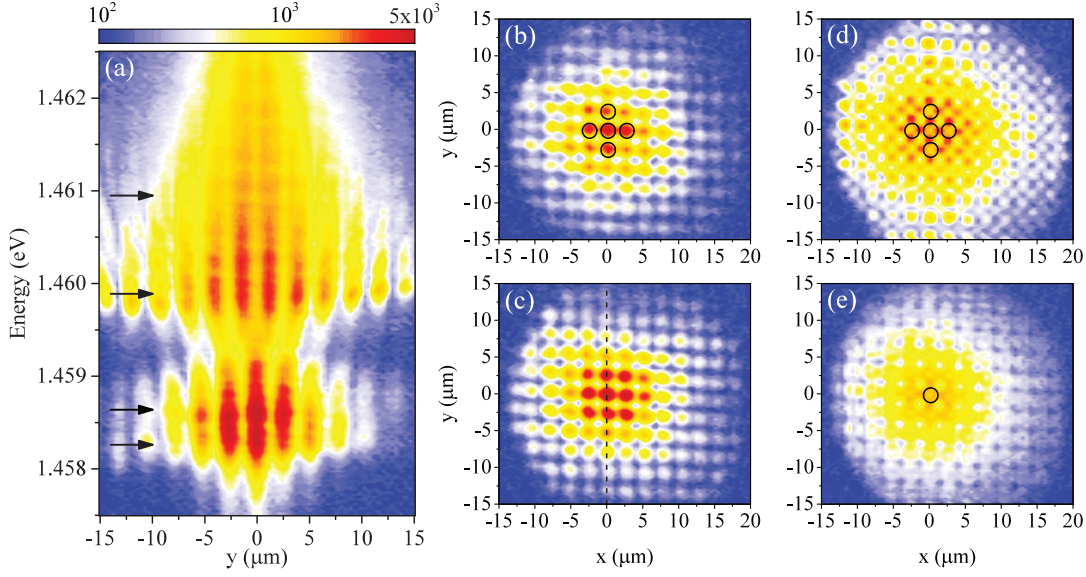


Figure 7.4 – (a) PL intensity of the real space distribution of a polariton square lattice measured along the y direction. The lattice is the same as in figure 7.3. (b)-(e) Measured PL in real space for increasing energy, as indicated by the black arrows in (a). (b)-(c) corresponds to the S band and (d)-(e) to the P band. The black circles have a diameter of $2\mu\text{m}$ and represent the position of individual lattice sites. The dashed black line indicates the position of the energy distribution shown in (a). The color scale is logarithmic and identical for each panels.

Hexagonal lattice

Figure 7.5 (a) shows the band structure measured for a hexagonal lattice along k_y , figure 7.5 (b) along k_x . Again, we can use the standard analytical solution for the band structure of graphene to fit the S band, and evaluate the coupling strength of our lattice. These equations read [206, 212]:

$$f(\mathbf{k}) = 2\cos(\sqrt{3}k_y a) + 4\cos\left(\frac{\sqrt{3}}{2}k_y a\right)\cos\left(\frac{3}{2}k_x a\right), \quad (7.2)$$

$$E(\mathbf{k}) = \pm t\sqrt{3 + f(\mathbf{k})} - t'f(\mathbf{k}), \quad (7.3)$$

were t , and t' correspond to the nearest and next nearest neighbour coupling constants. The fit is given by the black curve in figure 7.5 for both k_y , and k_x which gives $t = 150 \mu\text{eV}$, $t' = -0.047t$. These values are somewhat smaller compared to the ones obtained for the micropillar case ($t=250 \mu\text{eV}$, $t'=-0.08t$). Nonetheless, our value of t' agrees with the range of t' expected theoretically for graphene ($0.02t \leq |t'| \leq 0.2t$) [212]. This indicates that our polariton lattice gives a reasonable simulation of the band structure of graphene. The most important feature of this band structure is the crossing of linear dispersion

giving rise to the so-called Dirac points. In our case, the intensity reaches a maximum exactly at those points, as for the micropillar case [206]. The Dirac points are better seen in momentum space as shown in figure 7.5 (c). For comparison, figure 7.5 (d) shows the momentum space at the bottom of the band. These results indicate that we obtained the desired band structure, even though our photolithography mask was not optimal.

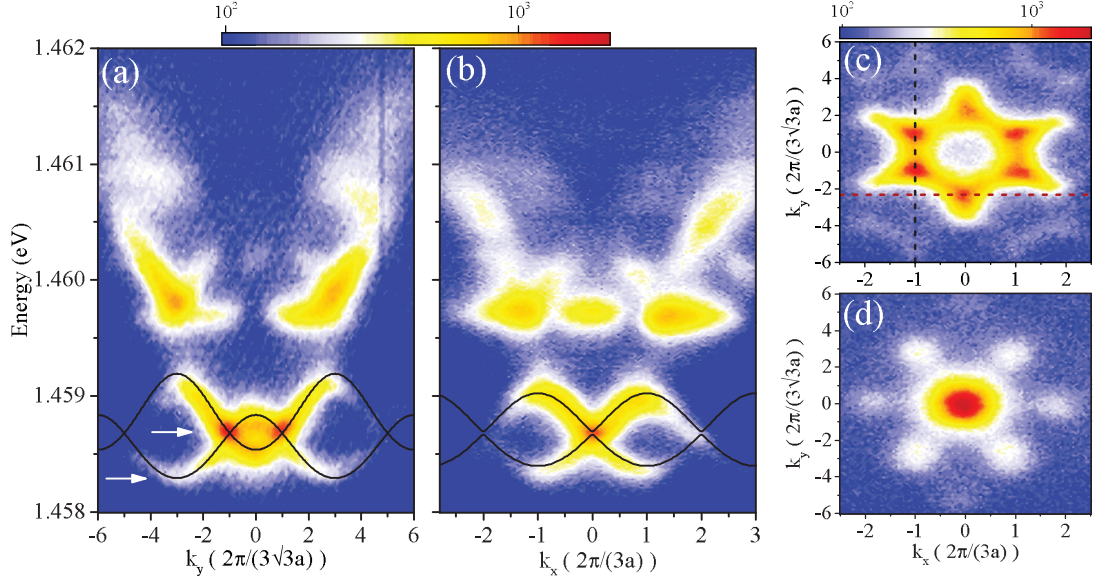


Figure 7.5 – PL intensity of the band structure of a polariton hexagonal lattice measured along the (a) y direction, and (b) x direction. The lattice sites have a diameter of $2 \mu\text{m}$, and a center to center distance of $3 \mu\text{m}$. (c)-(d) Measured PL in momentum space for decreasing energy as indicated by the white arrows in (a).

In figure 7.6 we present the real space distribution for specific energy position within the S band and P band. We observe similar features as for the square lattice. In figure 7.6 (a) we clearly see the transition from symmetric to antisymmetric wave functions as we move from the S band to the P band. Figure 7.6 (b)-(c) shows the real space profile taken at the bottom of the S band and at the energy of the Dirac points respectively. In the first case, the intensity seem to be located dominantly in pairs of mesas along the x direction while it follows a more circular profile for the latter. Comparing figure 7.6 (b) and (d) shows again that the intensity of the S band is located at the center of the mesas while it is the opposite for the P band. As we go to higher energy in the P band, the situation is even more clear as there is a minima of intensity at the center of the lattice sites (figure 7.6 (e)). Similarly to the square lattice, the intensity distribution is gaussian, over a spot of diameter of $\sim 30\mu\text{m}$ and there is no evidence for considerable disorder of the sample.

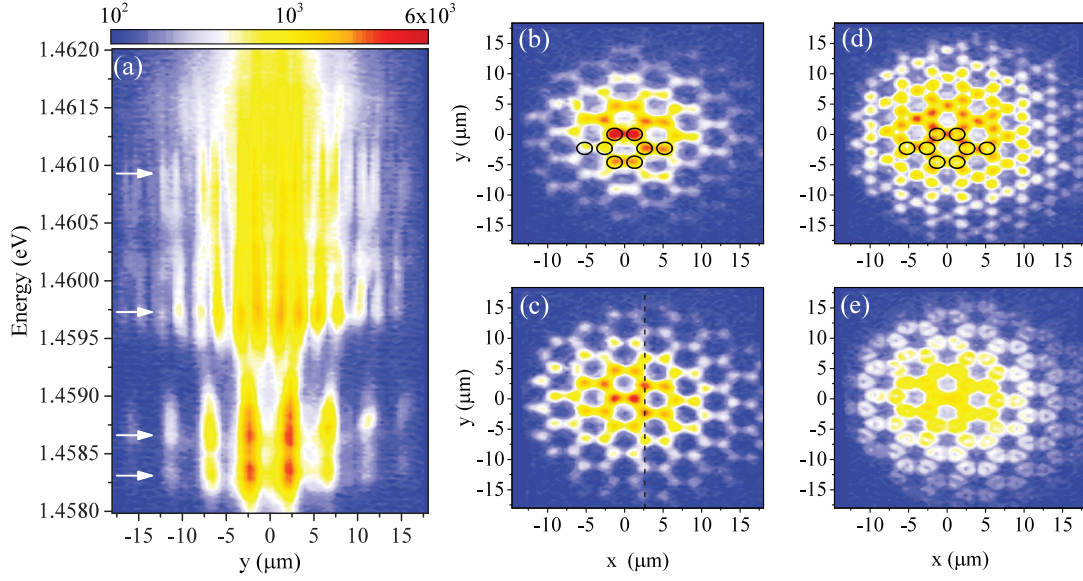


Figure 7.6 – PL intensity of the real space distribution of a polariton hexagonal lattice measured along the (a) y direction. The lattice is the same as in figure 7.5. (b)-(e) Measured PL in real space for increasing energy, as indicated by the white arrows in (a). (b)-(c) corresponds to the S band and (d)-(e) to the P band. The black circles have a diameter of $2\mu\text{m}$ and represent the position of individual lattice sites. The dashed black line indicates the position of the energy distribution shown in (a). The color scale is logarithmic and identical for each panels.

7.1.3 Square lattice under magnetic field

In figure 7.7, we present the polariton band structure for the square lattice when increasing the magnetic field from $B=0$ T to $B=5$ T. All measurements were performed at the center of the lattice, and analysed either in σ_+ or σ_- . As both polarization gave similar results (band shifted due to the Zeeman splitting), we present only the dispersion from the σ_+ polarization. All measurements were taken with the same excitation power and acquisition time. The weak interference pattern on the high energy background is caused by our spectrometer's grating.

Starting from the upper branch, we see the effect of the exciton diamagnetic shift which moves the exciton energy by ~ 2 meV. The most striking feature comes from the evolution of both S and P bands with increasing magnetic field. From $B=0$ T to $B=1$ T, we see almost no variation of the bands except for the effect of the exciton diamagnetic shift. At $B=3$ T, we start to see intensity coming from energy positions away from the bands: on the top of the S band, and on both sides of the dominant intensity of the P band. At our maximum magnetic field of $B=5$ T, the new states measured appear even brighter, although the intensity starts to decrease at the bottom of the S band.

The fragmentation of the bands is better seen in figure 7.8, where we compare both

bands measured at $B=0$ T, and $B=5$ T. We do not measure any structure at zero field, within almost three orders of magnitude of PL signal, while the new structure at high magnetic field is roughly ten times weaker than the brightest state. The fragmentation also occurs within the bands themselves, particularly in the P band. The energy splitting seen ($\Delta E_{Pband} = 130 \pm 20 \mu\text{eV}$) does not correspond to the interference background seen at high energy ($\Delta E_{back} = 230 \mu\text{eV}$). There is a slight decrease of linewidth for both bands at the edge of the first Brillouin zone of $\sim 30 \mu\text{eV}$, starting from $\text{FWHM}_{Sband-FBZ} = 200 \mu\text{eV}$, and $\text{FWHM}_{Pband-FBZ} = 230 \mu\text{eV}$ (the linewidth of the bottom of the S band stays constant at $\text{FWHM}_{Sb-k0} = 130 \pm 5 \mu\text{eV}$).

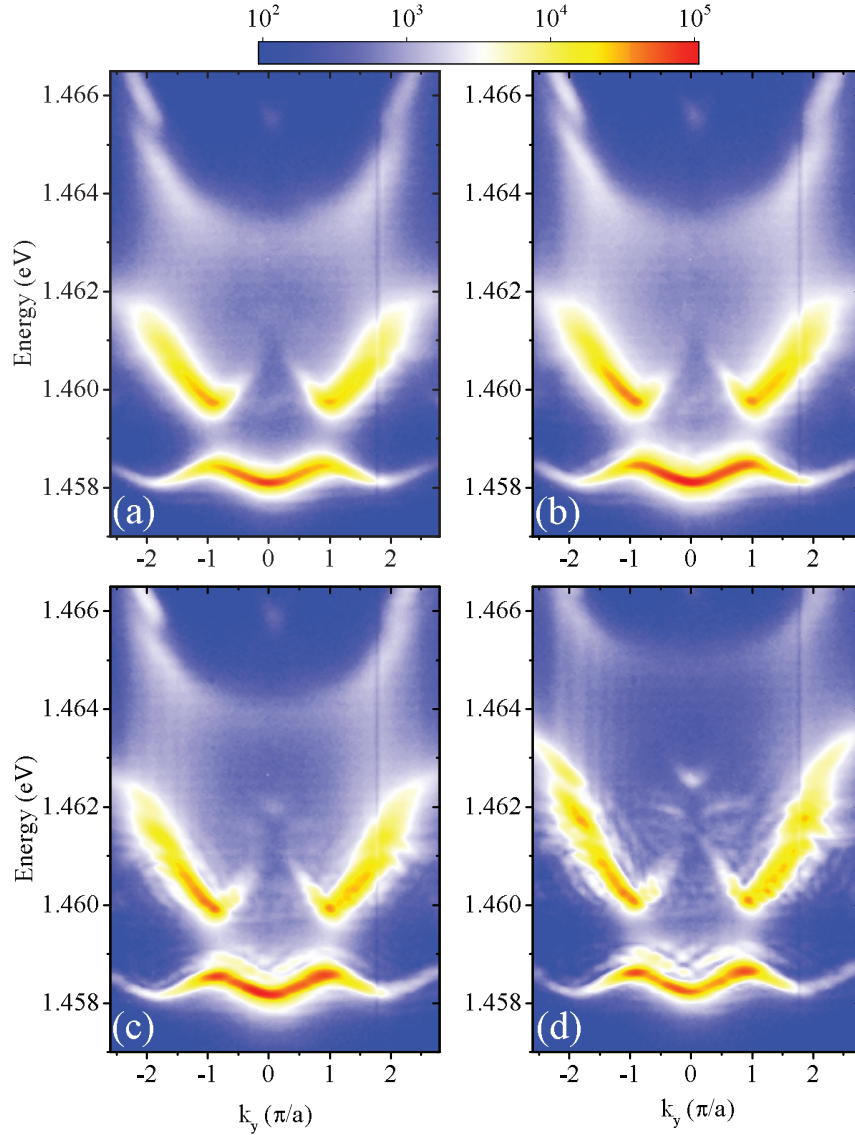


Figure 7.7 – Dispersion of a polariton lattice along k_y ($k_x = 0$) for increasing magnetic field measured in σ_+ polarization. (a) $B=0$ T, (b) $B=1$ T, (c) $B=3$ T, (d) $B=5$ T. All images have the same log color scale, and were taken for identical acquisition times.

Finally, we present in figure 7.9 the momentum space at $B=5$ T for two energy positions for both bands. The signal is saturated on purpose to emphasize the weaker signal. These figures indicate that the measured fragmentation within the FBZ seems to correspond to an interference pattern in k -space, specifically for the S band.

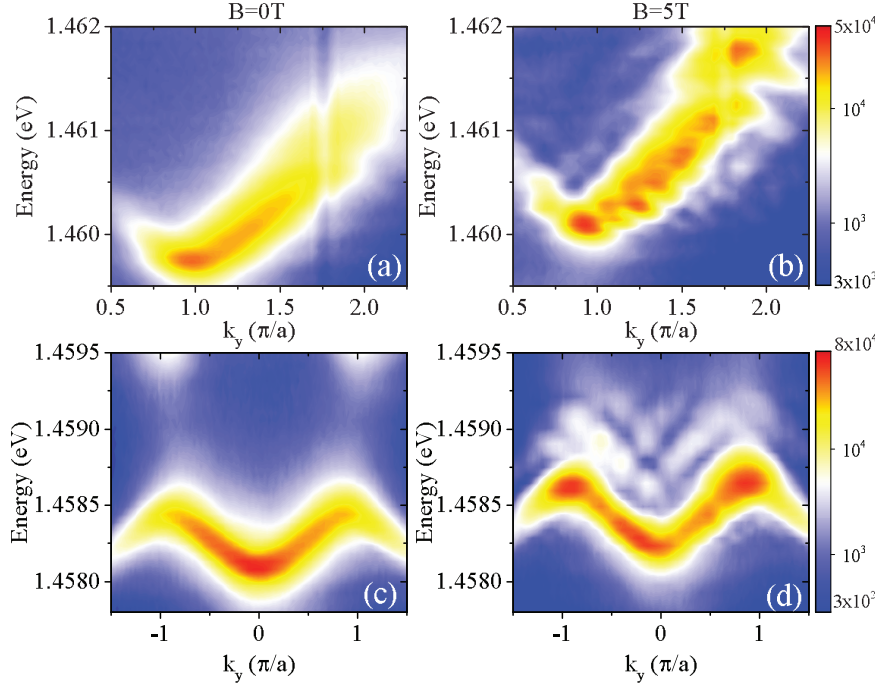


Figure 7.8 – Comparison of the dispersion at $B=0$ T, and $B=5$ T. (a)-(b) Close up of the P band at $k_y > 0$. (c)-(d) Close up of the S band. Figures from the same bands share the same log color scale.

Although these are preliminary results, we can list a number of points to investigate in order to determine the nature of this effect. First, we measure the same kind of fragmentation on hexagonal lattice but not for 2D polariton, 2D exciton, and for 0D polariton. This implies that the effect seen on the polariton lattice is either a consequence of the periodic potential, the finite size of our lattice or both. As the photon is not affected by a magnetic field, the effect must come from the exciton. The two known effects for the exciton (Zeeman and diamagnetic) come from its relative motion wave function (1S), while its center of mass part should not be affected. The fact that the polariton is delocalized over the lattice implies that the exciton center of mass wave function is delocalized as well. This should not modify its binding energy, meaning the polariton lattice should not affect how the exciton reacts to a magnetic field, although our results seem to indicate otherwise.

It is clear that the observed features go beyond a simple diamagnetic shift, or a Zeeman effect on the exciton, transposed to a polariton lattice. This would split the bands into

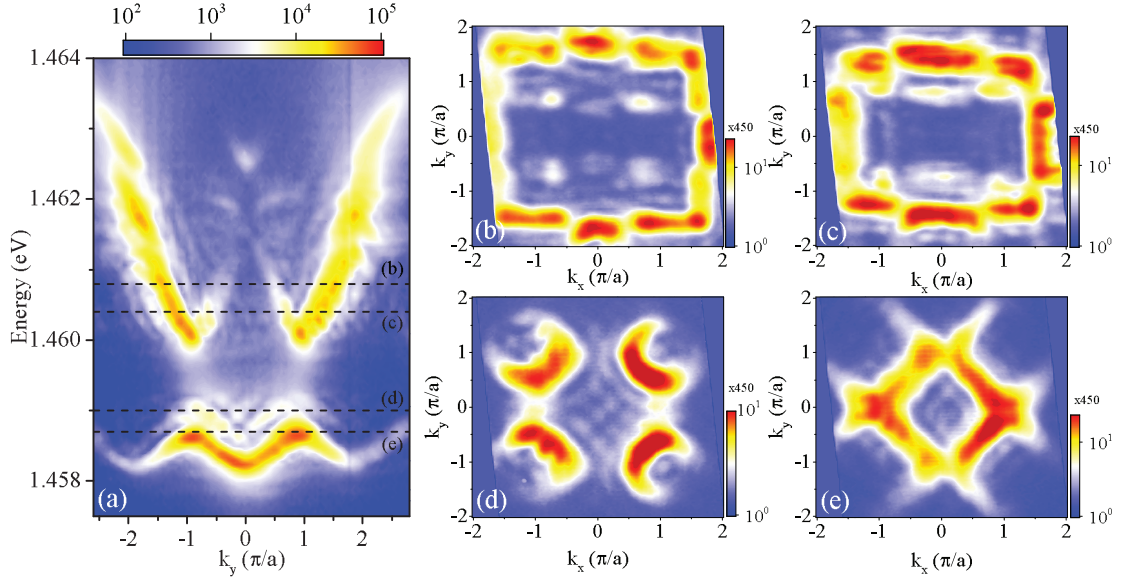


Figure 7.9 – (a) Dispersion of the polariton lattice along k_y ($k_x = 0$), for $B=5$ T (as in figure 7.7). (b)-(e) PL intensity in momentum space for the positions indicated by the dashed lines in (a). The intensity is shown in log color scale, and is saturated to emphasize the weaker signal.

two spin polarized bands, without creating new bands or states. The slight decrease of linewidth measured at the edge of the FBZ can be due to the diamagnetic shift, which increases the oscillator strength. The fragmentation of the bands cannot be due to the optical disorder of the sample; this causes an inhomogeneous broadening of the bands, and is independent of the magnetic field. Finally, it is not believed that the structures appearing in the band gap correspond to edge states, as there measurements were performed in the bulk.

The question is to understand whether these states are always present in the system and are evidenced with increasing magnetic field, or if the field changes the Hilbert space of the system, and increases the number of eigenstates. For the first case, we should investigate whether the finite size of our lattice can induce variations of the band structure compared to the infinite case. Intuitively, the finite size of the lattice is equivalent to cutting a Bloch wave function at the edges of the lattice. Mathematically, this is done by multiplying a plane wave with a rect function. The Fourier transform of the resulting wave function will create a sinc function centered at the k -vector of the plane wave. However, the periodicity of the sinc function is of the inverse of the lattice size ($\pi/(16a)$) which is much less than what we see in momentum space. Numerical simulations of the band structure of our finite size system should be done in order to confirm this.

Another possibility is that these states appear as a consequence of the lattice disorder due to inhomogeneity of the photolithography mask. Assuming that the states are already

present, this would imply that some phonon-polariton scattering increases by about two orders of magnitude from zero to 5 T while phonon-polariton scattering on the S and P band stays roughly constant. This hypothesis seems unlikely at the moment. Another possibility would be that we observe these states because the linewidth decreases with the field. However, the splitting that appears with the magnetic field is comparable to the linewidth (at the FBZ), hence the small decrease of linewidth is not enough to explain that we suddenly start to measure them. The linewidth past the FBZ does increase for the P band, meaning that there could be more than one state even at zero magnetic field. This could explain the fragmentation of the band, but not why new states appear in forbidden regions inside the P band.

Last, a change of Hilbert space with the field could be envisioned in a similar way as the band structure of a charged particle in a lattice is affected at large magnetic field (Hofstadter/Harper hamiltonian) [213,214]. In this regime, the ratio between the magnetic flux passing through a plaquette of the lattice, and the flux quanta dictates the number of eigenstates. Hence, this number varies with the field, but requires a large magnetic field since the area of a unit cell is quite small ($\sim 5.6 \times 5.6 \text{ \AA}^2$). In principle, this should not occur in our system because we are dealing with neutral quasiparticles. However, if the phase acquired by the electron, and the hole is not exactly the same, then the total phase might be considerable since the area of a single plaquette is relatively large ($3 \times 3 \text{ \mu m}^2$). A more complete theoretical model should be developed in order to see if this hypothesis is reasonable.

7.2 Proposals for future experiments

In the following, we give a brief description of experiments that could be done to follow up on the results obtained in the main chapters of the thesis. Recommendations for polariton condensation using InGaAs QWs were discussed in section 4.5. The topics are in the same order as the chapters.

7.2.1 Multimode interactions with coupled quantum well polaritons

We have seen in chapter 5 that, in a multimode polariton system, we must consider polariton-polariton cross interactions when we go beyond the linear regime. This was a consequence of the nature of the interaction (contact interaction), and the small energy difference between the polariton modes that allowed them to be excited all at once. In principle, such interactions should occur in the coupled quantum well polariton system, for instance in a pump probe experiment using femto-second pulses at positive detuning. Apart from the apparent complexity, there might not be that much interest for this study.

Where this system might prove more interesting is for studying polariton Feshbach

resonances [175], which occurs when the lower polariton energy comes into resonance with half of the biexciton energy. Two polaritons of opposite spin can create a biexciton which changes the interaction from repulsive to attractive as the lower branch becomes resonant with the biexciton. In the case of multiple QW polaritons, we can expect more than one biexciton channel, hence possibly more than one polariton Feshbach resonance. Another possibility would be to work at lower detuning in a situation where two polaritons from different branches can form a biexciton. In this case, both the biexciton absorption, and cross interactions should come into play.

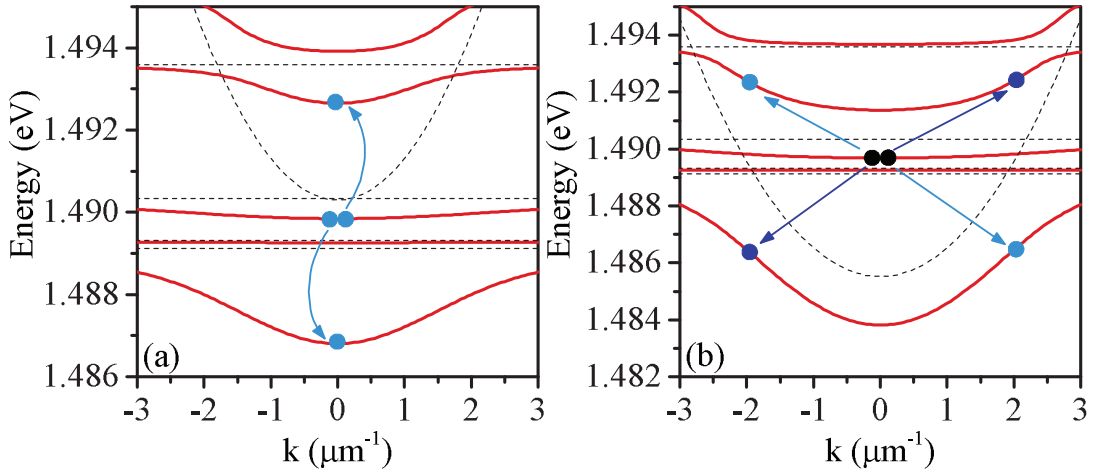


Figure 7.10 – Scheme for parametric scattering using coupled QW polaritons. (a) phase matching at $k = 0$. (b) Phase matching close to the magic angle.

Another use for these multiple polariton modes could be for parametric scattering experiments [5]. In the single mode case, parametric scattering occurs when exciting at the magic angle. Other schemes were proposed, and investigated using a triple cavity [21, 197] or multiple modes in a polariton microwire [215]. In the former case, the energy and phase matching conditions were tuned by changing the detuning of one cavity with respect to the other. Similarly to the triple cavity, it is possible to get phase matching with our sample either with all beams at $k = 0$ or for two degenerate paths at a given $\pm k$ (see figure 7.10). Here, the phase matching will occur at a specific position on the sample i.e. negative detuning for $k = 0$ scattering, and more positive for the other scheme. However, as for the triple cavity experiment, it is doubtful that entangled photon pairs can be achieved using the second scheme, mainly because of dephasing, and creation of a reservoir either by the same scattering discussed in chapter 6 or because of relaxation for the upper branches to exciton in the bottleneck.

7.2.2 Crossover between spatial multistability and polariton lasing

In chapter 5, we have used a large mesa to study the effect of polariton-polariton cross interactions. In this experiment, the system was mainly governed by the interactions; phonon relaxation between the modes was almost absent. A previous study (also discussed in that chapter) investigated polariton lasing [163], in the same experimental configuration but using a small mesa ($3\ \mu\text{m}$). The study showed that, after the upward threshold originating from the highest energy state, there was a population transfer between the lower polariton modes, that was explained in terms of bosonic stimulation. Hence, it seems that in this case, the system is mainly driven by phonon relaxation, and cross interactions have less effect. The system was simulated using a single GPE for the resonantly driven mode, while the others were Boltzmann equations, which included bosonic stimulation. However, the effect of cross interaction was not properly considered on the lower polariton modes, which, as we have seen, affects the population of each modes as well. It would be interesting to see how the system evolves between these two limits. This could be achieved, by designing a series of mesas while increasing the diameter from $3\ \mu\text{m}$ to $9\ \mu\text{m}$ (in steps of $1\ \mu\text{m}$). By repeating the same experiment on each mesa (at approximately the same cavity detuning), it should be possible to see this crossover between the two regimes. This experiment could also be useful to help build a theoretical model which takes into account coherence, interactions, and phonon scattering all at once.

7.2.3 Biexciton, exciton reservoir, and RID

In both experiments on polariton bi-multistability in mesas, we have purposely avoided effects of spinor interactions by exciting the system with circularly polarized light. Two effects have been shown to come into play when spin is involved, namely the appearance of a multistability when the degree of polarization of the excitation laser is scanned [148], and the effect of biexciton formation [158] (see also [160]). The latter work showed that the multistability was different if the polariton ground state was either slightly above the biexciton or few meV below. Losses seemed to be induced if the laser energy was set closer to the biexciton energy for the positive cavity detuning case. As the study was limited to two cavity detunings only, it would be interesting to study in a more gradual way the effect of getting into resonance with the biexciton (similar to the polariton Feshbach resonance [175]). This could be achieved either by scanning a number of mesas while keeping the laser detuning fixed. Conversely, if the polariton ground state is slightly below the biexciton resonance, and within less than $\Delta/3$ from it (where Δ is the laser detuning, see section 5.1), we should cross the Feshbach resonance as the polariton ground state blue shifts, and before reaching the upward threshold. The effect could be seen by comparing bistability curves for circularly or linearly polarized excitation.

Based on our work on dephasing it would be interesting to see how the GPE with biexciton reservoir formalism compares to a spinor EBE. As the latter includes direct and cross

EID terms for both exciton spin polarization, a spinor EBE might mimic similar effects as the biexciton losses. Increasing the population of the orthogonal spin (say σ_-) compared to the other (σ_+) will change the EID, which will cause an increase of the population N_{\pm} . This population can act as a reservoir with a longer lifetime, the same way as the biexciton equation in the spinor GPE (equations 5.8). Of course, the idea here is not to doubt on the effect of the biexciton resonance, but to investigate in greater detail two different sources of dephasing. We saw in chapter 6 that there was a considerable discrepancy between the GPE and EBE formalism when dephasing is scanned. We can hope to see similar effects regarding the biexciton, which might be visible if we plot the threshold power, and intensity as we cross the resonance either in a single blue shift or because of the cavity detuning.

7.2.4 "Synthetic" gauge fields in polariton lattice

This last proposition is inspired by recent results obtained using cold atoms in an optical lattice [216,217]. The idea is to use neutral particles in a lattice to simulate a charged particle in a strong magnetic field, which give rise to the so-called Hofstadter butterfly [213] (see chapter 2 of ref. [214] for a clear overview on the subject). A charged particle acquires a phase when moving in a closed loop in a high magnetic field (Aharonov-Bohm effect). For a charge particle in a lattice, the band structure follows the self-similarity characteristic of the Hofstadter butterfly if the magnetic flux within a given plaquette is comparable to the magnetic flux quanta $\Phi_0 = h/e$. The principle is to prepare cold atoms in an optical lattice in such a way that they acquire a considerable phase shift as they hop between sites in a closed loop. If this phase shift is identical for each plaquette, then the system is equivalent to a charged particle in a strong magnetic field.

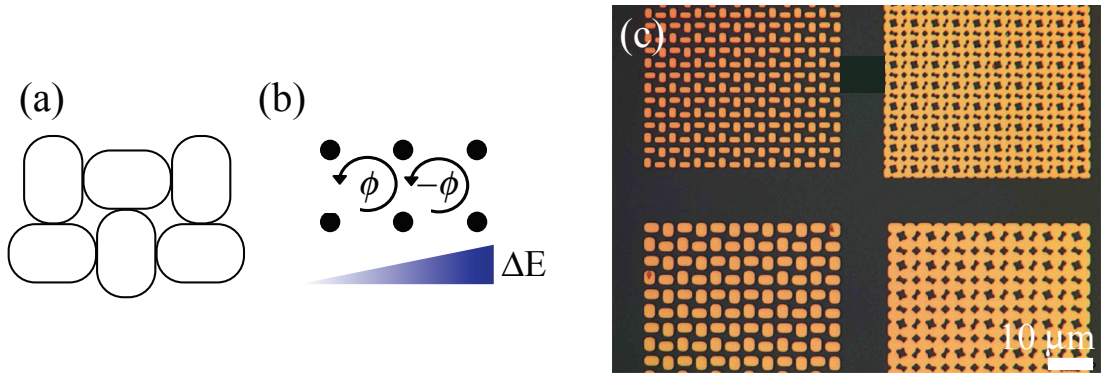


Figure 7.11 – (a) Scheme of two plaquettes for an square lattice with oval sites. (b) Corresponding phase (from the ground state polarization) acquired for the two plaquettes in (a). The triangle indicates a potential that might be used to compensate the staggered flux. (c) Image of the mask where the design was transposed, with an unwanted position offset between half of the lattice sites.

The idea for polaritons would be to use the phase shift associated to a change in

polarization to create the synthetic gauge field. The idea is to use a square lattice with rectangular sites instead of circular as it is shown in figure 7.11 (a). The use of an rectangular mesa causes the polariton ground state to split into two linearly polarized states. If we consider only the ground state, then creating a square lattice following the pattern in figure 7.11 would mean that hopping from one site to an adjacent one causes a $\pi/2$ phase shift. The trick would be to use a real magnetic field to change the polarization from linear to circular by the Zeeman effect. That way, we scan the phase shift from 2π to 0, which is the complete span of the Hofstadter butterfly. Of course, this means that we need a real magnetic field to create a synthetic magnetic field.

There are a few important aspects that need to be addressed to see whether the simulation described can actually work. The first problem is that we obtain a staggered flux if we look at the phase shift for a complete lattice. If we acquire a phase shift of $+\phi$ when hopping from a horizontal site to a vertical one, then hopping in the same direction from vertical to horizontal yields a phase shift of $-\phi$ (see figure 7.11 (b)). In the cold atom system, this was compensated by using a tilted optical lattice such that there was an energy shift associated to the phase shift. Combining both allowed to recover the same phase shift for each plaquette. For the case of polaritons, this could be done either by engineering the cavity wedge such that the energy shift occurs naturally from the sample. However, since the wedge is usually fixed by the growth conditions, this might not be so practical. Another possibility is to use a large gaussian beam focused on one side of the lattice to excite quasi resonantly the whole lattice. That way, we can create an asymmetric energy shift using the polariton-polariton interactions. In this case however, we would need to look for weak signal below the laser energy to measure the band structure. Finally, all of this resides in a single particle hopping formalism. Proper simulation of the system might be necessary to verify whether the effect can be measured at the mean field level in our polariton system.

Conclusions

This thesis was been devoted to the study of multimode polaritons in samples based on InGaAs QWs. Multimode coupling, and interactions can occur in a variety of contexts: by coupling many exciton states to a single cavity mode, by creating a number of cavity modes due to lateral light confinement, or even by coupling spatially separated confined polariton modes. These systems have been investigated in the linear and non-linear regime, both experimentally, and theoretically. The work was separated in two main parts, the first one focusing on non-resonant excitation of 2D multimode polaritons, and the second on resonant excitation of 0D confined polariton modes. In the following, we recall the main results and conclusions for each of the studies presented.

In chapter 3, we studied in the linear regime the properties of a microcavity sample with embedded stacks of three swallow InGaAs QWs. We first demonstrated using PL, and PLE that the QWs were coupled with one another, giving rise to a series of excitonic states. These levels correspond to bound states of electrons, and holes delocalized over the whole QW stack. Numerical simulations allowed to compute the electron and hole wave functions, and the relative oscillator strengths of the optical transitions. When placed inside a microcavity, we observed a series of polariton modes corresponding to the strong coupling of all excitonic states with a single cavity mode. Having access to the wave function allowed us to evaluate the relative coupling strengths of each mode, and to fit our data using a coupled oscillator model. We demonstrated that the Rabi splitting of the highest coupled exciton state of the QW stack was less than the one obtained from a single QW in a λ -cavity. Finally, we compared the relative coupling strengths to the ones obtained by fitting them manually. We showed that the binding energy of the different exciton states was not the same, hence that the spatial extension in the growth direction had an effect on the Coulomb interaction that binds the excitons.

In chapter 4, we investigated the non-linear properties of InGaAs QW based microcavities when excited non resonantly. For all samples tested, we measured a single intensity threshold corresponding to VCSEL lasing. We have investigated samples with low In content (3-5 %) with stacks of 3 QWs, with either 9 or 12 QWs in total, and 20/24 DBRs. We also tested microcavity with high In content with 12 or 15 QWs in stacks of two or three respectively. This way, we reduced the inter well coupling, and improved

phonon scattering, but did not obtain polariton condensation. In order to hopefully reach condensation with InGaAs QWs, the optical disorder of the top DBR should be improved, and the placement of the QWs inside the spacer should be optimized to reach the highest coupling strength. It should be interesting to compare the Mott density between GaAs and InGaAs QWs to understand whether the latter system is limited by the saturation density of individual QW. This could help for future microcavity designs or to understand if we need a larger number of QWs in the microcavity, which will inevitably decrease the coupling strength.

In chapter 5, we studied laterally confined 0D polariton excited quasi resonantly. We performed an experiment where five confined polariton modes of a $9\text{ }\mu\text{m}$ mesa are excited with a *cw* laser. As we cycled the power, we measured a series of intensity thresholds of the transmitted laser, leading to a polariton multihysteresis curve. For each of the stable states on the curve, the transmitted laser had a well-defined spatial distribution, each time corresponding to one of the confined polariton modes. Therefore, we created a spatially multistable system, where the transverse spatial profile of the transmitted laser can be switched simply by changing its power. We demonstrated experimentally that the main ingredient for the effect to work was the repulsive cross interactions between the polariton modes. These cross interactions forbid the system to have more than one polariton mode locked to the laser at one time. Finally, we developed a multimode version of the GPE in the exciton photon basis to show the occurrence of polariton-polariton cross interactions. We successfully simulated our system with this model, and confirmed that the observed multistability was a consequence of these cross-interactions.

Finally, in chapter 6, we investigated the effect of dephasing in 0D polariton system. We used the polariton hysteresis generated by exciting resonantly a single polariton mode confined in a $3\text{ }\mu\text{m}$ mesa as a sensitive tool to study the effect of dephasing. We measured the polariton bistability under two experimental conditions: as a function of temperature, and at a fix temperature while exciting non resonantly the sample with a second laser. In both cases, the upward threshold decreased significantly while the downward threshold was almost unaffected until the collapse of the bistability. The transmitted intensity also decreased steadily until the collapse. We simulated accurately this behavior using the EBE formalism, including terms to simulate an exciton reservoir. We showed that the stability of the downward threshold with temperature or non-resonant excitation was a clear proof of reservoir induced decoherence. Furthermore, our theoretical investigation demonstrated that the upward threshold power was an indicator of the total exciton population of the system while the transmitted intensity above threshold was an indicator of the coherent population. Our results have an important implication for the investigation of polariton systems in general: the exciton density will be underestimated if it is evaluated only using the coherent emission.

We believe the results obtained in this thesis have paved the way for a better understanding of the rich physics of multimode polaritons. As the research of microcavity is aiming

7.2. Proposals for future experiments

more and more on the study of complex structures, the effect of multimode coupling, and interactions should inevitably be considered in future works. In that regard, we have proposed in chapter 7 some ideas for the continuity of the work presented.

Appendix **Part V**

A Derivation of multimode EBE and GPE

In chapter 5, we made a derivation of the multimode exciton-photon Hamiltonian based on the multiple modes of the mesa. If we express for the exciton-exciton interaction strength as a simple mode dependent coupling constant (we do not use the expression given by equation 5.16, which is specific to the mesa), this Hamiltonian is:

$$H = H_0 + H_{lm} + H_c + H_{sat} \quad (\text{A.1})$$

$$H_0 = \sum_i E_{xi} x_i^\dagger x_i + \sum_i E_{ci} c_i^\dagger c_i \quad (\text{A.2})$$

$$H_{lm} = \frac{1}{2} \sum_i \Omega_i \left(x_i^\dagger c_i + x_i c_i^\dagger \right) \quad (\text{A.3})$$

$$H_c = \sum_{ij} g_{ij} x_i^\dagger x_j^\dagger x_i x_j \quad (\text{A.4})$$

$$H_{sat} = - \sum_{ij} g_{pij} \left(x_i^\dagger x_j^\dagger x_j c_i + x_i^\dagger x_i x_j c_j^\dagger \right) \quad (\text{A.5})$$

where H_0 is the single particle energy, H_{lm} is the light-matter part, H_c is the exciton-exciton interaction and H_{sat} is the effect of phase space filling on the exciton-photon coupling. This Hamiltonian represents any case of multimode coupling between exciton and photon. For instance, if $i, j = 1, 2$, this gives the spinor interactions with $g_{11} = g_{22} = \alpha_1$ and $g_{12} = g_{21} = \alpha_2$. The mean field of this Hamiltonian will give in the coherent limit the spinor GPE presented in section 5.1.3, equations 5.8 [158]. Another possibility is to assume that each indices correspond to an exciton state along its dispersion. In this case, the light-matter coupling will be zero if the state is above the light cone, but cross interactions and saturation can be expected from these states. This scenario correspond to the interaction of polaritons with an exciton reservoir. Of course, extra care should be taken to assure momentum conservation between states i, j as well as considering the dependence on the momentum exchange of the exciton-exciton interaction [57]. None of these effect are

Appendix A. Derivation of multimode EBE and GPE

explicitly considered in this effective Hamiltonian. For an effective interaction with a reservoir, we can simply assume two exciton modes, one in strong coupling, and the other representing the effective reservoir population. This is the approach used in chapter 6 to derive the reservoir terms included in EBE (see equation 6.3), and from this perspective, the density dependent coupling is well justified within this approximation.

In the following, we give an extended derivation of the mean field equations, that will give the multimode EBE and multimode GPE in the coherent limit. First, we need a series of multimode bosonic commutation relation for the exciton polarization equations:

$$[a_i^\dagger, a_m] = -\delta_{im} \quad (\text{A.6})$$

$$[a_i, a_j] = 0 \quad (\text{A.7})$$

$$[a_i^\dagger a_i, a_m] = -a_m \delta_{im} \quad (\text{A.8})$$

$$[a_i^\dagger a_j^\dagger a_i, a_m] = -2a_m^\dagger a_m \delta_{ijm} - a_j^\dagger a_m \delta_{im \neq j} - a_i^\dagger a_i \delta_{jm \neq i} \quad (\text{A.9})$$

$$[a_i^\dagger a_i a_j, a_m] = -a_m \delta_{ijm} - a_j a_m \delta_{im \neq j} \quad (\text{A.10})$$

$$[a_i^\dagger a_j^\dagger a_i a_j, a_m] = -a_j^\dagger a_j a_m \delta_{im \neq j} - a_i^\dagger a_i a_m \delta_{jm \neq i} \quad (\text{A.11})$$

where δ_{ijm} and δ_{im} are Kronecker deltas. Second, the ones needed for the incoherent population:

$$[a_i^\dagger a_i, a_m^\dagger a_m] = 0 \quad (\text{A.12})$$

$$[a_i, a_m^\dagger a_m] = a_m \delta_{im} \quad (\text{A.13})$$

$$[a_i^\dagger, a_m^\dagger a_m] = -a_m^\dagger \delta_{im} \quad (\text{A.14})$$

$$[a_i^\dagger a_i a_j, a_m^\dagger a_m] = a_i^\dagger a_i a_m \delta_{jm}, \forall i \quad (\text{A.15})$$

$$[a_i^\dagger a_j^\dagger a_i, a_m^\dagger a_m] = -a_i^\dagger a_i a_m^\dagger \delta_{jm}, \forall i \quad (\text{A.16})$$

$$[a_i^\dagger a_j^\dagger a_i a_j, a_m^\dagger a_m] = 0 \quad (\text{A.17})$$

These commutation relations already show the cross interaction terms (of the type $a_i^\dagger a_i a_m \delta_{jm}$) that will occur in the mean field equations. We begin with the derivation of the equation of motion for the exciton operator in a given mode i :

$$-i\hbar\dot{x}_i = [H, x_i] \quad (\text{A.18})$$

$$= [H_0, x_i] + [H_{lm}, x_i] + [H_c, x_i] + [H_{sat}, x_i] \quad (\text{A.19})$$

$$= \sum_j E_{xj} [x_j^\dagger x_j, x_i] + \frac{1}{2} \sum_j \Omega_j \left(c_j [x_j^\dagger, x_i] + c_j^\dagger [x_j, x_i] \right) \\ + \sum_{jk} g_{ij} [x_j^\dagger x_k^\dagger x_j x_k, x_i] \\ - \sum_{jk} g_{pij} \left(c_j [x_j^\dagger x_k^\dagger x_k, x_i] + c_k^\dagger [x_j^\dagger x_j x_k, x_i] \right) \quad (\text{A.20})$$

$$i\hbar\dot{x}_i = E_{xi} x_i + \frac{\Omega_i}{2} c_i + 2 \sum_j g_{ij} x_j^\dagger x_j x_i \\ - \sum_j 2^\alpha g_{pij} x_j^\dagger x_j c_i - \sum_{j \neq i} g_{pij} c_j x_j^\dagger x_i \quad (\text{A.21})$$

Here $\alpha = 1$ if $i = j$ and zero otherwise. For the exciton number operator of a given mode i :

$$-i\hbar\dot{x}_i^\dagger x_i = [H, x_i^\dagger x_i] \quad (\text{A.22})$$

$$= [H_0, x_i^\dagger x_i] + [H_{lm}, x_i^\dagger x_i] + [H_c, x_i^\dagger x_i] + [H_{sat}, x_i^\dagger x_i] \quad (\text{A.23})$$

$$= \sum_j E_{xj} [x_j^\dagger x_j, x_i^\dagger x_i] + \frac{1}{2} \sum_j \Omega_j \left(c_j [x_j^\dagger, x_i^\dagger x_i] + c_j^\dagger [x_j, x_i^\dagger x_i] \right) \\ + \sum_{jk} g_{ij} [x_j^\dagger x_k^\dagger x_j x_k, x_i^\dagger x_i] \\ - \sum_{jk} g_{pij} \left(c_j [x_j^\dagger x_k^\dagger x_k, x_i^\dagger x_i] + c_k^\dagger [x_j^\dagger x_j x_k, x_i^\dagger x_i] \right) \quad (\text{A.24})$$

$$i\hbar\dot{x}_i^\dagger x_i = +\frac{\Omega_i}{2} (c_i x_i^\dagger - c_i^\dagger x_i) + \sum_j g_{pij} (x_j^\dagger x_j x_i c_i^\dagger - x_j^\dagger x_j x_i^\dagger c_i) \\ = (c_i x_i^\dagger - c_i^\dagger x_i) \left(\frac{\Omega_i}{2} - \sum_j x_j^\dagger x_j \right) \quad (\text{A.25})$$

Appendix A. Derivation of multimode EBE and GPE

Lastly, for the photon operator:

$$-i\hbar\dot{c}_i = [H, c_i] \quad (\text{A.26})$$

$$= [H_0, c_i] + [H_{lm}, x_i] + [H_c, x_i] + [H_{sat}, x_i] \quad (\text{A.27})$$

$$\begin{aligned} &= \sum_j E_{cj} [c_j^\dagger c_j, x_i] + \frac{1}{2} \sum_j \Omega_j \left(x_j^\dagger [c_j, c_i] + x_j [c_j^\dagger, c_i] \right) \\ &\quad - \sum_{jk} g_{pij} \left(x_j^\dagger x_k^\dagger x_k [c_j, c_i] + x_j^\dagger x_j x_k [c_k^\dagger, c_i] \right) \end{aligned} \quad (\text{A.28})$$

$$i\hbar\dot{c}_i = E_{ci}c_i + \frac{\Omega_i}{2}x_i - \sum_j g_{pij}x_j^\dagger x_j x_i \quad (\text{A.29})$$

We then define the mean fields as:

$$N_i = \langle x_i^\dagger x_i \rangle, \quad (\text{A.30})$$

$$P_i = \langle x_i \rangle, \quad (\text{A.31})$$

$$E_i = \langle c_i \rangle. \quad (\text{A.32})$$

As we mentioned in section 5.5, we use the following approximations which keeps the number of particle within each mode: $\langle \hat{x}_i^\dagger \hat{x}_i \hat{x}_j \rangle \cong \langle \hat{x}_i^\dagger \hat{x}_i \rangle \langle \hat{x}_j \rangle$ and $\langle \hat{x}_i^\dagger \hat{x}_i^\dagger \rangle = \langle \hat{x}_j \hat{x}_j \rangle = 0 \forall (i, j)$. Applying these mean field conditions on equations A.21, A.25, and A.29 and adding the modes linewidths gives the multimode EBE:

$$i\hbar\dot{N}_i = -i\Gamma_{xi} - 2\text{Im}(P_i E_i^*) \left(\frac{\Omega_i}{2} - \sum_j g_{pij} N_j \right), \quad (\text{A.33a})$$

$$i\hbar\dot{P}_i = \left(E_{xi} - i\gamma_{xi} + \sum_j g_{ij} N_j \right) P_i + \left(\frac{\Omega_i}{2} - \sum_j 2^\alpha g_{pij} N_j \right) E_i, \quad (\text{A.33b})$$

$$i\hbar\dot{E}_i = E_{ci} - i\gamma_{ci} + \left(\frac{\Omega_i}{2} - \sum_j g_{pij} N_j \right) P_i, \quad (\text{A.33c})$$

where we have used $E_i^* P_i - P_i^* E_i = 2i\text{Im}(P_i E_i^*)$ and a factor 2 is included in g_{ij} . The term $\alpha = 1$ if $i = j$ and zero otherwise. If we include a real and imaginary part to the exciton-exciton interactions, we get the following exciton linewidth which include EID from all modes and pure dephasing γ^* :

$$\gamma_{xi} = \Gamma_{xi}/2 + \sum_j g'_{ij} N_j + \gamma^*. \quad (\text{A.34})$$

It is easy to see that we recover EBE with the reservoir (equations 6.3) if the summation is over two modes, one exciton in strong coupling, the other being an effective reservoir

with no coupling to light. In the coherent limit these will give the multimode GPE (equations 5.15). The single mode limit gives the EBE (equations 1.46) and the GPE (equations 1.47) presented in section 1.5.

B Description of the samples

In this appendix we summarise the structure of all of the samples presented in this thesis as well as the section where they are first mentioned. The first table is for QW samples, the second for the microcavity samples. All samples were grown by F. Jabeen except for sample 1485 that was grown by F. Morier-genoud and processed by O. El Daif. All the values given are the theoretical thicknesses that were expected for the growth.

Table B.1 – Description of the QW samples. T is for QW thickness and S is for spacer thickness.

Name	In content (%)	Number of wells	T (nm)	S (nm)	chapter
D-03	4.5	1	9	–	2.2.2
D1-12-10-13C	3	3	12	10	3.1
D-13	5	1	9	–	4.3.4
D-15	5	3	9	8	4.3.4
D-34	9	1	7	–	4.4.1
D-35	9	3	7	12	4.4.1
D-36	9	3	7	6	4.4.1
D-37	9	3	7	10	4.4.1
D-39	13	1	7	–	4.4.1
D-40	11	1	7	–	4.4.1

Appendix B. Description of the samples

Table B.2 – Description of the microcavity samples. The number of DBR pairs are noted top/bottom, T is for QW thickness and S is for spacer thickness. The number in parentheses in the QW/stacks indicates the total number of QWs.

Name	DBR	spacer	In (%)	# stacks	QW/stack	T (nm)	S (nm)	section
D-49	20/24	λ	5	1	1	8.5	–	2.2.3
D-55	20/24	λ	5	1	1	8.5	–	2.2.3
E-65	20/24	λ	10	1	1	9	–	2.2.3
D1-12-12-14C	20/23	2λ	3	3	3 (9)	12	10	3.1
D1-13-02-15C	20/23	2λ	3	3	3 (9)	12	10	4.3
B-31	20/24	$5\lambda/2$	5	4	3 (12)	8	12	4.4.2
F-40b	27/30	$7\lambda/2$	10	6	2 (12)	8	12	4.4.2
F-46b	27/30	$5\lambda/2$	10	5	3 (15)	8	15	4.4.2
1485	21/22	λ	4	1	1	8	–	5.2.2
F-43b-II	20/24	λ	6	1	1	10	–	7.1.2

Bibliography

- [1] J. J. Hopfield, “Theory of the Contribution of excitons to the Complex Dielectric Constant of Crystals,” *Phys. Rev.*, vol. 112, no. 5, p. 1555, 1958.
- [2] C. Weisbuch, M. Nishioka, A. Ishikawa, and Y. Arakawa, “Observation of the coupled exciton-photon mode splitting in a semiconductor quantum microcavity,” *Phys. Rev. Lett.*, vol. 69, no. 23, p. 3314, 1992.
- [3] J. Baumberg, P. Savvidis, R. Stevenson, A. Tartakovskii, M. Skolnick, D. Whittaker, and J. Roberts, “Parametric oscillation in a vertical microcavity: A polariton condensate or micro-optical parametric oscillation,” *Phys. Rev. B*, vol. 62, p. R16247, dec 2000.
- [4] P. G. Savvidis, J. J. Baumberg, R. M. Stevenson, M. S. Skolnick, D. M. Whittaker, and J. S. Roberts, “Angle-resonant stimulated polariton amplifier,” *Phys. Rev. Lett.*, vol. 84, p. 1547, feb 2000.
- [5] C. Ciuti, P. Schwendimann, B. Deveaud, and A. Quattropani, “Theory of the angle-resonant polariton amplifier,” *Phys. Rev. B*, vol. 62, p. R4825, aug 2000.
- [6] A. Baas, J. P. Karr, H. Eleuch, and E. Giacobino, “Optical bistability in semiconductor microcavities,” *Phys. Rev. A*, vol. 69, no. 2, p. 023809, 2004.
- [7] J. Kasprzak, M. Richard, S. Kundermann, A. Baas, P. Jeambrun, J. M. J. Keeling, F. M. Marchetti, M. H. Szymanska, R. André, J. L. Staehli, V. Savona, P. B. Littlewood, B. Deveaud, and L. S. Dang, “Bose – Einstein condensation of exciton polaritons,” *Nature*, vol. 443, no. September, p. 409, 2006.
- [8] E. Wertz, L. Ferrier, D. D. Solnyshkov, P. Senellart, D. Bajoni, A. Miard, A. Lemàtre, G. Malpuech, and J. Bloch, “Spontaneous formation of a polariton condensate in a planar GaAs microcavity,” *Appl. Phys. Lett.*, vol. 95, no. 2009, p. 051108, 2009.
- [9] D. Bajoni, P. Senellart, E. Wertz, I. Sagnes, A. Miard, A. Lemaître, and J. Bloch, “Polariton Laser Using Single Micropillar GaAs-GaAlAs Semiconductor Cavities,” *Phys. Rev. Lett.*, vol. 100, p. 047401, jan 2008.

Bibliography

- [10] G. Christmann, R. Butté, E. Feltin, J. F. Carlin, and N. Grandjean, “Room temperature polariton lasing in a GaNAlGaN multiple quantum well microcavity,” *Appl. Phys. Lett.*, vol. 93, no. 5, p. 051102, 2008.
- [11] K. G. Lagoudakis, T. Ostatnický, A. V. Kavokin, Y. G. Rubo, R. André, and B. Deveaud-Plédran, “Observation of half-quantum vortices in an exciton-polariton condensate,” *Science*, vol. 326, p. 974, nov 2009.
- [12] G. Nardin, G. Grosso, Y. Léger, B. Pietka, F. Morier-Genoud, and B. Deveaud-Plédran, “Hydrodynamic nucleation of quantized vortex pairs in a polariton quantum fluid,” *Nat. physics*, vol. 7, p. 635, apr 2011.
- [13] F. Manni, K. G. Lagoudakis, T. C. H. Liew, R. André, V. Savona, and B. Deveaud, “Dissociation dynamics of singly charged vortices into half-quantum vortex pairs,” *Nat. commun.*, vol. 3, p. 1309, 2012.
- [14] A. Amo, J. Lefrère, S. Pigeon, C. Adrados, C. Ciuti, I. Carusotto, R. Houdré, E. Giacobino, and A. Bramati, “Superfluidity of polaritons in semiconductor microcavities,” *Nat. physics*, vol. 5, p. 805, sep 2009.
- [15] M. Sich, D. N. Krizhanovskii, M. S. Skolnick, A. V. Gorbach, R. Hartley, D. V. Skryabin, E. A. Cerda-Méndez, K. Biermann, R. Hey, and P. V. Santos, “Observation of bright polariton solitons in a semiconductor microcavity,” *Nat. photon.*, vol. 6, p. 50, nov 2011.
- [16] G. Grosso, G. Nardin, F. Morier-Genoud, Y. Léger, and B. Deveaud-Plédran, “Dynamics of dark-soliton formation in a polariton quantum fluid,” *Phys. Rev. B*, vol. 86, p. 020509, jul 2012.
- [17] R. Hivet, H. Flayac, D. D. Solnyshkov, D. Tanese, T. Boulier, D. Andreoli, E. Giacobino, J. Bloch, A. Bramati, G. Malpuech, and A. Amo, “Half-solitons in a polariton quantum fluid behave like magnetic monopoles,” *Nat. physics*, vol. 8, p. 724, aug 2012.
- [18] A. Armitage, M. S. Skolnick, A. V. Kavokin, D. M. Whittaker, V. N. Astratov, G. A. Gehring, and J. S. Roberts, “Polariton-induced optical asymmetry in semiconductor microcavities,” *Phys. Rev. B*, vol. 58, no. 23, p. 15367, 1998.
- [19] G. Panzarini, L. C. Andreani, A. Armitage, D. Baxter, M. S. Skolnick, V. N. Astratov, J. S. Roberts, A. V. Kavokin, M. R. Vladimirova, and M. A. Kaliteevski, “Exciton-light coupling in single and coupled semiconductor microcavities: Polariton dispersion and polarization splitting,” *Phys. Rev. B*, vol. 59, no. 7, p. 5082, 1999.
- [20] M. Emam-Ismael, V. N. Astratov, M. S. Skolnick, D. M. Whittaker, and J. S. Roberts, “Asymmetric photoluminescence spectra from excitons in a coupled microcavity,” *Phys. Rev. B*, vol. 62, p. 1552, jul 2000.

-
- [21] C. Diederichs and J. Tignon, “Design for a triply resonant vertical-emitting micro-optical parametric oscillator,” *Appl. Phys. Lett.*, vol. 87, no. 25, p. 251107, 2005.
 - [22] O. El Daif, A. Baas, T. Guillet, J.-P. Brantut, R. I. Kaitouni, J. L. Staehli, F. Morier-Genoud, and B. Deveaud, “Polariton quantum boxes in semiconductor microcavities,” *Appl. Phys. Lett.*, vol. 88, no. 6, p. 061105, 2006.
 - [23] H. Cao, S. Pau, Y. Yamamoto, and G. Björk, “Exciton-polariton ladder in a semiconductor microcavity,” *Phys. Rev. B*, vol. 54, p. 8083, sep 1996.
 - [24] J. Wainstain, C. Delalande, D. Gendt, M. Voos, J. Bloch, V. Thierry-Mieg, and R. Planel, “Dynamics of polaritons in a semiconductor multiple-quantum-well microcavity,” *Phys. Rev. B*, vol. 58, p. 7269, sep 1998.
 - [25] R. Rapaport, R. Harel, E. Cohen, A. Ron, E. Linder, and L. N. Pfeiffer, “Negatively charged quantum well polaritons in a GaAs/AlAs microcavity: An analog of atoms in a cavity,” *Phys. Rev. Lett.*, vol. 84, p. 1607, feb 2000.
 - [26] M. Perrin, P. Senellart, A. Lemaître, and J. Bloch, “Polariton relaxation in semiconductor microcavities: Efficiency of electron-polariton scattering,” *Phys. Rev. B*, vol. 72, p. 075340, aug 2005.
 - [27] C. Ouellet-Plamondon, G. Sallen, F. Jabeen, D. Y. Oberli, and B. Deveaud, “Multiple polariton modes originating from the coupling of quantum wells in planar microcavity,” *Phys. Rev. B*, vol. 92, no. 7, p. 075313, 2015.
 - [28] C. Ouellet-Plamondon, G. Sallen, F. Morier-Genoud, D. Y. Oberli, M. T. Portella-Oberli, and B. Deveaud, “Spatial multistability induced by cross interactions of confined polariton modes,” *Phys. Rev. B*, vol. 93, p. 085313, 2016.
 - [29] C. Ouellet-Plamondon, G. Sallen, F. Morier-Genoud, D. Y. Oberli, M. T. Portella-Oberli, and B. Deveaud, “Reservoir-induced decoherence of resonantly excited confined polaritons,” *Phys. Rev. B*, vol. 95, p. 085302, 2017.
 - [30] P. Y. Yu and M. Cardona, *Fundamentals of Semiconductors: Physics and Material Properties*. Springer, 3rd ed., 2005.
 - [31] V. Savona, Z. Hradil, A. Quattropani, and P. Schwendimann, “Quantum theory of quantum-well polaritons in semiconductor microcavities,” *Phys. Rev. B*, vol. 49, no. 13, p. 8774, 1994.
 - [32] G. Bastard, *Wave Mechanics Applied to Semiconductor Heterostructures*. Les éditions de physique, Les Ulis Cedex, 1988.
 - [33] M. Kira and S. W. Koch, *Semiconductor Quantum Optics*. Cambridge University Press, 1 ed., 2012.

Bibliography

- [34] H. Haug and S. W. Koch, *Quantum theory of the Optical and Electronic Properties of Semiconductors*. World scientific, 4th ed., 2004.
- [35] A. Tredicucci, Y. Chen, F. Bassani, J. Massies, C. Deparis, and G. Neu, “Center-of-mass quantization of excitons and polariton interference in GaAs thin layers,” *Phys. Rev. B*, vol. 47, no. 16, p. 10348, 1993.
- [36] V. Savona, L. C. Andreani, P. Schwendimann, and A. Quattropani, “Quantum well excitons in semiconductor microcavities: unified treatment of weak and strong coupling regimes,” *Solid State Commun.*, vol. 93, no. 9, p. 733, 1995.
- [37] V. Savona, *Optical properties of quantum well polaritons in microcavities*. PhD thesis, EPFL, 1997.
- [38] L. C. Andreani, F. Tassone, and F. Bassani, “Radiative lifetime of free excitons in quantum wells,” *Solid State Commun.*, vol. 77, no. 9, p. 641, 1991.
- [39] M. S. Skolnick, T. A. Fisher, and D. M. Whittaker, “Strong coupling phenomena in quantum microcavity structures,” *Semicond. Sci. Technol.*, vol. 13, p. 645, 1998.
- [40] B. E. A. Saleh and M. C. Teich, *Fundamentals of photonics*. John Wiley & Sons, Inc, 2nd editio ed., 2007.
- [41] H. Deng, H. Haug, and Y. Yamamoto, “Exciton-polariton Bose-Einstein condensation,” *Rev. Mod. Phys.*, vol. 82, p. 1489, 2010.
- [42] J. M. Gérard, B. Sermage, B. Gayral, B. Legrand, E. Costard, and V. Thierry-Mieg, “Enhanced Spontaneous Emission by Quantum Boxes in a Monolithic Optical Microcavity,” *Phys. Rev. Lett.*, vol. 81, p. 1110, 1998.
- [43] K. Winkler, C. Schneider, J. Fischer, A. Rahimi-Iman, M. Amthor, A. Forchel, S. Reitzenstein, S. Höfling, and M. Kamp, “Electroluminescence from spatially confined exciton polaritons in a textured microcavity,” *Appl. Phys. Lett.*, vol. 102, p. 041101, 2013.
- [44] K. Winkler, J. Fischer, A. Schade, M. Amthor, R. Dall, J. Geßler, M. Emmerling, E. A. Ostrovskaya, M. Kamp, C. Schneider, and S. Höfling, “A polariton condensate in a photonic crystal potential landscape,” *New Journ. Phys.*, vol. 17, no. 2, p. 023001, 2015.
- [45] J. M. Zajac, W. Langbein, M. Hugues, and M. Hopkinson, “Polariton states bound to defects in GaAs/AlAs planar microcavities,” *Phys. Rev. B*, vol. 85, p. 165309, apr 2012.
- [46] P. Lugan, D. Sarchi, and V. Savona, “Theory of trapped polaritons in patterned microcavities,” *Phys. Stat. Sol. C*, vol. 3, p. 2428, aug 2006.

-
- [47] S. Pau, G. Björk, J. Jacobson, H. Cao, and Y. Yamamoto, “Microcavity exciton-polariton splitting in the linear regime,” *Phys. Rev. B*, vol. 51, no. 9, p. 14437, 1995.
- [48] F. Tassone, C. Piermarocchi, V. Savona, A. Quattropani, and P. Schwendimann, “Photoluminescence decay times in strong-coupling semiconductor microcavities,” *Phys. Rev. B*, vol. 53, p. R7642, mar 1996.
- [49] V. Savona and C. Piermarocchi, “Microcavity Polaritons: Homogeneous and Inhomogeneous Broadening in the Strong Coupling Regime,” *phys. stat. sol. (a)*, vol. 164, no. 1, p. 45, 1997.
- [50] V. Savona, C. Piermarocchi, A. Quattropani, F. Tassone, and P. Schwendimann, “Microscopic Theory of Motional Narrowing of Microcavity Polaritons in a Disordered Potential,” *Phys. Rev. Lett.*, vol. 78, p. 4470, 1997.
- [51] V. Savona, “Effect of interface disorder on quantum well excitons and microcavity polaritons,” *Journal of physics. Condensed matter : an Institute of Physics journal*, vol. 19, no. 29, p. 295208, 2007.
- [52] D. M. Whittaker, “What Determines Inhomogeneous Line Widths in Semiconductor Microcavities?,” *Phys. Rev. Lett.*, vol. 80, p. 4791, 1997.
- [53] T. A. Fisher, A. M. Afshar, M. S. Skolnick, D. M. Whittaker, and J. S. Roberts, “Vacuum Rabi coupling enhancement and Zeeman splitting in semiconductor quantum microcavity structures in a high magnetic field,” *Phys. Rev. B*, vol. 53, p. R10469, apr 1996.
- [54] G. Rochat, C. Ciuti, V. Savona, C. Piermarocchi, A. Quattropani, and P. Schwendimann, “Excitonic Bloch equations for a two-dimensional system of interacting excitons,” *Phys. Rev. B*, vol. 61, p. 13856, may 2000.
- [55] A. Verger, C. Ciuti, and I. Carusotto, “Polariton quantum blockade in a photonic dot,” *Phys. Rev. B*, vol. 73, p. 193306, may 2006.
- [56] N. Takemura, S. Trebaol, M. D. Anderson, V. Kohnle, Y. Leger, D. Y. Oberli, M. T. Portella-Oberli, and B. Deveaud, “Two-dimensional Fourier transform spectroscopy of exciton-polaritons and their interactions,” *Phys. Rev. B*, vol. 92, p. 125415, 2015.
- [57] C. Ciuti, V. Savona, C. Piermarocchi, A. Quattropani, and P. Schwendimann, “Role of the exchange of carriers in elastic exciton-exciton scattering in quantum wells,” *Phys. Rev. B*, vol. 58, no. 12, p. 7926, 1998.
- [58] N. Takemura, M. D. Anderson, S. Trebaol, S. Biswas, D. Y. Oberli, M. T. Portella-Oberli, and B. Deveaud, “Dephasing effects on coherent exciton-polaritons and the breakdown of the strong coupling regime,” *Phys. Rev. B*, vol. 92, p. 235305, 2015.

Bibliography

- [59] S. Mukamel, *Principles of nonlinear optical spectroscopy*. New York: Oxford University Press, 1995.
- [60] G. Rochat, “Travail Pratique de Diplome: Effets des corrélations Coulombiennes sur les Propriétés Optiques de Systèmes Confinés,” 1999.
- [61] M. Wouters and I. Carusotto, “Excitations in a Nonequilibrium Bose-Einstein Condensate of Exciton Polaritons,” *Phys. Rev. Lett.*, vol. 99, p. 140402, oct 2007.
- [62] I. Carusotto and C. Ciuti, “Quantum fluids of light,” *Rev. Mod. Phys.*, vol. 85, no. March, p. 299, 2013.
- [63] S. Stringari and L. Pitaevskii, *Bose-Einstein condensation*. Oxford: Clarendon Press, 2003.
- [64] S. Kéna-Cohen and S. R. Forrest, “Room-temperature polariton lasing in an organic single-crystal microcavity,” *Nat. photon.*, vol. 4, no. 6, p. 371, 2010.
- [65] F. Tassone, C. Piermarocchi, V. Savona, A. Quattropani, and P. Schwendimann, “Bottleneck effects in the relaxation and photoluminescence of microcavity polaritons,” *Phys. Rev. B*, vol. 56, no. 12, p. 7554, 1997.
- [66] J. Kasprzak, D. D. Solnyshkov, R. André, L. S. Dang, and G. Malpuech, “Formation of an exciton polariton condensate: Thermodynamic versus kinetic regimes,” *Phys. Rev. Lett.*, vol. 101, no. October, p. 146404, 2008.
- [67] D. D. Solnyshkov, H. Terças, K. Dini, and G. Malpuech, “Hybrid Boltzmann–Gross-Pitaevskii theory of Bose-Einstein condensation and superfluidity in open driven-dissipative systems,” *Phys. Rev. A*, vol. 89, p. 033626, mar 2014.
- [68] H. Flayac, I. G. Savenko, M. Mottonen, and T. Ala-Nissila, “Quantum treatment of the Bose-Einstein condensation in nonequilibrium systems,” *Phys. Rev. B*, vol. 92, no. 11, p. 5117, 2015.
- [69] J. Y. Marzin, M. N. Charasse, and B. Sermage, “Optical investigation of a new type of valence-band configuration on $\text{In}_x\text{Ga}_{1-x}\text{As}$ -GaAs strained superlattices,” *Phys. Rev. B*, vol. 31, no. 12, p. 8298, 1985.
- [70] D. J. Arent, K. Deneffe, C. Van Hoof, J. De Boeck, and G. Borghs, “Strain effects and band offsets in GaAs/InGaAs strained layered quantum structures,” *J. Appl. Phys.*, vol. 66, no. 4, p. 1739, 1989.
- [71] M. Moran, P. Dawson, and K. J. Moore, “The nature of the light-hole potential profile in GaAs-InGaAs double quantum well structures,” *Solid State Commun.*, vol. 107, no. 3, p. 119, 1998.

-
- [72] K. Radhakrishnan, "Indium desorption from strained InGaAs/GaAs quantum wells grown by molecular beam epitaxy," *Journal of Vacuum Science & Technology A: Vacuum, Surfaces, and Films*, vol. 12, no. 1994, p. 1124, 1994.
 - [73] H. Yu, C. Roberts, and R. Murray, "Influence of indium segregation on the emission from InGaAs/GaAs quantum wells," *Appl. Phys. Lett.*, vol. 66, no. 17, p. 2253, 1995.
 - [74] NextNano, "Nextnano."
 - [75] C. Sirtori, F. Capasso, J. Faist, and S. Scandolo, "Nonparabolicity and a sum rule associated with bound-to-bound and bound-to-continuum intersubband transitions in quantum wells," *Phys. Rev. B*, vol. 50, no. 12, p. 8663, 1994.
 - [76] I. Vurgaftman, J. R. Meyer, and L. R. Ram-Mohan, "Band parameters for III-V compound semiconductors and their alloys," *J. Appl. Phys.*, vol. 89, no. 11 I, p. 5815, 2001.
 - [77] J. Szczytko, L. Kappei, F. Morier-Genoud, T. Guillet, M. T. Portella-Oberli, and B. Deveaud, "Excitons or free carriers? That is the question," *Phys. Stat. Sol. C*, vol. 1, p. 493, feb 2004.
 - [78] J. Szczytko, L. Kappei, J. Berney, F. Morier-Genoud, M. T. Portella-Oberli, and B. Deveaud, "Origin of excitonic luminescence in quantum wells: Direct comparison of the exciton population and Coulomb correlated plasma models," *Phys. Rev. B*, vol. 71, p. 195313, may 2005.
 - [79] M. Portella-Oberli, J. Berney, L. Kappei, F. Morier-Genoud, J. Szczytko, and B. Deveaud-Plédran, "Dynamics of Trion Formation in $\text{In}_x\text{Ga}_{1-x}\text{As}$ Quantum Wells," *Phys. Rev. Lett.*, vol. 102, p. 096402, mar 2009.
 - [80] J. Szczytko, L. Kappei, J. Berney, F. Morier-Genoud, M. T. Portella-Oberli, and B. Deveaud, "Determination of the Exciton Formation in Quantum Wells from Time-Resolved Interband Luminescence," *Phys. Rev. Lett.*, vol. 93, p. 137401, sep 2004.
 - [81] S. Gehrsitz, F. K. Reinhart, C. Gourgon, N. Herres, A. Vonlanthen, and H. Sigg, "The refractive index of $\text{Al}_x\text{Ga}_{1-x}\text{As}$ below the band gap: Accurate determination and empirical modeling," *J. Appl. Phys.*, vol. 87, no. 11, p. 7825, 2000.
 - [82] T. Wang, M. Bayer, A. Forchel, N. A. Gippius, and V. Kulakovskii, "Magneto-optical study of excitonic states in $\text{In}_{0.045}\text{Ga}_{0.955}\text{As}/\text{GaAs}$ multiple coupled quantum wells," *Phys. Rev. B*, vol. 62, no. 11, p. 7433, 2000.
 - [83] G. Nardin, G. Moody, R. Singh, T. M. Autry, H. Li, F. Morier-Genoud, and S. T. Cundiff, "Coherent Excitonic Coupling in an Asymmetric Double InGaAs Quantum Well Arises from Many-Body Effects," *Phys. Rev. Lett.*, vol. 112, p. 046402, aug 2014.

Bibliography

- [84] G. R. Hayes, S. Haacke, M. Kauer, R. P. Stanley, R. Houdré, U. Oesterle, and B. Deveaud, “Resonant Rayleigh scattering versus incoherent luminescence in semiconductor microcavities,” *Phys. Rev. B*, vol. 58, no. 16, p. 10175, 1998.
- [85] R. Houdre, C. Weisbuch, R. P. Stanley, U. Oesterle, and M. Ilegems, “Nonlinear emission of semiconductor microcavities in the strong coupling regime,” *Phys. Rev. Lett.*, vol. 85, p. 2793, sep 2000.
- [86] M. Saba, F. Quochi, C. Ciuti, U. Oesterle, J. L. Staehli, B. Deveaud, G. Bongiovanni, and A. Mura, “Crossover from exciton to biexciton polaritons in semiconductor microcavities,” *Phys. Rev. Lett.*, vol. 85, p. 385, jul 2000.
- [87] R. Houdré, C. Weisbuch, R. P. Stanley, U. Oesterle, P. Pellandini, and M. Ilegems, “Measurement of Cavity-Polariton Dispersion Curve from Angle-Resolve Photoluminescence Experiments,” *Phys. Rev. Lett.*, vol. 73, no. 15, p. 2043, 1994.
- [88] R. Houdré, R. P. Stanley, and M. Ilegems, “Vacuum-field Rabi splitting in the presence of inhomogeneous broadening: Resolution of a homogeneous linewidth in an inhomogeneously broadened system,” *Phys. Rev. A*, vol. 53, p. 2711, apr 1996.
- [89] G. Bongiovanni, A. Mura, F. Quochi, S. Gürtler, J. L. Staehli, F. Tassone, R. P. Stanley, U. Oesterle, and R. Houdré, “Coherent exciton-photon dynamics in semiconductor microcavities: The influence of inhomogeneous broadening,” *Phys. Rev. B*, vol. 55, p. 7084, mar 1997.
- [90] A. I. Tartakovskii, M. Emam-Ismaïl, R. M. Stevenson, M. S. Skolnick, V. N. Astratov, D. M. Whittaker, J. J. Baumberg, and J. S. Roberts, “Relaxation bottleneck and its suppression in semiconductor microcavities,” *Phys. Rev. B*, vol. 62, p. R2283, jul 2000.
- [91] R. Butté, G. Delalleau, A. I. Tartakovskii, M. S. Skolnick, V. N. Astratov, J. J. Baumberg, G. Malpuech, A. Di Carlo, A. V. Kavokin, and J. S. Roberts, “Transition from strong to weak coupling and the onset of lasing in semiconductor microcavities,” *Phys. Rev. B*, vol. 65, p. 205310, apr 2002.
- [92] R. M. Stevenson, V. N. Astratov, M. S. Skolnick, J. S. Roberts, and G. Hill, “Uncoupled excitons in semiconductor microcavities detected in resonant Raman scattering,” *Phys. Rev. B*, vol. 67, p. 081301, feb 2003.
- [93] A. A. Khalifa, A. P. D. Love, D. N. Krizhanovskii, M. S. Skolnick, and J. S. Roberts, “Electroluminescence emission from polariton states in GaAs-based semiconductor microcavities,” *Appl. Phys. Lett.*, vol. 92, no. 2008, p. 061107, 2008.
- [94] B. Deveaud, J. Y. Emery, A. Chomette, B. Lambert, and M. Baudet, “Observation of one-monolayer size fluctuations in a GaAs/GaAlAs superlattice,” *Appl. Phys. Lett.*, vol. 45, no. 1984, p. 1078, 1984.

-
- [95] H. Q. Hou, Y. Segawa, Y. Aoyagi, S. Namba, and J. M. Zhou, “Exciton binding energy in $\text{In}_x\text{Ga}_{1-x}\text{As}/\text{GaAs}$ strained quantum wells,” *Phys. Rev. B*, vol. 42, no. 2, p. 1284, 1990.
 - [96] R. Houdré, J. L. Gibernon, P. Pellandini, R. P. Stanley, U. Oesterle, C. Weisbuch, J. O’Gorman, B. Roycroft, and M. Ilegems, “Saturation of the strong-coupling regime in a semiconductor microcavity: Free-carrier bleaching of cavity polaritons,” *Phys. Rev. B*, vol. 52, no. 11, p. 7810, 1995.
 - [97] A. Chomette, B. Lambert, B. Deveaud, F. Cleerot, A. Regreny, and G. Bastard, “Exciton Binding Energy in Small-Period $\text{GaAs} / \text{Ga}_{1-x}\text{Al}_x\text{As}$,” *EPL (Europhysics Letters)*, vol. 4, p. 461, 1987.
 - [98] C. Schneider, A. Rahimi-Iman, N. Y. Kim, J. Fischer, I. G. Savenko, M. Amthor, M. Lerner, A. Wolf, L. Worschech, V. D. Kulakovskii, I. a. Shelykh, M. Kamp, S. Reitzenstein, A. Forchel, Y. Yamamoto, and S. Höfling, “An electrically pumped polariton laser,” *Nature*, vol. 497, p. 348, may 2013.
 - [99] P. Bhattacharya, A. Das, S. Bhowmick, M. Jankowski, and C. S. Lee, “Effect of magnetic field on polariton emission characteristics of a quantum-well microcavity diode,” *Appl. Phys. Lett.*, vol. 100, p. 171106, 2012.
 - [100] P. Bhattacharya, B. Xiao, A. Das, S. Bhowmick, and J. Heo, “Solid State Electrically Injected Exciton-Polariton Laser,” *Phys. Rev. Lett.*, vol. 110, no. May, p. 206403, 2013.
 - [101] P. Cilibrizzi, A. Askitopoulos, M. Silva, F. Bastiman, E. Clarke, J. M. Zajac, W. Langbein, P. G. Lagoudakis, P. Cilibrizzi, A. Askitopoulos, M. Silva, F. Bastiman, E. Clarke, J. M. Zajac, W. Langbein, and P. G. Lagoudakis, “Polariton condensation in a strain-compensated planar microcavity with InGaAs quantum wells,” *Appl. Phys. Lett.*, vol. 105, no. 2014, p. 191118, 2015.
 - [102] M. Richard, *Quasi-condensation de polaritons sous excitation incohérente dans les microcavités II-VI à base de CdTe*. PhD thesis, Grenoble, 2004.
 - [103] M. Richard, J. Kasprzak, R. Romestain, R. André, and L. S. Dang, “Spontaneous Coherent Phase Transition of Polaritons in CdTe Microcavities,” *Phys. Rev. Lett.*, vol. 94, no. 18, p. 187401, 2005.
 - [104] L. Tinkler, P. M. Walker, E. Clarke, D. N. Krizhanovskii, F. Bastiman, M. Durska, and M. S. Skolnick, “Design and characterization of high optical quality $\text{InGaAs}/\text{GaAs}/\text{AlGaAs}$ -based polariton microcavities,” *Appl. Phys. Lett.*, vol. 106, no. 2, p. 021109, 2015.
 - [105] M. Pieczarka, M. Syperek, Ł. Dusanowski, J. Misiewicz, F. Langer, and G. Sęk, “Ghost Branch Photoluminescence From a Polariton Fluid Under Nonresonant Excitation,” *Phys. Rev. Lett.*, vol. 115, no. October, p. 186401, 2015.

Bibliography

- [106] B. Besga, C. Vanepf, J. Reichel, J. Estève, A. Reinhard, J. Miguel-Sánchez, A. Imamoglu, and T. Volz, “Polariton boxes in a tunable fiber cavity,” *Phys. Rev. Appl.*, vol. 3, no. 1, p. 014008, 2015.
- [107] D. Bajoni, P. Senellart, A. Lemaître, and J. Bloch, “Photon lasing in GaAs microcavity: Similarities with a polariton condensate,” *Phys. Rev. B*, vol. 76, p. 201305, nov 2007.
- [108] D. N. Krizhanovskii, K. G. Lagoudakis, M. Wouters, B. Pietka, R. Bradley, K. Guda, D. Whittaker, M. S. Skolnick, B. Deveaud-Plédran, M. Richard, R. André, and L. Dang, “Coexisting nonequilibrium condensates with long-range spatial coherence in semiconductor microcavities,” *Phys. Rev. B*, vol. 80, p. 045317, jul 2009.
- [109] J. D. Berger, O. Lyngnes, H. M. Gibbs, G. Khitrova, T. R. Nelson, E. K. Lindmark, A. V. Kavokin, M. A. Kaliteevski, and V. V. Zapasskii, “Magnetic-field enhancement of the exciton-polariton splitting in a semiconductor quantum-well microcavity: The strong coupling threshold,” *Phys. Rev. B*, vol. 54, p. 1975, jul 1996.
- [110] A. Armitage, T. A. Fisher, M. S. Skolnick, D. M. Whittaker, and P. Kinsler, “Exciton polaritons in semiconductor quantum microcavities in a high magnetic field,” *Phys. Rev. B*, vol. 55, no. 24, p. 395, 1997.
- [111] T. Wimbauer, K. Oettinger, A. L. Efros, B. K. Meyer, and H. Brugger, “Zeeman splitting of the excitonic recombination in $\text{In}_{\{x\}}\text{Ga}_{\{1-x\}}\text{As}/\text{GaAs}$ single quantum wells,” *Phys. Rev. B*, vol. 50, no. 12, p. 8889, 1994.
- [112] R. Kotlyar, T. Reinecke, M. Bayer, and A. Forchel, “Zeeman spin splittings in semiconductor nanostructures,” *Phys. Rev. B*, vol. 63, p. 085310, feb 2001.
- [113] E. Wertz, L. Ferrier, D. D. Solnyshkov, R. Johne, D. Sanvitto, A. Lemaître, I. Sagnes, R. Grousson, A. V. Kavokin, P. Senellart, G. Malpuech, and J. Bloch, “Spontaneous formation and optical manipulation of extended polariton condensates,” *Nat. physics*, vol. 6, p. 860, aug 2010.
- [114] K. Lagoudakis, *On the Physics of Exciton-Polariton Condensates*. PhD thesis, EPFL, 2010.
- [115] N. F. Mott, “The Basis of the Electron Theory of Metals, with Special Reference to the Transition Metals,” *Proc. Phys. Soc. A*, vol. 62, p. 416, 1949.
- [116] M. Greiner, O. Mandel, T. Esslinger, T. W. Hänsch, and I. Bloch, “Quantum phase transition from a superfluid to a Mott insulator in a gas of ultracold atoms,” *Nature*, vol. 415, no. 6867, p. 39, 2002.
- [117] L. Kappei, J. Szczytko, F. Morier-Genoud, and B. Deveaud, “Direct Observation of the Mott Transition in an Optically Excited Semiconductor Quantum Well,” *Phys. Rev. Lett.*, vol. 94, p. 147403, apr 2005.

- [118] H. Schweizer, A. Forchel, A. Hangleiter, S. Schmitt-Rink, J. P. Lowenau, and H. Haug, “Ionization of the Direct-Gap Exciton in Photoexcited Germanium,” *Phys. Rev. Lett.*, vol. 51, no. 8, p. 698, 1983.
- [119] D. A. Kleinman and R. C. Miller, “Band-gap renormalization in semiconductor quantum wells containing carriers,” *Phys. Rev. B*, vol. 32, no. 4, p. 2266, 1985.
- [120] G. Rossbach, *High-Density Excitonic Effects in GaN : Mott-Transition and Polariton Lasing*. PhD thesis, EPFL, 2014.
- [121] A. Yariv, *Quantum electronics*. John Wiley & Sons, Inc, 3rd ed., 1989.
- [122] A. Patanè, A. Polimeni, M. Capizzi, and F. Martelli, “Linewidth analysis of the photoluminescence of $\text{In}_x\text{Ga}_{1-x}\text{As}/\text{GaAs}$ quantum wells ($x=0.09, 0.18, 1.0$),” *Phys. Rev. B*, vol. 52, no. 4, p. 2784, 1995.
- [123] G. Malpuech, A. Kavokin, J. Leymarie, P. Disseix, and A. Vasson, “Optical spectroscopy study of the phase of the reflection coefficient of a single quantum well in the exciton resonance region,” *Phys. Rev. B*, vol. 60, p. 13298, nov 1999.
- [124] S. Martini, A. A. Quivy, A. Tabata, and J. R. Leite, “Influence of the temperature and excitation power on the optical properties of $\text{InGaAs}/\text{GaAs}$ quantum wells grown on vicinal $\text{GaAs}(001)$ surfaces,” *J. Appl. Phys.*, vol. 90, no. 001, p. 2280, 2001.
- [125] G. Tosi, G. Christmann, N. G. Berloff, P. Tsotsis, T. Gao, Z. Hatzopoulos, P. G. Savvidis, and J. J. Baumberg, “Sculpting oscillators with light within a nonlinear quantum fluid,” *Nat. physics*, vol. 8, p. 190, jan 2012.
- [126] P. Tsotsis, P. S. Eldridge, T. Gao, S. I. Tsintzos, Z. Hatzopoulos, and P. G. Savvidis, “Lasing threshold doubling at the crossover from strong to weak coupling regime in GaAs microcavity,” *New Journ. Phys.*, vol. 14, p. 023060, 2012.
- [127] B. Nelsen, G. Liu, M. Steger, D. W. Snoke, R. Balili, K. West, and L. Pfeiffer, “Dissipationless Flow and Sharp Threshold of a Polariton Condensate with Long Lifetime,” *Phys. Rev. X*, vol. 3, no. 4, p. 041015, 2013.
- [128] D. Ballarini, D. Caputo, C. S. Muñoz, M. De Giorgi, L. Dominici, M. H. Szymańska, K. West, L. N. Pfeiffer, G. Gigli, F. P. Laussy, and D. Sanvitto, “Formation of a macroscopically extended polariton condensate without an exciton reservoir,” *arXiv*, vol. 1, p. 1609.05717, 2016.
- [129] G. Grosso, G. Nardin, F. Morier-Genoud, Y. Léger, and B. Deveaud-Plédran, “Soliton Instabilities and Vortex Street Formation in a Polariton Quantum Fluid,” *Phys. Rev. Lett.*, vol. 107, p. 245301, dec 2011.

Bibliography

- [130] a. Tartakovskii, D. Krizhanovskii, D. Kurysh, V. Kulakovskii, M. Skolnick, and J. Roberts, “Polariton parametric scattering processes in semiconductor microcavities observed in continuous wave experiments,” *Phys. Rev. B*, vol. 65, p. 081308, feb 2002.
- [131] H. M. Gibbs, *Optical Bistability: Controlling light with light*. London: Academic press, 1985.
- [132] S. Cecchi, G. Giusfredi, E. Petriella, and P. Salieri, “Observation of Optical Tristability in Sodium Vapors,” *Phys. Rev. Lett.*, vol. 49, no. 26, p. 1928, 1982.
- [133] J. Nalik, W. Lange, and F. Mitschke, “Complexity out of a Simple Structure: The Intricate Multistable Behaviour of an Optical Resonator Filled with Sodium Atoms,” *Appl. Phys. B*, vol. 49, p. 191, 1983.
- [134] A. Joshi and M. Xiao, “Optical multistability in three-level atoms inside an optical ring cavity,” *Phys. Rev. Lett.*, vol. 91, no. 14, p. 143904, 2003.
- [135] J. Sheng, U. Khadka, and M. Xiao, “Realization of all-optical multistate switching in an atomic coherent medium,” *Phys. Rev. Lett.*, vol. 109, no. 22, p. 223906, 2012.
- [136] C. Tamm and C. O. Weiss, “Bistability and optical switching of spatial patterns in a laser,” *Journal of the Optical Society of America B*, vol. 7, no. 6, p. 1034, 1990.
- [137] D. Wilkowski, D. Hennequin, D. Dangoisse, and P. Glorieux, “Multistability and Periodic Alternance in a Multimode $C0_{\{2\}}$ Laser with a Saturable Absorber,” *Chaos, Solitons & Fractals*, vol. 4, p. 1683, 1994.
- [138] A. B. Coates, C. O. Weiss, C. Green, E. J. D’Angelo, J. R. Tredicce, M. Brambilla, M. Cattaneo, L. A. Lugiato, R. Pirovano, F. Prati, A. J. Kent, and G.-L. Oppo, “Dynamical transverse laser patterns. II. Experiments,” *Phys. Rev. A*, vol. 49, no. 2, p. 1452, 1994.
- [139] M. Brambilla, L. A. Lugiato, V. Penna, F. Prati, C. Tamm, and C. O. Weiss, “Transverse laser patterns. II. Variational principle for pattern selection, spatial multistability, and laser hydrodynamics,” *Phys. Rev. A*, vol. 43, no. 9, p. 5114, 1991.
- [140] M. Travagnin, M. Pinna, F. Prati, and L. A. Lugiato, “Optical switching of spatial modes in lasers with a square pump,” *Optics comm*, vol. 108, no. 94, p. 377, 1994.
- [141] N. A. Gippius, I. A. Shelykh, D. D. Solnyshkov, S. S. Gavrilov, Y. G. Rubo, A. V. Kavokin, S. G. Tikhodeev, and G. Malpuech, “Polarization Multistability of Cavity Polaritons,” *Phys. Rev. Lett.*, vol. 98, no. 23, p. 236401, 2007.
- [142] S. S. Gavrilov, N. A. Gippius, S. G. Tikhodeev, and V. D. Kulakovskii, “Multistability of the optical response in a system of quasi-two-dimensional exciton polaritons,” *Journal of Experimental and Theoretical Physics*, vol. 110, no. 5, p. 825, 2010.

-
- [143] E. Cancellieri, F. M. Marchetti, M. H. Szymanska, and C. Tejedor, “Multistability of a two-component exciton-polariton fluid,” *Phys. Rev. B*, vol. 83, no. 21, p. 214507, 2011.
- [144] D. V. Vishnevsky, D. D. Solnyshkov, N. A. Gippius, and G. Malpuech, “Multistability of cavity exciton polaritons affected by the thermally generated exciton reservoir,” *Phys. Rev. B*, vol. 85, no. 15, p. 155328, 2012.
- [145] O. Bozat, I. G. Savenko, and I. A. Shelykh, “Spin multistability in dissipative polariton channels,” *Phys. Rev. B*, vol. 86, no. 3, p. 035413, 2012.
- [146] O. Kyriienko, E. A. Ostrovskaya, O. A. Egorov, I. A. Shelykh, and T. C. H. Liew, “Bistability in microcavities with incoherent optical or electrical excitation,” *Phys. Rev. B*, vol. 90, no. 12, p. 125407, 2014.
- [147] G. Slavcheva, A. V. Gorbach, A. Pimenov, A. G. Vladimirov, and D. V. Skryabin, “Multi-stability and polariton solitons in microcavity wires,” *Opt. Lett.*, vol. 40, no. 8, p. 1787, 2015.
- [148] T. K. Paraïso, M. Wouters, Y. Léger, F. Morier-Genoud, and B. Deveaud-Plédran, “Multistability of a coherent spin ensemble in a semiconductor microcavity,” *Nat. mater.*, vol. 9, p. 655, aug 2010.
- [149] C. Adrados, A. Amo, T. C. H. Liew, R. Hivet, R. Houdré, E. Giacobino, A. V. Kavokin, and A. Bramati, “Spin Rings in Bistable Planar Semiconductor Microcavities,” *Phys. Rev. Lett.*, vol. 105, no. 21, p. 216403, 2010.
- [150] M. De Giorgi, D. Ballarini, E. Cancellieri, F. M. Marchetti, M. H. Szymanska, C. Tejedor, R. Cingolani, E. Giacobino, a. Bramati, G. Gigli, and D. Sanvitto, “Control and Ultrafast Dynamics of a Two-Fluid Polariton Switch,” *Phys. Rev. Lett.*, vol. 109, no. 26, p. 266407, 2012.
- [151] R. Cerna, Y. Léger, T. K. Paraïso, M. Wouters, F. Morier-Genoud, M. T. Portella-Oberli, and B. Deveaud, “Ultrafast tristable spin memory of a coherent polariton gas,” *Nat. commun.*, vol. 4, no. May, p. 2008, 2013.
- [152] S. S. Gavrilov, A. V. Sekretenko, N. A. Gippius, C. Schneider, S. Höfling, M. Kamp, A. Forchel, and V. D. Kulakovskii, “Spin multistability of cavity polaritons in a magnetic field,” *Phys. Rev. B*, vol. 87, p. 201303, may 2013.
- [153] T. Boulier, M. Bamba, A. Amo, C. Adrados, A. Lemaitre, E. Galopin, I. Sagnes, J. Bloch, C. Ciuti, E. Giacobino, and A. Bramati, “Polariton-generated intensity squeezing in semiconductor micropillars,” *Nat. commun.*, vol. 5, p. 3260, 2014.
- [154] H. Abbaspour, S. Trebaol, F. Morier-Genoud, M. T. Portella-Oberli, and B. Deveaud, “Stochastic Resonance in Collective Exciton-Polariton Excitations inside a GaAs Microcavity,” *Phys. Rev. Lett.*, vol. 113, p. 057401, jul 2014.

Bibliography

- [155] H. Abbaspour, S. Trebaol, F. Morier-Genoud, M. T. Portella-Oberli, and B. Deveaud, “Spinor stochastic resonance,” *Phys. Rev. B*, vol. 91, no. 15, p. 155307, 2015.
- [156] H. Abbaspour, G. Sallen, S. Trebaol, F. Morier-Genoud, M. T. Portella-Oberli, and B. Deveaud, “Effect of a noisy driving field on a bistable polariton system,” *Phys. Rev. B*, vol. 92, no. 16, p. 165303, 2015.
- [157] T. Paraïso, *Dynamics of Interactions of Confined Microcavity Polaritons*. PhD thesis, EPFL, 2010.
- [158] M. Wouters, T. K. Paraïso, Y. Léger, R. Cerna, F. Morier-Genoud, M. T. Portella-Oberli, and B. Deveaud-Plédran, “Influence of a nonradiative reservoir on polariton spin multistability,” *Phys. Rev. B*, vol. 87, no. 4, p. 045303, 2013.
- [159] G. Panzarini and L. C. Andreani, “Quantum theory of exciton polaritons in cylindrical semiconductor microcavities,” *Phys. Rev. B*, vol. 60, no. 24, p. 16799, 1999.
- [160] H. Abbaspour, *Noise-Induced Phenomena in Collective Spinor Polariton Excitations*. PhD thesis, EPFL, 2015.
- [161] R. I. Kaitouni, O. El Daïf, A. Baas, M. Richard, T. Paraiso, P. Lugan, T. Guillet, F. Morier-Genoud, J. Ganière, J. Staehli, V. Savona, and B. Deveaud, “Engineering the spatial confinement of exciton polaritons in semiconductors,” *Phys. Rev. B*, vol. 74, p. 155311, oct 2006.
- [162] G. Nardin, Y. Léger, B. Pietka, F. Morier-Genoud, and B. Deveaud-Plédran, “Phase-resolved imaging of confined exciton-polariton wave functions in elliptical traps,” *Phys. Rev. B*, vol. 82, p. 045304, jul 2010.
- [163] G. Grosso, S. Trebaol, M. Wouters, F. Morier-Genoud, M. T. Portella-Oberli, and B. Deveaud, “Nonlinear relaxation and selective polychromatic lasing of confined polaritons,” *Phys. Rev. B*, vol. 90, p. 045307, jul 2014.
- [164] T. Paraïso, D. Sarchi, G. Nardin, R. Cerna, Y. Leger, B. Pietka, M. Richard, O. El Daïf, F. Morier-Genoud, V. Savona, and B. Deveaud-Plédran, “Enhancement of microcavity polariton relaxation under confinement,” *Phys. Rev. B*, vol. 79, p. 045319, jan 2009.
- [165] M. H. Luk, Y. C. Tse, N. H. Kwong, P. T. Leung, P. Lewandowski, R. Binder, and S. Schumacher, “Transverse optical instability patterns in semiconductor microcavities: Polariton scattering and low-intensity all-optical switching,” *Phys. Rev. B*, vol. 87, no. 20, p. 205307, 2013.
- [166] O. A. Egorov, A. Werner, T. C. H. Liew, E. A. Ostrovskaya, and F. Lederer, “Motion of patterns in polariton quantum fluids with spin-orbit interaction,” *Phys. Rev. B*, vol. 89, no. 23, p. 235302, 2014.

-
- [167] R. Cerna, D. Sarchi, T. K. Paraïso, G. Nardin, Y. Léger, M. Richard, B. Pietka, O. El Daif, F. Morier-Genoud, V. Savona, M. T. Portella-Oberli, and B. Deveaud-Plédran, “Coherent optical control of the wave function of zero-dimensional exciton polaritons,” *Phys. Rev. B*, vol. 80, no. 12, p. 121309, 2009.
- [168] L. Ferrier, E. Wertz, R. Johne, D. D. Solnyshkov, P. Senellart, I. Sagnes, A. Lemaître, G. Malpuech, and J. Bloch, “Interactions in Confined Polariton Condensates,” *Phys. Rev. Lett.*, vol. 106, no. March, p. 126401, 2011.
- [169] P. Cristofolini, A. Dreismann, G. Christmann, G. Franchetti, N. G. Berloff, P. Tsotsis, Z. Hatzopoulos, P. G. Savvidis, and J. J. Baumberg, “Optical Superfluid Phase Transitions and Trapping of Polariton Condensates,” *Phys. Rev. Lett.*, vol. 110, p. 186403, may 2013.
- [170] C. Sturm, D. Tanese, H. S. Nguyen, H. Flayac, E. Galopin, a. Lemaître, I. Sagnes, D. Solnyshkov, a. Amo, G. Malpuech, and J. Bloch, “All-optical phase modulation in a cavity-polariton Mach-Zehnder interferometer,” *Nat. commun.*, vol. 5, p. 3278, feb 2014.
- [171] A. Askitopoulos, T. C. H. Liew, H. Ohadi, Z. Hatzopoulos, P. G. Savvidis, and P. G. Lagoudakis, “Robust platform for engineering pure-quantum-state transitions in polariton condensates,” *Phys. Rev. B*, vol. 92, no. 3, p. 035305, 2015.
- [172] T. C. H. Liew, A. V. Kavokin, and I. A. Shelykh, “Optical circuits based on polariton neurons in semiconductor microcavities,” *Phys. Rev. Lett.*, vol. 101, no. 1, p. 016402, 2008.
- [173] M. Vladimirova, S. Cronenberger, D. Scalbert, K. V. Kavokin, A. Miard, A. Lemaître, J. Bloch, D. Solnyshkov, G. Malpuech, and A. V. Kavokin, “Polariton-polariton interaction constants in microcavities,” *Phys. Rev. B*, vol. 82, p. 075301, aug 2010.
- [174] A. Amo, T. C. H. Liew, C. Adrados, R. Houdré, E. Giacobino, a. V. Kavokin, and A. Bramati, “Exciton–polariton spin switches,” *Nat. photon.*, vol. 4, p. 361, apr 2010.
- [175] N. Takemura, S. Trebaol, M. Wouters, and B. Deveaud, “Polaritonic Feshbach resonance,” *Nat. physics*, vol. 10, no. June, p. 500, 2014.
- [176] N. Takemura, S. Trebaol, M. Wouters, M. T. Portella-Oberli, and B. Deveaud, “Heterodyne spectroscopy of polariton spinor interactions,” *Phys. Rev. B*, vol. 90, p. 195307, 2014.
- [177] H. Ohadi, A. Dreismann, Y. G. Rubo, F. Pinsker, Y. del Valle-Inclan Redondo, S. I. Tsintzos, Z. Hatzopoulos, P. G. Savvidis, and J. J. Baumberg, “Spontaneous Spin Bifurcations and Ferromagnetic Phase Transitions in a Spinor Exciton-Polariton Condensate,” *Phys. Rev. X*, vol. 5, no. 3, p. 031002, 2015.

Bibliography

- [178] I. Shelykh, G. Malpuech, K. V. Kavokin, A. V. Kavokin, and P. Bigenwald, “Spin dynamics of interacting exciton polaritons in microcavities,” *Phys. Rev. B*, vol. 70, p. 115301, sep 2004.
- [179] A. Kavokin, G. Malpuech, and M. Glazov, “Optical Spin Hall Effect,” *Phys. Rev. Lett.*, vol. 95, p. 136601, sep 2005.
- [180] C. Leyder, M. Romanelli, J. P. Karr, E. Giacobino, T. C. H. Liew, M. M. Glazov, A. V. Kavokin, G. Malpuech, and A. Bramati, “Observation of the optical spin Hall effect,” *Nat. physics*, vol. 3, p. 628, jul 2007.
- [181] F. Manni, Y. Léger, Y. G. Rubo, R. André, and B. Deveaud, “Hyperbolic spin vortices and textures in exciton-polariton condensates,” *Nat. commun.*, vol. 3, p. 1309, jan 2013.
- [182] D. Sarchi, I. Carusotto, M. Wouters, and V. Savona, “Coherent dynamics and parametric instabilities of microcavity polaritons in double-well systems,” *Phys. Rev. B*, vol. 77, no. 12, p. 125324, 2008.
- [183] T. C. H. Liew and V. Savona, “Single photons from coupled quantum modes,” *Phys. Rev. Lett.*, vol. 104, no. 18, p. 183601, 2010.
- [184] O. Kyriienko and T. C. H. Liew, “Triggered single-photon emitters based on stimulated parametric scattering in weakly nonlinear systems,” *Phys. Rev. A*, vol. 90, no. 6, p. 063805, 2014.
- [185] C. Ciuti, “Branch-entangled polariton pairs in planar microcavities and photonic wires,” *Phys. Rev. B*, vol. 69, p. 245304, jun 2004.
- [186] S. Portolan, O. Di Stefano, S. Savasta, and V. Savona, “Emergence of entanglement out of a noisy environment: The case of microcavity polaritons,” *EPL (Europhysics Letters)*, vol. 88, p. 20003, 2009.
- [187] T. C. H. Liew and V. Savona, “Multipartite polariton entanglement in semiconductor microcavities,” *Phys. Rev. A*, vol. 84, no. 3, p. 032301, 2011.
- [188] T. C. H. Liew and V. Savona, “Multimode entanglement in coupled cavity arrays,” *New Journ. Phys.*, vol. 15, p. 025015, 2013.
- [189] D. Pagel, H. Fehske, J. Sperling, and W. Vogel, “Multipartite entangled light from driven microcavities,” *Phys. Rev. A*, vol. 88, no. 4, p. 042310, 2013.
- [190] T. Byrnes, K. Wen, and Y. Yamamoto, “Macroscopic quantum computation using Bose-Einstein condensates,” *Phys. Rev. A*, vol. 85, no. 4, p. 040306, 2012.
- [191] S. S. Demirchyan, I. Y. Chestnov, A. P. Alodjants, M. M. Glazov, and A. V. Kavokin, “Qubits based on polariton rabi oscillators,” *Phys. Rev. Lett.*, vol. 112, no. 19, p. 196403, 2014.

-
- [192] D. D. Solnyshkov, O. Bleu, and G. Malpuech, “All optical controlled-NOT gate based on an exciton-polariton circuit,” *Superlattices and Microstructures*, vol. 83, p. 466, 2015.
 - [193] O. Kyriienko and T. C. H. Liew, “Exciton-Polariton Quantum Gates Based on Continuous Variables,” *Phys. Rev. B*, vol. 93, p. 035301, 2016.
 - [194] X. Marie, P. Renucci, S. Dubourg, T. Amand, P. Le Jeune, J. Barrau, J. Bloch, and R. Planel, “Coherent control of exciton polaritons in a semiconductor microcavity,” *Phys. Rev. B*, vol. 59, no. 4, p. R2494, 1999.
 - [195] P. Borri, J. R. Jensen, W. Langbein, and J. M. Hvam, “Direct evidence of reduced dynamic scattering in the lower polariton of a semiconductor microcavity,” *Phys. Rev. B*, vol. 61, no. 20, p. R13377, 2000.
 - [196] S. Savasta, O. Di Stefano, V. Savona, and W. Langbein, “Quantum complementarity of microcavity polaritons,” *Phys. Rev. Lett.*, vol. 94, no. 24, p. 246401, 2005.
 - [197] C. Diederichs, J. Tignon, G. Dasbach, C. Ciuti, A. Lemaître, J. Bloch, P. Roussignol, and C. Delalande, “Parametric oscillation in vertical triple microcavities,” *Nature*, vol. 440, p. 904, apr 2006.
 - [198] M. Romanelli, C. Leyder, J. P. Karr, E. Giacobino, and A. Bramati, “Four Wave Mixing Oscillation in a Semiconductor Microcavity : Generation of Two Correlated Polariton Populations,” *Phys. Rev. Lett.*, vol. 98, no. March, p. 106401, 2007.
 - [199] M. Wouters, I. Carusotto, and C. Ciuti, “Spatial and spectral shape of inhomogeneous nonequilibrium exciton-polariton condensates,” *Phys. Rev. B*, vol. 77, p. 115340, mar 2008.
 - [200] A. P. D. Love, D. N. Krizhanovskii, D. M. Whittaker, R. Bouchekioua, D. Sanvitto, S. A. Rizeiqi, R. Bradley, M. S. Skolnick, P. R. Eastham, R. André, and L. S. Dang, “Intrinsic Decoherence Mechanisms in the Microcavity Polariton Condensate,” *Phys. Rev. Lett.*, vol. 101, p. 067404, aug 2008.
 - [201] L. Dominici, D. Colas, S. Donati, J. P. R. Cuartas, M. D. Giorgi, D. Ballarini, G. Guirales, A. Bramati, G. Gigli, F. P. Laussy, and D. Sanvitto, “Ultrafast Control and Rabi Oscillations of Polaritons,” *Phys. Rev. Lett.*, vol. 113, no. November, p. 226401, 2014.
 - [202] S. S. Gavrilov, A. S. Brichkin, A. A. Demenev, A. A. Dorodnyy, S. I. Novikov, V. D. Kulakovskii, S. G. Tikhodeev, and N. A. Gippius, “Bistability and nonequilibrium transitions in the system of cavity polaritons under nanosecond-long resonant excitation,” *Phys. Rev. B*, vol. 85, no. 7, p. 075319, 2012.
 - [203] E. B. Magnusson, I. G. Savenko, and I. A. Shelykh, “Bistability phenomena in one-dimensional polariton wires,” *Phys. Rev. B*, vol. 84, no. 19, p. 195308, 2011.

Bibliography

- [204] P. Borri, W. Langbein, J. M. Hvam, and F. Martelli, “Well-width dependence of exciton-phonon scattering in $\text{In}_x\text{Ga}_{1-x}\text{As}/\text{GaAs}$ single quantum wells,” *Phys. Rev. B*, vol. 59, no. 3, p. 2215, 1999.
- [205] V. Sala, D. Solnyshkov, I. Carusotto, T. Jacqmin, A. Lemaître, H. Terças, A. Nalitov, M. Abbarchi, E. Galopin, I. Sagnes, J. Bloch, G. Malpuech, and A. Amo, “Spin-Orbit Coupling for Photons and Polaritons in Microstructures,” *Phys. Rev. X*, vol. 5, no. 1, p. 011034, 2015.
- [206] T. Jacqmin, I. Carusotto, I. Sagnes, M. Abbarchi, D. D. Solnyshkov, G. Malpuech, E. Galopin, A. Lemaître, J. Bloch, and A. Amo, “Direct Observation of Dirac Cones and a Flatband in a Honeycomb Lattice for Polaritons,” *Phys. Rev. Lett.*, vol. 112, no. March, p. 116402, 2014.
- [207] M. Milićević, T. Ozawa, P. Andreakou, I. Carusotto, T. Jacqmin, E. Galopin, A. Lemaître, L. Le Gratiet, I. Sagnes, J. Bloch, and A. Amo, “Edge states in polariton honeycomb lattices,” *2D Materials*, vol. 2, no. 3, p. 034012, 2015.
- [208] T. Gao, E. Estrecho, G. Li, O. A. Egorov, X. Ma, K. Winkler, M. Kamp, C. Schneider, S. Höfling, A. G. Truscott, and E. A. Ostrovskaya, “Talbot effect for exciton-polaritons,” *Phys. Rev. Lett.*, vol. 117, no. August, p. 097403, 2016.
- [209] T. Karzig, C. E. Bardyn, N. H. Lindner, and G. Refael, “Topological polaritons,” *Phys. Rev. X*, vol. 5, no. 3, p. 031001, 2015.
- [210] O. Bleu, D. D. Solnyshkov, and G. Malpuech, “Interacting quantum fluid in a polariton topological insulator,” *Phys. Rev. B*, vol. 93, p. 085438, 2016.
- [211] K. Yi and T. Karzig, “Topological polaritons from photonic Dirac cones coupled to excitons in a magnetic field,” *Phys. Rev. B*, vol. 93, p. 104303, 2016.
- [212] A. H. Castro Neto, F. Guinea, N. M. R. Peres, K. S. Novoselov, and A. K. Geim, “The electronic properties of graphene,” *Rev. Mod. Phys.*, vol. 81, no. 1, p. 109, 2009.
- [213] D. R. Hofstadter, “Energy levels and wave functions of Bloch electrons in rational and irrational magnetic fields,” *Phys. Rev. B*, vol. 14, no. 6, p. 2239, 1976.
- [214] M. Aidelsburger, *Artificial gauge fields with ultracold atoms in optical lattices*. Springer, 2015.
- [215] T. Lecomte, V. Ardizzone, M. Abbarchi, C. Diederichs, A. Miard, A. Lemaître, I. Sagnes, P. Senellart, J. Bloch, C. Delalande, J. Tignon, and P. Roussignol, “Optical parametric oscillation in one-dimensional microcavities,” *Phys. Rev. B*, vol. 87, p. 155302, apr 2013.

- [216] H. Miyake, G. a. Siviloglou, C. J. Kennedy, W. C. Burton, and W. Ketterle, “Realizing the Harper Hamiltonian with Laser-Assisted Tunneling in Optical Lattices,” *Phys. Rev. Lett.*, vol. 111, p. 185302, oct 2013.
- [217] M. Aidelsburger, M. Atala, M. Lohse, J. T. Barreiro, B. Paredes, and I. Bloch, “Realization of the Hofstadter Hamiltonian with Ultracold Atoms in Optical Lattices,” *Phys. Rev. Lett.*, vol. 111, p. 185301, oct 2013.

Claudéric Ouellet-Plamondon

Personal details

Address: Avenue de Tivoli 66, 1007 Lausanne, Suisse
Tel: +41 078 973 4447
Email: clauderic.ouellet-plamondon@epfl.ch
Date/Place of Birth: October 19, 1983 (Longueuil, Canada)
Nationality: Canadian
Languages: French (mother tongue), English (full proficiency)

Education

- | | |
|---------------------------------|--|
| April 2012 - present | PhD in Physics, École Polytechnique Fédérale de Lausanne (CH)
Multimode physics in microcavity polariton systems
Supervisor: Benoit Deveaud |
| January 2008 to August 2010 | Master in Engineering Physics (M. Sc. A), École Polytechnique de Montréal (CAN)
Magneto-photoluminescence study of excitons bound to single isoelectronic centers.
Supervisor: Sébastien Francoeur
Nominated for best master's thesis award. |
| September 2003 to December 2007 | Bachelor in Engineering Physics (B. Eng), École Polytechnique de Montréal (CAN)
Applied physics curriculum
Final project on quantum tomography. |

Complementary Formation

- | | |
|-------------|---|
| Summer 2014 | International school of physics "Enrico Fermi" in Varena, Italy
Course titled: Quantum Matter at Ultralow Temperatures |
| Summer 2007 | Internship at the Nuclear Engineering Institute, École Polytechnique de Montréal (CAN)
Validation of cross section calculations in different routines of the software DRAGON.
Supervisor: Guy Marleau |
| Summer 2006 | Internship at the Nuclear Engineering Institute, École Polytechnique de Montréal (CAN)
Conception of a tool for visualising the geometry of nuclear reactor cells using the meshing data for neutron transport calculation from the software DRAGON.
Supervisor: Guy Marleau |

Professional Experience

From september
2010 to july 2011

Research assistant at Scribens laboratory, École polytechnique de Montréal (CAN)

Transposing pattern recognition paradigm to different physics problems
Supervisor: Réjean Plamondon

Teaching assistance (EPFL)

- General physics II: Thermodynamics (23h)
- General physics III: Waves and electromagnetism (69h)
- General physics IV: Geometric and wave optics, quantum mechanics (69h)
- General physics II-IV: exam preparation and correction

Informatic Skills

- Software: Matlab, Origin, Mathematica, Maple, Nextnano
- Programming languages: Labview, C++, Fortran
- OS: Windows, Mac OSX, Linux

Technical Skills

- Optical spectroscopy techniques: Photoluminescence, Magneto-photoluminescence, Reflectivity, Imaging, Fourier optics, polarization optics
- III-V Semiconductor: Design, simulation and characterization of planar microcavities and quantum wells
- Cryogenics: Experience working with He-cooled cryostats (cold finger, He-bath, closed circuit)
- Clean Room: Process optimization for photolithography, wet etching, metal deposition and lift-off

Conference contributions

- 2016 ‘‘International Conference on Spontaneous Coherence in Excitonic Systems’’ (ICSCE8) in St-Andrews, UK
Poster presentation titled : Spatial multistability induced by cross interactions of confined polariton modes
C. Ouellet-Plamondon, G. Sallen, F. Morier-Genoud, D. Y. Oberli, M. T. Portella-Oberli, B. Deveaud
- 2015 Polatom2015 in Bad Honnef, Germany
Oral presentation titled: Multiple polariton modes originating from the coupling of quantum wells in planar microcavity
C. Ouellet-Plamondon, G. Sallen, F. Jabeen, D. Y. Oberli, B. Deveaud
- 2015 EuroMBE 2015 in Canazei, Italy
Oral presentation titled: Polariton modes arising from coupled quantum wells in planar microcavity
C. Ouellet-Plamondon, G. Sallen, F. Jabeen, D. Y. Oberli, B. Deveaud

- 2010 APS March Meeting in Portland, USA
Oral presentation titled: Single nitrogen dyad magnetoluminescence in GaAs
C. Ouellet-Plamondon, S. Marcet, J. F. Klem, S. Francoeur

Publications

- 2017 **Periodic squeezing in a polariton Josephson junction**
A. F. Adiyatullin, M. D. Anderson, H. Flayac, M. T. Portella-Oberli, F. Jabeen,
C. Ouellet-Plamondon, G. Sallen, B. Deveaud
Submitted
- 2017 **Reservoir-induced decoherence of resonantly excited confined polaritons**
C. Ouellet-Plamondon, G. Sallen, F. Morier-Genoud, D. Y. Oberli,
M. T. Portella-Oberli, B. Deveaud
Phys. Rev. B, **95**, 085302
- 2016 **Spatial multistability induced by cross interactions of confined polariton modes**
C. Ouellet-Plamondon, G. Sallen, F. Morier-Genoud, D. Y. Oberli,
M. T. Portella-Oberli, B. Deveaud
Phys. Rev. B, **93**, 085313
- 2015 **Multiple polariton modes originating from the coupling of quantum wells in planar**
C. Ouellet-Plamondon, G. Sallen, F. Jabeen, D. Y. Oberli, B. Deveaud
Phys. Rev. B, **92**, 075313
- 2013 **Spontaneous self-ordered states of vortex-antivortex pairs in a polariton condensate**
F. Manni, T. C. H. Liew, K. G. Lagoudakis, C. Ouellet-Plamondon, R. André,
V. Savona, B. Deveaud
Phys. Rev. B, **88**, 201303 (R)
- 2011 **Excitonic fine structure of out-of-plane nitrogen dyads in GaAs**
C. Ouellet-Plamondon, S. Marcet, J.F. Klem, S. Francoeur
J. Lumin. **131**, 2339
- 2010 **Charged excitons and biexcitons bound to isoelectronic centers**
S. Marcet, C. Ouellet-Plamondon, G. Éthier-Majcher, P. Saint-Jean, R. André,
J. F. Klem, S. Francoeur
Phys. Rev. B, **82**, 235311
- 2009 **Single nitrogen dyad magnetoluminescence in GaAs**
S. Marcet, C. Ouellet-Plamondon, J. F. Klem, S. Francoeur
Phys. Rev. B, **80**, 245404
- 2009 **High spatial resolution confocal microscope with independent excitation and detection scanning capabilities**
S. Marcet, C. Ouellet-Plamondon, S. Francoeur
Rev. Sci. Instr. **80**, 063101

Personal Interests

Jazz guitar and composition, improvised music, biking, hiking